APPROVAL SHEET

Title of Dissertation: NEW METHODS IN MODAL ANALYSIS AND STRUCTURAL DAMAGE IDENTIFICATION

Name of Candidate: Yongfeng Xu
Doctor of Philosophy, 2017

Dissertation and Abstract Approved: Weidong Zhu
Weidong Zhu
Professor
Department of Mechanical Engineering

Date Approved: 4/10/2017

NOTE: *The Approval Sheet with the original signature must accompany the thesis or dissertation. No terminal punctuation is to be used.

ABSTRACT

Title of dissertation: NEW METHODS IN
MODAL ANALYSIS AND
STRUCTURAL DAMAGE IDENTIFICATION

Yongfeng Xu, Doctor of Philosophy, 2017

Dissertation directed by: Dr. Weidong Zhu
Department of Mechanical Engineering

Modal analysis is a subject of structural dynamics, as it describes properties of a linear structure in the modal space with modal properties, including natural frequencies, modal damping ratios, and mode shapes. With the development of transducer and computer technologies, accuracy and efficiency of modal property evaluation have been drastically boosted in the past few decays. As modal properties of a structure are directly related to its structural properties, such as mass, damping, and stiffness, measured modal properties can be processed to identify structural damage.

In this dissertation, new methods in modal analysis and structural damage identification are developed and investigated. In the area of modal analysis, two modal testing methods and two digital signal processing methods for modal analysis are proposed for accurate and efficient modal property evaluation. Specifically, an operational modal analysis method that uses non-contact excitation and measurement to measure out-of-plane and in-plane vibration modes of a plate and a

vibro-acoustic modal test method that uses sound pressure transducers at fixed locations and an impact hammer roving over a test structure are studied; a digital signal processing method for calculating correlation functions and power spectra and one for calculating impulse response functions and frequency response functions are studied. In the area of structural damage identification, two methods for beam structures and two methods for plate structures are proposed without use of models of associated undamaged structures. Specifically, a method using curvature mode shapes of beams and a method using continuous wavelet transforms of mode shapes are studied; a method using mode shapes of plates and one using various curvature mode shapes are studied. In addition, a structural damage identification method that uses free response shapes of beam structures by use of a continuously scanning laser Doppler vibrometer system is proposed. The above mentioned methods are numerically verified and experimentally validated.

NEW METHODS IN MODAL ANALYSIS AND STRUCTURAL DAMAGE IDENTIFICATION

by

Yongfeng Xu

Dissertation submitted to the Faculty of the Graduate School of the University of Maryland, Baltimore County in partial fulfillment of the requirements for the degree of Doctor of Philosophy
2017

Committee:

Dr. Weidong Zhu (Advisor)	Professor, Mechanical Engineering
Dr. Panos Charalambides	Professor, Mechanical Engineering
Dr. Tülay Adali	Distinguished University Professor, Computer Science and Electrical Engineering
Dr. Soobum Lee	Assistant Professor, Mechanical Engineering
Dr. Meilin Yu	Assistant Professor, Mechanical Engineering
Dr. Bedřich Sousedík	Assistant Professor, Mathematics and Statistics

Epigraph

"Every cloud has a silver lining."

— *Anonymous*

This dissertation is dedicated

TO MY PARENTS

for raising me in a warm family with love and freedom

TO MY WIFE AND SON

for inspiring me to push myself beyond limits

Acknowledgments

I am very fortunate to have Dr. Weidong Zhu as my advisor. I would not be writing this dissertation without his patience and generousness. At the beginning of my Ph.D. study, I struggled and had no idea whether I would eventually finish it as I was not making satisfying progress in research. Dr. Zhu kept encouraging me and fully supporting my study at UMBC. He constantly provided me with insightful suggestions to my research, taught me how to organize, draft, and revise a scientific article, and trained me with various projects and research-related tasks. He has set a good example to me as a scholar of integrity and tenacity. All his guidance will definitely benefit me for life. I would like to thank Dr. Shuhui Chen at my alma mater, Sun Yat-sen University in China, for timely referring me to Dr. Zhu as Dr. Zhu planned to recruit a Ph.D. student then. I would also like to thank my dissertation committee members: Dr. Panos Charalambides, Dr. Tülay Adali, Dr. Soobum Lee, Dr. Meilin Yu and Dr. Bedřich Sousedík for agreeing to serve on the committee and reviewing my dissertation.

I would like to thank all my friends and labmates for their friendship and assistance to my study at UMBC. Special thanks go to Kai Wu and Chao Hou for being there for me all these years, especially during my bitter days. I would also like to acknowledge the help and support from staff members in the Department of Mechanical Engineering. Chuck Smithson and Cindy Lutz have been warmhearted and helpful since I came to UMBC.

I would like to gratefully acknowledge financial support from the National Science Foundation through Grant No. CMMI-0600559, CMMI-1229532 and CMMI-1335024.

Last but not least, I owe my deepest thanks to my family. As far as I remember, my parents have never compared me with my peers so that I was able to happily grow up without much pressure from them. They grant me with great freedom to choose what I want to be and how to make it. When I told them “I would like to pursue a Ph.D. in the United States”, they replied “OK, go ahead” without hesitation. My wife has been very considerate as I could completely focus on research in the final year of my Ph.D. study. Whenever I think of our son’s lovely face and hear him saying “baba” (daddy), all my exhaustion will vanish into air. He is our sunshine! Their love has been and will always be my source of courage and energy.

Table of Contents

List of Tables

List of Figures

List of Abbreviations

ABS	Acrylonitrile Butadiene Styrene
CDI	Curvature Damage Index
CMS	Curvature Mode Shape
CPSD	Cross-power Spectral Density
CSLDV	Continuous Scanning Laser Doppler Vibrometer
CWT	Continuous Wavelet Transform
CWTDI	Continuous Wavelet Transform Damage Index
DFT	Discrete Fourier Transform
DOF	Degree-of-freedom
EMA	Experimental Modal Analysis
FFT	Fast Fourier Transform
FRDI	Free-response Damage Index
FRF	Frequency Response Function
FRS	Free Response Shape
IDFT	Inverse Discrete Fourier Transform
IFFT	Inverse Fast Fourier Transform
IRF	Impulse Response Function
MAC	Modal Assurance Criterion
MS	Mode Shape
MSDI	Mode Shape Damage Index
NExT	Natural Excitation Test
ODS	Operating Deflection Shape
OMA	Operational Modal Analysis
SLDV	Scanning Laser Doppler Vibrometer
SNR	Signal-to-noise Ratio
STFT	Short-time Fourier Transform
VMT	Vibro-acoustic Modal Test

Chapter 1

INTRODUCTION

1.1 Modal Analysis

Modal properties of a structure, including natural frequencies, mode shapes, and modal damping ratios, can be identified via modal analysis [1]. There are two types of modal analysis methods: experimental modal analysis (EMA) [1, 2] and operational modal analysis (OMA) or output-only modal analysis [3]. The former requires measurements of excitation on a structure, while the latter does not. In addition, the former analyzes frequency response functions (FRFs) and impulse response functions (IRFs) of a structure that show relationships between measured responses and excitation in the frequency and time domains [1], respectively, while the latter analyzes cross-power spectra and cross-correlation functions between reference and measured responses in the frequency and time domains, respectively [3].

To conduct EMA, IRFs and FRFs of a structure that show relations between measured responses and excitations in time and frequency domains, respectively, are analyzed to estimate its modal properties [1, 2]. If there exist unmeasured excitations that can introduce non-negligible responses of a structure in EMA, the resulting IRFs, FRFs, and estimated modal properties can be erroneous [4]. Moreover, excitations given to a structure should have relatively large amplitudes to maintain high signal-to-noise ratios (SNRs) of the resulting IRFs and FRFs, but it can be difficult to excite a large structure to measure its IRFs and FRFs with high SNRs [5]. Hence EMA is suitable for a small- or intermediate-sized structure in a laboratory environment, where excitation to the structure can be well controlled and precisely measured. Unlike EMA, OMA can be conducted on a structure of any size under excitation that is unknown or difficult to measure [3], and cross-correlation functions and cross-power spectra between a reference response and measured responses of the structure can be analyzed to estimate its modal properties. For large-sized structures in ordinary operations, such as bridges under traffic loads, rotating blades of wind turbines, and high-rise buildings under wind excitations, it can be relatively easy to conduct OMA, which can provide more practical modal properties in that only modes that are excited in operations or under environmental influences are measured [6]. However, its repeatability can be weak, since cross-power spectra and cross-correlation functions in OMA vary with environmental or operational excitation that can be uncontrollable in some cases. Compared with OMA, EMA is more repeatable, informative, and objective due to use of FRFs and IRFs that are independent of excitation, if excitation is appropriately generated.

With the development of sensor technology, two new modal analysis methods are studied. One method is a OMA method performed on a small rectangular aluminum plate using white noise acoustic excitation in the frequency range of up to 15,000 Hz, which can be an operation frequency range of a turbine bladd. Both the out-of-plane and in-plane modes of the plate within the frequency range are measured. While measuring the out-of-plane modes is relatively easy, measuring the in-plane modes can be difficult. A free-field microphone is used to measure the pressure near the reference point, which can be a measurement point on the plate surface for the out-of-plane mode measurement and a point on a side of the plate for the in-plane mode measurement; the position and the orientation of the microphone remain unchanged in a whole test for an out-of-plane or in-plane mode measurement. The derived cross-correlation functions between the velocities and accelerations of the measurement points and the reference point, respectively, contain modal characteristics of the test structure, which is also true for the cross-correlation functions between other different types of measurement. It is also shown that the pressure measured by a microphone near a vibrating surface is proportional to the normal surface acceleration at the reference point in front of the microphone. Measured natural frequencies and mode shapes from the OMA method and EMA are compared with the calculated ones from commercial finite element (FE) software. The method is a vibro-acoustic modal test (VMT) method, where an impact hammer roves over the test structure and sound pressure transducers at fixed locations are used to measure its dynamic responses. The formulation of a damped structuralacoustic system in an open environment and the associated eigenvalue problem are provided. The biorthonormality relations between the left and right eigenvectors and the relations between the structural and acoustic components of the left and right eigenvectors are proved. the FRFs used in the VMT method are derived, which contain the modal characteristics of the coupled system, and the assumptions used in the acoustic modal analysis in are validated. The VMT method and EMA were carried out on an automotive disk brake and the experimental results were compared; the results were validated by comparing them with those from an associated FE model.

Besides the two modal analysis methods, an efficient and accurate methodology for calculating discrete FRFs and IRFs and that for calculating discrete correlation functions and power spectra are proposed. In the methodology for calculating discrete FRFs and IRFs, a sampling period is evenly divided into multiple subsampling periods, and the length of a subsampling period is long enough for free responses of a structure to decay to zero; all subsampling periods of response and excitation series are superposed to corresponding single subsampling periods to form pseudoperiodic response and excitation series, respectively, in calculation of FRFs and IRFs. Data lengths of response and excitation series for calculating discrete Fourier transforms (DFTs) can be shortened by a factor equal to the number of subsampling periods. A coherence function extended from a new type of coherence functions is used to evaluate qualities of FRFs and IRFs from the proposed methodology in the frequency domain. The proposed methodology was numerically and experimentally applied to a two-degree-of-freedom (2-DOF) massspringdamper system and an aluminum plate, respectively, to estimate their FRFs and IRFs. In the methodology for calculating discrete correlation functions and power spectra, before applying the cross-correlation theorem and transforms at each sampling period, a zero series that has the same length as the reference data series is padded to its end, and the measured series is extended by stitching the measured data series of the next sampling period to its end, which makes the lengths of the two series be that of two sampling periods. Time for calculating a cross-correlation function can be greatly reduced, compared with that by directly applying its definition; the resulting cross-correlation function is in perfect accordance with the exact one, and so is the associated half spectrum. The methodology is extended to calculate cross-correlation functions of any time delays, including negative and non-negative ones, and associated full spectra in an accurate and efficient manner. The new methodology was numerically and experimentally applied to an ideal 2-DOF massspringdamper system and a damaged aluminum beam, respectively, and OMA was conducted using half spectra to estimate their natural frequencies, damping ratios, and mode shapes, which were compared with those from complex modal analysis and EMA, respectively.

1.2 Structural Damage Identification

Vibration-based damage detection has become one of the major research topics in the application of structural dynamics in the past few decades. Various methodologies have been developed to detect, locate, and characterize damage in structures based on vibration measurements, since physical properties of a structure, such as mass, stiffness, and damping, directly determine modal characteristics of the structure, i.e., natural frequencies, mode shapes (MSs), and modal damping ratios [7]. One criterion to categorize the methodologies is whether a model of the structure being monitored is needed [8]. If it is needed, the methodology is model-based; otherwise, it is non-model-based. Model-based methods are capable of detecting locations and extent of damage in structures with a minimum amount of measurement information. Model-based methods could have problems due to inaccuracy of models, environmental and other non-stationary effects on measurements, and lack of measurement data in certain frequency ranges. In practice, it is difficult to construct models of most existing structures with high accuracy [9]. Hence, methods that only analyze measured MSs or operating deflection shapes (ODSs) of a structure without the aid of a model can be good alternatives to model-based methods to locate damage, and they are non-model-based ones.

Two non-model-based methods are studied to identify embedded horizontal cracks in beams without the use of any a priori information of associated undamaged beams, if the beams are geometrically smooth and made of materials that have no stiffness discontinuities. Curvature mode shapes (CMSs) are presented with multiple resolutions to alleviate adverse effects of measurement noise. The relationship between continuous wavelet transforms (CWTs) of MSs and CMSs is shown. MSs from polynomials of MS-dependent orders, which fit those of a damaged beam, can well approximate MSs of the associated undamaged one; the MSs of the damaged beam are virtually extended beforehand, beyond boundaries of the beam, in order to improve the approximation of the CMSs from the resulting polynomial fits to those of the associated undamaged one near the boundaries. Differences between MSs of the damaged beam and those from the resulting polynomial fits are used to yield two damage indices: the curvature damage index (CDI) and the CWT damage index (CWTDI) with a Gaussian wavelet function.

A new non-model-based method to identify damage in plates is studied, where MSs of undamaged plates are not used. A MS of a pseudo-undamaged plate is constructed using a polynomial that fits the corresponding MS of a damaged plate, and differences between the MSs of the pseudo-undamaged and damaged plates are processed to yield MS damage indices (MSDIs) at each measurement point. Damage can be identified near regions with consistently high values of MSDIs. Use of a MS of an undamaged plate and that of a pseudo-undamaged plate from a polynomial fit is compared with respect to effectiveness of damage identification. Effectiveness and robustness of the proposed method on different MSs for damage of different positions and areas are numerically investigated; effects of crucial factors that determine effectiveness of the proposed method are also numerically investigated. Besides, a new non-model-based method based on principal, mean and Gaussian CMSs to identify damage in plates is studied. Theoretical bases of principal CMSs of a plate are shown. A multi-scale discrete differential-geometry scheme is proposed to calculate principal, mean and Gaussian CMSs associated with a mode shape of a plate, which can alleviate adverse effects of measurement noise on calculating the CMSs. Principal CMSs are directly related to principal stresses of a deformed plate, and mean and Gaussian CMSs can quantify differential-geometry features of a mode shape of the plate. Differences between principal, mean and Gaussian CMSs of a damaged plate and those of the associated undamaged one are used to yield four CDIs, including Maximum-CDI, Minimum-CDI, Mean-CDI and Gaussian-CDI. The applicability and robustness of this method to a mode shape of a low elastic mode on a coarse measurement grid are numerically investigated. An aluminum plate with damage in the form of a machined thickness reduction area was constructed, and a mode shape of the damaged plate was measured using non-contact excitation and measurement to investigate effectiveness of the two studied methods.

1.3 Continuous Scanning Laser Doppler Vibrometer System

A laser Doppler vibrometer is a noncontact measurement instrument that can measure the surface velocity of a vibrating structure along the laser line-of-sight direction, using the Doppler shift between the incident light and the scattered light that returns to the instrument [10]. It has distinct advantages of measuring lightweight structures without having to attach a transducer that can locally stiffen or mass load the structures. A laser beam emitted from a laser Doppler vibrometer can be directed to any visible position on a structure by installing a scanner that consists of a pair of orthogonal scan mirrors in front of the laser Doppler vibrometer, and the whole system is called a scanning laser Doppler vibrometer system. This technique has greatly increased the spatial resolution of field measurement since the laser spot on the structure, resulting from the laser beam, can stay at one point long enough to acquire sufficient vibration data of that point and then move to the next one by controlling rotation angles of the scan mirrors.

The point-by-point measurement method using a scanning laser Doppler vibrometer system usually takes a long acquisition time in order to get a full-field measurement of a structure, especially when the measurement grid is large and dense. In the early 1990s, Sriram et al. [11, 12] proposed a new scanning laser Doppler vibrometer measurement method where the laser spot was continuously swept over a surface of a structure under sinusoidal excitation; they also built a prototype of a continuous scanning laser Doppler vibrometer (CSLDV) system. Since the laser spot continuously moves, the CSLDV velocity output is modulated by an ODS and can be processed in the frequency domain to directly obtain the ODS in the form of a Chebyshev series. Later, Stanbridge and Ewins [13, 14] developed two CSLDV measurement methods to obtain ODSs of a structure under sinusoidal excitation, and the methods can be applied to different scan patterns, such as line scans, circular scans and area scans. One measurement method is the demodulation method, where the CSLDV output is multiplied by sinusoidal signals at the excitation frequency and a low-pass filter is applied to obtain an ODS. The other one is the polynomial method, where an ODS is represented by a polynomial and its coefficients are obtained by processing the discrete Fourier transform of the CSLDV output. These two methods were also applied to structures under impact [15] and multi-sine [16] excitation. Allen and Sracic [17] proposed a "lifting" method to treat the CSLDV output of a structure as the free response of a linear time-periodic system and decompose it into a set of frequency response functions, from which mode shapes and modal damping ratios of the structure can be obtained using conventional curve fitting methods. This method was extended to output-only modal analysis to identify modal characteristics of a structure under unmeasurable broadband random excitation [18]. Yang and Allen [19] used a harmonic transfer function to process the CSLDV output of a downhill ski and obtain translational and rotational velocities with a circular scan. Khan et al. [20] applied the demodulation method to measure ODSs of various structures with surface cracks. Short scan lines were assigned on cracked surfaces to intersect with the cracks, and discontinuities could be observed in the ODSs. However, discontinuities in ODSs may not be obvious when a scan line is on an intact surface with cracks existing on the opposite one.

A new type of vibration shapes called a free response shape (FRS) that can be obtained by use of a CSLDV system is introduced. An analytical expression of FRSs of a damped beam structure is derived. It is shown in the analytical expression that amplitudes of FRSs exponentially decay to zero with time. Numbers of non-zero FRSs associated with a mode can be determined by use of the short-time Fourier transform (STFT) of free response of the structure measured by a CSLDV system. A finite element model of a damped beam structure is constructed, and a CSLDV system is simulated to measure free response of the structure. FRSs associated with the structure are obtained from the response measured by the simulated CSLDV system from the demodulation method, and they are compared with those from the analytical expression. A new damage identification methodology that uses FRSs is proposed for beam structures. A free-response damage index (FRDI) is defined, which consists of differences between curvatures of FRSs obtained by use of a CSLDV system and those from polynomials that fit the FRSs, and damage regions can be identified near neighborhoods with consistently high values of FRDIs associated with different modes; an auxiliary FRDI is proposed to assist identification of the neighborhoods. A criterion based on a convergence index is proposed to determine orders of the polynomial fits. Effectiveness of the methodology for identifying damage in beam structures is numerically and experimentally investigated, and effects of the scan frequency of a CSLDV system on qualities of obtained FRSs were experimentally investigated.

Chapter 2

MODAL ANALYSIS METHODS

2.1 Operational Modal Analysis of a Rectangular Plate Using Non-contact Excitation and Measurement

2.1.1 Introduction

There are numerous cyclic excitations in the operation of a turbine that can excite the vibrations of its blades. Most turbine blades fail due to high cycle fatigue that derive from cyclic stresses [21], and a turbine blade vibrating at or near one of its natural frequencies is more likely to fail due to high cycle fatigue. Modal analysis on a turbine blade is necessary since it can provide an accurate estimation of the modal parameters, such as the natural frequencies and mode shapes. In addition, the experimental results can be used to validate a finite element model of a turbine blade and eventually improve the design of the turbine blade.

There are many types of modal analysis methods, and they can be classified as either OMA or experimental modal analysis EMA. OMA, which is an output-only modal analysis method, is a powerful technique for extracting modal parameters of a test structure using only the response data of the structure. It has been widely used on structures whose inputs are unknown, and/or difficult or even unable to measure, such as wind turbines [22], bridges [23, 24], and other civil structures

[24, 25]. The natural excitation test (NExT) [3], where the input is assumed to be white noise, is a kind of OMA. It requires multiple response measurements, one of which serves as the reference, and the cross-correlation functions between the other measurements and the reference can be generated and used for modal parameter estimation. Besides NExT, there are other operational modal estimation schemes that have been developed to extract modal parameters [6]. They are established in either the time domain or the frequency domain. The former includes the auto-regression moving average (ARMA) model-based method [26], the stochastic realization-based method [27], and the stochastic subspace identification technique [28]; the latter includes the frequency domain decomposition method [29] and the least-square complex frequency-domain estimation [30]. An OMA method using mode-isolated signals based on an approach for a single-degree-of-freedom system in the time domain is proposed in Ref. [31]. Unlike OMA, EMA requires the input measurement to obtain the FRF for modal parameter estimation [1]. In addition, EMA often requires a laboratory environment, while OMA does not and can be performed on site. Hence OMA is a more practical method than EMA, and the dominating modes of a test structure in an operation environment can be observed, which gives more valuable information about the test structure.

EMA usually uses an impact hammer or a shaker to excite a test structure. There are some drawbacks associated with this kind of excitation. First, the output quality can vary because an excitation point can be a nodal point of a test structure and the output signal-to-noise ratio can be relatively low. Some tests need to be repeated several times with different excitation locations in order to completely understand the dynamic characteristics of the structure; this can be tedious and time consuming. Second, a contact excitation force can damage a fragile structure. Third, the input frequency bandwidth can be too low to fully excite the high frequency modes of a test structure. Fourth, the excitation force from an impact hammer is not fully controllable, the impact location can vary, and the signal-to-noise ratio can be low for a single impact. A shaker needs to be attached to a test structure and can introduce mass loading. The use of non-contact acoustic excitation can resolve the above problems: acoustic excitation can be distributed over an area of a test structure, it can be easily repeated, and its bandwidth is controllable. However, acoustic excitation cannot be easily measured and used in EMA. Since OMA does not need the input measurement, acoustic excitation can be used in OMA. At least two response measurements are needed for OMA, one of which serves as the reference. While OMA does not need the input measurement, it requires the input to a test structure to be white noise, which can be generated using acoustic excitation. To avoid mass loading to a test structure, non-contact measurements using a laser vibrometer or a microphone are preferred.

In this work, OMA is performed on a small rectangular aluminum plate using white noise acoustic excitation in the frequency range of up to 15,000 Hz, which can be an operation frequency range of a turbine blade. Both the out-of-plane and in-plane modes of the plate within the frequency range are measured. While measuring the out-of-plane modes is relatively easy, measuring the in-plane modes can be difficult. The in-plane vibration of an interior point of a plate was measured in Ref. [32] by attaching a side of an accelerometer to the plate surface, which can introduce measurement error. OMA of a wind turbine wing using acoustic excitation and accelerometers attached to the wing is performed in Ref. [33]. Such contact measurements can introduce mass loading to a structure, especially for a small and light one. Vibro-acoustic OMA is performed in Ref. [34] using probes from Microflown near the test structure and a microphone near the speaker to measure the particle velocities for measurements and the pressure for reference, respectively. Only one single-point laser vibrometer is available in this work to measure the velocities of various measurement points on the plate surface using a roving sensor approach. A free-field microphone is used to measure the pressure near the reference point, which can be a measurement point on the plate surface for the out-of-plane mode measurement and a point on a side of the plate for the in-plane mode measurement; the position and the orientation of the microphone remain unchanged in a whole test for an out-of-plane or in-plane mode measurement. The derived cross-correlation functions between the velocities and accelerations of the measurement points and the reference point, respectively, contain modal characteristics of the test structure, which is also true for the cross-correlation functions between other different types of measurement. It is also shown that the pressure measured by a microphone near a vibrating surface is proportional to the normal surface acceleration at the reference point in front of the microphone. The measured data are acquired and processed by an LMS spectrum analyzer, and the corresponding cross-power spectral densities (CPSDs), which are the Fourier transforms of the cross-correlation functions, are used to extract the modal characteristics of the test structure, including the natural frequencies, damping ratios, and mode shapes. In addition, a method for accurately measuring the in-plane modes of the plate is developed. The laser beam from the laser vibrometer is shined at the measurement points on the plate surface with an incident angle, and the measured CPSDs are summed. The in-plane modes can be identified by comparing the resulting summed CPSD with that for the out-of-plane modes, which is obtained by shining the laser beam perpendicular to the plate surface. EMA using an impact hammer to excite the plate and the laser vibrometer to measure its responses is also performed to obtain the out-of-plane and in-plane modal parameters. A method similar to that for the in-plane mode measurement in OMA is used for the in-plane mode measurement in EMA except that the FRFs are measured and summed to identify the in-plane modes. The measured natural frequencies and mode shapes from OMA and EMA are compared with the calculated ones from commercial finite element (FE) software ABAQUS.

2.1.2 OMA Using a Microphone to Measure the Response of the Reference Point

In OMA, the cross-correlation functions between the responses of the measurement points and that of the reference point due to a single-point white noise input can be expressed as sums of decaying sinusoids that contain modal parameters of the test structure [3], where the same type of measured responses, such as displacements, velocities, or accelerations, are used. However, when the types of measurement at the measurement and reference points are different, OMA can still be performed, as shown below.

The equations of motion of a test structure are

$$\mathbf{M}\ddot{\mathbf{x}}\left(t\right)+\mathbf{C}\dot{\mathbf{x}}\left(t\right)+\mathbf{K}\mathbf{x}\left(t\right)=\mathbf{f}\left(t\right) \tag{2.1}$$

where t is time, $\mathbf{x}$ is the displacement vector, $\mathbf{M}$ is the mass matrix, $\mathbf{C}$ is the damping matrix, $\mathbf{K}$ is the stiffness matrix, and $\mathbf{f}$ is the force vector. By a coordinate transformation

$$\mathbf{x}=\mathbf{\Phi}\mathbf{q} \tag{2.2}$$

where Φ is the modal matrix, whose r-th column is the r-th mass-normalized mode shape of the test structure, and $\mathbf{q}$ is the modal coordinate vector, Eq. (2.1) can be expressed in terms of modal coordinates. It is assumed that the test structure is classically damped [35] for convenience. Substituting Eq. (2.2) into Eq. (2.1) and pre-multiplying the resulting equation by $\mathbf{\Phi}^{\mathrm{T}}$, where the superscript T denotes transpose of a matrix or a vector, yield a set of scalar equations for modal coordinates

$$\ddot{q}\left(t\right)+2\xi^{r}\omega_{n}^{r}\dot{q}^{r}\left(t\right)+\omega_{n}^{r2}q^{r}\left(t\right)=\phi^{r\mathrm{T}}\mathbf{f}\left(t\right) \tag{2.3}$$

where ω_n^r is the r-th undamped natural frequency of the test structure, ξ^r is the r-th modal damping ratio, and ϕ^r is the r-th mass-normalized mode shape. Assuming zero initial conditions, one has the solution to Eq. (2.3) :

$$q^{r}\left(t\right)=\int_{-\infty}^{t}\phi^{r\mathrm{T}}\mathbf{f}\left(t\right)g^{r}\left(r-\tau\right)\mathrm{d}\tau \tag{2.4}$$

where

$$g^r(t) = \frac{1}{\omega_d^r} \mathrm{e}^{-\xi^r \omega_n^r t} \sin(\omega_d^r t) \tag{2.5}$$

is the unit impulse response function corresponding to the r-th modal coordinate. By Eq. (2.2), the solution to Eq. (2.1) is

$$\mathbf{x}(t) = \sum_{r=1}^{n} \phi^r \int_{-\infty}^{t} \phi^{r\mathrm{T}} \mathbf{f}(t)\, g^r(r-\tau)\, \mathrm{d}\tau \tag{2.6}$$

Note that the solution in Eq. (2.6) is the sum of the displacement. The corresponding velocity is

$$\mathbf{v} = \dot{\mathbf{x}} = \mathbf{\Phi}\dot{\mathbf{q}} \tag{2.7}$$

where $\dot{\mathbf{q}}$ is the modal velocity vector and its r-th component is

$$\dot{q}^r(t) = \int_{-\infty}^{t} \phi^{r\mathrm{T}} \mathbf{f}(t)\, \dot{g}^r(r-\tau)\, \mathrm{d}\tau \tag{2.8}$$

in which

$$\dot{g}^r(t) = \frac{A^r}{\omega_d^r} \mathrm{e}^{-\xi^r \omega_n^r t} \sin(\omega_d^r t + \theta^r) \tag{2.9}$$

with

$$A^r = \sqrt{(\xi^r \omega_n^r)^2 + \omega_d^{r2}} \tag{2.10}$$

$$\theta^r = \pi - \arcsin \frac{\omega_d^r}{\sqrt{(\xi^r \omega_n^r)^2 + \omega_d^{r2}}} \tag{2.11}$$

Similarly, the corresponding acceleration is

$$\mathbf{a} = \mathbf{\Phi}\ddot{\mathbf{q}} \tag{2.12}$$

where $\ddot{\mathbf{q}}$ is the modal acceleration vector and its r-th component is

$$\ddot{q}^r(t) = \int_{-\infty}^{t} \phi^{r\mathrm{T}}\mathbf{f}(t)\,\ddot{g}^r(r-\tau)\,\mathrm{d}\tau + \phi^{r\mathrm{T}}\mathbf{f}(t)\,\dot{g}^r(0) \tag{2.13}$$

in which

$$\ddot{g}^r(t) = \frac{A^{r2}}{\omega_d^r}\mathrm{e}^{-\xi^r\omega_n^r t}\sin\left(\omega_d^r t + 2\theta^r\right) \tag{2.14}$$

The cross-correlation function between the velocity at a measurement point i, $\mathbf{v}_i$, and the acceleration at a reference point j, $\mathbf{a}_j$, due to a white noise input at an excitation point k, $\mathbf{f}_k$, is

$$\begin{aligned} R_{ij}(T) \;=\; & \mathrm{E}\left[v_i(t+T)\,a_j(t)\right] = \textstyle\sum_{r=1}^{n}\sum_{s=1}^{n}\phi_i^r\phi_k^r\phi_j^s\phi_k^s \left\{\int_{-\infty}^{t}\int_{-\infty}^{t+T}\dot{g}^r(t+T-\sigma)\,\ddot{g}^s(t-\tau)\right. \\ & \left.\mathrm{E}\left[f_k(\sigma)\,f_k(\tau)\right]\mathrm{d}\sigma\mathrm{d}\tau + \int_{-\infty}^{t+T}\dot{g}^r(t+T-\tau)\,\dot{g}^s(0)\,\mathrm{E}\left[f_k(\tau)\,f_k(t)\right]\mathrm{d}\tau\right\} \end{aligned} \tag{2.15}$$

where T is the time difference, E is the expectation operator, ϕ_i^r is the i-th component of the r-th mode shape, and f_k is the k-th component of the force vector. Since f_k is assumed to be white noise, one has

$$\begin{cases} \mathrm{E}\left[f_k(\sigma)\,f_k(\tau)\right] = R_{ff}(\tau-\sigma) = c\delta(\tau-\sigma) \\ \mathrm{E}\left[f_k(\tau)\,f_k(t)\right] = c\delta(\tau-t) \end{cases} \tag{2.16}$$

where c is a constant and δ is the Dirac delta function. Substituting Eq. (2.16) into Eq. (2.15) yields

$$R_{ij}\left(T\right)=\sum_{r=1}^{n}\sum_{s=1}^{n}c\phi_i^r\phi_k^r\phi_j^s\phi_k^s\left\{\int_{-\infty}^{t}\dot{g}^r\left(t+T-\tau\right)\ddot{g}^s\left(t-\tau\right)\mathrm{d}\tau+\dot{g}^r\left(T\right)\dot{g}^s\left(0\right)\right. \tag{2.17}$$

Let $\lambda=t-\tau$; one has

$$R_{ij}\left(T\right)=\sum_{r=1}^{n}\sum_{s=1}^{n}c\phi_i^r\phi_k^r\phi_j^s\phi_k^s\left\{\int_{0}^{\infty}\dot{g}^r\left(\lambda+T\right)\ddot{g}^s\left(\lambda\right)\mathrm{d}\lambda+\dot{g}^r\left(T\right)\dot{g}^s\left(0\right)\right. \tag{2.18}$$

where

$$\begin{aligned}\omega_n^r\left(\lambda+T\right)\sin\left[\omega_d^r\left(\lambda+T\right)+\theta^r\right] &= \tfrac{A^r}{\omega_d^r}\mathrm{e}^{-\xi^r\omega_n^r T}\Big[\sin\left(\omega_d^r T\right)\mathrm{e}^{-\xi^r\omega_n^r\lambda}\cos\left(\omega_d^r\lambda+\theta^r\right)\\ &\quad+\cos\left(\omega_d^r T\right)\mathrm{e}^{-\xi^r\omega_n^r\lambda}\sin\left(\omega_d^r\lambda+\theta^r\right)\Big]\end{aligned} \tag{2.19}$$

and the cross-correlation function $R_{ij}\left(T\right)$ can be written as

$$R_{ij}\left(T\right)=\sum_{r=1}^{n}\phi_i^r\mathrm{e}^{-\xi^r\omega_n^r T}\left[G^r\sin\left(\omega_d^r T\right)+H^r\cos\left(\omega_d^r T\right)\right] \tag{2.20}$$

where

$$\begin{aligned}\left\{\begin{array}{c}G^r\\ H^r\end{array}\right\} &= \textstyle\sum_{s=1}^{n}\frac{cA^{r2}\phi_k^r\phi_j^s\phi_k^s}{\omega_d^s}\Big\{A^r\int_0^\infty \mathrm{e}^{\left(-\xi^r\omega_n^r-\xi^s\omega_n^s\right)\lambda}\sin\left(\omega_d^s\lambda+2\theta^s\right)\\ &\quad\left\{\begin{array}{c}\cos\left(\omega_d^r\lambda+2\theta^r\right)\\ \sin\left(\omega_d^r\lambda+2\theta^r\right)\end{array}\right\}\mathrm{d}\lambda+\left\{\begin{array}{c}\cos\left(\theta^r\right)\sin\left(\theta^s\right)\\ \sin\left(\theta^r\right)\cos\left(\theta^s\right)\end{array}\right\}\Big\}\end{aligned} \tag{2.21}$$

Eq. (2.20) can be further written as

$$R_{ij}\left(T\right)=\sum_{r=1}^{n}\frac{\phi_i^r B^r}{\omega_d^r}\mathrm{e}^{-\xi^r\omega_n^r T}\sin\left(\omega_d^r T+\Theta^r\right) \tag{2.22}$$

where

$$B^r = \sqrt{G^{r2} + H^{r2}} \tag{2.23}$$

and

$$\Theta^r = \arctan 2\left(H^r, G^r\right) \tag{2.24}$$

Eq. (2.22) indicates that the cross-correlation functions between the velocities and accelerations are sums of decaying sinusoids that contain modal characteristics of the test structure, and each decaying sinusoid is similar to that in Ref. [3]. One can further show that the cross-correlation functions between the displacements and velocities and those between the displacements and accelerations also contain the modal characteristics of the test structure. Hence OMA can be performed even though the types of measurement at the measurement and reference points are different.

When a speaker is used to provide white noise acoustic excitation to the test structure, the excitation can be considered as multiple inputs since it is distributed over an area of the test structure. The cross-correlation functions between the responses of two points of the test structure, i and j, due to multiple white noise input can be expressed as [36]

$$R_{ij}\left(T\right) = \sum_{r=1}^{n} \frac{\phi_i^r B^r}{\omega_d^r} \mathrm{e}^{-\xi^r \omega_n^r T} \sin\left(\omega_d^r T + \Phi^r\right) \tag{2.25}$$

where the point i is a measurement point, the point j is the reference point, and C_j^r and Φ^r are a constant and a phase angle associated with the response of the reference point, respectively. In this study, the operational polyreference least-squares complex frequency-domain method, referred to as Operational PolyMax

[37], is used to perform modal parameter estimation using CPSDs, which are Fourier transforms of the cross-correlation functions in Eq. (2.25).

A free-field microphone is placed near the reference point on the surface of a test structure with a minimum distance d, as shown in Fig. 2.1, and there is no contact between the microphone and the structure during the vibration of the structure. It is assumed that the small area of the structure in front of the microphone can be considered as a point sound source, the velocity of an air particle next to the source is equal to the normal surface velocity of the source, and the microphone measures only the pressure generated by the source. The measured pressure is

$$p\left(d,t\right) = \mathrm{j}\omega\rho_0\frac{\tilde{Q}}{4\pi d}\mathrm{e}^{\mathrm{j}(\omega t-kd)} \tag{2.26}$$

where $\mathrm{j} = \sqrt{-1}$, ρ_0 is the air density, $\tilde{Q}$ is the complex amplitude of the volume velocity of the source, and k is the wavenumber of sound generated by the source. Let the normal surface velocity of the source be

$$v_n\left(t\right) = \tilde{v}_n\mathrm{e}^{\mathrm{j}\omega t} \tag{2.27}$$

where $\tilde{v}_n$ is the complex amplitude of the normal surface velocity of the source [38]. Let the area of the source be S; $\tilde{Q}$ can be expressed by

$$\tilde{Q} = 2\tilde{v}_n S \tag{2.28}$$

Substituting Eq. (2.28) into Eq. (2.26) yieldes

$$p\left(d,t\right) = \mathrm{j}\omega\rho_0\frac{\tilde{v}_n S}{2\pi d}\mathrm{e}^{\mathrm{j}(\omega t-kd)} \tag{2.29}$$

Let

$$\tilde{a}_n = \mathrm{j}\omega\tilde{v}_n \tag{2.30}$$

where is the complex amplitude of the normal surface acceleration of the source. Eq. (2.29) can be written as

$$p\left(d,t\right) = \tilde{a}_n\rho_0\frac{S}{2\pi d}\mathrm{e}^{-\mathrm{j}kd}\mathrm{e}^{\mathrm{j}\omega t} \tag{2.31}$$

Eq. (2.31), the complex amplitude of the pressure measured by the microphone is

$$\tilde{p}_n\left(d,t\right) = \tilde{a}_n\rho_0\frac{S}{2\pi d}\mathrm{e}^{-\mathrm{j}kd} = \tilde{a}_n d_e \tag{2.32}$$

where d_e is the proportionality constant. An equation similar to Eq. (2.32) can be found in Ref. [39] for measurement of the normal surface velocity of a vibrating beam using a microphone. According to Eq. (2.32), the pressure generated by the reference point can be directly related to the acceleration of the reference point, which is valid when the wavelengths of the vibrating structure are relatively large compared with the radius of the diaphragm of the microphone. Hence when a laser vibrometer and a free-field microphone are used to measure the velocities of the measurement points in a roving sensor approach and the associated pressures near the reference point, respectively, the resulting cross-correlation functions between the measured velocities and pressures contain modal characteristics of the test structure, as shown in Eq. (2.25), and the associated CPSDs can be used for modal parameter estimation.

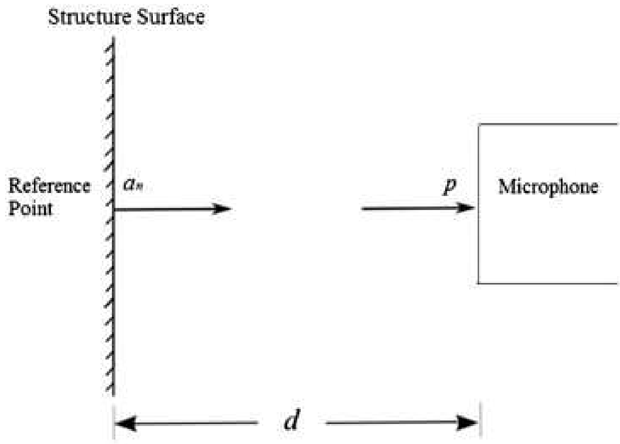

Figure 2.1: Schematic of pressure measurement near the reference point.

2.1.3 Method for Measuring the In-plane Modes of a Rectangular Plate

The in-plane vibration of a side of the plate can be easily measured, but the in-plane vibration of an interior point of the plate cannot be easily measured. A non-contact method for measuring the in-plane modes of the plate using OMA is developed here. A laser vibrometer is used to measure the velocities of the interior measurement points of the plate and a microphone is used to measure the pressure near the reference point, which is located on a side of the plate. A laser vibrometer is capable of measuring the velocity component in the direction of the incident laser beam [40]. When the laser beam from the laser vibrometer is shined on the plate with an incident angle θ, as shown in Fig. 2.2, where the Z- and X -axes are in the out-of-plane and in-plane vibration directions, respectively, the velocity

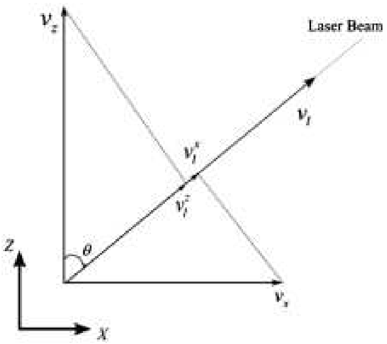

Figure 2.2: Velocity measured by the laser beam v_l with an incident angle θ .

measured by the vibrometer vl is along the laser beam direction, and it contains the velocities of both the out-of-plane and in-plane vibrations. The velocity of the out-of-plane vibration contained in the measured velocity along the laser beam v_l^z can be expressed as $v_l^z = v_z \cos\theta$, where v_z is the velocity of the out-of-plane vibration (Fig. 2.2). The velocity of the in-plane vibration measured by the laser vibrometer v_l^X can be expressed as $v_l^X = v_X \sin\theta$, where v_X is the velocity of the in-plane vibration (Fig. 2.2). The velocity measured by the laser vibrometer can be expressed as $v_l = v_l^Z + v_l^X$. It is obvious that the larger the incident angle, the more the in-plane vibration and the less the out-of-plane vibration that will be measured by the laser vibrometer, which is desirable for measuring the in-plane vibration. However, the incident angle should not be too large in order to prevent the laser beam from being scattered, which can reduce the light intensity of the reflected laser beam and cause inaccurate measurement. A proper non-zero incident angle should be selected, which can measure an adequate amount of the in-plane vibration and does not affect the accuracy of the measurement.

The in-plane modes of the plate can be measured using OMA in an indirect way. First, the CPSDs for the out-of-plane modes are measured. The microphone is used to measure the pressure near the reference point, which can be any point on the plate surface, and the laser vibrometer shines the laser beam perpendicular to the plate surface to measure the velocities of the measurement points in a roving sensor approach. The measured CPSDs are summed; the resulting summed CPSD is referred to as the out-of-plane CPSD. Second, the microphone is used to measure the pressure in the X direction near the reference point on a side of the plate. The laser vibrometer shines the laser beam on the measurement points with an incident angle, which remains constant throughout the test. The measured CPSDs are then summed; the resulting summed CPSD is referred to as the mixed CPSD, where the word "mixed" is used since the measured CPSDs contain both the out-of-plane and in-plane vibrations of the plate. It is impossible to determine whether a mode is an out-of-plane or in-plane mode if only the mixed CPSD is used since the measured velocity contains the velocities of both the out-of-plane and in-plane vibrations. The in-plane modes can be identified, however, by comparing the mixed CPSD with the out-of-plane CPSD, since both the out-of-plane and in-plane modes would manifest themselves as peaks in the mixed CPSD, and only the peaks corresponding to the out-of-plane modes can be found in the out-of-plane CPSD; one can then conclude that the modes that can only be found in the mixed CPSD are the in-plane modes. Note that the summed CPSDs are used to distinguish the in-plane modes from the out-of-plane modes since they can show the overall characteristics of the measured CPSDs.

The method described above can be adapted for use in EMA to identify the in-plane modes of the plate. An impact hammer is used to excite the plate by hitting a point on the plate surface, and the laser vibrometer shines the laser beam perpendicular to the plate surface to measure the velocities of the measurement points in a roving sensor approach. A series of FRFs are obtained and summed; the resulting summed FRF is referred to as the out-of-plane FRF. The impact hammer is then used to hit a point on a side of the plate. The laser beam is shined with an incident angle on the measurement points of the plate in a roving sensor approach. The measured FRFs are summed, and the resulting summed FRF is referred to as the mixed FRF. The in-plane modes can be identified by comparing the mixed FRF with the out-of-plane FRF.

Since the out-of-plane and in-plane modes are orthogonal to each other, in the vicinity of one of the in-plane mode natural frequencies, the velocity measured by the laser beam with the incident angle θ mainly derives from the in-plane vibration; the out-of-plane vibration measured by the laser beam is negligible. Further, the velocity of the in-plane vibration measured by the laser beam is equal to that of the in-plane vibration of the measurement point multiplied by $\sin\theta$, which can be considered as a multiplier of the magnitudes of the estimated mode shapes and does not change the estimated mode shapes. Hence the measured CPSDs or FRFs using the laser beam with the incident angle θ can be used to perform modal parameter estimation for the in-plane modes of the plate.

2.1.4 Test Setup and Procedure

2.1.4.1 Test Specimen and Setup

The dimensions and material properties of the rectangular aluminum 6061 plate being studied are shown in Table 2.1. Fig. 2.3(a) shows a schematic of the complete experimental setup. The plate is laid on two slim elastic rubber bands, which simulate free boundaries of the plate (Fig. 2.3(b) and (c)). There are 42 measurement points on the plate surface, as shown in Fig. 2.4; a small reflective tape is attached to the plate surface at each measurement point to enhance the reflection of the laser beam. Two speakers (Fostex FT17H) are placed near the plate in a direction of interest; the white noise signals are generated by the LMS spectrum analyzer and powered by an amplifier (QSC PLX-1802). The frequency range of the white noise signals is set to 0-15,000 Hz. A free-field microphone is placed near the reference point in a direction of interest; the maximum frequency that the microphone can measure is 15,000 Hz. Both the microphone and the laser vibrometer are connected to the LMS spectrum analyzer. Modal analysis is performed using LMS Test.Lab Rev. 9b modal analysis software. The directions in which the laser beam is shined on the plate surface, the directions towards which the speakers and the microphone are pointing, and the locations of the reference points for the out-of-plane and in-plane mode measurements using OMA are shown in Fig. 2.3(b) and (c), respectively.

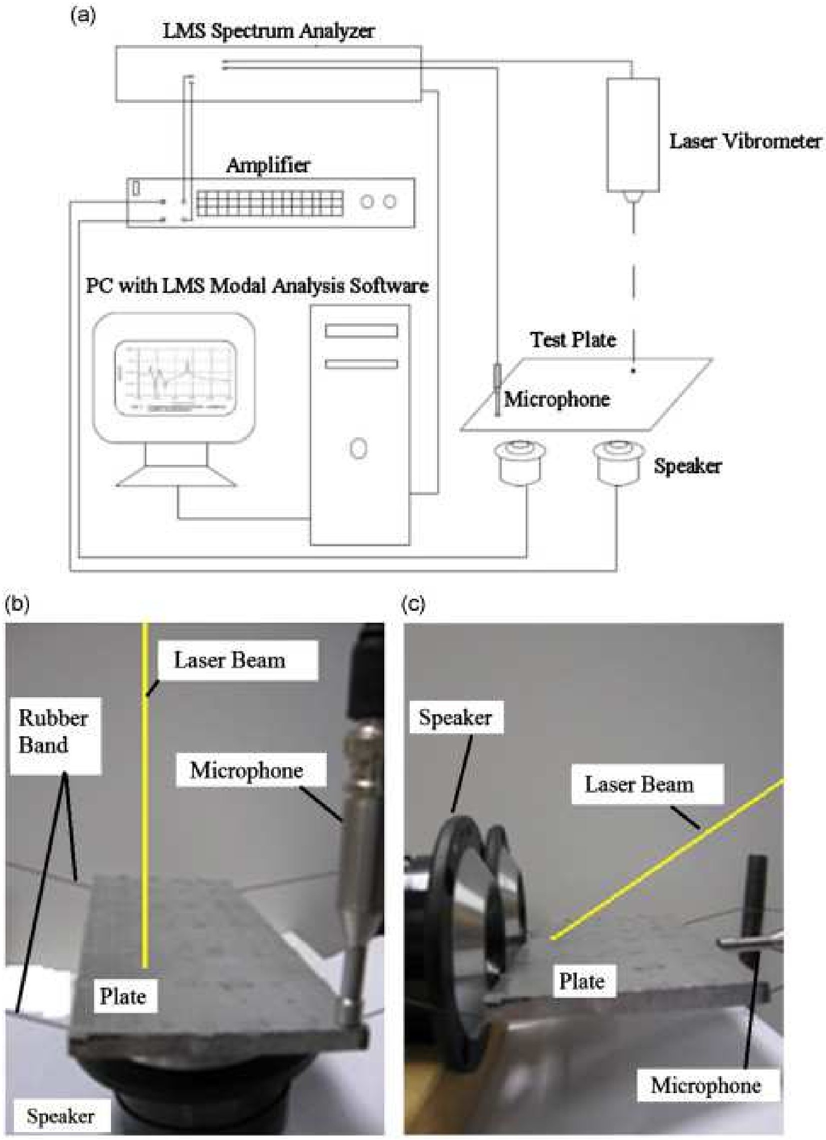

Figure 2.3: Experimental setup for OMA: (a) schematic of the complete experimental setup; (b) excitation and measurement setups for the out-of-plane mode measurement; and (c) excitation and measurement setups for the in-plane mode measurement.

Table 2.1: Test specimen parameters.

Parameter	Value
Length	0.18 m
Width	0.075 m
Thickness	0.006 m
Young's modulus	69 GN/m
Poison's ratio	0.33
Density	2700 kg/m^3

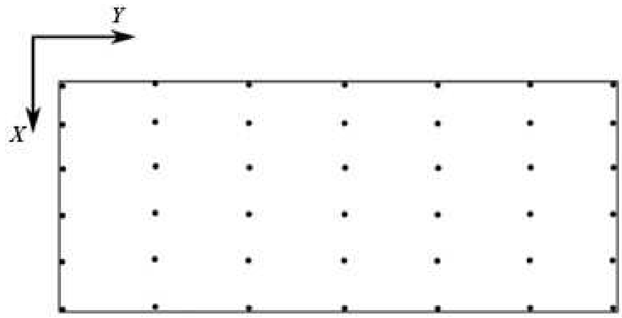

Figure 2.4: Distribution of the measurement points (shown as dots) on the plate surface; X- and Y-axes are two in-plane axes.

2.1.4.2 Test Procedure

For the out-of-plane mode measurement using OMA, a measurement point at a corner of the plate is used as the reference point since the distances between the measurement points are small and the microphone setup can be an obstacle for the laser beam if the reference point is an interior point on the plate surface.

The laser vibrometer shines the laser beam perpendicular to the plate surface at the other 41 measurement points. The white noise acoustic excitation from the two speakers is triggered to excite the plate. The CPSD between the velocity measured by the laser vibrometer at a measurement point and the pressure measured by the microphone at the reference point is calculated by the LMS modal analysis software and averaged over 40 samples. A total of 41 averaged CPSDs are obtained for the 41 measurement points in a roving sensor approach; the resulting summed out-of-plane CPSD is shown in Fig. 2.5(a).

For the in-plane mode measurement using OMA, the reference point is on a side of the plate and the laser beam is shined to the measurement point with $\theta = 45^o$, for which an adequate amount of the in-plane vibration can be captured by the laser beam and the light intensity of the reflected laser beam is not too low. In order to completely measure the in-plane modes, the in-plane vibrations in both the X and Y directions (Fig. 2.3) need to be measured at each measurement point. Hence there are two measured CPSDs at each measurement point, and the position of the microphone remains unchanged throughout the test. A CPSD is averaged over 40 samples. Since there are 42 measurement points and two averaged CPSDs at each measurement point, a total of 84 averaged CPSDs are obtained in a roving sensor approach; the resulting summed mixed CPSD is shown in Fig. 2.5(a). The in-plane modes can be identified by comparing the out-of-plane CPSD with the mixed CPSD. The two peaks labeled as A and B, which appear only in the mixed

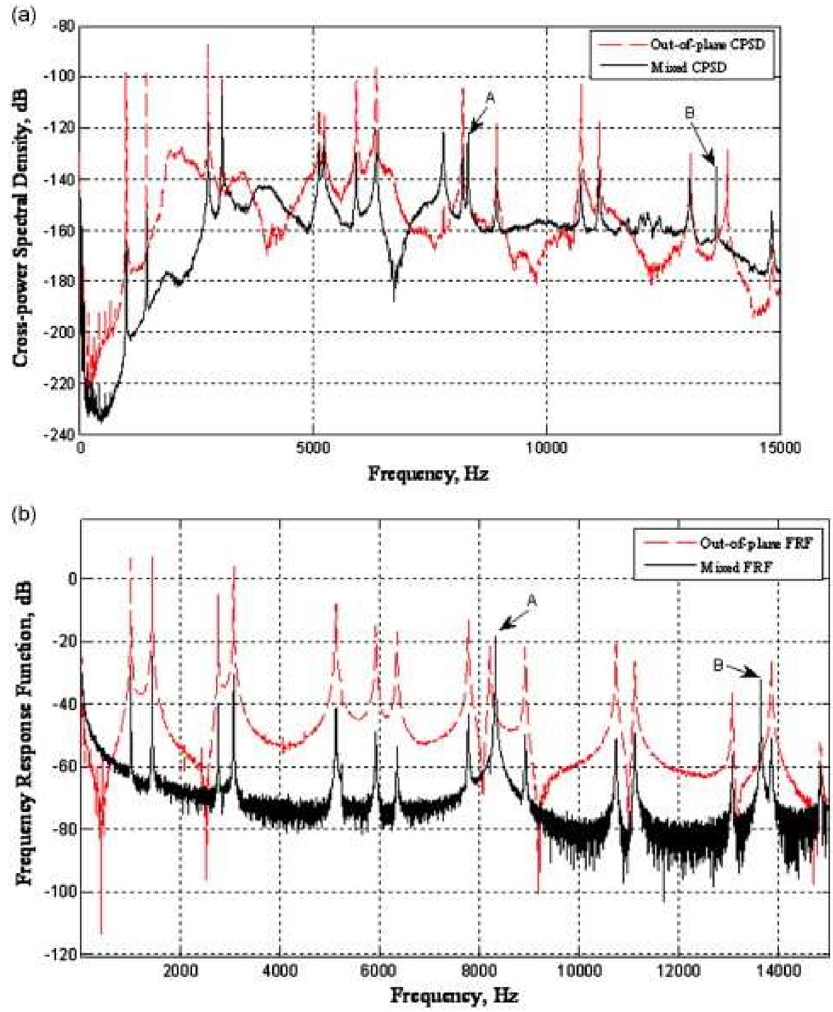

Figure 2.5: Plots of (a) the out-of-plane and mixed CPSDs from OMA and (b) the out-of-plane and mixed FRFs from EMA.

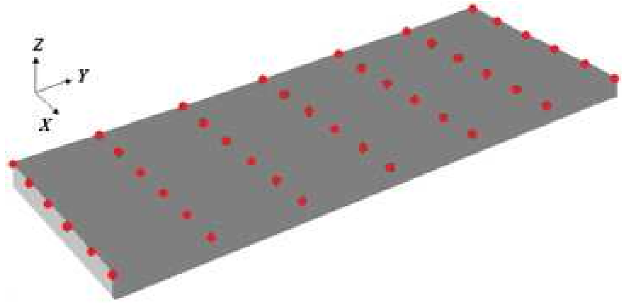

Figure 2.6: The FE model of the plate, with the measurement points indicated.

CPSD, correspond to the in-plane modes. Since the highest rigid body mode natural frequency in the out-of-plane and in-plane mode measurements is 29.16 Hz, which is lower than 10 percent of the first elastic mode natural frequency (999 Hz), the boundaries can be considered to be free [1]. Note that the peak corresponding to the 15th out-of-plane elastic mode, at the frequency 13,877 Hz, is not prominent in the mixed CPSD because the speakers are placed in the vicinity of two nodal lines of that mode (Fig. 2.7(a)) and the mode is not completely excited. The modal parameters of the out-of-plane modes are estimated using the 41 averaged CPSDs obtained in the out-of-plane mode measurement, and those of the in-plane modes are estimated using the 84 averaged CPSDs obtained in the in-plane mode measurement.

In addition, EMA is performed to measure the out-of-plane and in-plane modes. An impact hammer and the laser vibrometer are used to excite the plate and measure its response, respectively. For the out-of-plane mode measurement, the hammer hits a point on the plate surface in the out-of-plane direction and the

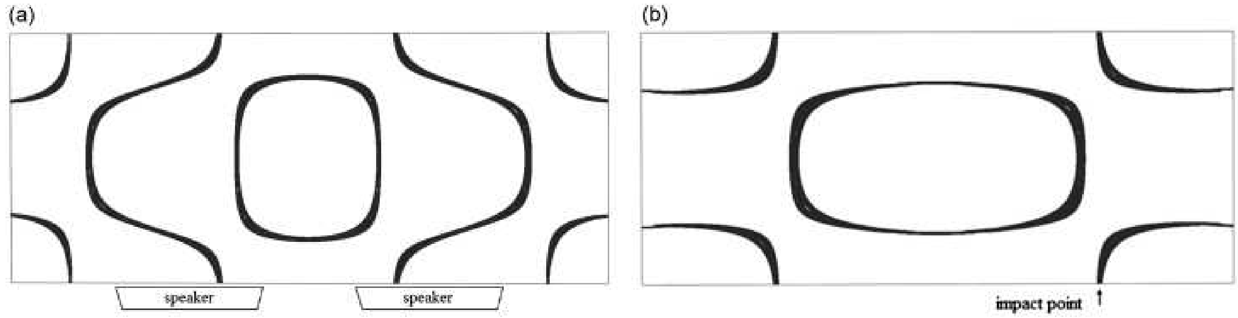

Figure 2.7: (a) The nodal lines of the 15th out-of-plane elastic mode and the locations of the two speakers; and (b) the nodal lines of the 10th out-of-plane mode and the impact location.

laser vibrometer shines the laser beam perpendicular to the plate surface; the FRF is then measured and averaged over 40 samples. A total of 42 averaged FRFs are obtained in a roving sensor approach for the 42 measurement points; the resulting summed out-of-plane FRF is shown in Fig. 2.5(b). For the in-plane mode measurement, the hammer hits a point on a side of the plate in the in-plane direction and the laser vibrometer shines the laser beam with $\theta = 45^o$. Similar to OMA, the FRFs in both the X and Y directions are measured at each measurement point and averaged over 40 samples; the position and direction of the impact by the hammer do not change throughout the test. A total of 84 averaged FRFs are obtained; the resulting summed, mixed FRF is shown in Fig. 2.5(b). The two peaks labeled as A and B, which appear only in the mixed FRF, correspond to the in-plane modes. The boundaries can be considered to be free since the highest rigid body mode natural frequency in the out-of-plane and in-plane mode measurements is 31.78 Hz, which is lower than 10 percent of the first elastic mode natural frequency (998 Hz) [1].

Note that there is not a peak corresponding to the 10th out-of-plane elastic mode at the frequency 8204 Hz because the impact location is in the vicinity of a nodal line of that mode (Fig. 2.7(b)) and the mode is not excited. The modal parameters of the out-of-plane modes are estimated using the 42 averaged FRFs obtained in the out-of-plane mode measurement, and those of the in-plane modes are estimated using the 84 averaged FRFs obtained in the in-plane mode measurement.

2.1.5 Numerical and Experimental Results

Numerical simulation is conducted for the out-of-plane and in-plane modes of the plate using commercial FE software ABAQUS. To accurately simulate the plate, linear hexahedron solid elements (C3D8R) are used to construct the FE model (Fig. 2.6). The boundary conditions of the plate are set to be free. The natural frequencies and mode shapes of the first 18 elastic modes, including 16 out-of-plane and two in-plane modes, are calculated and compared with the experimental results. Table 2.2 shows the comparisons between the natural frequencies from the FE model, denoted by f_n, and those from OMA and EMA, denoted by f_e. The modal damping ratios of each mode ξ obtained from OMA and EMA are also shown in Table 2.2. The maximum errors of the measured natural frequencies from OMA and EMA, compared with those from the FE model, are 1.53 percent and 1.52 percent, respectively, for the first 18 elastic modes.

Table 2.2: Comparisons between the natural frequencies from the FE model and those from OMA and EMA, where the superscript + denotes an in-plane mode; measured damping ratios from OMA and EMA are also shown.

Mode	f_n(Hz)	Results from OMA			Results from EMA		
		f_n(Hz)	ξ(%)	Frequency error (%)	f_n(Hz)	ξ(%)	Frequency error (%)
1	1000	999	0.01	- 0.10	998	0.02	- 0.20
2	1421	1431	0.03	0.7	1430	0.02	0.63
3	2756	2757	0.06	0.04	2756	0.05	0
4	3051	3068	0.01	0.56	3069	0.03	0.59
5	5103	5129	0.14	0.51	5127	0.08	0.47
6	5255	5241	0.13	- 0.27	5238	0.11	- 0.32
7	6007	5923	0.08	- 1.41	5921	0.08	- 1.43
8	6426	6346	0.11	- 1.24	6347	0.08	- 1.23
9	7746	7792	0.04	0.59	7790	0.06	0.57
10	8195	8204	0.04	0.11	8203	0.07	0.1
1^+	8209	8335	0.01	1.53	8334	0.05	1.52
11	8885	8936	0.03	0.57	8936	0.01	0.57
12	10663	10748	0.04	0.8	10747	0.05	0.79
13	11053	11134	0.04	0.73	11133	0.05	0.72
14	12971	13080	0.02	0.84	13078	0.03	0.82
2^+	13679	13650	0.01	-0.21	13648	0.01	-0.23
15	13726	13877	0.03	1.1	13875	0.04	1.09
16	14816	14838	0.03	0.15	14840	0.04	0.16

Modal assurance criteria (MAC) values are employed to compare the measured mode shapes from OMA and EMA with those from the FE model; the numerical mode shapes are extracted at the 42 measurement points. The MAC values between the measured out-of-plane and in-plane mode shapes from OMA and those from the FE model are shown in Table 2.3(a) and (b), respectively. Note that the measurement point used as the reference point in the out-of-plane mode measurement in OMA is not included in calculating the MAC values. The MAC values between the measured out-of-plane and in-plane mode shapes from EMA and those from the FE model are shown in Table 2.4(a) and (b), respectively. The diagonal MAC values from OMA and EMA are all above 94 percent and 93 percent, respectively, indicating that the measured and calculated mode shapes are in excellent correlation; the off-diagonal MAC values are all below 20 percent, indicating that the mode shapes of different modes can be considered to be uncorrelated to each other, the number of the measurement points is adequate, and the distribution of their positions is proper [41]. The first 16 out-of-plane and first two in-plane elastic mode shapes measured from OMA are shown in Fig. 2.8.

Table 2.3: MAC values (in percentage) between the measured (Exp.) mode shapes from OMA and those from the FE model (Num.): (a) out-of-plane modes, and (b) in-plane modes.

(a)

	Exp.															
Num.	1	2	3	4	5	6	7	8	9	10	11	12	13	14	15	16
1	96.1	0.6	0.1	1.3	0.5	14.9	4.3	0.5	1.3	2.9	0.1	0.7	0.7	17.1	1.7	0.1
2	0.4	95.8	1.1	2.6	6.9	0.0	0.2	0.6	2.9	0.2	1.6	1.2	9.3	0.1	0.6	0.0
3	0.5	0.8	98.6	0.2	0.8	0.1	0.3	0.7	0.1	0.7	14.9	7.9	0.6	0.1	0.6	0.0
4	1.2	0.3	0.3	97.8	0.1	0.6	0.6	1.8	7.1	0.5	1.5	1.9	1.0	0.2	1.1	5.7
5	0.1	8.0	3.3	1.9	95.9	0.2	0.2	1.2	3.2	0.3	1.7	2.0	17.5	0.1	0.4	0.1
6	15.2	0.0	0.6	0.1	0.2	97.8	0.1	0.0	0.0	1.3	0.5	0.1	0.0	11.6	3.5	0.0
7	4.0	0.0	1.0	1.1	0.0	1.9	94.7	2.5	2.4	1.9	1.5	2.4	0.1	2.0	12.5	0.2
8	0.9	2.1	0.8	1.1	2.1	0.1	1.2	97.5	0.7	1.9	0.0	9.0	1.5	0.1	2.5	0.2
9	1.6	2.3	0.0	13.1	2.9	0.5	1.4	0.7	97.4	1.5	0.0	0.7	2.3	0.7	1.5	10.4
10	2.4	0.2	0.4	1.4	0.5	1.9	2.1	1.3	5.2	95.9	0.4	2.1	0.7	0.1	11.0	0.1
11	1.1	0.7	19.0	0.3	1.1	0.5	1.6	0.1	0.0	1.0	97.5	0.5	0.5	0.5	1.4	0.0
12	1.3	1.0	2.3	1.8	1.6	0.3	1.0	5.8	1.4	1.6	0.0	96.8	0.1	0.4	1.8	0.0
13	0.4	7.7	1.0	1.6	15.9	0.1	0.6	1.6	1.5	0.4	0.9	4.4	95.2	0.2	0.7	0.2
14	14.9	0.3	0.3	0.2	0.3	10.4	2.6	0.2	0.3	0.0	0.1	0.4	0.0	99.0	1.9	0.1
15	1.7	0.3	0.5	1.6	0.2	2.0	8.1	1.6	0.8	9.8	0.5	2.0	0.3	0.1	95.6	0.3
16	0.8	0.2	0.1	5.4	0.1	0.8	0.3	0.1	8.0	0.1	0.1	0.1	0.2	0.6	2.1	97.0

(b)

	Exp.	
Num.	1	2
1	97.46	0.03
2	0.27	96.56

Table 2.4: MAC values (in percentage) between the measured (Exp.) mode shapes from EMA and those from the FE model (Num.): (a) out-of-plane modes, and (b) in-plane modes.

(a)

	Exp.															
Num.	1	2	3	4	5	6	7	8	9	10	11	12	13	14	15	16
1	99.8	0.7	0.4	0.8	0.6	14.1	3.4	0.7	0.8	6.0	0.4	0.9	0.3	17.9	3.7	0.1
2	0.4	99.3	0.5	1.4	7.1	0.0	1.0	1.6	1.1	0.7	0.6	1.8	7.7	0.1	0.8	0.1
3	0.5	0.5	99.7	0.6	0.8	0.0	0.5	0.5	0.3	0.6	18.4	7.7	0.7	0.2	0.8	0.0
4	0.4	2.1	0.5	99.4	2.2	0.0	1.4	1.0	12.2	1.7	0.5	1.0	1.3	0.1	2.2	7.0
5	0.7	7.3	0.2	2.5	98.9	0.1	0.7	1.7	1.8	1.5	0.7	2.0	17.2	0.0	0.7	0.4
6	13.3	0.1	0.0	0.0	0.5	98.6	0.1	0.0	0.3	0.9	0.0	0.0	0.0	10.9	4.5	0.2
7	4.2	0.8	1.0	1.2	0.6	1.6	97.1	2.1	1.1	2.1	1.1	2.3	0.3	2.2	12.8	0.0
8	2.3	0.4	1.3	0.4	0.8	0.1	3.0	95.7	0.2	2.4	0.1	6.6	0.6	0.5	2.3	0.1
9	0.5	1.2	0.4	11.5	1.9	0.0	1.0	0.7	98.8	3.1	0.1	1.0	1.3	0.1	2.6	12.1
10	1.8	0.7	1.9	0.3	0.7	1.9	1.1	2.6	0.2	95.7	1.5	3.4	0.2	0.2	8.5	0.0
11	0.4	0.5	19.3	0.4	0.8	0.2	0.9	0.2	0.6	0.8	99.2	0.6	0.7	0.0	1.3	0.0
12	2.1	1.9	2.5	0.8	1.4	0.5	1.9	7.2	0.2	3.1	0.0	95.4	3.8	0.7	3.0	0.0
13	0.6	7.5	0.1	1.4	17.2	0.1	1.2	0.3	2.5	1.2	0.1	0.1	98.5	0.0	1.4	0.1
14	16.6	0.1	0.2	0.4	0.1	11.6	3.6	0.2	0.2	0.0	0.1	0.3	0.4	98.7	2.9	0.3
15	1.4	0.5	2.1	1.7	0.8	1.8	7.8	1.8	1.2	10.0	2.1	3.6	0.3	0.1	96.4	0.4
16	0.0	0.0	0.3	5.2	0.0	0.0	0.1	0.0	12.8	0.0	0.3	0.1	0.0	0.0	0.0	96.7

(b)

	Exp.	
Num.	1	2
1	93.33	0.01
2	0.01	98.67

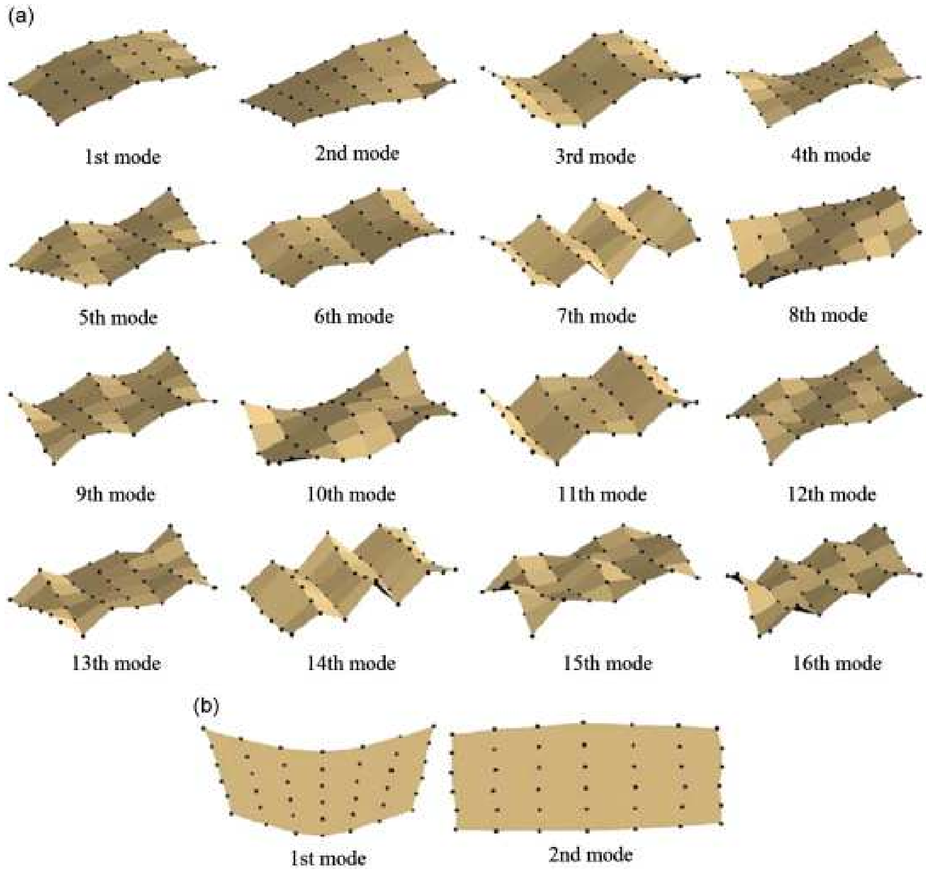

Figure 2.8: Measured mode shapes from OMA: (a) out-of-plane modes, and (b) in-plane modes.

2.1.6 Conclusion

A non-contact OMA test method is presented to measure the out-of-plane and in-plane modes of a rectangular plate using white noise acoustic excitation in the frequency range of up to 15,000 Hz. A single-point laser vibrometer is used to measure the velocities of the measurement points on the plate surface and a free-field microphone is used to measure the pressure near the reference point. It is shown that OMA can be performed even when the types of measurement at the measurement points and the reference point are different and the pressure near a point of a vibrating structure is proportional to the normal surface acceleration at that point. The cross-correlation functions between the velocities of the measurement points and the pressure near the reference point contain modal characteristics of the test structure, which can be extracted using the associated CPSDs. The in-plane modes of the plate are identified by comparing the out-of-plane and mixed CPSDs. EMA is also performed to measure the out-of-plane and in-plane modes of the plate. A FE model of the plate is created and the numerical results are compared with the experimental ones from OMA and EMA. The maximum error between the measured and calculated natural frequencies is 1.53 percent for the first 16 out-of-plane and first two in-plane elastic modes, and the corresponding MAC values are all above 93 percent.

2.2 Modal Test Method Using Sound Pressure Transducers Based on Vibro-acoustic Reciprocity

2.2.1 Introduction

EMA is one of the standard experimental approaches to validate the FE model of a structure, where the input to the test structure is in the form of a force and the output from the structure a displacement, velocity, or acceleration response [1, 42]. When the roving hammer technique is used in EMA, a measurement point is fixed on the test structure and an impact hammer roves over the structure. The location of the measurement point is crucial since some mode may not be captured in the test if the measurement point lies on a nodal line of a mode [43] or in an inactive area of a local mode. In order to mitigate the problem, EMA can be conducted using multiple measurement points at different locations. However, it can be difficult to find the proper locations for the measurement points at which all the modes of interest can be captured unless an accurate FE model of the structure is available, providing accurate mode shape information. On the other hand, mass loading due to the use of multiple sensors on the test structure can affect the accuracy of measurement [44], especially for a symmetric structure, whose repeated or close natural frequencies can be destroyed. A laser vibrometer can be used to avoid mass loading in EMA, but it may not be available in many laboratories. Another critical aspect of EMA is the excitation method. A shaker can be connected to the test structure to generate a prescribed excitation force, but the response measurements, especially in the neighborhoods of resonant frequencies, can have low signal-to-noise ratios due to impedance mismatch between the shaker and the test structure [45]. An impact hammer can be used in EMA, but the sensors attached on the structure far away from the excitation point may not capture much vibration. While acoustic excitation can excite the surface of the test structure, it is difficult to measure the acoustic excitation on the surface of the structure. An acoustic modal analysis method was proposed in [46] to measure the modal characteristics of a structure by using an impact hammer and microphones, and the time delay due to the use of microphones was corrected [47]. However, the method does not consider the effects of the structural-acoustic coupling. When acoustic excitation or measurement is involved in a modal test, coupling exists in the corresponding structural-acoustic system, and asymmetry is introduced in the model formulation [48, 49]. As a result, left and right eigenvectors can be defined for the associated eigenvalue problem, and the relations between the structural and acoustic components in the left and right eigenvectors of an undamped coupled system were provided in [50]. The formulation of a damped structural-acoustic system was given for a closed cavity in [51].

In this section, a VMT method is developed, where an impact hammer roves over the test structure and sound pressure transducers at fixed locations are used to measure its dynamic responses. The formulation of a structurally damped structural-acoustic system in an open environment and the associated eigenvalue problem are provided. The biorthonormality relations between the left and right eigenvectors and the relations between the structural and acoustic components of the left and right eigenvectors are proved. The FRFs used in the VMT method are derived, which contain the modal characteristics of the coupled system, and the assumptions used in the acoustic modal analysis in [46, 47] are validated. It is assumed in the VMT method that the natural frequencies and the structural components of the right eigenvectors of the coupled system can be used to approximate the natural frequencies and mode shapes of the structure. Based on the vibro-acoustic reciprocity, the VMT method is equivalent to the one, where acoustic excitation sources are used to excite the test structure and the resulting acceleration is measured, and the guidelines for using the VMT method, including the types of structures that are suitable for the method, the positions of the sound pressure transducers, and the orientation of the test structure relative to the transducers, are provided. The VMT method and EMA were carried out on an automotive disk brake and the experimental results were compared. It is experimentally shown that the VMT method can capture all the out-of-plane modes, including global and local ones, and EMA can miss certain modes. The differences between the measured natural frequencies of the first 18 elastic modes by the VMT method and EMA are less than 1% and the MAC values [1] of the associated modes are all above 90%. The errors between the measured natural frequencies by the VMT method and the calculated ones from the FE model are less than 3% for the first 18 elastic modes, and the associated MAC values are all above 90%. The VMT method was also carried out on a light circuit board to measure its natural frequencies and mode shapes in the frequency range of up to 2500 Hz, for which the use of accelerometers can introduce relatively large mass loading.

2.2.2 Structural-acoustic System Formulation

2.2.2.1 Eigenvalue Problem

The FE formulation of an undamped, coupled structural-acoustic system has been given in [48] using a displacement-pressure model for a closed cavity. A similar FE formulation has been given in [52] for a coupled fluid-structural system, based on which the FE formulation of a coupled structural-acoustic system in an open environment can be obtained. To apply this formulation, it is assumed that the structure is totally submerged in air and the effects of the boundary of air can be neglected, which yields the following governing equation:

$$\begin{bmatrix} M_s & 0 \\ M_c & M_a \end{bmatrix} \begin{Bmatrix} \ddot{u}_s \\ \ddot{p}_a \end{Bmatrix} + \begin{bmatrix} K_s & K_c \\ 0 & K_a \end{bmatrix} \begin{Bmatrix} u_s \\ p_a \end{Bmatrix} = \begin{Bmatrix} f_s \\ f_a \end{Bmatrix} \tag{2.33}$$

where u_s is the n-dimensional displacement vector of the structure and p_a is the m-dimensional sound pressure vector of the acoustic field; f_s is the n-dimensional structural force vector and f_a is the m-dimensional sound source in the acoustic field; M_s and K_s are the $n \times n$ structural mass and stiffness matrices, respectively; M_a and K_a are the $m \times m$ acoustic mass and stiffness matrices, respectively; and M_c and K_c are the coupling matrices of the system of dimensions $m \times n$ and $n \times m$, respectively. Note that M_s, M_a, K_s, and K_a are symmetric. In Eq. (2.33), the upper and lower equations represent the structural and acoustic parts of the system, respectively. The relationship between the two coupling matrices can be expressed by [52]

$$M_c = -K_C^T \tag{2.34}$$

A similar relation between the two coupling matrices has been derived for a closed cavity. Assume that viscous damping effects exist in the structural part in Eq. (2.33) and those in the acoustic part can be neglected; no coupling exists between the structural and acoustic damping [53]. Adding structural damping to Eq. (2.33) yields

$$\begin{bmatrix} M_s & 0 \\ M_c & M_a \end{bmatrix} \begin{Bmatrix} \ddot{u}_s \\ \ddot{p}_a \end{Bmatrix} + \begin{bmatrix} C_s & 0 \\ 0 & 0 \end{bmatrix} \begin{Bmatrix} \dot{u}_s \\ \dot{p}_a \end{Bmatrix} + \begin{bmatrix} K_s & K_c \\ 0 & K_a \end{bmatrix} \begin{Bmatrix} u_s \\ p_a \end{Bmatrix} = \begin{Bmatrix} f_s \\ f_a \end{Bmatrix} \tag{2.35}$$

where C_s is the symmetric structural damping matrix of dimensions $n \times n$. In order to determine the natural frequencies and mode shapes of the structural-acoustic system, it is assumed that the system has no excitation, which yields the following equation:

$$\begin{bmatrix} M_s & 0 \\ M_c & M_a \end{bmatrix} \begin{Bmatrix} \ddot{u}_s \\ \ddot{p}_a \end{Bmatrix} + \begin{bmatrix} C_s & 0 \\ 0 & 0 \end{bmatrix} \begin{Bmatrix} \dot{u}_s \\ \dot{p}_a \end{Bmatrix} + \begin{bmatrix} K_s & K_c \\ 0 & K_a \end{bmatrix} \begin{Bmatrix} u_s \\ p_a \end{Bmatrix} = \begin{Bmatrix} 0 \\ 0 \end{Bmatrix} \tag{2.36}$$

Due to the coupling between the structure and the acoustic field, it is difficult to directly solve Eq. (2.36). Let

$$\widetilde{M} = \begin{bmatrix} M_s & 0 \\ M_c & M_a \end{bmatrix}, \quad \widetilde{C} = \begin{bmatrix} C_s & 0 \\ 0 & 0 \end{bmatrix}, \quad \widetilde{K} = \begin{bmatrix} K_s & K_c \\ 0 & K_a \end{bmatrix}, \; y = \begin{Bmatrix} u_s \\ p_a \end{Bmatrix} \tag{2.37}$$

Equation (2.36) can be written in an equivalent state space form:

$$\begin{bmatrix} -\widetilde{K} & 0 \\ 0 & \widetilde{M} \end{bmatrix} \begin{Bmatrix} \dot{y} \\ \ddot{y} \end{Bmatrix} + \begin{bmatrix} 0 & \widetilde{K} \\ \widetilde{K} & \widetilde{C} \end{bmatrix} \begin{Bmatrix} y \\ \dot{y} \end{Bmatrix} = \begin{Bmatrix} 0 \\ 0 \end{Bmatrix} \tag{2.38}$$

The solution to Eq. (2.38) is assumed in the form:

$$\begin{Bmatrix} y \\ \dot{y} \end{Bmatrix} = \begin{Bmatrix} ve^{\lambda t} \\ \lambda ve^{\lambda t} \end{Bmatrix} \tag{2.39}$$

where λ is an undetermined constant and v is an $(n+m)$-dimensional vector. Let

$$\eta = \begin{Bmatrix} v \\ \lambda v \end{Bmatrix} \tag{2.40}$$

and the following expressions can be obtained:

$$\begin{Bmatrix} y \\ \dot{y} \end{Bmatrix} = \eta e^{\lambda t}, \; \begin{Bmatrix} \dot{y} \\ \ddot{y} \end{Bmatrix} = \lambda \eta e^{\lambda t} \tag{2.41}$$

Substituting Eq. (2.41) into Eq. (2.38) and canceling $e^{\lambda t}$ yield

$$\lambda \begin{bmatrix} -\widetilde{K} & 0 \\ 0 & \widetilde{M} \end{bmatrix} \eta + \begin{bmatrix} 0 & \widetilde{K} \\ \widetilde{K} & C \end{bmatrix} \eta = \begin{Bmatrix} 0 \\ 0 \end{Bmatrix} \tag{2.42}$$

Let

$$S = \begin{bmatrix} -\widetilde{K} & 0 \\ 0 & \widetilde{M} \end{bmatrix} \quad , \quad R = \begin{bmatrix} 0 & \widetilde{K} \\ \widetilde{K} & C \end{bmatrix} \tag{2.43}$$

and Eq. (2.42) can be written as a generalized eigenvalue problem associated with the structural-acoustic system:

$$(\lambda S + R)\, \eta = 0 \tag{2.44}$$

Due to asymmetry of the matrices S and R, there exist right and left eigenvectors of the eigenvalue problem in Eq. (2.44). Let η_i^r be the right eigenvector corresponding to the eigenvalue λ_i of the eigenvalue problem in Eq. (2.44), which satisfies

$$(\lambda_i S + R)\, \eta_i^r = 0 \tag{2.45}$$

The left eigenvector η_j^l satisfies

$$\eta_j^{lT}\, (\lambda_j S + R) = 0 \tag{2.46}$$

where the superscript T denotes the transpose of a matrix, or

$$\left(\lambda_j S^T + R^T\right) \eta_j^l = 0 \tag{2.47}$$

It is assumed that all the eigenvalues of the eigenvalue problem in Eq. (2.44) are distinct. Note that while the eigenvalues in Eqs. (2.45) and (2.46) are the same, the corresponding left and right eigenvectors are not the same [54]. Pre-multiplying Eq. (2.45) by η_j^{lT} yields

$$\eta_j^{lT}\left(\lambda_i S + R\right)\eta_i^r = 0 \tag{2.48}$$

Post-multiplying Eq. (2.46) by η_i^r yields

$$\eta_j^{lT}\left(\lambda_j S + R\right)\eta_i^r = 0 \tag{2.49}$$

Subtracting Eq. (2.49) from Eq. (2.48) yields

$$\left(\lambda_i - \lambda_j\right)\eta_j^{lT} S \eta_i^r = 0 \tag{2.50}$$

If $i \neq j$, since all the eigenvalues are distinct, by Eq. (2.50), one has

$$\eta_j^{lT} S \eta_i^r = 0 \tag{2.51}$$

Substituting Eq. (2.51) into Eq. (2.48) yields

$$\eta_j^{lT} R \eta_i^r = 0 \tag{2.52}$$

When $i = j$, the right and left eigenvectors can be normalized as follows:

$$\eta_i^{lT} S \eta_i^r = 1 \tag{2.53}$$

Using Eq. (2.53) in Eq. (2.48) yields

$$\eta_i^{lT} R \eta_i^r = -\lambda_i \tag{2.54}$$

Equations (2.51) - (2.54) are the biorthonormality relations between the left and right eigenvectors of the system.

Assuming that the structural and acoustic components in the left eigenvector η_i^l, which are ϕ_{si}^l and ϕ_{ai}^l, respectively, can be related to those in the right eigenvector η_i^r, which are ϕ_{si}^r and ϕ_{ai}^r, respectively:

$$\phi_{si}^l = a\phi_{si}^r,\ \phi_{ai}^l = b\phi_{ai}^r \tag{2.55}$$

then the left eigenvector η_i^l can be expressed by

$$\eta_i^l = \begin{Bmatrix} \phi_{si}^l \\ \phi_{ai}^l \\ \lambda_i\phi_{si}^l \\ \lambda_i\phi_{ai}^l \end{Bmatrix} = \begin{Bmatrix} a\phi_{si}^r \\ b\phi_{ai}^r \\ \lambda_i a\phi_{si}^r \\ \lambda_i b\phi_{ai}^r \end{Bmatrix} \tag{2.56}$$

Substituting Eq. (2.56) into Eq. (2.46) yields

$$\begin{cases} -a\phi_{si}^{rT}\lambda_i K_s + a\phi_{si}^{rT}\lambda_i K_s = 0 \\ -a\phi_{si}^{rT}\lambda_i K_c - b\phi_{ai}^{rT}\lambda_i K_s + a\phi_{si}^{rT}\lambda_i K_c + b\phi_{ai}^{rT}\lambda_i K_s = 0 \\ a\phi_{si}^{rT}K_s + a\phi_{si}^{rT}\lambda_i\left(\lambda_i M_s + C_s\right) + b\phi_{ai}^{rT}\lambda_i^2 M_c = 0 \\ a\phi_{si}^{rT}K_c + b\phi_{ai}^{rT}K_a + b\phi_{ai}^{rT}\lambda_i^2 M_a = 0 \end{cases} \tag{2.57}$$

Since the first two equations in Eq. (2.57) are identically satisfied, Eq. (2.57) becomes

$$\begin{cases} a\phi_{si}^{rT}K_s + a\phi_{si}^{rT}\lambda_i\left(\lambda_i M_s + C_s\right) + b\phi_{ai}^{rT}\lambda_i^2 M_c = 0 \\ a\phi_{si}^{rT}K_c + b\phi_{ai}^{rT}K_a + b\phi_{ai}^{rT}\lambda_i^2 M_a = 0 \end{cases} \tag{2.58}$$

Due to symmetry of K_s, K_a, M_s, and M_a, taking the transpose of Eq. (2.58) and using Eq. (2.34) in the resulting expressions yield

$$\begin{cases} aK_s\phi_{si}^r + a\lambda_i\left(\lambda_i M_s + C_s\right)\phi_{si}^r - b\lambda_i^2 K_c\phi_{ai}^r = 0 \\ -aM_c\phi_{si}^r + bK_a\phi_{ai}^r + b\lambda_i^2 M_a\phi_{ai}^r = 0 \end{cases} \tag{2.59}$$

Expanding Eq. (2.45) using Eqs. (2.40) and (2.43) yields

$$\begin{cases} -\lambda_i K_s\phi_{si}^r - \lambda_i K_c\phi_{ai}^r + \lambda_i K_s\phi_{si}^r + \lambda_i K_c\phi_{ai}^r = 0 \\ -\lambda_i K_a\phi_{si}^r + \lambda_i K_a\phi_{si}^r = 0 \\ K_s\phi_{si}^r + K_c\phi_{ai}^r + \lambda_i\left(\lambda_i M_s + C_s\right)\phi_{si}^r = 0 \\ K_a\phi_{ai}^r + \lambda_i^2 M_c\phi_{si}^r + \lambda_i^2 M_a\phi_{ai}^r = 0 \end{cases} \tag{2.60}$$

Since the first two equations in Eq. (2.60) are identically satisfied, Eq. (2.60) becomes

$$\begin{cases} K_s\phi_{si}^r + K_c\phi_{ai}^r + \lambda_i\left(\lambda_i M_s + C_s\right)\phi_{si}^r = 0 \\ K_a\phi_{ai}^r + \lambda_i^2 M_c\phi_{si}^r + \lambda_i^2 M_a\phi_{ai}^r = 0 \end{cases} \tag{2.61}$$

Comparing Eqs. (2.59) and (2.61), one has $a = \kappa$ and $b = -\frac{\kappa}{\lambda_i^2}$, where κ can be any non-zero constant. Hence, by Eq. (2.56), the left eigenvector η_i^l can be expressed by

$$\eta_i^l = \begin{Bmatrix} \phi_{si}^l \\ \phi_{ai}^l \\ \lambda_i\phi_{si}^l \\ \lambda_i\phi_{ai}^l \end{Bmatrix} = \kappa \begin{Bmatrix} \phi_{si}^r \\ -\frac{1}{\lambda_i^2}\phi_{ai}^r \\ \lambda_i\phi_{si}^r \\ -\frac{1}{\lambda_i}\phi_{ai}^r \end{Bmatrix} \tag{2.62}$$

For the convenience of discussion, let $\kappa = 1$, and one can obtain from Eq. (2.62) the relation between the structural components of the left and right eigenvectors:

$$\phi_{si}^l = \phi_{si}^r \tag{2.63}$$

and that between the acoustic components:

$$\phi_{ai}^{l} = -\frac{1}{\lambda_i^2}\phi_{ai}^{r} \tag{2.64}$$

2.2.2.2 FRFs

A sinusoidal force $Fe^{i\omega t}$ with frequency ω is applied on the structural part of the system described by Eq. (2.44), where $F = \left\{ \begin{array}{cc} F_s^T & 0^T \end{array} \right\}^T$ is an $(n+m)$-dimensional vector, in which $F_s = \left\{ \begin{array}{cccc} f_{s1} & f_{s2} & \dots & f_{sn} \end{array} \right\}^T$ is an n-dimensional structural force vector. Assuming a harmonic response of the system with frequency ω and canceling $e^{i\omega t}$ yield

$$(R + i\omega S)\,\eta = \left\{ \begin{array}{c} 0 \\ \\ F \end{array} \right\} \tag{2.65}$$

A coordinate transformation is applied on η by letting

$$\eta = \Phi^r q \tag{2.66}$$

where $\Phi^r = \left[\begin{array}{cccccc} \eta_1^r & \dots & \eta_{(m+n)}^r & \eta_1^{r*} & \dots & \eta_{(m+n)}^{r*} \end{array} \right]$, in which the superscript $*$ denotes complex conjugation, is a matrix containing the right eigenvectors, and q is a $2\times(n+m)$-dimensional modal coordinate vector. Substituting Eq. (2.66) into Eq. (2.65), pre-multiplying the resulting expression by Φ^{lT}, where $\Phi^l = \left[\begin{array}{ccccc} \eta_1^l & \dots & \eta_{(m+n)}^l & \eta_1^{l*} & \dots \end{array} \right.$ is a matrix containing the left eigenvectors, and applying the biorthonormality relations of the left and right eigenvectors in Eqs. (2.51) - (2.54) yield

$$\Lambda q = \Phi^{lT} \begin{Bmatrix} 0 \\ F \end{Bmatrix} \tag{2.67}$$

where $\Lambda = \text{diag}\begin{bmatrix} -\lambda_1 + i\omega, & \ldots, & -\lambda_{m+n} + i\omega, & -\lambda_1^* + i\omega, & \ldots, & -\lambda_{m+n}^* + i\omega \end{bmatrix}$. The modal coordinate vector q can be obtained from Eq. (2.67):

$$q = \Lambda^{-1}\Phi^{lT} \begin{Bmatrix} 0 \\ F \end{Bmatrix} \tag{2.68}$$

Substituting Eq. (2.68) into Eq. (2.66) yields

$$\eta = \Phi^r q = \Phi^r \Lambda^{-1}\Phi^{lT} \begin{Bmatrix} 0 \\ F \end{Bmatrix} \tag{2.69}$$

The ratio of the pressure p_{ai} measured at point i in the acoustic field to the applied force f_{sj} at point j on the structure is

$$\frac{p_{ai}}{f_{sj}} = \sum_{h=1}^{m+n} \left(\frac{\lambda_h \phi_{ahi}^r \phi_{shj}^l}{-\lambda_h + i\omega} + \frac{\left(\lambda_h \phi_{ahi}^r \phi_{shj}^l\right)^*}{-\lambda_h^* + i\omega} \right) \tag{2.70}$$

Using Eq. (2.63) in Eq. (2.70) yields

$$\frac{p_{ai}}{f_{sj}} = \sum_{h=1}^{m+n} \left(\frac{\lambda_h \phi_{ahi}^r \phi_{shj}^r}{-\lambda_h + i\omega} + \frac{\left(\lambda_h \phi_{ahi}^r \phi_{shj}^r\right)^*}{-\lambda_h^* + i\omega} \right) \tag{2.71}$$

While the matrices $\widetilde{M}$ and $\widetilde{K}$ are non-symmetric, the modal characteristics of the system described by Eq. (2.35) are contained in Eqs. (2.70) and (2.71), and can be extracted from the FRFs in Eqs. (2.70) and (2.71) with the roving hammer technique using a well-developed modal analysis algorithm, such as PolyMax [30].

In the acoustic modal analysis in [46, 47],it is assumed that the sound pressure linearly varies with the amplitude of vibration of the test structure at a certain frequency , which is proportional to the amplitude of excitation at an input point. Hence the sound pressure is proportional to the amplitude of excitation at the input point at a certain frequency, which can be validated by Eq. (2.70). It is further assumed in [46, 47] that the amplitude of vibration of the test structure at a certain natural frequency varies with the modal coefficient of the input point, and the sound pressure per unit excitation force at the input point at the natural frequency is proportional to the modal coefficient of the input point. In Eq. (2.70), let $\omega = \omega_k$, where ω_k is the natural frequency of the k-th mode of the structural-acoustic system; the sound pressure per unit excitation force at the natural frequency ω_k can be approximated by

$$\frac{p_{ai}}{f_{sj}} = \frac{\lambda_k \phi^l_{aki} \phi^l_{skj}}{-\lambda_k + i\omega_k} \tag{2.72}$$

where ϕ^l_{skj} is the modal coefficient of the input point j for the k-th mode, and the second assumption in the acoustic modal analysis in [46, 47] can be validated. Note that in the acoustic modal analysis in [46, 47], the measured natural frequencies of the test structure are the ones of the structural-acoustic system, and the measured mode shapes are the structural components of the left eigenvectors of the coupled system; this would also be the case for the VMT method, as illustrated below.

2.2.3 Modal Test Based on Vibro-acoustic Reciprocity

Based on Eq. (2.70), the VMT method can measure the natural frequencies and the structural components of the left eigenvectors of the coupled system using an impact hammer and one or multiple sound pressure transducers. By Eqs. (2.63) and (2.71), the VMT method can measure the natural frequencies and the structural components of the right eigenvectors of the coupled system. Assuming that the natural frequencies and mode shapes of the structure in the structural-acoustic system described by Eq. (2.35) can be approximated by the natural frequencies and the structural components of the right eigenvectors of the coupled system, respectively, one can use the VMT method to measure the natural frequencies and mode shapes of the structure.

A vibro-acoustic reciprocity can be applied to a structural-acoustic system consisting of a linear elastic structure that is contiguous with air, based on which the transfer function between a structural force applied to the structure and the resulting sound pressure in rest contiguous air can be determined by exciting the structure with an omnidirectional point sound source and measuring the resulting acceleration of the structure [55]. The vibro-acoustic reciprocity is also referred to as Lyamshev reciprocity, and can be expressed by

$$\frac{p_{ai}}{f_{sj}} = -\frac{a_{sj}}{\dot{q}_{ai}} \tag{2.73}$$

where f_{sj} is the applied force to point j on the structure, p_{ai} is the measured sound pressure at point i in air induced by f_{sj}, $\dot{q}_{ai}$ is the volume acceleration of the point sound source at point i in air, and a_{sj} is the acceleration of point j on the structure induced by the point sound source. Note that f_{sj} and a_{sj} are in the same direction and $\dot{q}_{ai}$ represents the strength of the point sound source.

Based on the vibro-acoustic reciprocity, the VMT method is equivalent to the one where one or multiple omnidirectional point sound sources of known strengths are used to excite the structure and the resulting acceleration is measured. When the roving hammer technique is used, the measured mode shapes by the VMT method and EMA are in the directions of impacts. Since the impact directions are usually perpendicular to the surfaces being impacted, the merely in-plane modes cannot be excited by the VMT method and EMA, and only the out-of-plane components of mode shapes can be measured. A difference between the VMT method and EMA lies in the measurements of the dynamic responses of the structure since the former measures the pressure in air and the latter measures the acceleration of the structure. If one sound pressure transducer and one accelerometer are used in the VMT method and EMA, respectively, the FRFs from the former can be considered to be obtained by multiple inputs and a single output as if a point sound source and an accelerometer were used, according to Eq. (2.73), while those from the latter are obtained by a single input and a single output. Assuming that the excitation points are properly selected on the test structure and all the modes within a frequency range of interest can be excited, this difference enables the VMT method to capture all the out-of-plane modes of the structure of interest, including global and local ones, while EMA can miss some of the modes if the positions of the measurement points are improperly selected. The problem can occur when a measurement point in EMA is on a nodal line of a mode or in an inactive area of a local mode, which cannot be captured by the resulting FRFs. This problem will not occur in the VMT method, since the sound pressure transducer is located away from the test structure. Though the value of ϕ^r_{ahi} for a certain mode h in Eq. (2.71) can be relatively low, it does not vanish in that the pressure measured at the natural frequency ω_h by the sound pressure transducer does not vanish unless the excitation point is on a nodal line or in an inactive area of the mode. Use of multiple sound pressure sensors in the VMT method can help improve the measurement quality.

The VMT method is applicable to structures of any shapes when no noise is involved in the measurement of sound pressure. When noise is involved, the method may not be suitable for slender structures and structures with small surface areas. As illustrated in Fig. 2.9, the area of the surface of a structure facing an ideal point sound source is S_f; projecting the surface to a sphere with the center at the sound source, a constant radius r, and a surface area $S_t = 4\pi r^2$ gives a surface with an area S_p. The portion of the sound power that can reach the structure from the point source with a power W is βW, where $\beta = \frac{S_p}{S_t}$ is independent of r. A structure with a small value of β cannot be well excited by the point source, and the measured transfer functions between the strength of the point sound source and the resulting accelerations on the structure have low SNRs. Consequently, based on the vibro-acoustic reciprocity, the measured FRFs in the VMT method using an ideal omnidirectional point sound pressure transducer at the location of the point sound source have low SNRs. Since the value of β is almost inversely proportional to the square of the distance between the sound pressure transducer and the structure, placing the sound pressure transducer close to the structure can increase the value of β. The sound pressure transducers should also be placed on the same side of the impacted surfaces of the structure to increase the SNRs of the measured FRFs. One should adjust the orientation of the structure so that a larger projected surface area can be obtained, which results in a larger β. However, for slender structures such as cables, and structures with small surface areas such as truss structures, the values of β can remain relatively small even if a sound pressure transducer is placed close to them. Hence the VMT method is more suitable for plate-like structures and structures with relatively large surface areas.

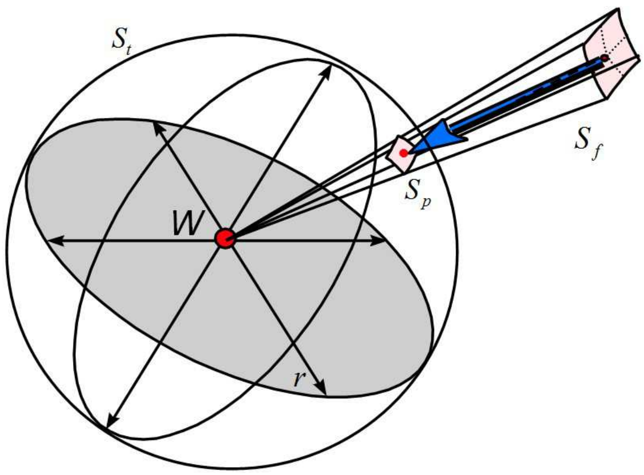

Figure 2.9: Portion of the acoustic power from a point sound source with a power W transmitted to the area S_p projected from the surface of a structure facing the point source.

2.2.4 Experimental Validation

A case study was performed on an automotive disk brake using both the VMT method and EMA in Sec. 4.1. The experimental results from the two methods were compared and validated using the FE model in Sec. 4.2. The VMT method was also used on a light circuit board to measure its natural frequencies and mode shapes in Sec. 4.3.

2.2.4.1 VMT Method and EMA on a Disk Brake

The disk brake was placed on foams, as shown in Fig. 2.10a, to simulate the free boundary conditions. For both the VMT method and EMA, the brake was excited at 146 points on the flange and in the bolted area, as shown in Fig. 2.10b, using a PCB 086D80 impact hammer. The excitation direction was perpendicular to the brake surfaces. In order to distinguish some of the modes with close natural frequencies due to almost axial-symmetry of the brake, multiple random impacts [56] were given at every excitation point for four seconds in each test, which results in a frequency resolution of 0.25 Hz, and three tests were averaged to ensure repeatable results with a good coherence. The responses of the brake were measured using one PCB U130D20 and two PCB 130E20 microphones and four PCB 352C66 accelerometers for the VMT method and EMA, respectively; the data were collected using an LMS spectrum analyzer. For the VMT method, the three microphones were placed at fixed locations near the brake and pointing towards it, as shown in Fig. 2.10a. For EMA, two sets of tests were conducted; the four accelerometers were attached in one set of tests on the bottom surface of the flange, and in the other set of tests on the bottom surface of the bolted area. Note that the microphones used in the VMT method here are of the free-field type, whose measurements are most accurate when the sound pressure from a single source and a single direction is measured. Since the flange and the bolted area of the brake are flat surfaces, and the microphones were placed not too close to the brake and pointing towards the brake, the measurements of the sound pressure by the microphones can be used in the VMT method by assuming that the sound pressure in the directions perpendicular to those in which the microphones can accurately measure the sound pressure can be neglected.

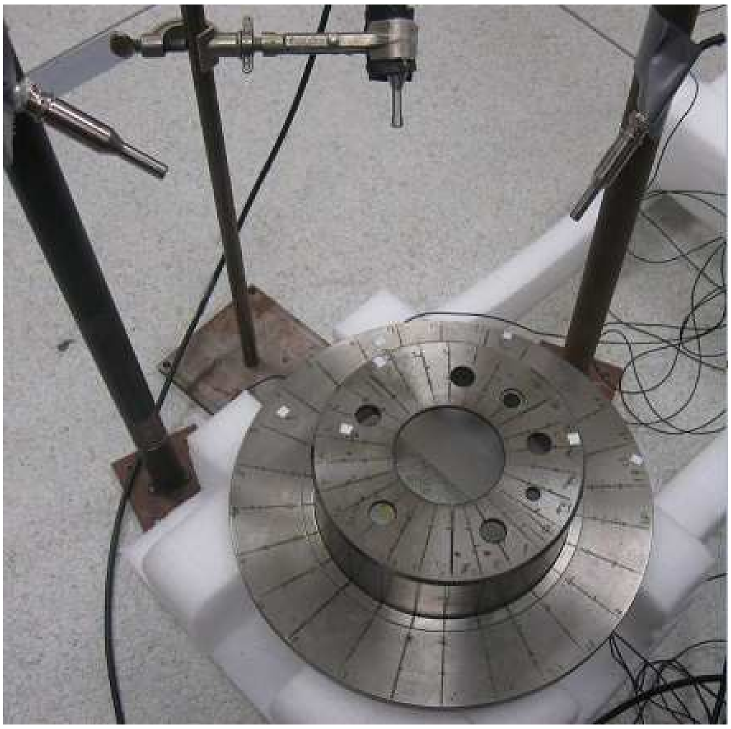

(a)

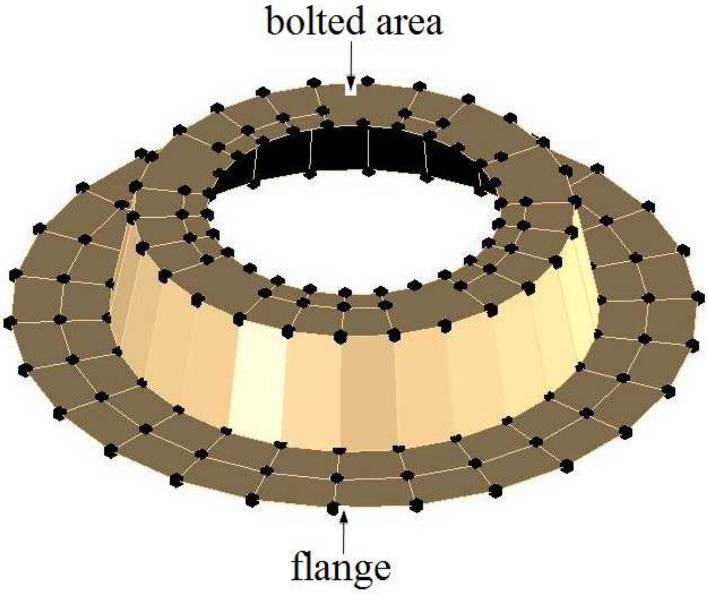

(b)

Figure 2.10: (a) Test setup for the VMT method on the disk brake, and (b) excitation points for the VMT method and EMA.

2.2.4.2 Results and Discussion

Modal analysis was conducted using PolyMax [30] in the modal analysis software LMS Test.Lab Rev. 9b; the measured natural frequencies and mode shapes of the brake by the VMT method were extracted from three sets of measured FRFs from the three microphones, and those by EMA from eight sets of measured FRFs from the four accelerometers. The highest natural frequency of the rigid body modes of the brake in the tests is 36.75 Hz, which is lower than 10% of the natural frequency of the first elastic mode, and the boundary conditions can be considered to be free [1]. In order to experimentally validate the assumption in Sec. 3 that the natural frequencies and mode shapes of the structure can be approximated by the natural frequencies and the structural components of the right eigenvectors of the coupled system, respectively, the natural frequencies of the first 18 elastic modes of the brake from the VMT method and EMA were compared in Tables 2.5 and 2.6, respectively, and the maximum natural frequency difference is 0.74%. The differences between the two sets of measured natural frequencies mainly derive from mass loading introduced by the accelerometers in EMA, since all of the measured natural frequencies from EMA, except that of the fifth elastic mode, are lower than the corresponding ones from the VMT method; the measured natural frequency of the fifth elastic mode from EMA is higher than that from the VMT method due to measurement error. The MAC values of the associated mode shapes, which are the diagonal entries of the MAC matrix [1] in Table 2.6, are all over 90%. Some off-diagonal entries in Table 2.6 are relatively high due to two reasons. One reason is that the number of excitation points is not large enough and some mode shapes cannot be well distinguished from others. The second reason is that the mode shapes were not measured in three dimensions in the tests using the two methods. The impact hammer excited the brake in the direction perpendicular to the surfaces of the flange and the bolted area, and only the out-of-plane mode shapes were measured; one cannot excite the brake in the directions parallel to the surfaces of the flange and the bolted area and the interior points of the brake. If the in-plane components of two distinct modes are not measured, their out-of-plane components can be similar and the corresponding MAC value of the two mode shapes can be relatively high [2].

Table 2.5: Measured natural frequencies of the disk brake by the VMT method and EMA.

Mode	VMT Frequency (Hz)	EMA Frequency (Hz)	Frequency Difference (%)
1	1072.4	1064.5	0.74%
2	1073.8	1070.2	0.34%
3	1237.2	1231.0	0.50%
4	1576.5	1574.5	0.13%
5	1576.7	1578.1	-0.09%
6	1617.4	1608.9	0.53%
7	1620.4	1612.8	0.47%
8	2004.4	2003.2	0.06%
9	2115.5	2113.3	0.10%
10	2115.9	2114.1	0.09%
11	2428.3	2412.1	0.67%
12	2429.3	2421.0	0.34%
13	2591.6	2591.0	0.02%
14	2600.8	2600.2	0.02%
15	3504.0	3503.3	0.02%
16	3504.1	3503.4	0.02%
17	3918.8	3918.1	0.02%
18	3940.5	3938.7	0.05%

Table 2.6: Entries of the MAC matrix in percent corresponding to the first 18 measured mode shapes of the disk brake by the VMT method and EMA; the horizontal and vertical mode numbers correspond to the measured modes by the VMT method and EMA, respectively.

Mode	1	2	3	4	5	6	7	8	9	10	11	12	13	14	15	16	17	18
1	96	49	6	4	4	6	2	1	17	29	11	2	0	0	4	2	1	2
2	41	95	5	2	7	7	4	1	32	28	5	3	0	1	2	3	4	3
3	10	3	98	17	7	5	0	57	5	5	4	3	5	8	1	5	3	8
4	1	2	8	92	34	2	8	9	3	6	1	3	45	22	2	5	3	3
5	0	8	4	29	91	13	13	3	4	2	3	0	18	21	1	3	0	2
6	3	4	2	10	3	91	28	1	2	3	5	10	3	2	2	2	1	1
7	2	7	2	3	9	46	97	1	2	3	3	6	2	3	5	3	1	1
8	1	1	64	9	5	2	1	100	7	3	3	2	7	7	1	1	5	11
9	20	25	6	3	11	4	5	8	90	16	5	4	1	1	4	2	25	2
10	26	37	6	2	2	7	2	4	40	94	4	2	2	3	1	1	15	25
11	9	6	4	2	4	7	2	1	5	6	92	29	3	3	8	7	1	1
12	3	6	3	3	2	6	4	0	2	7	43	96	0	0	6	12	0	1
13	0	0	3	36	20	0	1	2	0	2	5	3	91	11	1	1	5	3
14	0	0	7	17	36	3	5	6	1	3	2	0	28	99	1	1	7	5
15	1	3	3	3	1	3	5	0	1	3	2	5	0	0	95	14	0	1
16	3	2	0	1	2	6	3	0	2	4	6	6	0	0	26	94	1	0
17	1	2	5	4	2	0	0	8	31	9	1	1	11	8	2	2	94	11
18	3	1	7	2	4	0	1	7	9	34	1	0	13	4	0	0	34	97

The sums of the measured FRFs in the neighborhoods of the first two elastic modes by the VMT method and EMA are shown in Fig. 2.12a, where the measurements are from a microphone away from the brake and an accelerometer on the flange, respectively. Since the brake is almost axial-symmetric, there are pairs of close frequencies, and the associated peaks in the measured FRFs can be close to each other or overlapped depending on the frequency resolution used. As shown in Fig. 2.12a, there is only one peak that can be observed in the summed FRF from the VMT method, from which two distinct modes can be identified by the modal analysis software and their natural frequency difference is 1.6 Hz. The actual natural frequency difference between the two modes may be smaller than 1.6 Hz and two separate peaks representing the two close natural frequencies may be observed if a higher frequency resolution is used in the test. On the other hand, there are two separate peaks corresponding to the two modes in the summed FRF from EMA due to mass loading from the accelerometers, which increases the natural frequency difference to 5.7 Hz. Hence the VMT method is more suitable for an axial-symmetric structure since it can preserve close natural frequencies of the structure due to axial-symmetry.

The sums of the measured FRFs by EMA, where the measurement points are on the flange and in the bolted area of the brake, and that of the measured FRFs by the VMT method are shown in Fig. 2.12b. As shown in Fig. 2.12b, the peaks correspondingto modes 11 and 12 cannot be identified in the summed FRF for which the measurement point is in the bolted area; the same observation can be made for modes 15 and 16. The reason is that the bolted area is inactive for the four modes, whose vibrations cannot be measured by the accelerometer. On the other hand, the peaks corresponding to the four modes can be clearly identified in the summed FRF by the VMT method. The peaks corresponding to modes 17 and 18 cannot be observed in the two summed FRFs for which the measurement points were on the flange and in the bolted area, respectively. However, the peaks corresponding to the two modes can be clearly identified in the summed FRF from the VMT method, as shown in Fig. 2.12b, since the VMT method can capture all the out-of-plane modes, including global and local ones. In the VMT method, the pressure measured by a microphone is from the vibration of the impacted surface of the brake; the quality of the pressure measurement would not be affected much by the nodal lines and local modes of the brake. If the locations of the microphones and the orientation of the brake relative to the microphones comply with the guidelines in Sec. 3, the VMT method would be more efficient than EMA.

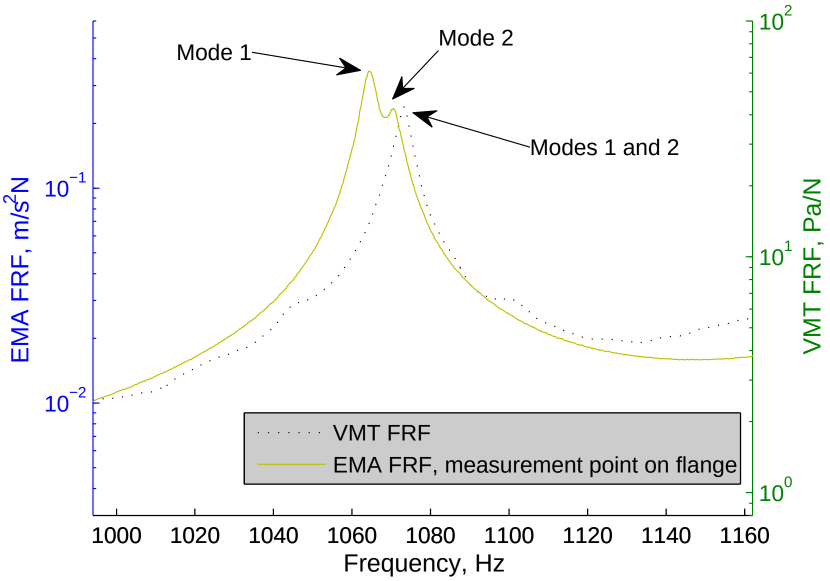

(a)

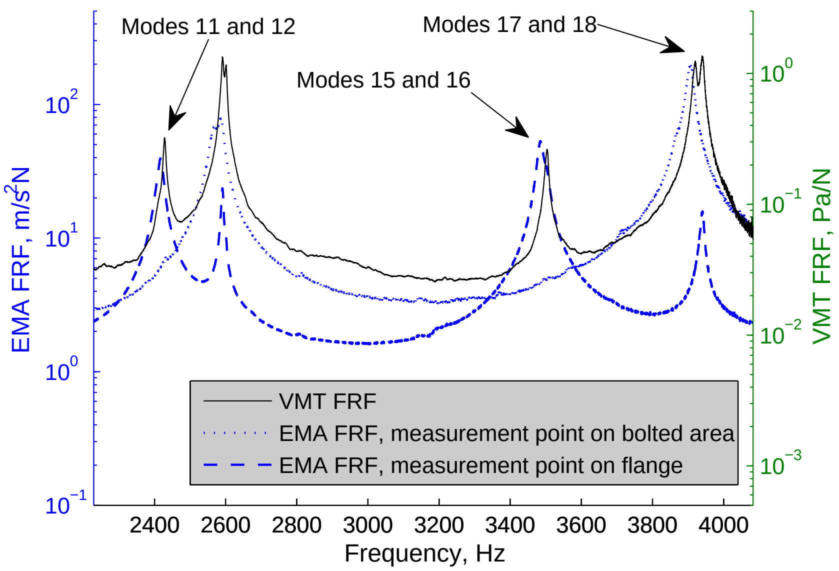

(b)

Figure 2.11: (a) Summed FRFs by the VMT method and EMA in the neighborhood of the first two elastic modes, and (b) summed FRFs by the VMT method and EMA from 2250 Hz to 4050 Hz.

In order to validate the experimental results, an intensive FE model of the brake was created using solid tetrahedral elements in the commercial FE software Abaqus 6.9 EF. The brake is made of cast iron Class 25 with an elastic modulus of 113.7 GPa, a Poisson's ratio of 0.28, and a mass density of 7200 kg/m^3. The profile and the FE model of the brake are shown in Fig. 2.12. Note that the unit in the profile is mm.

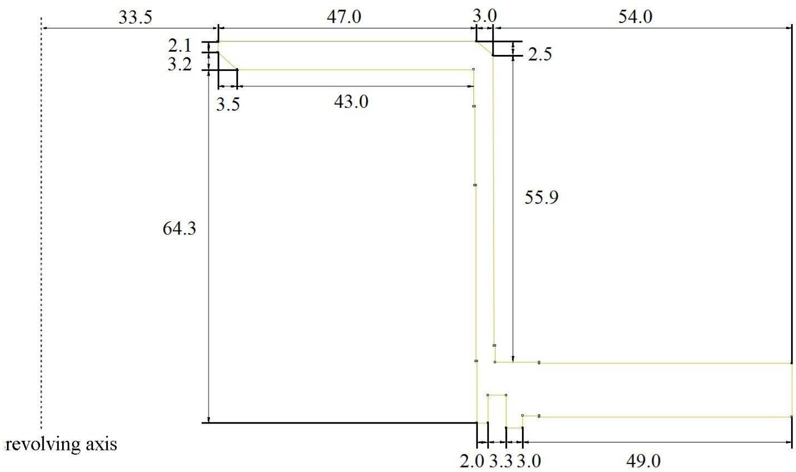

(a)

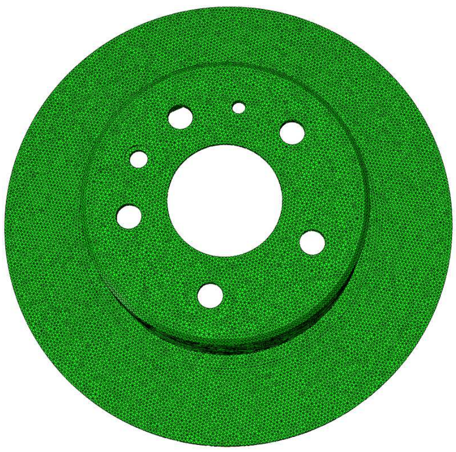

(b)

Figure 2.12: (a) The profile and (b) the FE model of the disk brake.

The calculated natural frequencies of the first 18 elastic modes of the brake from the FE model and the measured ones by the VMT method and EMA are shown in Table 2.7. The errors between the measured natural frequencies by the VMT method and EMA and the calculated ones from the FE model are less than 3%, except that the error for the 11th elastic mode by EMA is 3.26%. The calculated three-dimensional mode shapes from the FE model and the measured out-of-plane ones by the VMT method are shown in Table 2.8. Note that the in-plane components of the calculated eighth and ninth elastic mode shapes in Table 2.8 are relatively large compared to their out-of-plane ones. Note also that the eighth through tenth modes from the VMT method and EMA in Table 2.5 correspond to the tenth, eighth, and ninth modes from the FE model, respectively, and the order for the three modes from the VMT method and EMA has been shifted in Tables 2.7 and 2.8 according to that of the FE model. The MAC matrices for the out-of-plane components of the measured mode shapes by the VMT method and EMA and the calculated ones from the FE model are shown in Tables 2.9 and 2.10, respectively; the MAC values are all over 90%.

Table 2.7: Comparison of measured natural frequencies by the VMT method and EMA with the calculated ones from the FE model.

Mode	Numerical Frequency (Hz)	VMT Frequency (Hz)	Error (%))	EMA Frequency (Hz)	Error (%))
1	1062.5	1072.4	0.93%	1064.5	0.19%
2	1062.7	1073.8	1.04%	1070.2	0.71%
3	1236.7	1237.2	0.03%	1231.0	-0.46%
4	1593.3	1576.5	-1.05%	1574.5	-1.18%
5	1594.0	1576.7	-1.09%	1578.1	-1.00%
6	1651.1	1617.4	-2.04%	1608.9	-2.56%
7	1651.3	1620.4	-1.87%	1612.8	-2.33%
8	2055.3	2115.5	2.93%	2113.3	2.82%
9	2055.5	2115.9	2.94%	2114.1	2.85%
10	2061.8	2004.4	-2.78%	2003.2	-2.84%
11	2493.3	2428.3	-2.61%	2412.1	-3.26%
12	2493.6	2429.3	-2.58%	2421.0	-2.91%
13	2656.5	2591.6	-2.44%	2591.0	-2.47%
14	2666.7	2600.8	-2.47%	2600.2	-2.49%
15	3601.3	3504.0	-2.70%	3503.3	-2.72%
16	3601.5	3504.1	-2.70%	3503.4	-2.72%
17	3995.1	3918.8	-1.91%	3918.1	-1.93%
18	4015.1	3940.5	-1.86%	3938.7	-1.90%

Table 2.8: Mode shapes of the first 18 elastic modes of the brake from the FE model and the VMT method.

Mode	FE Mode Shape	VMT Mode Shape	Mode	FE Mode Shape	VMT Mode Shape
1	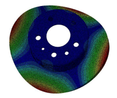	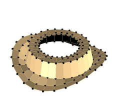	10	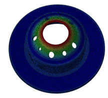	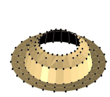
2	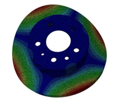	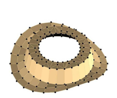	11	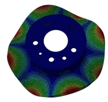	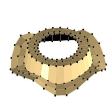
3	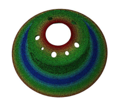	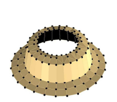	12	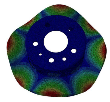	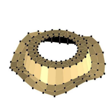
4	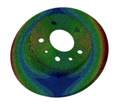	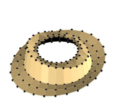	13	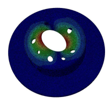	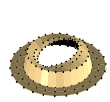
5	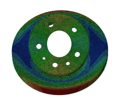	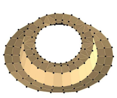	14	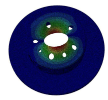	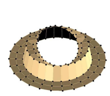
6	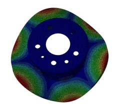	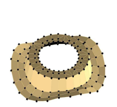	15	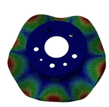	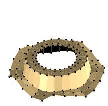
7	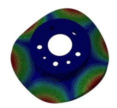	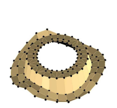	16	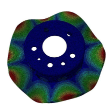	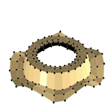
8	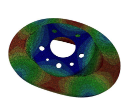	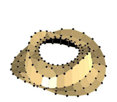	17	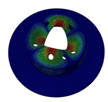	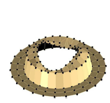
9	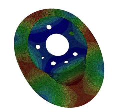	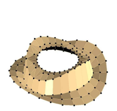	18	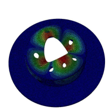	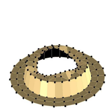

Table 2.9: Entries of the MAC matrix in percent corresponding to the first 18 calculated mode shapes of the disk brake from the FE model and the measured ones by the VMT method; the horizontal and vertical mode numbers correspond to the calculated and measured modes, respectively.

Mode	1	2	3	4	5	6	7	8	9	10	11	12	13	14	15	16	17	18
1	96	15	5	1	3	11	2	2	23	49	6	7	0	0	6	6	1	2
2	29	91	3	4	5	17	8	1	36	45	4	9	0	0	2	4	1	1
3	2	3	99	1	3	1	1	54	4	1	0	5	5	4	1	6	5	6
4	10	2	16	90	32	3	7	7	6	6	7	8	39	4	5	9	2	3
5	8	5	7	9	93	9	11	5	4	7	3	1	5	37	0	3	4	4
6	8	1	3	2	8	92	22	2	1	6	16	3	1	3	6	7	0	0
7	5	6	2	11	13	16	94	1	4	1	3	15	1	4	3	8	0	1
8	0	1	70	3	2	0	0	99	1	0	0	1	5	2	0	1	7	7
9	19	33	7	4	2	6	4	7	91	24	4	1	1	0	2	4	35	11
10	28	20	4	6	2	9	3	3	26	90	5	8	2	3	1	1	20	34
11	1	6	4	2	3	6	1	2	4	2	94	16	6	3	12	18	1	1
12	5	2	2	1	2	8	7	2	2	2	28	92	3	1	11	12	1	0
13	1	0	6	43	19	1	1	7	2	3	1	1	98	13	0	0	5	12
14	0	0	7	28	33	1	0	8	1	3	0	1	33	91	0	0	9	8
15	5	2	1	2	1	4	5	1	2	2	3	10	1	1	94	15	2	1
16	3	3	5	5	3	4	4	2	3	2	10	15	2	1	8	90	1	1
17	1	3	2	3	2	1	0	4	27	6	1	0	6	5	0	1	97	9
18	3	2	9	4	1	0	0	11	6	26	1	1	7	4	1	0	34	93

Table 2.10: Entries of the MAC matrix in percent corresponding to the first 18 calculated mode shapes of the disk brake from the FE model and the measured ones by EMA; the horizontal and vertical mode numbers correspond to the calculated and measured modes, respectively.

Mode	1	2	3	4	5	6	7	8	9	10	11	12	13	14	15	16	17	18
1	95	18	5	2	3	12	4	2	19	51	10	6	0	0	3	3	0	1
2	25	95	3	1	2	12	3	1	41	41	9	6	0	0	1	6	2	1
3	4	3	98	0	4	2	1	48	1	4	3	4	3	5	1	7	5	6
4	2	2	7	90	36	2	2	8	1	4	5	4	41	6	3	5	2	4
5	7	1	3	19	96	11	3	5	3	4	3	1	18	27	2	4	0	1
6	5	10	3	5	7	95	14	1	7	2	8	6	3	4	4	3	1	0
7	4	8	0	8	8	28	93	1	6	1	3	12	1	3	2	4	1	0
8	1	0	71	2	2	0	0	99	1	0	0	1	3	3	0	1	7	7
9	23	38	6	2	9	4	2	7	94	14	6	1	0	0	2	4	31	10
10	24	27	7	3	2	7	4	3	31	90	5	5	1	3	1	3	17	29
11	11	2	3	1	4	7	2	1	3	8	93	8	2	3	12	14	0	1
12	3	1	2	1	1	2	7	1	2	1	29	92	0	0	16	11	0	0
13	0	0	3	34	33	0	0	4	1	1	1	1	91	46	0	0	2	4
14	0	0	6	26	35	0	0	7	1	3	1	0	26	94	0	0	10	7
15	5	1	2	2	2	7	3	1	1	2	8	10	0	0	94	2	0	0
16	1	1	0	1	3	2	3	0	0	2	8	7	0	0	24	90	0	0
17	1	2	6	4	1	0	0	8	29	2	0	0	9	2	0	0	95	18
18	1	2	7	5	1	0	0	8	5	30	0	0	10	1	0	0	33	95

2.2.4.3 VMT Method on a Circuit Board

The circuit board, with a length of 174 mm and a width of 120 mm, was hung using four light cotton ropes to simulate the free boundary conditions, and there were 143 excitation points on the surface of the board, as shown in Fig. 2.13. The board was excited using an MSC-1 miniature impact hammer connected to an INV1841A amplifier, and the dynamic responses of the board were measured using two INV9206 microphones; the data were collected using an INV3020C-CPCI data acquisition system. Since the two microphones used in the test are of the free-field type, they were pointing towards the board and placed on the same side of the impacted surface of the board and close to it. Modal analysis was performed using the eigensystem realization algorithm in the modal analysis software DASP-V10 Pro. to extract the natural frequencies and mode shapes of the first 18 elastic modes of the board, as shown in Table 2.11. Since the highest natural frequency of the rigid body modes is less than 10 Hz, which is lower than 10% of the natrual frequency of the first elastic mode, the boundary conditions can be considered to be free.

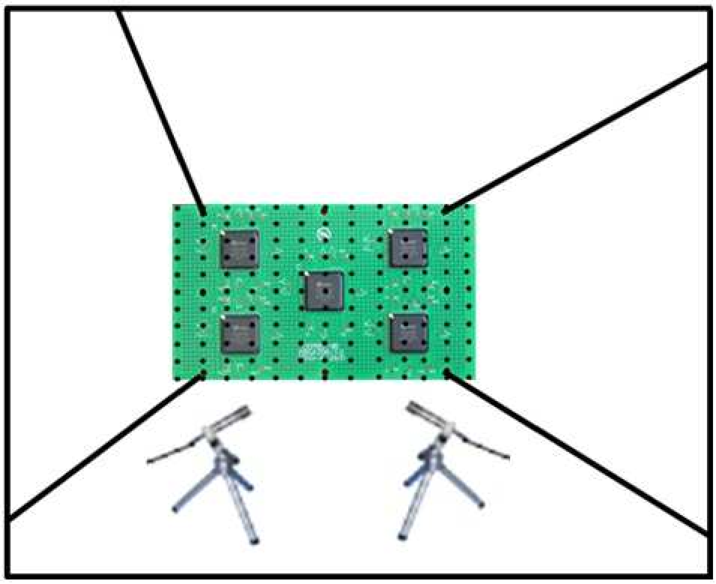

Figure 2.13: Test setup for the VMT method on the circuit board and the excitation points on it.

Table 2.11: Natural frequencies and mode shapes of the first 18 elastic modes of the circuit board from the VMT method.

Mode	Natural Frequency (Hz)	Mode Shape	Mode	Natural Frequency (Hz)	Mode Shape
1	225.3	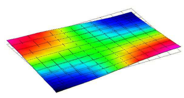	10	1201.9	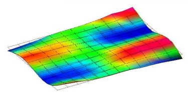
2	311.7	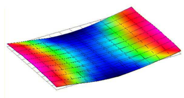	11	1556.6	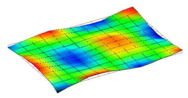
3	397.6	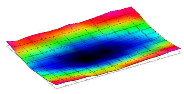	12	1577.2	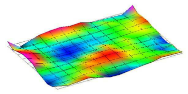
4	539.4	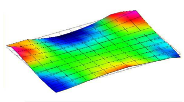	13	1603.6	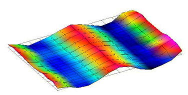
5	574.9	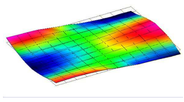	14	1762.4	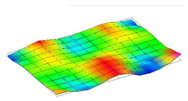
6	863.8	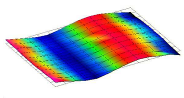	15	1984.6	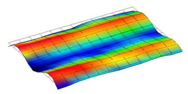
7	983.5	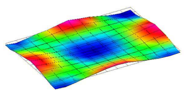	16	2088.1	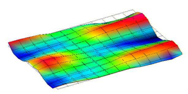
8	1031.0	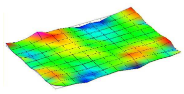	17	2172.9	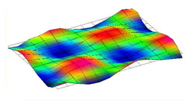
9	1053.3	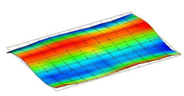	18	2264.9	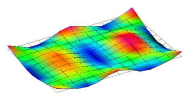

2.2.5 Conclusion

The VMT method developed here is based on the assumption that the natural frequencies and mode shapes of the test structure can be approximated by the natural frequencies and the structural components of the right eigenvectors of the structurally damped structural-acoustic system, respectively. The coupling between the structure and the acoustic field in a structural-acoustic system introduces asymmetry in the model formulation. The associated eigenvalue problem is derived using an equivalent state space formulation for the coupled system. The biorthonormality relations between the left and right eigenvectors and the relations between the structural and acoustic components in the left and right eigenvectors are proved. The frequency response function used in the VMT method is derived, which contains the modal characteristics of the coupled system. Based on the vibro-acoustic reciprocity, the VMT method can measure all the out-of-plane modes and its measurement quality will not be affected by a nodal line of a mode and an inactive area of a local mode of the structure; the guidelines for using the VMT method are provided, including the types of structures that are suitable for the method, the positions of the sound pressure transducers, and the orientation of the test structure relative to the transducers. Modal tests were carried out on an automotive disk brake using the VMT method and EMA, where multiple microphones and accelerometers were used to measure its dynamic responses induced by impacts, respectively. The differences between the measured natural frequencies of the first 18 elastic modes by the VMT method and EMA are less than 1% and the MAC values of the associated mode shapes are all above 90%. The errors between the measured natural frequencies by the VMT method and those from the FE model are less than 3% for the first 18 elastic modes, and the MAC values of the associated mode shapes are all above 90%. It is shown that the VMT method can not only preserve close natural frequencies of the brake due to axial-symmetry, but also measure all the out-of-plane modes within the frequency range of interest, including global and local ones. The VMT method was also successfully carried out on a light circuit board to measure the natural frequencies and mode shapes of its first 18 elastic modes.

Chapter 3

DIGITAL SIGNAL PROCESSING FOR MODAL ANALYSIS

3.1 Accurate and Efficient Calculation of Correlation Functions and Power Spectra

3.1.1 Introduction

Modal analysis is the study of modal properties of a structure, including natural frequencies, mode shapes, and damping ratios [1]. One criterion to categorize a modal analysis technique is whether excitation given to a structure needs to be measured. If it is needed, the technique is referred to as EMA; otherwise, it is referred to as OMA, or output-only modal analysis. To conduct EMA, IRFs and FRFs of a structure that show relations between measured responses and excitations in time and frequency domains are analyzed to estimate its modal properties, respectively. If there exist unmeasured excitations that can introduce non-negligible responses of a structure in EMA, the resulting IRFs, FRFs, and estimated modal properties can be erroneous. Moreover, excitations given to a structure should have relatively large amplitudes to maintain high SNRs of the resulting IRFs and FRFs, but it can be difficult to excite a large structure to measure its IRFs and FRFs with high SNRs. Hence EMA is suitable for a small or intermediate structure in a laboratory environment, where excitation to the structure can be well controlled and precisely measured. Unlike EMA, OMA can be conducted on a structure of any size under excitation that is unknown or difficult to measure [57, 9], and cross-correlation functions and cross-power spectra between a reference response and other measured responses of the structure can be analyzed to estimate its modal properties. For large structures in ordinary operations, such as bridges under traffic loads [58, 59], rotating blades of wind turbines [60], and high-rise buildings under wind excitations [61, 62], it can be relatively easy to conduct OMA, which can provide more practical modal properties in that only modes that are excited in operations or under environmental influences are measured.

OMA was first proposed as a modal analysis technique for a structure under natural excitation (known as NExT), i.e., white noise excitation [3], where a cross-correlation function of a non-negative time delay between a reference response and a measured response of the structure is shown to be a sum of sinusoidals with modal properties of the structure, which is similar to an IRF [63]. It is proposed in Ref. [63] that cross-power spectra associated with such cross-correlation functions, referred to as half spectra, be used in OMA to avoid false results. Besides NExT, there are other OMA techniques, such as the random decrement computation technique [64], stochastic subspace identification technique [65], frequency domain decomposition technique [66], sparse component analysis technique [67], and short-time Fourier-transformed independent component analysis technique [68]. Due to the similarity between a cross-correlation function of a non-negative time delay and an IRF, any modal property estimation techniques that are applicable for IRFs and FRFs in EMA can be applied to cross-correlation functions of non-negative time delays and half spectra in NExT, respectively. NExT has become one of the most widely used OMA techniques in modal analysis software. Cross-correlation functions and associated cross-power spectra can be efficiently calculated using the cross-correlation theorem and transforms, including the discrete Fourier transform (DFT) and inverse DFT (IDFT). However, the resulting functions and spectra can be physically erroneous due to periodic extension of the DFT, which is false most of the time [69]. While the error, if it exists, has been identified and a methodology has been proposed to reduce it [70], the resulting functions and spectra are still physically erroneous. By now, the problem has not been fundamentally solved in an efficient manner; cross-correlation functions and cross-power spectra can be accurately but inefficiently calculated using their definitions.

In this work, errors in calculating discrete cross-correlation functions and associated cross-power spectra between a reference data series and a measured data series due to direct application of the cross-correlation theorem and transforms are shown. While the errors can be reduced by padding zero series that have the same length as the reference and measured data series to their ends [70], the results are still physically erroneous. A new methodology for calculating cross-correlation functions of non-negative time delays and associated half spectra between the reference and measured data series is proposed. A coherence function, a convergence function in the frequency domain, and a convergence index are introduced to evaluate qualities of measured cross-correlation functions and cross-power spectra. In the new methodology, before applying the cross-correlation theorem and transforms at each sampling period, a zero series that has the same length as the reference data series is padded to its end, and the measured series is extended by stitching the measured data series of the next sampling period to its end, which makes the lengths of the two series be that of two sampling periods. Time for calculating a cross-correlation function can be greatly reduced, compared with that by directly applying its definition; the resulting cross-correlation function is in perfect accordance with the exact one, and so is the associated half spectrum. The methodology is extended to calculate cross-correlation functions of any time delays, including negative and non-negative ones, and associated full spectra in an accurate and efficient manner. The new methodology was numerically and experimentally applied to an ideal two-degree-of-freedom (2-DOF) mass-spring-damper system and a damaged aluminum beam, respectively, and OMA was conducted using half spectra to estimate their natural frequencies, damping ratios, and mode shapes, which were compared with those from complex model analysis [71] and EMA, respectively.

3.1.2 Methodology

An accurate and efficient methodology for calculating discrete cross-correlation functions of non-negative time delays between two measured data series and associated half spectra is proposed in Secs. 2.1 and 2.2, respectively; the methodology is then extended to calculate cross-correlation functions of any time delays and associated full spectra in an accurate and efficient manner. A coherence function, a convergence function in the frequency domain, and a convergence index are introduced in Sec. 2.3.

3.1.2.1 Accurate and Efficient Calculation of Discrete Cross-correlation Functions

The cross-correlation function between two real continuous functions $u(t)$ and $v(t)$ can be defined by [2]

$$R^{u,v}(t) = \int_{-\infty}^{\infty} u(\tau)v(\tau + t)\mathrm{d}\tau \tag{3.1}$$

where t is the time delay, and $u(t)$ and $v(t)$ can be considered as a reference and a measurement function in OMA, respectively. If $u(t) = v(t)$, $R^{u,v}(t)$ is referred to as the auto-correlation function of $u(t)$. When both $u(t)$ and $v(t)$ are discrete, the cross-correlation function becomes

$$R^{u,v}_{m} = \lim_{N\to\infty} \sum_{r=-N}^{N} \frac{1}{F_s} u_r v_{r+m} \tag{3.2}$$

where $\frac{1}{F_s}$ is the time increment of u_r and v_r, in which F_s is the sampling frequency, and m is directly related to the time delay, since $\frac{m}{F_s}$ is equivalent to t in Eq. (3.1). When both $u(t)$ and $v(t)$ are discrete and have finite lengths, which is a usual case for OMA, the cross-correlation function becomes

$$R^{u,v}_{m} = \sum_{r=0}^{N_s-1} \frac{1}{F_s} u_r v_{r+m} \tag{3.3}$$

where $N_s = T_s F_s$ is the number of sampling period in one sampling period of $u(t)$ and $v(t)$, in which T_s is the length of the period.

If full sequential values of $R^{u,v}_{m}$ are calculated using Eq. (3.3), one needs to conduct N_s multiplications for each $R^{u,v}_{m}$, and it can be computationally inefficient. In order to accelerate the calculation, the cross-correlation theorem can be applied:

$R^{u,v}(t)$ is equal to the inverse Fourier transform of the product of the complex conjugate of Fourier transform of $u(t)$ and Fourier transform of $v(t)$ [72], i.e.,

$$R^{u,v}(t) = \mathscr{F}^{-1}(U^*V) \tag{3.4}$$

where $\mathscr{F}(\cdot)$ denotes Fourier transform operation; $U(f) = \mathscr{F}[u(t)]$ and $V(f) = \mathscr{F}[v(t)]$, in which f denotes frequency in Hz; the superscript $*$ denotes complex conjugation. The cross-correlation theorem states that the product of the complex conjugate of Fourier transform of the reference function and Fourier transform of the measurement function is equal to Fourier transform of the cross-correlation function between the two functions. It can be applied to continuous and discrete functions of an infinite length. However, application of the theorem to a case where $u(t)$ and $v(t)$ have the same finite length, in combination with transforms, including the DFT and IDFT, is erroneous. The error arises from periodic extension of the DFT of $v(t)$: $v(t + kT_s) = v(t)$ or $v_{r+kN_s} = v_r$, where k is an integer; consequently, $v(t)$ has an infinite length and is periodic with a period equal to T_s or N_s. When $r + m \geq N_s$ in Eq. (3.3), since the DFT is applied to N_s sampling points of $v(t)$, v_{r+m} does not exist in $v(t)$. However, v_{r+m} is equal to v_{r+m-N_s}, which does exist in $v(t)$, due to the periodic extension. Similarly, when $r + m < 0$ in Eq. (3.3), v_{r+m} is equal to v_{r+m+N_s}. The periodic extension is valid if $v(t)$ is truly periodic with a period equal to T_s, but it is not the case most of the time.

The cross-correlation function between two discrete functions that have the same finite length, obtained by directly applying the cross-correlation theorem and transforms, can be expressed by

$$R_m^{u,v} = \begin{cases} \sum\limits_{r=0}^{N_s-1} \frac{1}{F_s} u_r v_r & , m = 0 \\ \sum\limits_{r=0}^{N_s-m-1} \frac{1}{F_s} u_r v_{r+m} + \sum\limits_{r=N_s-m}^{N_s-1} \frac{1}{F_s} u_r v_{r+m-N_s} & , m > 0 \\ \sum\limits_{r=0}^{-m-1} \frac{1}{F_s} u_r v_{r+m+N_s} + \sum\limits_{r=-m}^{N_s-1} \frac{1}{F_s} u_r v_{r+m} & , m < 0 \end{cases} \tag{3.5}$$

When $m = 0$, the function value is in accordance with its definition in Eq. (3.3); when $m > 0$ and $m < 0$, the function values are erroneous due to existence of $\sum\limits_{r=N_s-m}^{N_s-1} \frac{1}{F_s} u_r v_{r+m-N_s}$ and $\sum\limits_{r=0}^{-m-1} \frac{1}{F_s} u_r v_{r+m+N_s}$ in the second and third equations in Eq. (3.5), respectively, which originate from the periodic extension, and the error becomes larger for a larger $|m|$ value, which gives a smaller $N_s - m$ and a larger $-m$, respectively. Note that the length of a cross-correlation function in the methodology is N_s. Moreover, when $m = N_s - p$ with $1 \leq p \leq N_s - 1$, the cross-correlation function becomes

$$\begin{aligned} R_m^{u,v} &= R_{N_s-p}^{u,v} \\ &= \sum_{r=0}^{N_s-(N_s-p)-1} \frac{1}{F_s} u_r v_{r+(N_s-p)} + \sum_{r=N_s-(N_s-p)}^{N_s-1} \frac{1}{F_s} u_r v_{r+(N_s-p)-N_s} \\ &= \sum_{r=0}^{p-1} \frac{1}{F_s} u_r v_{r+N_s-p} + \sum_{r=p}^{N_s-1} \frac{1}{F_s} u_r v_{r-p} \\ &= \sum_{r=0}^{p-1} \frac{1}{F_s} u_r v_{r-p} + \sum_{r=p}^{N_s-1} \frac{1}{F_s} u_r v_{r-p} \\ &= \sum_{r=0}^{N-1} \frac{1}{F_s} u_r v_{r-p} \end{aligned} \tag{3.6}$$

which is equal to the cross-correlation function $R_{-p}^{u,v}$ of a negative time delay $-\frac{p}{F_s}$; this shows that a cross-correlation function obtained by directly applying the cross-correlation theorem and transforms becomes periodic and has the same period as $v(t)$, which is extended to be periodic in the DFT. Since there are only N_s cross-correlation function values here, one cannot strictly distinguish cross-correlation function values associated with non-negative time delays from those with negative time delays.

To reduce the error caused by the periodic extension, it is proposed in Ref. [70] that an N_s zero series be padded to each end of $u(t)$ and $v(t)$ as a buffer zone before applying the cross-correlation theorem and transforms; the lengths of $u(t)$ and $v(t)$ then become $2N_s$. Values of the cross-correlation function between the two padded functions of time delays ranging from $-\frac{N}{F_S}$ to $\frac{N_s-1}{F_S}$ can be obtained in a wrap-around order: the first and last N_s values of the resulting IDFT series correspond to values of the cross-correlation function of time delays ranging from 0 to $\frac{N_s-1}{F_S}$ and from $-\frac{N_s}{F_S}$ to $-\frac{1}{F_S}$, respectively. The resulting cross-correlation function can be expressed by

$$R_m^{u,v} = \begin{cases} \sum\limits_{r=0}^{N_s-1} \frac{1}{F_s} u_r v_r & , m = 0 \\ \sum\limits_{r=0}^{N_s-m-1} \frac{1}{F_s} u_r v_{r+m} & , m > 0 \\ \sum\limits_{r=-m}^{N_s-1} \frac{1}{F_s} u_r v_{r+m} & , m < 0 \end{cases} \tag{3.7}$$

Different from the methodology of directly applying the cross-correlation theorem and transforms, the methodology here gives a cross-correlation function of length $2N_s$, and one can extract values associated with $m \geq 0$ to form the cross-correlation function of a non-negative time delay. More importantly, the erroneous terms $\sum\limits_{r=N_s-m}^{N_s-1} \frac{1}{F_s} u_r v_{r+m-N_s}$ and $\sum\limits_{r=0}^{-m-1} \frac{1}{F_s} u_r v_{r+m+N_s}$ in the second and third equations in Eq. (3.5), respectively, are eliminated here. However, this methodology is merely a compromise, since the resulting cross-correlation function values are still erroneous, compared with the definition in Eq. (3.3).

Assuming that both $u(t)$ and $v(t)$ are continuously measured for n $(n \geq 2)$ sampling periods, the problems described above related to calculation of full sequential values of a cross-correlation function of a non-negative time delay can be fundamentally solved by a new methodology in an accurate and efficient manner. The new methodology for calculating a cross-correlation function of a non-negative time delay using measured data of the i-th $(i \leq n-1)$ sampling period is described below:

Step 1. N_s and $2N_s$ sampling points of $u(t)$ and $v(t)$ are extracted, respectively, at the start of the i-th period.

Step 2. An N_s zero series is padded to the end of $u(t)$, making the length of $u(t)$ be $2N_s$, which is the same as that of $v(t)$ extracted in Step 1.

Step 3. A cross-correlation function is obtained by applying the cross-correlation theorem and transforms.

Step 4. The first N_s values of $R_m^{u;v}$ obtained in Step 3 are extracted, which are values of the cross-correlation function of non-negative time delays ranging from 0 to $T_s - \frac{1}{F_s}$.

Note that up to $n-1$ cross-correlation functions can be calculated in this case, since at the n-th sampling period, $v(t)$ cannot be extracted as proposed in Step 1. The first and last N_s values of the resulting $R_m^{u;v}$ correspond to positive and negative time delays up to T_s and $-T_s$, respectively, in a wrap-around order. However, values of $R_m^{u,v}$ with negative time delays should be dropped, because when $m + r < 0$ in Eq. (3.3), v_{m+r} is not available in the extracted data series, and $v_{m+r} = v_{m+r+2N_s}$ due to periodic extension of the DFT, which is erroneous due to the reason described above. Hence only values of $R_m^{u,v}$ with non-negative time delays are correct and should be extracted in this case.

Based on Eq. (3.5), when $m = 0$, the cross-correlation function from the new methodology becomes

$$R_m^{u,v} = \sum_{r=0}^{N_s-1} \frac{1}{F_s} u_r v_r + \sum_{r=N_s}^{2N_s-1} \frac{1}{F_s} u_r v_r = \sum_{r=0}^{N_s-1} \frac{1}{F_s} u_r v_r \tag{3.8}$$

which is in accordance with its definition, since $u_r = 0$ when $N_s \leq r \leq 2N_s - 1$. When $m > 0$, the cross-correlation function becomes

$$R_m^{u,v} = \sum_{r=0}^{N_s-1} \frac{1}{F_s} u_r v_{r+m} + \sum_{r=N_s}^{2N_s-m-1} \frac{1}{F_s} u_r v_{r+m} + \sum_{r=2N_s-m}^{2N_s-1} \frac{1}{F_s} u_r v_{r+m-2N_s} = \sum_{r=0}^{N_s-1} \frac{1}{F_s} u_r v_{r+m} \tag{3.9}$$

Note that when $r + m \geq 2N_s$, $v_{r+m} = v_{r+m-2N_s}$ due to periodic extension of the DFT. Combining Eqs. (3.8) and (3.9) gives

$$R_m^{u,v} = \sum_{r=0}^{N_s-1} \frac{1}{F_s} u_r v_{r+m} \tag{3.10}$$

which is exactly the same as Eq. (3.3). With the new methodology, calculation time is shorter than that using the definition in Eq. (3.3), which will be shown in Sec. 3.

Since cross-correlation functions of non-negative time delays can be obtained from the new methodology proposed above, cross-correlation functions of any time delays can be obtained, if those of negative time delays are available. Assuming that both $u(t)$ and $v(t)$ are continuously measured for n ($n \geq 2$) sampling periods, full sequential values of $R_m^{u,v}$ of negative time delays can be obtained. The methodology for calculating a cross-correlation function of a negative time delay for the i-th ($2 \leq i \leq n$) sampling period is described below:

Step 1. N_s and $2N_s$ sampling points of $u(t)$ and $v(t)$ are extracted at starts of the i-th and $(i-1)$-th periods, respectively.

Step 2. An N_s zero series is padded to the start of $u(t)$, making the length of $u(t)$ be $2N_s$, which is the same as that of $v(t)$ extracted in Step 1.

Step 3. A cross-correlation function is obtained by applying the cross-correlation theorem and transforms.

Step 4. The last N_s values of $R_m^{u,v}$ obtained in Step 3 are extracted, which are values of the cross-correlation function of negative time delays ranging from $-T_s$ to $-\frac{1}{F_s}$.

Note that up to $n-1$ cross-correlation functions of negative time delays can be calculated in this case, since in the first sampling period, $v(t)$ cannot be extracted as proposed in Step 1.

Combining values of the cross-correlation function of negative time delays with those of non-negative time delays gives values of the function of any time delays. Up to $n-2$ cross-correlation functions of any time delays can be obtained, which is also the case using the definition in Eq. (3.3).

3.1.2.2 Accurate and Efficient Calculation of Discrete Cross-power Spectra

By the cross-correlation theorem described in Sec. 2.1, the cross-power spectrum between two real functions $u(t)$ and $v(t)$, denoted by $P^{u,v}(f)$, is equal to

Fourier transform of the cross-correlation function between the two functions:

$$P^{u,v}(f) = U^*V = \mathscr{F}\left(R^{u,v}(t)\right) \tag{3.11}$$

If N_s sampling points of $u(t)$ and those of $v(t)$, which is not periodic with a period T_s, are used to yield a cross-power spectrum by directly applying the cross-correlation theorem and transforms, the resulting spectrum is erroneous. The reason is that the cross-correlation function to be transformed is erroneous itself due to periodic extension of the DFT, as discussed in Sec. 2.1. To fundamentally solve this problem, it is proposed that a half spectrum and a full spectrum between $u(t)$ and $v(t)$ be DFTs of a cross-correlation function of a non-negative time delay and that of any time delay from the new methodology in Sec. 2.1, respectively. Note that while the DFT of a cross-correlation function of a non-negative time delay between $u(t)$ and $v(t)$ with padded zero series in Eq. (3.7) can be considered as a half spectrum, the cross-correlation function is not in perfect accordance with its definition.

3.1.2.3 Coherence Function, Convergence Function, and Convergence Index

A conventional type of coherence function has been widely used to evaluate qualities of measured FRFs in the frequency domain, if the FRFs are obtained by averaging; at least two sampling periods are needed to yield meaningful function values, since the coherence function is equal to one at all frequencies when measured data of only one sampling period are available [1, 2]. A new type of coherence function was developed in Ref. [73] to evaluate accuracies of calculated IRFs and

FRFs in the frequency domain. One advantage of the new type of coherence function is that a meaningful coherence function can be obtained even when measured data of only one sampling period are available. A similar type of coherence function was proposed in Ref. [74] to evaluate random variation of a signal at each frequency. This type of coherence function is introduced here to evaluate qualities of measured cross-correlation functions and associated cross-power spectra in the frequency domain; it is defined by

$$\gamma_x^2(f) = \frac{\hat{P}^{u,v}(f)}{\hat{P}^{u,v}(f) + \tilde{E}^{u,v}(f)} \tag{3.12}$$

where $\hat{P}^{u,v}(f)$ and $\tilde{E}^{u,v}(f)$ are the auto-power spectrum of the averaged cross-correlation function between $u(t)$ and $v(t)$ and averaged auto-power spectrum of error series $e_i^{u,v}(t)$, respectively; the error series $e_i^{u,v}(t)$ associated with the i-th cross-correlation function $R_i^{u,v}(t)$ is defined by

$$e_i^{u,v}(t) = R_i^{u,v}(t) - \hat{R}^{u,v}(t) \tag{3.13}$$

where $\hat{R}^{u,v}(t)$ is the current averaged cross-correlation function. For a case where only one cross-correlation function is available, the coherence function cannot be used, since $\hat{R}^{u,v}(t) = R_1^{u,v}(t)$ and $e_1^{u,v}(t) = 0$ for all t. At least two cross-correlation functions are needed to yield meaningful coherence function values. When a coherence function value is close to one, the measured cross-correlation functions and associated cross-power spectra have almost no variations relative to their averaged cross-correlation function and associated cross-power spectrum, respectively; the lower the coherence function value, the larger the variation at the corresponding frequency.

The coherence function in Ref. [74] can be modified to be a convergence function to evaluate convergence of averaged cross-correlation functions and associated cross-power spectra in the frequency domain. The convergence function is defined by

$$\xi_x^2(f) = \frac{\hat{P}^{u,v}(f)}{\hat{P}^{u,v}(f) + E^{u,v}(f)} \tag{3.14}$$

where $E^{u,v}(f)$ is the auto-power spectrum of an error series $e^{u,v}(t)$, which is defined by

$$e^{u,v}(t) = \hat{R}_n^{u,v}(t) - \hat{R}_{n-1}^{u,v}(t) \tag{3.15}$$

where $\hat{R}_n^{u,v}(t)$ and $\hat{R}_{n-1}^{u,v}(t)$ are the average of n cross-correlation functions and that of previous $n-1$ functions, respectively. According to its definition in Eq. (3.15), the error series quantifies the difference between the averaged cross-correlation functions of the n-th and $(n-1)$-th sampling periods; it can be expressed by

$$\begin{aligned} e^{u,v}(t) &= \hat{R}_n^{u,v}(t) - \hat{R}_{n-1}^{u,v}(t) \\ &= \frac{\sum\limits_{j=1}^{n} R_j^{u,v}(t)}{n} - \frac{\sum\limits_{j=1}^{n-1} R_j^{u,v}(t)}{n-1} \\ &= \frac{\sum\limits_{j=1}^{n}(n-1)R_j^{u,v}(t) - \sum\limits_{j=1}^{n-1} nR_j^{u,v}(t)}{n(n-1)} \\ &= \frac{\sum\limits_{j=1}^{n-1}(n-1)R_j^{u,v}(t) + (n-1)R_n^{u,v}(t) - \sum\limits_{j=1}^{n-1}(n-1)R_j^{u,v}(t) - \sum\limits_{j=1}^{n-1} R_j^{u,v}(t)}{n(n-1)} \\ &= \tfrac{1}{n}\left(R_n^{u,v}(t) - \hat{R}_{n-1}^{u,v}(t)\right) \end{aligned} \tag{3.16}$$

Equation (3.16) shows that the error series depends on n and the difference between the n-th cross-correlation function and averaged cross-correlation function of the first $n-1$ sampling periods. If the n-th cross-correlation function does not drastically deviate from the averaged one of the first $n-1$ sampling periods, the error series approaches a zero series when n increases. When a convergence function value is close to one, the averaged cross-correlation function and cross-power spectrum almost completely converge; the lower the convergence function value, the worse the convergence at the corresponding frequency. Similar to the coherence function introduced above, at least two cross-correlation functions are needed to yield meaningful convergence function values. The reason is that $\hat{R}^{u,v}_{n-1}(t)$ does not exist if only one cross-correlation function is available.

A convergence index is introduced to further evaluate convergence of the averaged cross-correlation function and cross-power spectrum:

$$con = \sqrt{\frac{\Xi\left(\hat{P}^{u,v}(f)\right)}{\Xi\left(\hat{P}^{u,v}(f) + E^{u,v}(f)\right)}} \tag{3.17}$$

where $\Xi(\cdot)$ denotes summation over all frequencies. If elements of the error series are equal to zero for all t, $E^{u,v}(f) = 0$ at all frequencies and $con = 1$; the closer to one the convergence index, the better the convergence of the averaged cross-correlation function and cross-power spectrum. The convergence index can help determine whether the averaged function and spectrum have converged and whether more sampling periods are needed.

3.1.3 Numerical Simulation and Experimental Example

3.1.3.1 Numerical Simulation

Numerical simulation is conducted on an ideal 2-DOF mass-spring-damper system shown in Fig. 3.25 with masses $m_1 = 1$ kg and $m_2 = 2$ kg; spring constants $k_1 = 6240\pi$ N/m, $k_2 = 4160\pi$ N/m, and $k_3 = 3120\pi$ N/m; and viscous damping coefficients $c_1 = 2$ N/(m/s), $c_2 = 1$ N/(m/s), and $c_3 = 2$ N/(m/s). An external force $f(t)$ of zero-mean white noise with a standard deviation of 9 N acts on the mass m_1. Responses of the two masses in the form of displacements, denoted by $y_1(t)$ and $y_2(t)$, are obtained by solving an associated ordinary differential equation set with zero initial conditions:

$$\begin{gathered} m_1\ddot{y}_1(t) + (c_1 + c_2)\dot{y}_1(t) - c_2\dot{y}_2(t) + (k_1 + k_2)y_1(t) - k_2y_2(t) = f(t) \\ m_2\ddot{y}_2(t) - c_2\dot{y}_1(t) + (c_2 + c_3)\dot{y}_2(t) - k_2y_1(t) + (k_2 + k_3)y_2(t) = 0 \\ y_1(0) = 0,\ \dot{y}_1(0) = 0,\ y_2(0) = 0,\ \dot{y}_2(0) = 0 \end{gathered} \tag{3.18}$$

using the ODE45 solver in MATLAB [75]. The responses are calculated up to the first 132 seconds with a sampling frequency $F_s = 1024$ Hz, and the total number of sampling points is $F_s \times 132$ for each mass. White noise is added to the calculated $y_1(t)$ and $y_2(t)$ with a SNR of 65 to simulate measurement noise.

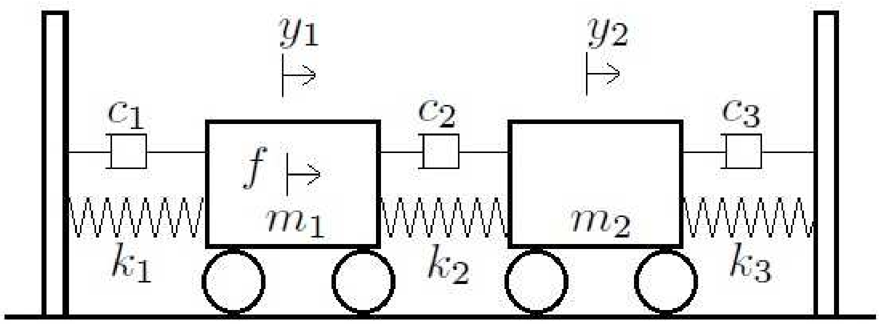

Figure 3.1: A 2-DOF mass-spring-damper system.

The length of a sampling period is set to be $T_s = 4$ s, and there are 32 cross-correlation functions of non-negative time delays and half spectra to be calculated using the new methodology. The number of sampling points in one sampling period is $N_s = F_s \times T_s = 1024 \times 4$. Time histories of $f(t)$, $y_1(t)$, and $y_2(t)$ of the first four seconds are shown in Figs. 3.2(a) through (c), respectively. In this simulation, $y_1(t)$ is chosen to be the reference function. The cross-correlation function between $y_1(t)$ and $y_2(t)$ of the first four seconds obtained by directly applying the cross-correlation theorem and transforms, as described in Eq. (3.5), is shown in Fig. 3.3(a), and the amplitude of the associated cross-power spectrum is shown in Fig. 3.3(b). It can be seen that the amplitude of the cross-correlation function increases near the end of the sampling period, which results from periodic extension of the DFT as discussed in Sec. 2.1. While the amplitude of the spectrum is noisy due to DFT leakage, two prominent peaks that correspond to natural frequencies of the system can be observed.

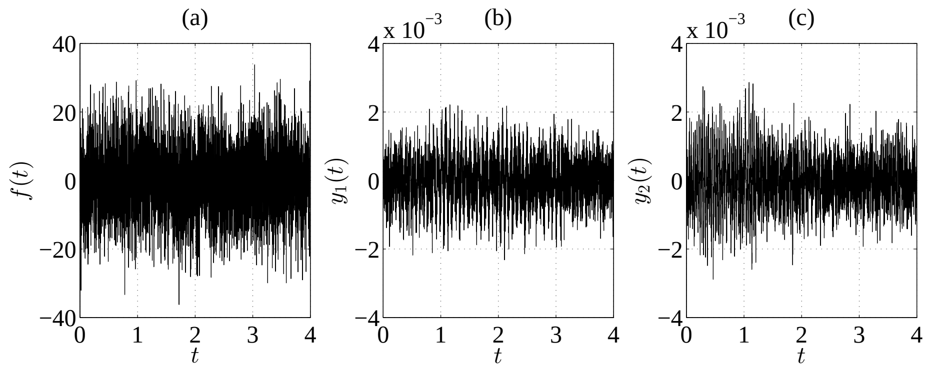

Figure 3.2: (a) External force of zero-mean white noise $f(t)$, (b) the response of m_1 in Fig. 3.25, and (c) the response of m_2 in Fig. 3.25 of the first four seconds.

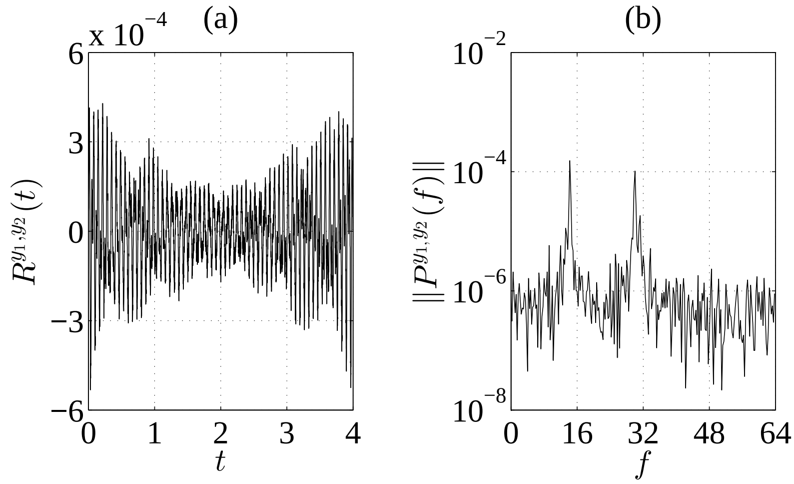

Figure 3.3: (a) Cross-correlation function between $y_1(t)$ and $y_2(t)$ of the first four seconds by directly applying the cross-correlation theorem and transforms, and (b) the amplitude of the associated cross-power spectrum.

To reduce the error described above, N_s zero series are padded to ends of $y_1(t)$ and $y_2(t)$ of the first four seconds, as shown in Figs. 3.4(a) and (b), respectively. The cross-correlation function of a non-negative time delay between padded $y_1(t)$ and $y_2(t)$ calculated using the cross-correlation theorem and transforms and associated half spectrum are shown in Figs. 3.5(a) and (b), respectively. It can be seen that the cross-correlation function decays with time as an IRF. The decay occurs mainly due to the fact that less non-zero terms exist in the summation in Eq. (3.7) than Eq. (3.5) as time evolves, and the function approaches zero near the end of a sampling period. Consequently, effects of DFT leakage can be reduced, and the amplitude of the spectrum is less noisy, compared with that in Fig. 3.3(b). Natural frequencies of the system can be identified at peaks of the amplitude of the half spectrum.

Note that the resulting cross-correlation function of a non-negative time delay and half spectrum are physically erroneous due to padded zero series. However, this methodology can be superior to the one that directly applies the cross-correlation theorem and transforms, based on the observation and reasoning above.

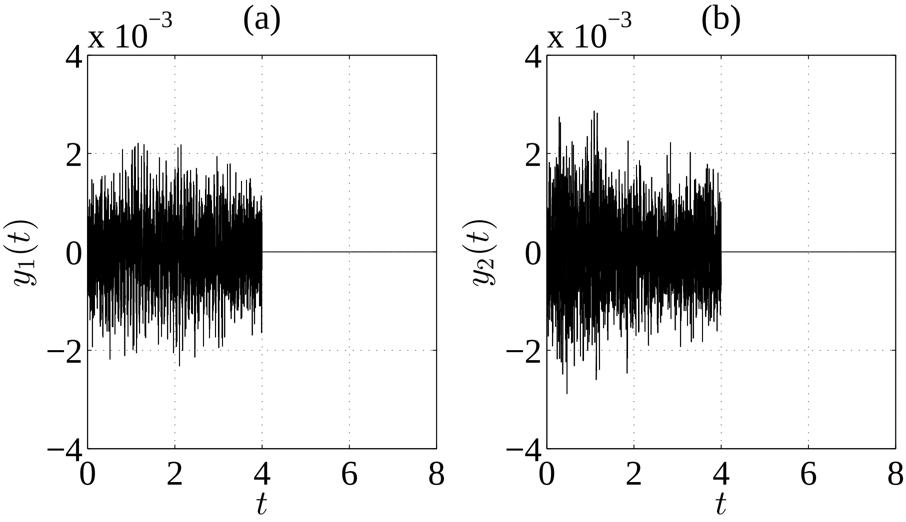

Figure 3.4: (a) Response of m_1 in Fig. 3.25 of the first four seconds with padded zero series of four seconds, and (b) the response of m_2 in Fig. 3.25 of the first four seconds with padded zero series of four seconds.

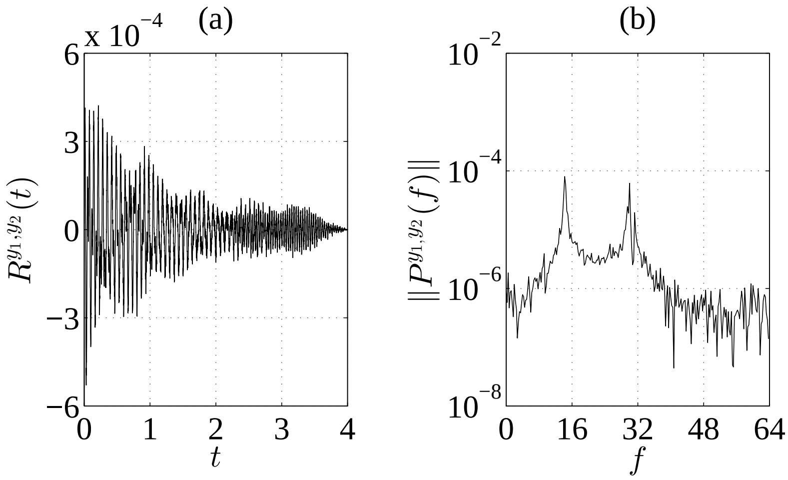

Figure 3.5: (a) Cross-correlation function of a non-negative time delay between $y_1(t)$ and $y_2(t)$ of the first four seconds with padded zero series of four seconds, and (b) the amplitude of the associated half spectrum.

To obtain an exact cross-correlation function of a non-negative time delay, $y_1(t)$ of one sampling period and $y_2(t)$ of two sampling periods are needed, according to the definition in Eq. (3.3). The response $y_2(t)$ of the first eight seconds, which has a length of two sampling periods, is shown in Fig. 3.6. The cross-correlation function from Eq. (3.3) and amplitude of the associated half spectrum are shown in Figs. 3.7(a) and (b), respectively. Time for calculating the cross-correlation function is 1.096 seconds.

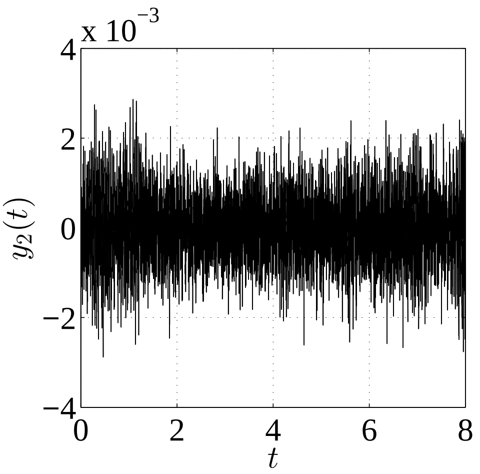

Figure 3.6: Response of m_2 in Fig. 3.25 of the first eight seconds.

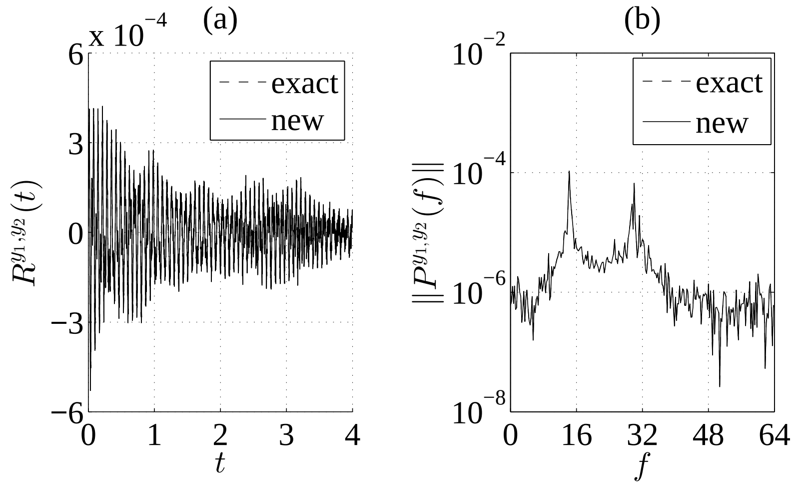

Figure 3.7: (a) Comparison of cross-correlation functions of non-negative time delays between $y_1(t)$ and $y_2(t)$ of the first four seconds from Eq. (3.3) (exact) and the new methodology (new), and (b) comparison of amplitudes of associated half spectra.

To apply the new methodology for calculating a cross-correlation function of a non-negative time delay, $y_1(t)$ of one sampling period with an N_s zero series padded to its end and $y_2(t)$ of the same sampling period as $y_1(t)$ and the next sampling period are needed. The response $y_1(t)$ of the first four seconds padded with an N_s zero series at its end and $y_2(t)$ of the first eight seconds are shown in Figs. 3.8(a) and (b), respectively. The cross-correlation function of a non-negative time delay and amplitude of the half spectrum using the new methodology in Secs. 2.1 and 2.2 are shown in Figs. 3.7(a) and (b), respectively. It can be seen that the cross-correlation function and amplitude of the half spectrum are almost identical to those from their definitions, while time for calculating the cross-correlation function is 0.007 seconds, which is less than 0.7 % of that using its definition. It can be seen that the function decays with time in the first two seconds. The cross-correlation functions between $y_1(t)$ and $y_2(t)$ of the first four seconds from the three methodologies are compared with the exact one of a non-negative time delay in Fig. 3.9(a). The cross-correlation function between $y_1(t)$ and $y_2(t)$ by directly applying the cross-correlation theorem and transforms and that between padded $y_1(t)$ and $y_2(t)$ compare well with the exact one at the beginning of the sampling period, but there are large errors afterwards, as shown in Figs. 3.9(b), (c), (d), and (e). The cross-correlation function from the new methodology is in perfect accordance with the exact one, as shown in Figs. 3.9(b), (c), and (f); the differences in Fig. 3.9(f) derive from numerical errors of the DFT and IDFT, which are negligible compared with the amplitude of the exact cross-correlation function.

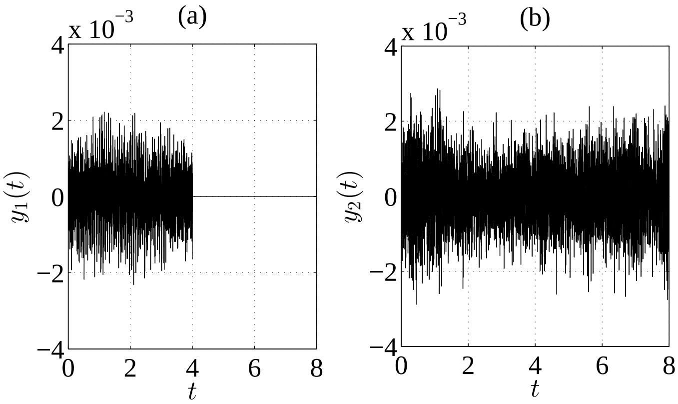

Figure 3.8: (a) Response of m_1 in Fig. 3.25 of the first four seconds with padded zero series of four seconds, and (b) the response of m_2 in Fig. 3.25 of the first eight seconds.

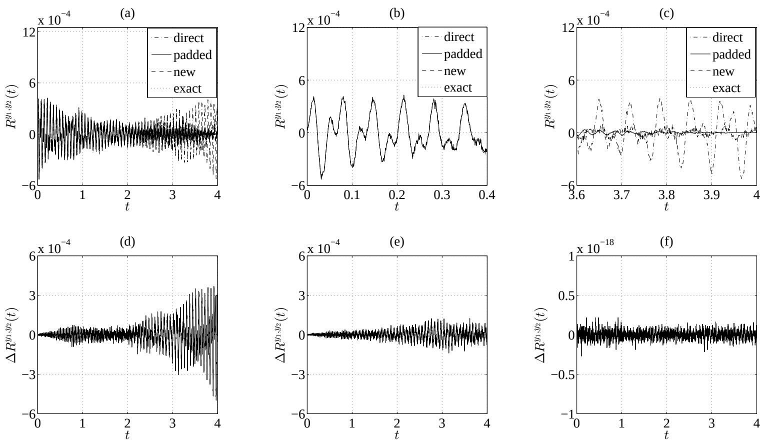

Figure 3.9: (a) Comparison of the cross-correlation function between $y_1(t)$ and $y_2(t)$ of the first four seconds by directly applying the cross-correlation theorem and transforms (direct), the cross-correlation function of a non-negative time delay between $y_1(t)$ and $y_2(t)$ of the first four seconds with padded zero series of four seconds (padded), the cross-correlation function of a non-negative time delay between $y_1(t)$ and $y_2(t)$ of the first four seconds from the new methodology (new), and the cross-correlation function of a non-negative time delay between $y_1(t)$ and $y_2(t)$ of the first four seconds from the definition (exact); (b) an enlarged view of the comparison of the first 0.4 second; (c) an enlarged view of the comparison of the last 0.4 second; (d) differences between the direct and exact cross-correlation functions; (e) differences between the padded and exact cross-correlation functions; and (f) differences between the new and exact cross-correlation functions.

To better visualize similarity of a cross-correlation function to an IRF, an averaged exact cross-correlation function of a non-negative time delay between $y_1(t)$

and $y_2(t)$ of four seconds with 32 sampling periods is calculated and shown in Fig. 3.10(a), which exponentially decays with time in the first two seconds. An averaged cross-correlation function between $y_1(t)$ and $y_2(t)$ of four seconds by directly applying the cross-correlation theorem and transforms with 32 sampling periods is shown in Fig. 3.10(b). It is similar to that in Fig. 3.3(a), whose amplitude increases near the end of the sampling period. An averaged cross-correlation function of a non-negative time delay between padded $y_1(t)$ and $y_2(t)$ with 32 sampling periods and that from the new methodology are shown in Figs. 3.10(c) and (d), respectively. The four averaged cross-correlation functions in Fig. 3.10 are compared in Fig. 3.11(a). Similar to the comparison in Fig. 3.9, the averaged cross-correlation function between $y_1(t)$ and $y_2(t)$ of four seconds by directly applying the cross-correlation theorem and transforms and that of a non-negative time delay between padded $y_1(t)$ and $y_2(t)$ compare well with the exact one at the beginning of a sampling period, but there are large errors afterwards, as shown in Figs. 3.11(b), (c), (d), and (e). The averaged cross-correlation from the new methodology is in perfect accordance with the exact one, as shown in Figs. 3.11(b), (c), and (f).

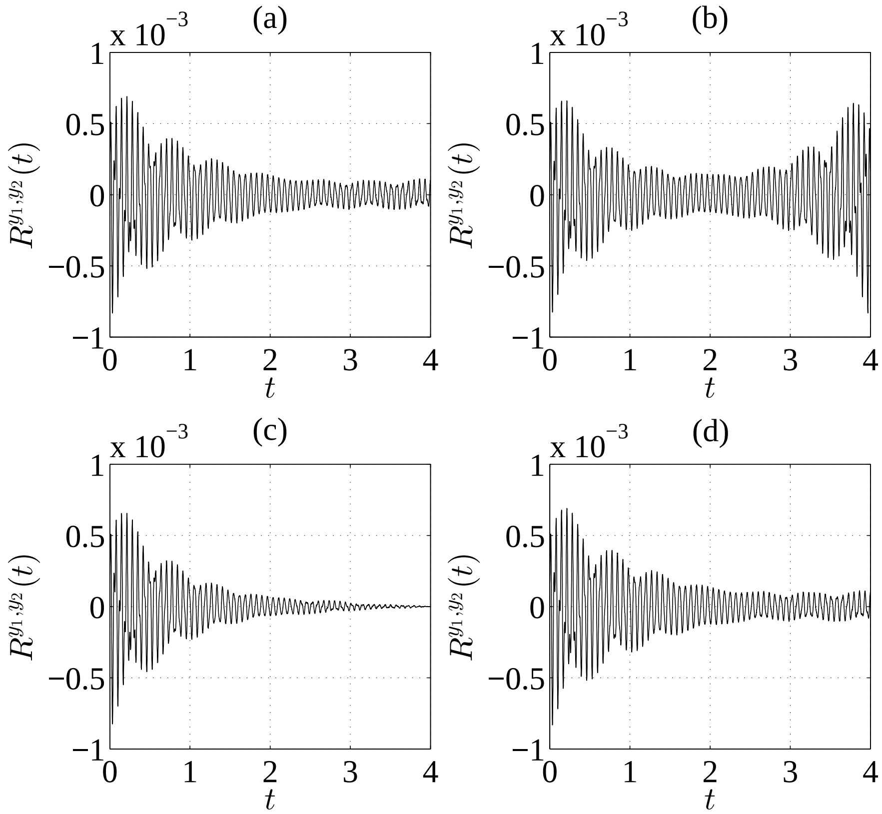

Figure 3.10: (a) An averaged cross-correlation function between $y_1(t)$ and $y_2(t)$ of four seconds by directly applying the cross-correlation theorem and transforms, (b) an averaged cross-correlation function of a non-negative time delay between $y_1(t)$ and $y_2(t)$ of four seconds with padded zero series of four seconds, (c) an averaged cross-correlation function of a non-negative time delay between $y_1(t)$ and $y_2(t)$ of four seconds from the new methodology, and (d) an averaged cross-correlation function of a non-negative time delay between $y_1(t)$ and $y_2(t)$ of four seconds from the definition. All the averaged cross-correlation functions are obtained with 32 sampling periods.

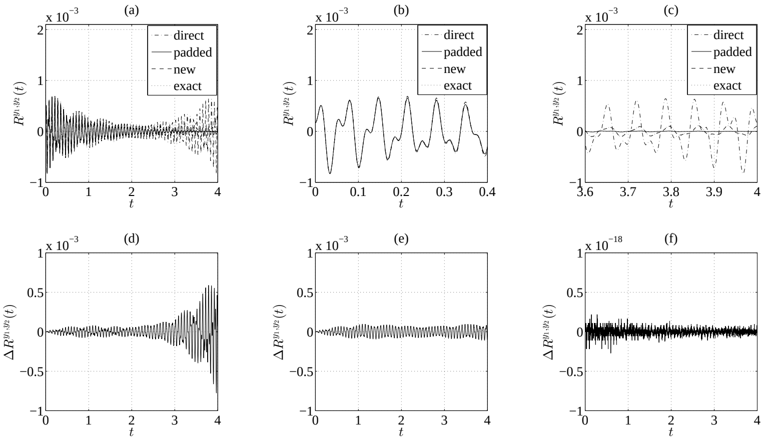

Figure 3.11: (a) Comparison of the averaged cross-correlation function between $y_1(t)$ and $y_2(t)$ of four seconds by directly applying the cross-correlation theorem and transforms (direct), the averaged cross-correlation function of a non-negative time delay between padded $y_1(t)$ and $y_2(t)$ of four seconds (padded), the averaged cross-correlation function of a non-negative time delay between $y_1(t)$ and $y_2(t)$ of four seconds from the new methodology (new), and the averaged cross-correlation function of a non-negative time delay between $y_1(t)$ and $y_2(t)$ of four seconds from the definition (exact); (b) an enlarged view of the comparison of the first 0.4 second; (c) an enlarged view of the comparison of the last 0.4 second; (d) differences between the direct and exact averaged cross-correlation functions; (e) differences between the padded and exact averaged cross-correlation functions; and (f) differences between the new and exact averaged cross-correlation functions. All the averaged cross-correlation functions are obtained with 32 sampling periods.

Since a cross-correlation function should be similar to an IRF [3, 63], an exponential window can be applied to cross-correlation functions of each sampling period to reduce the effect of DFT leakage before calculating averaged functions and associated half spectra. The decay rate of the exponential window should be sufficiently large so that values of the cross-correlation function are almost zero after the main decaying section, which is about the first two seconds in the simulation. The reason is that noise of a non-negligible amplitude can be observed in Fig. 3.3(b) after the main decaying section; such noise can have an adverse effect on the quality of the cross-correlation function. Like measuring a IRF and FRF by impact testing in EMA [2], an exponential window added to a cross-correlation function can increase estimated damping ratios, which can be corrected by a technique in Ref. [76]. An exponential window $w(t) = \mathrm{e}^{-\alpha t}$ with a decay rate $\alpha = 8$ and $t \in [0, 4]$ is added to $R^{y_1,y_2}(t)$, as shown in Fig. 3.12(a). The amplitude of the half spectrum associated with the windowed cross-correlation function is shown in Fig. 3.12(b), which is smoother than that in Fig. 3.7(b). Note that amplitudes of the half spectrum at two peaks in Fig. 3.12(a) are lower than those in Fig. 3.7(b) due to use of the exponential window. An averaged windowed cross-correlation function of a non-negative time delay with 32 sampling periods and the amplitude of the associated half spectrum are shown in Figs. 3.12(c) and (d), respectively.

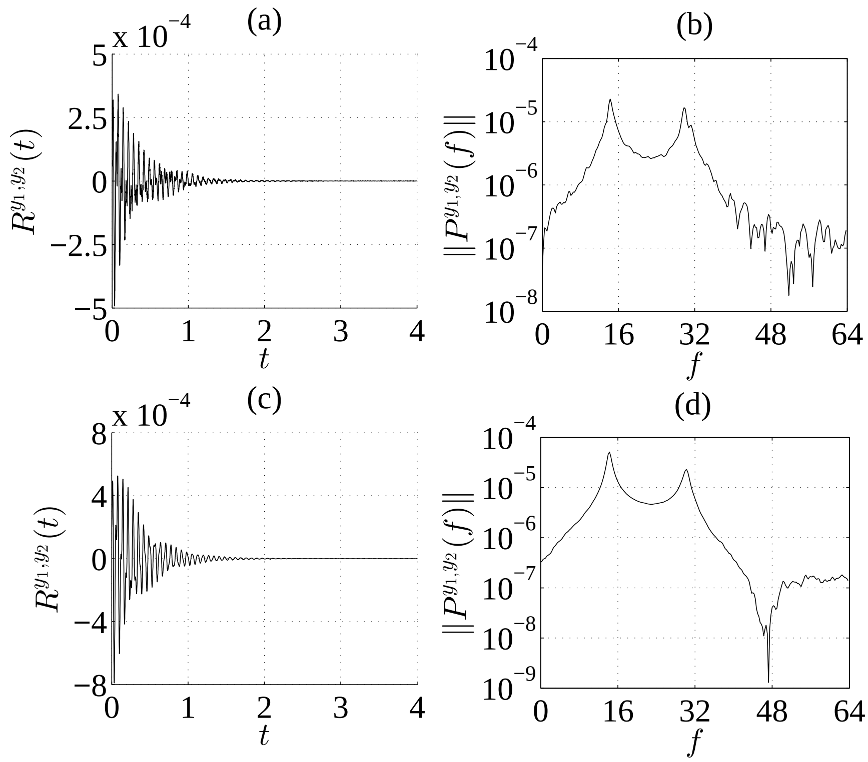

Figure 3.12: (a) Windowed cross-correlation function of a non-negative time delay between $y_1(t)$ and $y_2(t)$ of the first four seconds from the new methodology, (b) the amplitude of the associated half spectrum, (c) the averaged windowed cross-correlation function of a non-negative time delay between $y_1(t)$ and $y_2(t)$ of four seconds from the new methodology with 32 sampling periods, and (d) the amplitude of the associated half spectrum.

Cross-power spectra obtained by directly applying the cross-correlation theorem and transforms, half spectra by applying the theorem and transforms on $y_1(t)$ and $y_2(t)$ with N_s zero series padded to their ends, and half spectra from the new methodology averaged with 16 and 32 sampling periods are shown in Figs. 3.13 and 3.14, respectively. It can be seen that amplitudes and phases of the averaged cross-power spectra obtained by directly applying the theorem and transforms are noisy, and corresponding coherence function values are low in the frequency domain. Amplitudes and phases in the half spectra obtained by applying the theorem and transforms on $y_1(t)$ and $y_2(t)$ with N_s zero series padded to their ends are less noisy, and 180-degree phase shifts can be clearly observed at natural frequencies of the system, which is a characteristic of a FRF [1]; corresponding coherence functions have higher values than those obtained by directly applying the theorem and transforms. The coherence function values drop in neighborhoods of frequencies corresponding to peaks in the half spectra mainly due to DFT leakage. Amplitudes and phases in the half spectra from the new methodology have the best qualities, compared with those from the other two methodologies, and corresponding coherence functions have relatively high values in regions where amplitudes of the half spectra are high except in neighborhoods of frequencies corresponding to peaks in the half spectra (Figs. 3.13(i) and 3.14(i)). Some drops in neighborhoods of frequencies corresponding to peaks in the half spectra indicate that the spectra have relatively large variations near natural frequencies. The reason for such drops is that both $y_1(t)$ and $y_2(t)$ are caused by random excitation and can have varying amplitudes, amplitudes of cross-correlation functions between $y_1(t)$ and $y_2(t)$ can vary, while their overall shapes, which are similar to that of an IRF, do not change much especially in their main decaying sections, and amplitudes of $\tilde{E}^{u,v}(f)$ in Eq. (3.12) are relatively high near natural frequencies. Convergence functions corresponding to cross-correlation functions and associated cross-power spectra using the three methodologies are shown in Fig. 3.15. It can be seen that the averaged cross-correlation function and associated half spectrum from the new methodology have the best convergence. Convergence indices associated with the cross-power spectra using the three methodologies, with respect to the number of averages, are shown in Fig. 3.16. Averaged cross-correlation functions and associated half spectra from the new methodology have the highest convergence indices, which indicates that the corresponding functions and spectra have the best convergence.

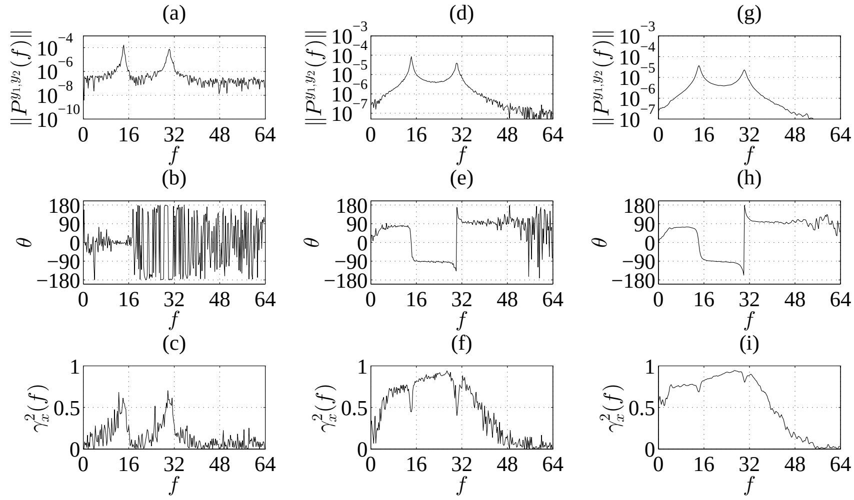

Figure 3.13: (a) Amplitude, (b) phase, and (c) coherence function of the cross-power spectrum between $y_1(t)$ and $y_2(t)$ by directly applying the cross-correlation theorem and transforms; (d) the amplitude, (e) phase, and (f) coherence function of the half spectrum by applying the theorem and transforms on padded $y_1(t)$ and $y_2(t)$; and (g) the amplitude, (h) phase, and (i) coherence function of the half spectrum from the new methodology. All the cross-power spectra are averaged with 16 sampling periods.

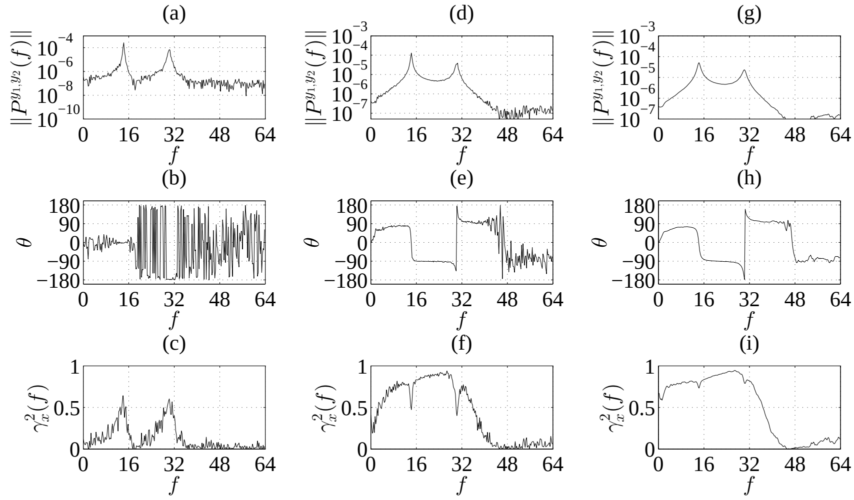

Figure 3.14: (a) Amplitude, (b) phase, and (c) coherence function of the cross-power spectrum between $y_1(t)$ and $y_2(t)$ by directly applying the cross-correlation theorem and transforms; (d) the amplitude, (e) phase, and (f) coherence function of the half spectrum by applying the theorem and transforms on padded $y_1(t)$ and $y_2(t)$; and (g) the amplitude, (h) phase, and (i) coherence function of the half spectrum from the new methodology. All the cross-power spectra are averaged with 32 sampling periods.

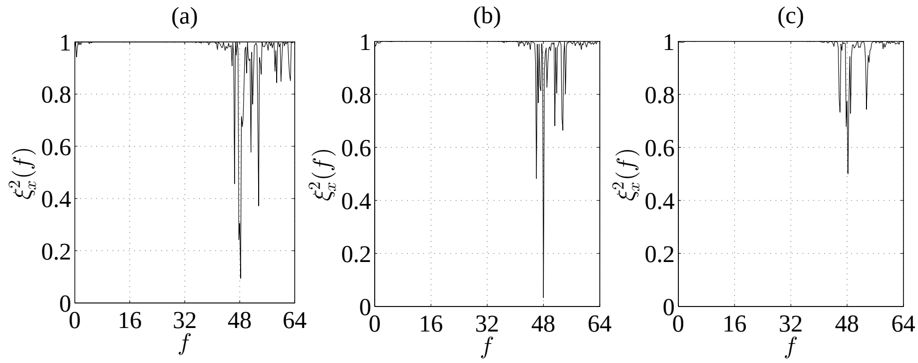

Figure 3.15: (a) Convergence function of the cross-power spectrum between $y_1(t)$ and $y_2(t)$ by directly applying the cross-correlation theorem and transforms, (b) the convergence function of the half spectrum by applying the theorem and transforms on padded $y_1(t)$ and $y_2(t)$, and (c) the convergence function of the half spectrum from the new methodology. All the cross-power spectra are averaged with 32 sampling periods.

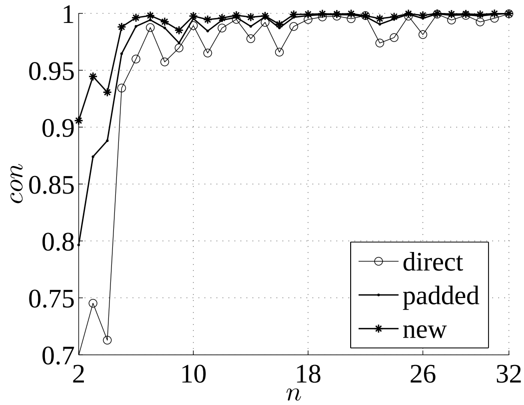

Figure 3.16: Convergence indices of averaged cross-power spectra between $y_1(t)$ and $y_2(t)$ by directly applying the cross-correlation theorem and transforms (direct), averaged half spectra by applying the theorem and transforms on $y_1(t)$ and $y_2(t)$ with N_s zero series padded to their ends (padded), and averaged half spectra from the new methodology (new).

Theoretical natural frequencies, damping ratios, and mode shapes of the 2-DOF system are calculated using complex modal analysis [71], and natural frequencies, damping ratios, and mode shapes are obtained from averaged P^{y_1,y_1} and P^{y_1,y_2} with 32 sampling periods with the three methodologies using Operational PolyMax of LMS Test.Lab Rev. 9b [77]. Resulting natural frequencies of the 2-DOF system are compared in Table 3.1; the natural frequencies from OMA on the averaged cross-power spectra with the three methodologies are close to the theoretical ones. Resulting damping ratios of the 2-DOF are compared in Table 3.2. It can be seen that the damping ratios from OMA on the averaged half spectra with the new methodology are closest to the theoretical ones, and those from OMA on the averaged half spectra with padded $y_1(t)$ and $y_2(t)$ are higher than those corresponding to the averaged half spectra from the new methodology. Mode shapes corresponding to the averaged cross-power spectra from the three methodologies are compared with the theoretical ones; MAC matrices [1] between the theoretical mode shapes and those corresponding to the averaged cross-power spectra from the three methodologies are listed in Table 3.3. The mode shapes corresponding to the averaged cross-power spectra from the three methodologies compare well with the theoretical ones; diagonal entries of the MAC matrices are all over 99%, which indicates that mode shapes from OMA on the averaged cross-power spectra with the three methodologies compare well with those from complex modal analysis.

Table 3.1: Comparison of natural frequencies of the 2-DOF system from complex modal analysis (theoretical) and those from OMA on the averaged cross-power spectra by directly applying the cross-correlation theorem and transforms (direct), the half spectra by applying the theorem and transforms on padded $y_1(t)$ and $y_2(t)$ (padded), and the half spectra from the new methodology (new). All the averaged cross-power spectra in OMA are obtained with 32 sampling periods.

Mode	Theoretical Frequency (Hz)	Direct Frequency (Hz)	Difference (%)	Padded Frequency (Hz)	Difference (%)	New Frequency (Hz)	Difference (%)
1	14.214	14.210	-0.03	14.222	0.06	14.217	0.02
2	30.251	30.233	-0.06	30.232	-0.06	20.227	-0.08

Table 3.2: Comparison of damping ratios of the 2-DOF system from complex modal analysis (theoretical) and those from OMA on the averaged cross-power spectra by directly applying the cross-correlation theorem and transforms (direct), the half spectra by applying the theorem and transforms on padded $y_1(t)$ and $y_2(t)$ (padded), and the half spectra from the new methodology (new). All the cross-power spectra in OMA are averaged with 32 sampling periods.

Mode	Theoretical Damping Ratio (%)	Direct Damping Ratio (%)	Difference (%)	Padded Damping Ratio (%)	Difference (%)	New Damping Ratio (%)	Difference (%)
1	0.68	0.91	33.82	1.07	57.35	0.65	-4.41
2	0.86	0.99	15.12	1.92	123.26	0.91	5.81

Table 3.3: (a) Entries of the MAC matrix in percent between the mode shapes of the 2-DOF system from OMA on the averaged cross-power spectra by directly applying the cross-correlation theorem and transforms and the theoretical ones, (b) entries of the MAC matrix in percent between the mode shapes of the 2-DOF system from OMA on the averaged half spectra by applying the cross-correlation theorem and transforms on padded $y_1(t)$ and $y_2(t)$ and the theoretical ones, and (c) entries of the MAC matrix in percent between the mode shapes of the 2-DOF system from OMA on the averaged half spectra from the new methodology and the theoretical ones. The horizontal and vertical mode numbers correspond to the mode shapes from OMA and the theoretical ones, respectively.

(a)

	1	2
1	99.90	5.02
2	5.59	99.97

(b)

	1	2
1	99.87	4.98
2	5.49	99.96

(c)

	1	2
1	100.00	4.87
2	5.36	99.98

After calculating a cross-correlation function of a non-negative time delay, that of a negative time delay is needed to calculate a cross-correlation function of any time delay. To calculate the cross-correlation function of a negative time delay using the new methodology, $y_1(t)$ of one sampling period with an N_s zero series padded to its start and $y_2(t)$ of the same sampling period as $y_1(t)$ and the previous sampling period are needed. The response $y_1(t)$ between the first four and eight seconds padded with an N_s zero series to its start and $y_2(t)$ of the first eight seconds are shown in Figs. 3.17(a) and (b), respectively. The cross-correlation function of a negative time delay is combined with that of a non-negative time delay and shown in Fig. 3.18(a). Differences between the cross-correlation function of any time delay from the new methodology and the exact one using its definition (Fig. 3.18(a)) are shown in Fig. 3.18(b). It can be seen that the two functions are almost identical, and their differences derive from numerical errors of the DFT and IDFT. Amplitudes of full spectra of the two cross-correlation functions of any time delays are almost identical, as shown in Fig. 3.18(c). Note that time for calculating the cross-correlation function using its definition is 1.220 seconds, and that using the new methodology is 0.009 seconds.

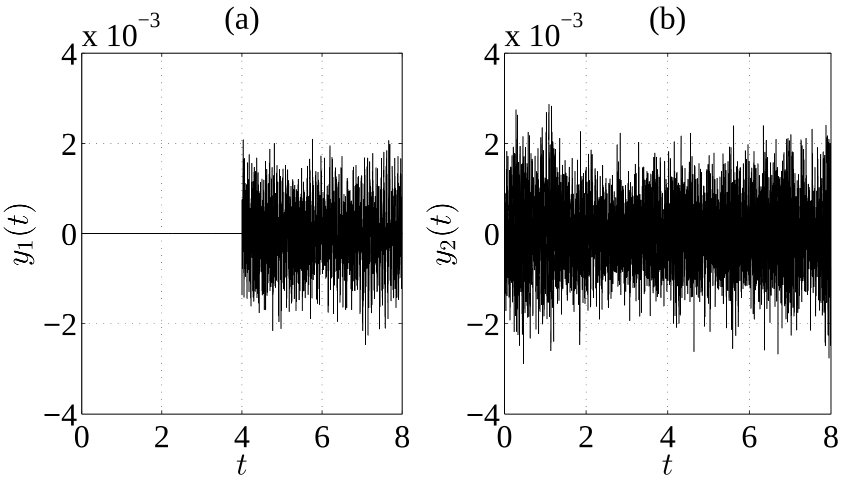

Figure 3.17: (a) Response of m_1 in Fig. 3.25 of the first four to eight seconds padded with N_s zero series to its start, and (b) that of m_2 in Fig. 3.25 of the first eight seconds.

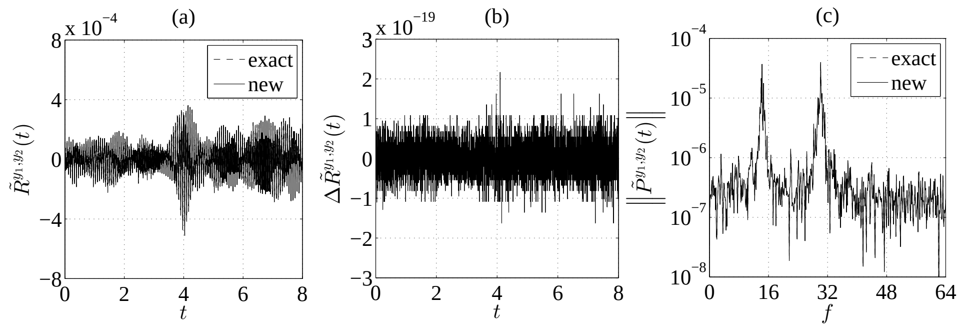

Figure 3.18: (a) Comparison of the cross-correlation function of any time delay between $y_1(t)$ and $y_2(t)$ of the first eight seconds from its definition (exact) and that from the new methodology (new), (b) differences between the two cross-correlation functions of any time delays in (a), and (c) comparison of amplitudes of full spectra of the two cross-correlation functions in (a).

3.1.3.2 Experimental Example

OMA was conducted on a damaged aluminum beam to measure natural frequencies, damping ratios, and mode shapes of its first four transverse vibration modes (Fig. 3.19(a)). The beam was of length 475.00 mm, width 25.60 mm, and thickness 6.50 mm, and it had a region of machined thickness reduction on top and bottom surfaces along its length. The width of the region was the same as that of the beam, and its length and thickness were 55.70 mm and 4.75 mm, respectively; thickness reduction on both the top and bottom surfaces of the region was 0.875 mm. The left end of the beam was clamped by a bench vice to simulate a fixed boundary. The distance between the clamped end of the beam and the left end of the region was 352.90 mm. Forty three equally spaced measurement points were assigned along the length of the beam, as shown in Fig. 3.19(b). The test setup for OMA is shown in Figs. 3.19(c) and (d): an MB Dynamics MODAL-50 shaker was fixed to the right end of the beam, and a laser head of a Polytec PSV-500-3D three-dimensional scanning laser vibrometer system (Laser 1) and a Polytec OFV-353 single-point laser vibrometer (Laser 2) were used to measure responses of the 43 measurement points and a reference point on the front surface of the beam, respectively. A strip of retroreflective tape was attached on the front surface of the beam to enhance laser reflection that directly determined SNRs of laser measurements.

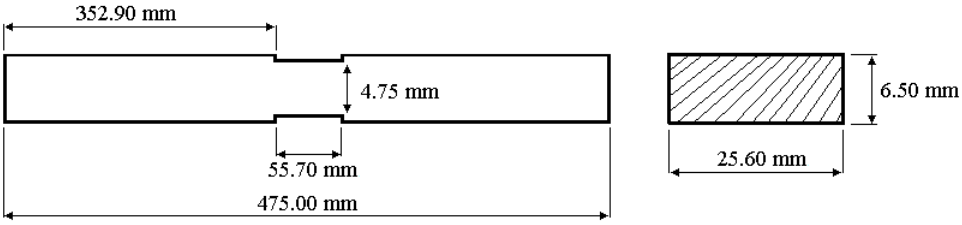

(a)

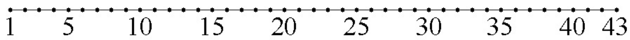

(b)

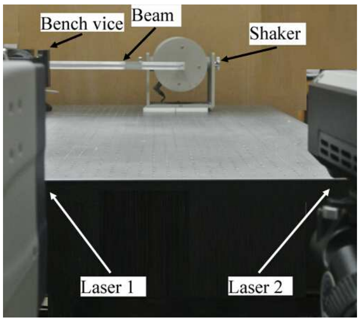

(c)

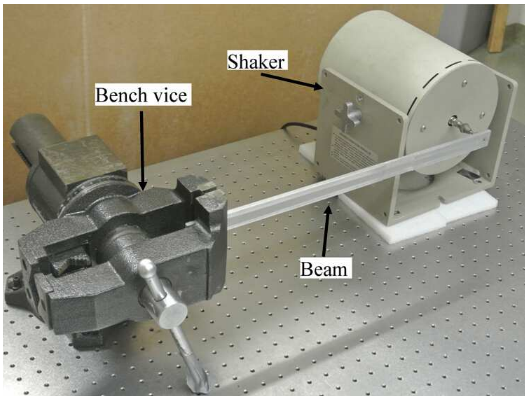

(d)

Figure 3.19: (a) Dimensions of a damaged aluminum beam with a region of machined thickness reduction, (b) numbered measurement points on the beam, (c) the test setup for OMA, and (d) the beam with its left end clamped by a bench vice and its right end connected to a shaker.

With a LMS spectrum analyzer and Test.Lab Rev. 9b [77], random excitation was generated to the shaker, and responses in the form of velocities of the 43 measurement points and the reference point were measured by Laser 1 and Laser 2, respectively, and denoted by v_i (i = 1, 2, ..., 43) and v_r, respectively. The excitation frequency ranged from 20 to 2048 Hz, the length of one sampling period was 0.4096 seconds with a sampling frequency of 5000 Hz, the number of sampling points in one sampling period was $N_s = 5000 \times 0.4096$, there were 33 continuous sampling periods, and the total measurement time was 0.4096×33 seconds. Thirty two cross-correlation functions and associated cross-power spectra were calculated using the three methodologies for each measurement point. Averaged spectra of the first 16 and 32 spectra between $v_r(t)$ and $v_{23}(t)$ are shown in Figs. 3.20 and 3.21, respectively. Note that the cross-correlation functions from the new methodology were windowed using an exponential window $w(t) = \mathrm{e}^{-\alpha t}$ with $\alpha = 8$. Calculation times for one cross-correlation function using its definition and the new methodology were 0.1839 and 0.0045 seconds, respectively. Similar to the numerical example in Sec. 3.1, amplitudes and phases of half spectra from the new methodology had the best qualities, and coherence function values were close to one except those near natural frequencies of the beam and in frequency regions with low SNRs; associated convergence functions and indices were closest to one, as shown in Figs. 3.15 and 3.16, respectively. Similar to the numerical example in Sec. 3.1, 180-degree phase shifts were observed at natural frequencies of the beam, and some drops in coherence functions were observed at the natural frequencies; the new methodology had the best convergence based on convergence functions and convergence indices.

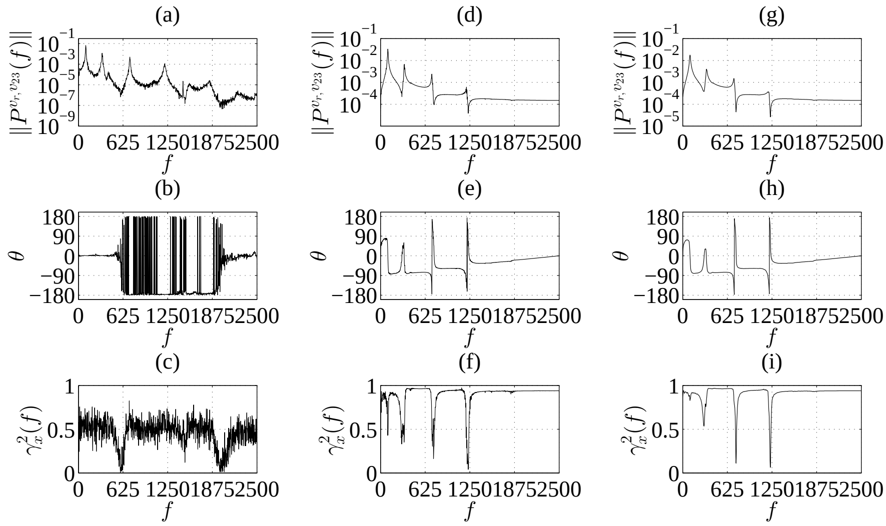

Figure 3.20: (a) Amplitude, (b) phase, and (c) coherence function of the cross-power spectrum between $v_r(t)$ and $v_{23}(t)$ by directly applying the cross-correlation theorem and transforms; (d) the amplitude, (e) phase, and (f) coherence function of the half spectrum by applying the theorem and transforms on padded $v_r(t)$ and $v_{23}(t)$; and (g) the amplitude, (h) phase, and (i) coherence function of the half spectrum from the new methodology. All the cross-power spectra were averaged with 16 sampling periods.

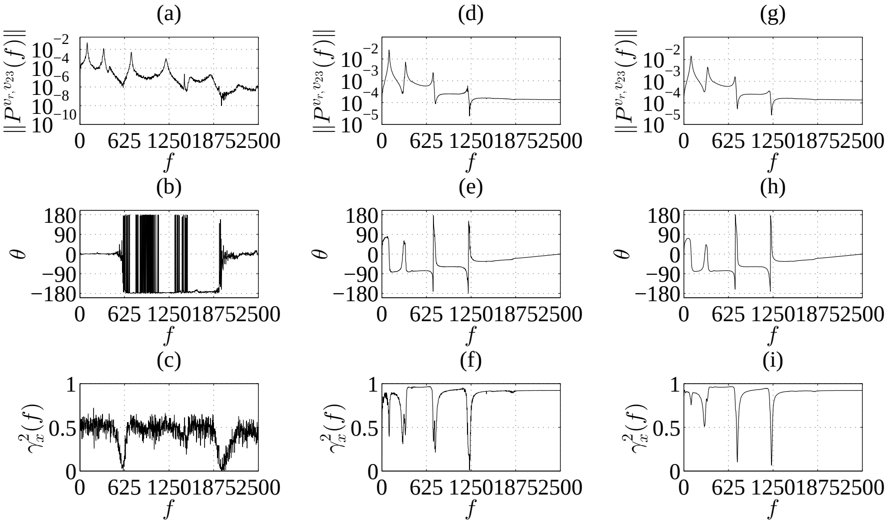

Figure 3.21: (a) Amplitude, (b) phase, and (c) coherence function of the cross-power spectrum between $v_r(t)$ and $v_{23}(t)$ by directly applying the cross-correlation theorem and transforms; (d) the amplitude, (e) phase, and (f) coherence function of the half spectrum by applying the theorem and transforms on padded $v_r(t)$ and $v_{23}(t)$; and (g) the amplitude, (h) phase, and (i) coherence function of the half spectrum from the new methodology. All the cross-power spectra were averaged with 32 sampling periods.

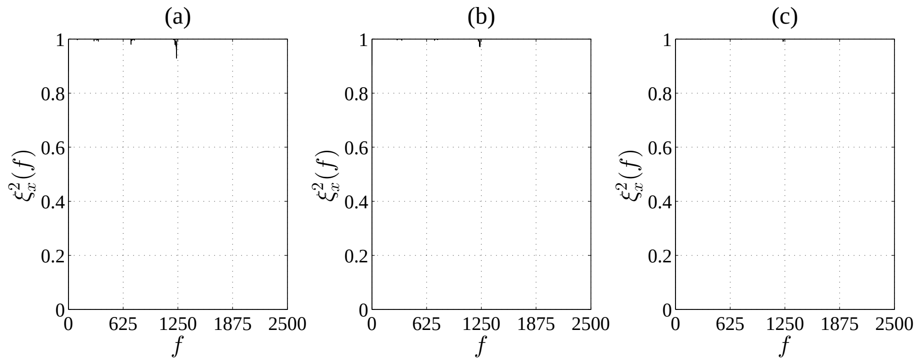

Figure 3.22: (a) Convergence function of the cross-power spectrum between $v_r(t)$ and $v_{23}(t)$ by directly applying the cross-correlation theorem and transforms, (b) the convergence function of the half spectrum by applying the theorem and transforms on padded $v_r(t)$ and $v_{23}(t)$, and (c) the convergence function of the half spectrum between $v_r(t)$ and $v_{23}(t)$ from the new methodology. All the cross-power spectra were averaged with 32 sampling periods.

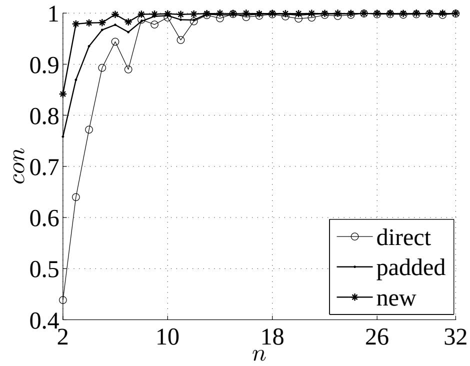

Figure 3.23: Convergence indices of averaged cross-power spectra between $v_r(t)$ and $v_{23}(t)$ by directly applying the cross-correlation theorem and transforms (direct), averaged half spectra by applying the theorem and transforms on padded $v_r(t)$ and $v_{23}(t)$ with N_s (padded), and averaged half spectra between $v_r(t)$ and $v_{23}(t)$ from the new methodology (new).

The aforementioned excitation frequency range of the shaker for OMA was sufficient for measuring natural frequencies of the beam in the range, since four peaks associated with the first four modes of the beam could be clearly identified in the resulting averaged cross-power spectra. However, resulting mode shapes had low SNRs due to the fact that the wider the excitation frequency range, the lower the distributed energy input from the shaker in the range. Hence excitations in narrower frequency ranges were needed to excite the first four modes of the beam with higher distributed energy inputs to measure mode shapes with higher SNRs. Excitation frequency ranges for the first through fourth modes were chosen to be between 20 and 200 Hz, between 200 and 500 Hz, between 550 and 950 Hz, and between 1100 and 1400 Hz, respectively. There were totally four groups of laser measurements for OMA; in each group of measurements, averaged cross-power spectra from the three methodologies corresponding to the 43 measurement points were obtained and analyzed using Operational PolyMax of LMS Test.Lab Rev. 9b to yield natural frequencies, damping ratios, and mode shapes of the beam [77].

To validate results from OMA, an impact test, which is one type of EMA, was conducted on the beam using a roving sensor technique to measure its natural frequencies, damping ratios, and mode shapes. A PCB 086C03 impact hammer connected to the spectrum analyzer was used to excite a point on the back surface of the beam, and resulting impact responses of the 43 measurement points were measured by the laser head of the Polytec PSV-500-3D 3D scanning laser vibrometer system. For each measurement point, five FRFs between the measurement point and hammer were obtained and averaged. Averaged FRFs of the 43 measurement points were analyzed using PolyMax of LMS Test.Lab Rev. 9b to yield natural frequencies, damping ratios, and mode shapes of the beam in the frequency range from 0 to 2048 Hz [77]. Measured natural frequencies from OMA on the averaged cross-power spectra with the three methodologies and EMA are compared in Table 3.4. The natural frequencies from OMA on the averaged cross-power spectra with the three methodologies compared well with those from EMA; the maximum difference was -0.69%. Measured damping ratios from OMA on the averaged cross-power spectra with the three methodologies and EMA are compared in Table 3.5. The damping ratios from OMA on the half spectra from the new methodology compared well with those from EMA. The damping ratios from OMA on the half spectra with padded responses of the measurement and reference points were higher than those using the half spectra with the new methodology, which was similar to the numerical example in Sec. 3.1. The damping ratios from OMA on the averaged cross-power spectra by directly applying the cross-correlation theorem and transforms deviated more from those from EMA. Measured mode shapes from OMA and EMA are compared in Fig. 3.24. MAC matrices between the mode shapes from OMA on the cross-power spectra with the three methodologies and EMA are listed in Table 3.6. Diagonal entries of the MAC matrices in Table 3.6 were all over 96%, which indicates that mode shapes from OMA on the averaged cross-power spectra with the three methodologies compared well with those from EMA.

Table 3.4: Comparison of measured natural frequencies of the damaged beam from EMA (EMA) and those from OMA using the cross-power spectra by directly applying the cross-correlation theorem and transforms (direct), the half spectra by applying the theorem and transforms on padded responses of the measurement and reference points (padded), and the half spectra from the new methodology (new). All the cross-power spectra in OMA were averaged with 32 sampling periods.

Mode	EMA Frequency (Hz)	Direct Frequency (Hz)	Difference (%)	Padded Frequency (Hz)	Difference (%)	New Frequency (Hz)	Difference (%)
1	101.59	101.76	0.18	101.69	0.10	101.42	-0.16
2	332.50	330.22	-0.68	330.23	-0.68	330.20	-0.69
3	718.21	719.09	0.12	719.39	0.16	719.09	0.12
4	1206.79	1209.48	0.22	1208.32	0.13	1209.62	0.23

Table 3.5: Comparison of measured damping ratios of the damaged beam from EMA (EMA) and those from OMA using the cross-power spectrum by directly applying the cross-correlation theorem and transforms (direct), the half spectrum by applying the theorem and transforms on padded responses of the measurement and reference points (padded), and the half spectrum from the new methodology (new). All the cross-power spectra in OMA were averaged with 32 sampling periods.

Mode	EMA Damping Ratio (%)	Direct Damping Ratio (%)	Difference (%)	Padded Damping Ratio (%)	Difference (%)	New Damping Ratio (%)	Difference (%)
1	2.86	3.63	26.92	3.76	31.47	2.94	2.80
2	1.06	1.55	46.23	1.63	53.77	1.48	39.62
3	0.57	0.50	-12.28	0.59	3.51	0.53	-7.02
4	0.95	0.86	-9.47	1.02	7.37	1.00	5.26

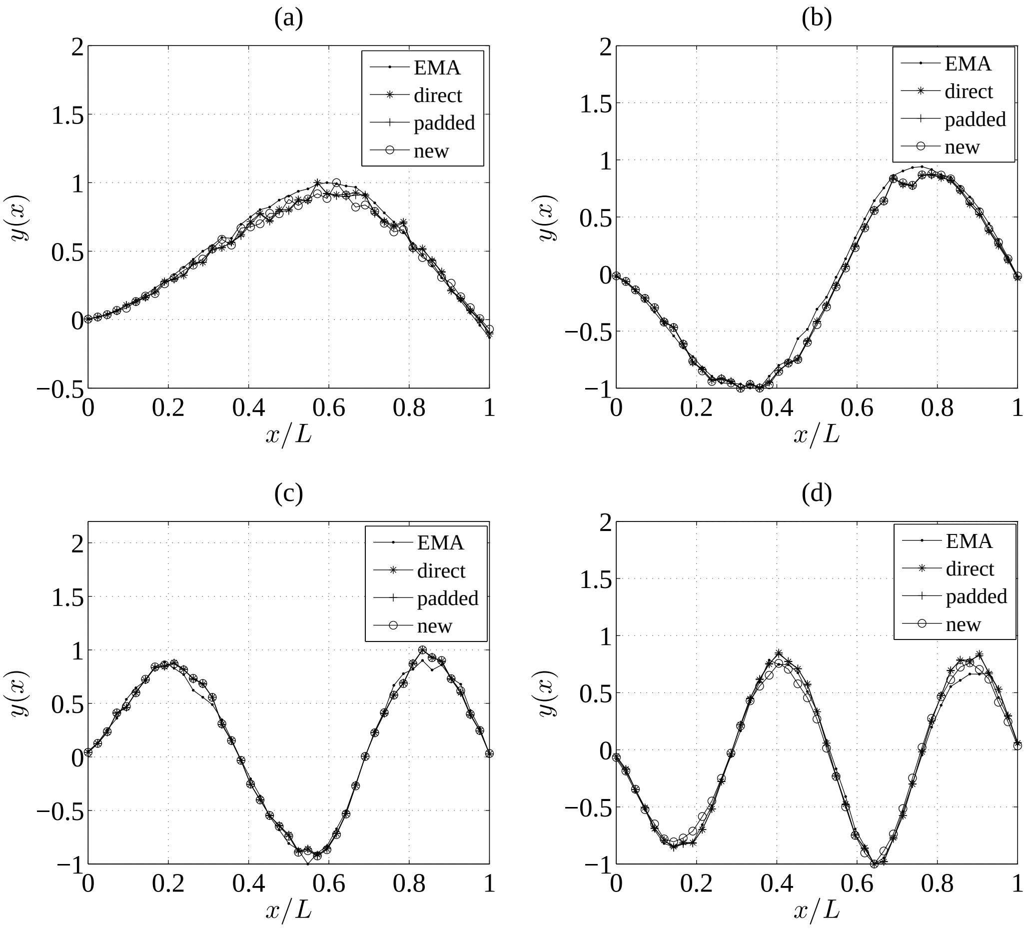

Figure 3.24: (a) The first measured mode shapes of the beam from OMA using the cross-power spectra with the three methodologies and EMA, (b) the second measured mode shapes of the beam from OMA using the cross-power spectra with the three methodologies and EMA, (c) the third measured mode shapes of the beam from OMA using the cross-power spectra with the three methodologies and EMA, and (d) the fourth measured mode shapes of the beam from OMA using the cross-power spectra with the three methodologies and EMA.

Table 3.6: (a) Entries of the MAC matrix in percent between the first four mode shapes of the beam from OMA using the cross-power spectra by directly applying the cross-correlation theorem and transforms and those from EMA, (b) entries of the MAC matrix in percent between the first four mode shapes of the beam from OMA using the half spectra by applying the theorem and transforms on padded responses of the measurement and reference points and those from EMA, and (c) entries of the MAC matrix in percent between the first four mode shapes of the beam from OMA using the half spectra with the new methodology and those from EMA. The horizontal and vertical mode numbers correspond to the modes from OMA and EMA, respectively.

(a)

	1	2	3	4
1	99.08	0.38	0.63	0.82
2	3.06	96.58	0.07	0.80
3	0.51	0.24	99.07	0.35
4	1.08	0.39	1.61	98.19

(b)

	1	2	3	4
1	98.98	0.40	0.65	0.84
2	3.06	96.77	0.08	0.78
3	0.51	0.28	99.10	0.33
4	1.09	0.37	1.54	98.26

(c)

	1	2	3	4
1	99.19	0.37	0.68	1.41
2	2.76	96.75	0.08	0.76
3	0.60	0.28	99.15	0.56
4	0.92	0.38	1.57	98.09

3.1.4 Conclusion

Direct use of the cross-correlation theorem and transforms, including the DFT and IDFT, can enable efficient calculation of discrete cross-correlation functions and cross-power spectra between a reference data series and a measured data series. However, resulting functions and spectra are physically erroneous due to use of the DFT, where a data series to be transformed is extended to be periodic with a period equal to the length of one sampling period, which is usually false in practice. While the error can be reduced by padding zero series that have the same length as the reference and measured data series to their ends, the results are still physically erroneous. A new methodology for calculating cross-correlation functions of non-negative time delays and associated half spectra is proposed in this work. Qualities of measured cross-correlation functions and associated cross-power spectra can be evaluated using a coherence function, a convergence function in the frequency domain, and a convergence index. Calculation time for one cross-correlation function from the new methodology can be greatly reduced, compared with that by directly applying its definition. A cross-correlation function from the new methodology is in perfect accordance with that by directly applying its definition, and so is the associated cross-power spectrum. Exponential windows are added to cross-correlation functions to reduce effects of DFT leakage and noise of non-negligible amplitudes that exist after main decaying sections. Half spectra of windowed cross-correlations functions are better than those from the other two methodologies with respect to smoothness of amplitudes and phases and high values of coherence functions. Based on the introduced convergence function and convergence index, averaged cross-correlation functions of non-negative time delays and associated half spectra from the new methodology have the best convergence. The new methodology is extended to calculate cross-correlation functions of negative time delays and the resulting cross-correlation function is in perfect accordance with that by directly applying its definition. Combining cross-correlations of non-negative and negative time delays gives those of any time delays, and associated full spectra can be obtained. OMA was numerically and experimentally conducted on an ideal 2-DOF mass-spring-damper system and a damaged aluminum beam, respectively, using half spectra from the new methodology to estimate their natural frequencies, damping ratios, and mode shapes, which compared well with theoretical ones from complex modal analysis and measured ones from EMA, respectively. While natural frequencies and mode shapes from OMA on cross-power spectra by directly applying the cross-correlation theorem and transforms and those with padded responses of measurement and reference points compared well with those from complex modal analysis and EMA in the numerical and experimental examples, respectively, damping ratios from OMA on cross-power spectra by the two methodologies deviated from those from complex modal analysis and EMA in the numerical and experimental examples, respectively.

3.2 Efficient and Accurate Calculation of FRFs and IRFs

3.2.1 Introduction

Modal properties of a structure, including natural frequencies, mode shapes, and modal damping ratios, can be identified via modal analysis [1]. There are two types of modal analysis methods: EMA and OMA. The former requires measurements of excitation on a structure, while the latter does not. In addition, the former analyzes FRFs and IRFs of a structure that show relationships between measured responses and excitation in the frequency and time domains, respectively, while the latter analyzes cross-power spectra and cross-correlation functions between reference and measured responses in the frequency and time domains, respectively [63, 3]. OMA can be easily conducted and considered to be practical, since it only measures modes that are excited under present environmental influence or operation [58, 59, 60, 61, 62]. However, its repeatability can be weak, since cross-power spectra and cross-correlation functions in OMA vary with environmental or operational excitation that can be uncontrollable in some cases. Compared with OMA, EMA is more repeatable, informative, and objective due to use of FRFs and IRFs that are independent of excitation, if excitation is appropriately generated.

Excitation of high amplitudes can be used to increase SNRs of FRF and IRF measurements, but it may induce nonlinear responses of a structure, which should be avoided in modal analysis. One can conduct measurements of multiple sampling periods to reduce effects of measurement noise [2], and the length of measurement time depends on an excitation technique used. There are various criteria to categorize an excitation technique in EMA, and one is whether an exciter needs to be fixed to a structure or not. If it does, it is a fixed exciter; otherwise, it is a non-fixed one [2]. A shaker is the most frequently used fixed exciter, by which different types of excitation can be generated in a well-controlled manner, such as pure random, periodic random, and burst random excitation, and responses can be measured with high SNRs, since a structure can be well excited with high input energy. When one calculates a discrete FRF, the DFT is applied to both response and excitation series, and the associated IRF can be obtained by applying the inverse IDFT to the FRF or using a least-squares (LS) method [73]. In the DFT, a transformed series is virtually extended to have an infinite length and be periodic with a period equal to the length of the series [69]. Errors caused by such extension in calculation of cross-correlation functions and cross-power spectra have been studied, and an accurate and efficient methodology was proposed in Ref. [78] to eliminate the errors. When periodic extension is physically incorrect, i.e., extended responses do not match those associated with extended excitation, errors can occur in estimated FRFs and associated IRFs. Among different types of excitation, FRFs with pure random excitation and associated responses often suffer from leakage due to physical incorrectness of periodic extension in the DFT. A more specific reason is that pure random excitation signals are not periodic and associated responses of a sampling period are not completely measured due to truncation of measurements at the end of the period. Hanning windows are often used to reduce effects of leakage, which can, however, distort resulting FRFs and associated IRFs. EMA using periodic random excitation do not suffer from leakage, but a structure needs to be repeatedly excited with the same random excitation so that steady-state responses can be reached, which can take a long measurement period. EMA using burst random excitation does not suffer from leakage either, and a shorter measurement period than that using periodic random is needed, due to the fact that burst random excitation has a zero-value interval of a proper length at its end, in which free responses of a structure can decay to zero and be completely measured, and extended excitation and response series are physically correct. An impact hammer is the most frequently used non-fixed exciter, which is relatively easy to set up for use and capable of generating broadband excitation. However, a hammer impact in one sampling period can yield FRFs and IRFs of low SNRs due to the fact that input energy from an impact to a structure can be relatively low. An excitation technique that uses a random impact series in EMA was proposed in Ref. [56] to increase input energy of hammer impacts. Similar to EMA using pure random excitation by shakers, that using a random impact series can suffer from leakage. A zero-value excitation interval of a proper length at the end of a sampling period can be used so that free responses can decay to zero and be completely measured, and leakage can be avoided, which is analogous to the case of burst random excitation. However, a problem of burst random excitation can be that a long sampling period is needed so that free responses of a structure can decay to zero and be completely measured, and a large number of spectral lines are needed especially for a high sampling frequency. Since one can have a limited number of spectral lines in some modal analysis software, measuring a FRF with a relatively high sampling frequency and a relatively long sampling period is sometimes impossible.

In this work, an efficient and accurate methodology for calculating discrete FRFs and IRFs is proposed: a sampling period is evenly divided into multiple sub-sampling periods, and the length of a sub-sampling period is long enough for free responses of a structure to decay to zero; all sub-sampling periods of response and excitation series are superposed to corresponding single sub-sampling periods to form pseudo-periodic response and excitation series, respectively, in calculation of FRFs and IRFs. Data lengths of response and excitation series for calculating DFTs can be shortened by a factor equal to the number of sub-sampling periods. The relationship between an IRF from the proposed methodology and that from the LS method is shown. A coherence function extended from a new type of coherence functions is used to evaluate qualities of FRFs and IRFs from the proposed methodology in the frequency domain. It can yield meaningful coherence function values even with excitation and response series of one sampling period. The proposed methodology was numerically and experimentally applied to a two-degree-of-freedom (2-DOF) mass-spring-damper system and an aluminum plate, respectively, to estimate their FRFs and IRFs. In the numerical example, FRFs from the proposed methodology agree well with theoretical ones. In the experimental example, a FRF and its associated IRF from the proposed methodology with a random impact series agreed well with benchmark ones from a single impact test.

3.2.2 Methodology

3.2.2.1 FRFs and IRFs

Let the IRF of a linear time-invariant, underdamped single-input-single-output system be denoted by $h(t)$, which has a nontrivial time duration T; $h(t) = 0$ when $t < 0$ or $t > T$. Assuming a general excitation $f(t)$ to the system with zero initial conditions, one can calculate the response of the system $y(t)$ using Duhamel's integral [79]:

$$y(t) = \int_0^T f(t-\tau)h(\tau)d\tau \tag{3.19}$$

Suppose that $f(t)$ and $y(t)$ are discretely sampled with a time interval $\triangle t$, and an excitation series $f_{\tilde{i}} = f\left(\tilde{i}\triangle t\right)$ and a response series $y_{\tilde{i}} = y\left(\tilde{i}\triangle t\right)$ are available, where $\tilde{i} = 1, 2, \ldots, m$; n values of the IRF $h_{\tilde{k}} = h(\tilde{k}\triangle t)$, where $n = \frac{T}{\triangle t}$ and $\tilde{k} = 0, 1, \ldots, n-1$ with $n < m$, are to be calculated. Equation (3.19) can be expressed in a discrete form:

$$[ft]_{m\times n}\,[ht]_{n\times 1} = \left(\frac{1}{\triangle t}\right)[yt]_{m\times 1} \tag{3.20}$$

where

$$[ft] = \begin{bmatrix} f_1 & 0 & \cdots & 0 \\ f_2 & f_1 & \cdots & 0 \\ \vdots & \vdots & \ddots & \vdots \\ f_n & f_{n-1} & \cdots & f_1 \\ f_{n+1} & f_n & \cdots & f_2 \\ \vdots & \vdots & \ddots & \vdots \\ f_m & f_{m-1} & \cdots & f_{m-n+1} \end{bmatrix}, \ [ht] = \begin{bmatrix} h_0 \\ h_1 \\ \vdots \\ h_{n-1} \end{bmatrix}, \ [yt] = \begin{bmatrix} y_1 \\ y_2 \\ \vdots \\ y_m \end{bmatrix} \tag{3.21}$$

A LS solution of $[ht]$ can be obtained by solving Eq. (3.20) using the Moore-Penrose pseudoinverse of $[ft]$, denoted by $[ft]^+$:

$$[ht]_{n\times 1} = [ft]^+_{n\times m} \left(\frac{1}{\triangle t}\right) [yt]_{m\times 1} \tag{3.22}$$

where $[ft]^+ = \left([ft]^{\mathrm{T}}[ft]\right)^{-1}[ft]^{\mathrm{T}}$, in which the superscript T denotes transpose of a matrix. However, the LS method for an IRF is sometimes impractical, since calculation of the Moore-Penrose pseudoinverse of $[ft]$ with a large n is computationally inefficient due to inversion of an $n \times n$ matrix $[ft]^{\mathrm{T}}[ft]$. When the time duration T is not exactly known a priori, one can have it equal to the duration of a sampling period, denoted by T_q, which is often longer than T. Equation (3.20) becomes

$$[ft^q]_{m\times m}[ht]_{m\times 1} = \left(\frac{1}{\triangle t}\right)[yt]_{m\times 1} \tag{3.23}$$

where

$$[ft^q] = \begin{bmatrix} f_1 & 0 & \cdots & 0 \\ f_2 & f_1 & \cdots & 0 \\ \vdots & \vdots & \ddots & \vdots \\ f_m & f_{m-1} & \cdots & f_1 \end{bmatrix}, \ [ht] = \begin{bmatrix} h_0 \\ h_1 \\ \vdots \\ h_{m-1} \end{bmatrix} \tag{3.24}$$

and $[ht] = ([ft^q])^{-1}[yt]$. Similarly, inversion of $[ft^q]$ in Eq. (3.23) can be computationally inefficient, and a more efficient way of calculating IRFs becomes necessary.

Based on the convolution theorem [80], applying Fourier transform on both sides of Eq. (3.19) yields

$$Y(s) = F(s)\,H(s) \tag{3.25}$$

where $Y(s) = \mathscr{F}[y(t)]$, $F(s) = \mathscr{F}[f(t)]$, and $H(s) = \mathscr{F}[h(t)]$, in which s and $\mathscr{F}(\cdot)$ denote a frequency in Hz and Fourier transform operation, respectively. Hence, $H(s)$ can be expressed by

$$H(s) = \frac{Y(s)}{F(s)} \tag{3.26}$$

which defines the FRF associated with $h(t)$. Since both $f_{\tilde{i}}$ and $y_{\tilde{i}}$ are of finite lengths, discrete $F(s)$ and $Y(s)$ can be obtained by directly applying the DFT to $f_{\tilde{i}}$ and $y_{\tilde{i}}$, respectively. The discrete IRF $h_{\tilde{i}}$ can be obtained as the IDFT of the discrete $H(s)$. While matrix inversion can be avoided here, the resulting IRF can be physically erroneous. The error is caused by periodic extension of the DFT applied to $f_{\tilde{i}}$: $f(t)$ becomes virtually infinitely long and periodic with a period equal to its duration, i.e., $f(t+\bar{p}T_q) = f(t)$ or $f_{\tilde{i}+\bar{p}m} = f_{\tilde{i}}$, where $\bar{p}$ is an integer. Based on Eq. (3.23), the resulting IRF is equal to the one that is obtained by solving

$$[ft^p]_{m\times m}\,[ht]_{m\times 1} = \left(\frac{1}{\triangle t}\right)[yt]_{m\times 1} \tag{3.27}$$

where

$$[ft^p] = \begin{bmatrix} f_1 & f_m & f_{m-1} & \cdots & f_2 \\ f_2 & f_1 & f_m & \cdots & f_3 \\ \vdots & \vdots & \vdots & \ddots & \vdots \\ f_{m-1} & f_{m-2} & f_{m-3} & \cdots & f_m \\ f_m & f_{m-1} & f_{m-2} & \cdots & f_1 \end{bmatrix} \tag{3.28}$$

is the excitation matrix that corresponds to periodic excitation with a period equal to the sampling period; the response vector $[yt]$ corresponds to the transient rather than steady-state response of the system. As a result, the IRF $[ht]$ in Eq. (3.27) can be erroneous, since $[ft^p]$ can violate the physics of the system, which is caused by the periodic extension. In practice, $f_{\tilde{i}}$ and $y_{\tilde{i}}$ are measured in N_s sampling periods to obtain a FRF and the error caused by the periodic extension and measurement noise can be reduced [2]. The FRF can be expressed by

$$H^1(s) = \frac{\hat{G}_{FY}(s)}{\hat{G}_{FF}(s)} \tag{3.29}$$

or

$$H^2(s) = \frac{\hat{G}_{YY}(s)}{\hat{G}_{YF}(s)} \tag{3.30}$$

where

$$\begin{aligned} \hat{G}_{YF}(s) &= \hat{G}^*_{FY}(s) = \tfrac{\sum_{j=1}^{N_s} Y_j^*(s)F_j(s)}{N_s} \\ \hat{G}_{FF}(s) &= \tfrac{\sum_{j=1}^{N_s} F_j^*(s)F_j(s)}{N_s} \\ \hat{G}_{YY}(s) &= \tfrac{\sum_{j=1}^{N_s} Y_j^*(s)Y_j(s)}{N_s} \end{aligned} \tag{3.31}$$

in which $Y_j(s)$ and $F_j(s)$ are DFTs of $y_{\tilde{i}}$ and $f_{\tilde{i}}$ of the j-th sampling period, respectively, and the hat $\wedge$ and superscript $*$ denote an averaged quantity and complex conjugation, respectively.

Assume that there are N_s sampling periods; each sampling period can be equally divided into n_s sub-sampling periods, and there is no excitation in the n_s-th sub-sampling period in one sampling period. A sub-sampling period has a duration longer than T and its data length is $m_s = \frac{m}{n_s}$, where m is the data length of $f_{\tilde{i}}$ and $y_{\tilde{i}}$ of one sampling period. An efficient and accurate methodology is proposed to calculate a discrete FRF and its associated IRF without matrix inversion. The proposed methodology is described below:

Step 1. In the j-th sampling period, calculate a pseudo-periodic excitation series $\widetilde{f}_i^p = \sum_{k=1}^{n_s-1} f_{i+(k-1)m_s+(j-1)m}$ and a pseudo-periodic response series $\widetilde{y}_i^p = \sum_{k=1}^{n_s} y_{i+(k-1)m_s+(j-1)m}$. Note that i ranges from 1 to m_s.

Step 2. Calculate DFTs of $\widetilde{f}_i^p$ and $\widetilde{y}_i^p$ in the j-th sampling period, denoted by $\widetilde{F}_j(s)$ and $\widetilde{Y}_j(s)$, respectively, using the fast Fourier transform (FFT).

Step 3. Calculate $G_{\widetilde{Y}\widetilde{F}}(s)$ and $G_{\widetilde{Y}\widetilde{Y}}(s)$ (or $G_{\widetilde{F}\widetilde{F}}(s)$) associated with the pseudo-periodic excitation and response series in the j-th sampling period, where $G_{\widetilde{Y}\widetilde{F}}(s) = \widetilde{Y}_j^*(s)\widetilde{F}_j(s)$, $G_{\widetilde{Y}\widetilde{Y}}(s) = \widetilde{Y}_j^*(s)\widetilde{Y}_j(s)$, and $G_{\widetilde{F}\widetilde{F}}(s) = \widetilde{F}_j^*(s)\widetilde{F}_j(s)$.

Step 4. Repeat Steps 1 through 3 for all N_s sampling periods.

Step 5. Calculate $H^1(s)$ (or $H^2(s)$) in Eq. (3.29) (or Eq. (3.30)) using results in Step 4.

Step 6. Calculate the IDFT of $H(s)$ in Step 5 for h_l using the inverse FFT (IFFT). Note that l ranges from 1 to m_s.

To calculate h_l using $y_{\tilde{i}}$ and $f_{\tilde{i}}$ of one sampling period based on Eq. (3.20), one needs to solve

$$[ft^c]_{m\times m_s}\,[ht]_{m_s\times 1} = \left(\frac{1}{\triangle t}\right)[yt^c]_{m\times 1} \tag{3.32}$$

where

$$[ft^c] = \begin{bmatrix} f_1 & 0 & 0 & \cdots & 0 & 0 \\ f_2 & f_1 & 0 & \cdots & 0 & 0 \\ \vdots & \vdots & \vdots & \ddots & \vdots & \vdots \\ f_{m_s} & f_{m_s-1} & f_{m_s-2} & \cdots & f_2 & f_1 \\ f_{m_s+1} & f_{m_s} & f_{m_s-1} & \cdots & f_3 & f_2 \\ \vdots & \vdots & \vdots & \ddots & \vdots & \vdots \\ f_{(n_s-1)\times m_s} & f_{(n_s-1)\times m_s-1} & f_{(n_s-1)\times m_s-2} & \cdots & f_{(n_s-2)\times m_s+2} & f_{(n_s-2)\times m_s+1} \\ 0 & f_{(n_s-1)\times m_s} & f_{(n_s-1)\times m_s-1} & \cdots & f_{(n_s-2)\times m_s+3} & f_{(n_s-2)\times m_s+2} \\ \vdots & \vdots & \vdots & \ddots & \vdots & \vdots \\ 0 & 0 & 0 & \cdots & f_{(n_s-1)\times m_s} & f_{(n_s-1)\times m_s-1} \\ 0 & 0 & 0 & \cdots & 0 & f_{(n_s-1)\times m_s} \\ 0 & 0 & 0 & \cdots & 0 & 0 \end{bmatrix}$$
$$[yt^c] = \begin{bmatrix} y_1 \\ \vdots \\ y_m \end{bmatrix} \tag{3.33}$$

in which $y_m = 0$. Note that a solution for h_l can be obtained by the LS method. In the proposed methodology, periodic extension is applied to $\widetilde{f}_i^p$, which is similar to the case in Eq. (3.27). The proposed methodology is equivalent to solving an equation that is obtained by pre-multiplying both sides of Eq. (3.32) by $\begin{bmatrix} \mathrm{I}_{m_s \times m_s}, \ \mathrm{I}_{m_s \times m_s}, \ \ldots, \quad \mathrm{I}_{m_s \times m_s} \end{bmatrix}_{m_s \times m}$, in which $\mathrm{I}_{m_s \times m_s}$ is an identity matrix of dimensions $m_s \times m_s$. The equation can be expressed by

$$\left[\widetilde{ft}^p\right]_{m_s \times m_s} [ht]_{m_s \times 1} = \left(\frac{1}{\triangle t}\right) \left[\widetilde{yt}^p\right]_{m_s \times 1} \tag{3.34}$$

where

$$\left[\widetilde{ft}^p\right] = \begin{bmatrix} \widetilde{f}_1^p & \widetilde{f}_{m_s}^p & \widetilde{f}_{m_s-1}^p & \cdots & \widetilde{f}_2^p \\ \widetilde{f}_2^p & \widetilde{f}_1^p & \widetilde{f}_{m_s}^p & \cdots & \widetilde{f}_3^p \\ \vdots & \vdots & \vdots & \ddots & \vdots \\ \widetilde{f}_{m_s-1}^p & \widetilde{f}_{m_s-2}^p & \widetilde{f}_{m_s-3}^p & \cdots & \widetilde{f}_{m_s}^p \\ \widetilde{f}_{m_s}^p & \widetilde{f}_{m_s-1}^p & \widetilde{f}_{m_s-2}^p & \cdots & \widetilde{f}_1^p \end{bmatrix}, \ \left[\widetilde{yt}^p\right] = \begin{bmatrix} \widetilde{y}_1^p \\ \vdots \\ \widetilde{y}_{m_s}^p \end{bmatrix} \tag{3.35}$$

The IRF h_l from Eq. (3.34) is physically correct, since Eq. (3.34) corresponds to a steady-state response series of the system $\widetilde{y}_i^p$ under a periodic excitation series $\widetilde{f}_i^p$, and the associated FRF is also physically correct, which indicates that the proposed methodology can be as accurate as the LS method. Measurements of multiple sampling periods in the proposed methodology can reduce measurement errors.

The proposed methodology is efficient due to use of the FFT and IFFT and suitable for EMA with excitation in the form of a random impact series and random excitation. It has been shown in Ref. [73] that the calculation time for FRFs and IRFs can be greatly shortened due to use of the FFT and IFFT, compared with that using the LS method. When excitation is in the form of a random impact series, a sampling period can have more than two sub-sampling periods. Step 1 in the proposed methodology in effect superposes excitation and response series of each sub-sampling period in one sampling period. The resulting superposed excitation and response series have higher SNRs due to more impacts in the resulting sub-sampling period, and fewer spectral lines are needed for associated DFTs. When excitation is in the form of zero-mean random excitation, a sampling period can have two sub-sampling periods, where one sub-sampling period has non-zero excitation, which is similar to the case of burst random excitation. Superposing more than two sub-sampling periods with non-zero excitation can cancel out some entries of excitation and response series in one sub-sampling period and result in FRFs and IRFs of lower SNRs and accuracies.

3.2.2.2 Coherence Function

A conventional coherence function that has been widely used to evaluate qualities of measured FRFs in the frequency domain is defined by

$$\gamma_c^2(s) = \frac{\hat{G}_{YF}\,(s)\,\hat{G}_{YF}^{*}\,(s)}{\hat{G}_{YY}\,(s)\,\hat{G}_{FF}\,(s)} \tag{3.36}$$

Measured excitation and response series of at least two sampling periods are needed to yield meaningful coherence function values, since the coherence function has a value of one at all frequencies when those of only one sampling period are used. A new coherence function was proposed in Ref. [73] to evaluate accuracies of calculated IRFs and FRFs in the frequency domain. A similar coherence function was developed in Ref. [74] to evaluate random variation of a signal at each frequency. This new type of coherence functions can be extended to evaluate qualities of FRFs and IRFs from the proposed methodology in the frequency domain. The extended coherence function is defined by

$$\gamma^2(s) = \frac{\hat{Y}(s)}{\hat{Y}(s) + \hat{E}(s)} \tag{3.37}$$

where $\hat{Y}(s)$ and $\hat{E}(s)$ are averaged auto-power spectra of measured response series $y_i^{j,k}$ and error series $e_i^{j,k}$ in $n_s \times N_s$ sub-sampling periods, respectively; $y_i^{j,k}$ and $e_i^{j,k}$ are the response and error series in the k-th sub-sampling period of the j-th sampling period, respectively. The error series is defined by

$$e_i^{j,k} = y_i^{j,k} - \bar{y}_i^{j,k} \tag{3.38}$$

where $\bar{y}_i^{j,k}$ is the predicted response series obtained by convolution between $f_{\tilde{i}}$ and h_l from the proposed methodology in the k-th sub-sampling period of the j-th sampling period. The extended coherence function in can yield meaningful values when measured excitation and response series of only one or multiple sampling periods are available. When it has a value close to one at a frequency, a FRF and its associated IRF are accurately estimated at the frequency. The lower the extended coherence function value the less accurately estimated the FRF and IRF at the frequency.

A fitting index is used to evaluate overall qualities of FRFs and IRFs based on the coherence function in Eq. (3.37):

$$fit = \sqrt{\frac{\Xi\left(\hat{Y}(s)\right)}{\Xi\left(\hat{Y}(s) + \hat{E}(s)\right)}} \tag{3.39}$$

where $\Xi(\cdot)$ denotes summation over all frequencies. When $\hat{E}(f) = 0$ at all frequencies, $fit = 1$. The lower the index the worse the overall qualities of FRFs and IRFs from the proposed methodology.

3.2.3 Numerical Simulation and Experimental Examples

3.2.3.1 Numerical Example

Numerical simulations are conducted on a 2-DOF mass-spring-damper system, as shown in Fig. 3.25, with masses $m_1 = 1$ kg and $m_2 = 2$ kg; spring constants $k_1 = 6240\pi$ N/m, $k_2 = 4160\pi$ N/m, and $k_3 = 3120\pi$ N/m; and viscous damping coefficients $c_1 = 2$ N/(m/s), $c_2 = 1$ N/(m/s), and $c_3 = 2$ N/(m/s). An external excitation $f(t)$ acts on the mass m_1; the excitation can be in the form of a random impact series and random excitation. Responses of the two masses in the form of displacements, denoted by $y_1(t)$ and $y_2(t)$, are obtained with a sampling frequency of 1024 Hz by solving the associated set of ordinary differential equations with zero initial conditions:

$$\begin{aligned} m_1\ddot{y}_1(t) + (c_1 + c_2)\dot{y}_1(t) - c_2\dot{y}_2(t) + (k_1 + k_2)y_1(t) - k_2 y_2(t) &= f(t) \\ m_2\ddot{y}_2(t) - c_2\dot{y}_1(t) + (c_2 + c_3)\dot{y}_2(t) - k_2 y_1(t) + (k_2 + k_3)y_2(t) &= 0 \\ y_1(0) = 0,\ \dot{y}_1(0) = 0,\ y_2(0) = 0,\ \dot{y}_2(0) &= 0 \end{aligned} \tag{3.40}$$

where an overdot denotes time differentiation, using the ODE45 solver in MATLAB [75].

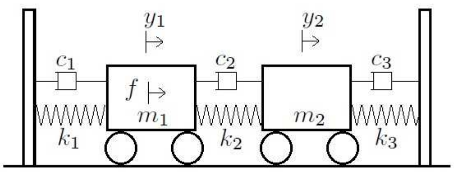

Figure 3.25: A 2-DOF mass-spring-damper system.

Equation (3.40) can be written as

$$\mathbf{M}\ddot{\mathbf{y}} + \mathbf{C}\dot{\mathbf{y}} + \mathbf{K}\mathbf{y} = \mathbf{F} \tag{3.41}$$

where

$$\begin{aligned}
&\mathbf{M} = \begin{bmatrix} m_1 & 0 \\ 0 & m_2 \end{bmatrix}, \mathbf{C} = \begin{bmatrix} c_1 + c_2 & -c_2 \\ -c_2 & c_2 + c_3 \end{bmatrix}, \mathbf{K} = \begin{bmatrix} k_1 + k_2 & -k_2 \\ -k_2 & k_2 + k_3 \end{bmatrix} \\
&\mathbf{y} = \begin{bmatrix} y_1(t) \\ y_2(t) \end{bmatrix}, \mathbf{F} = \begin{bmatrix} f(t) \\ 0 \end{bmatrix}
\end{aligned} \tag{3.42}$$

Analytical FRFs of the system can be derived as

$$\mathbf{H} = \begin{bmatrix} H_{1,1}(s) \\ H_{2,1}(s) \end{bmatrix} = \left[-4\pi^2 s^2 \mathbf{M} + 2\pi \mathrm{j} s \mathbf{C} + \mathbf{K}\right]^{-1} \begin{bmatrix} 1 \\ 0 \end{bmatrix} \tag{3.43}$$

where $\mathrm{j} = \sqrt{-1}$ and $H_{\check{i},\check{j}}(s)$ denotes a FRF between the output point $\check{i}$ and input point $\check{j}$.

Responses of the two masses under a random impact series $f(t)$ with a mean peak amplitude of 30 N and a standard deviation of 10 N are calculated in one sampling period with four sub-sampling periods. The duration of one sub-sampling period is eight seconds; the total duration of the random impact series is 8×3 seconds, and that of the responses is 8×4 seconds. The excitation $f(t)$ and response $y_1(t)$ are shown in Fig. 3.26 (a) and (b), respectively; $y_1(t)$ can be considered to be completely measured, since it has almost decayed to zero at the end of the last sub-sampling period. A FRF $H_{1,1}(s)$ in Eq. (3.26) is calculated using $y_1(t)$ and

$f(t)$ of the whole sampling period. Its amplitude and phase angle are shown in Figs. 3.27 (a) and (b), respectively, which compare well with those of the analytical one in Eq. (3.43). A FRF $H_{1,1}(s)$ in Eq. (3.29) is calculated using $y_1(t)$ and $f(t)$ of the first three sub-sampling periods, and rectangular windows are applied to $y_1(t)$ and $f(t)$ of each sub-sampling period before calculation of their DFTs. The amplitude and phase angle of the resulting FRF are shown in Figs. 3.27 (a) and (b), respectively, which do not compare well with those of the analytical one. The reason is that $y_1(t)$ of one sub-sampling period is not completely measured due to truncation of response and excitation series at the end of the sub-sampling period; the error derives from periodic extension of the DFT on $f(t)$, as discussed in Sec. 2.1. To apply the proposed methodology, pseudo-periodic excitation and response series associated with $y_1(t)$ and $f(t)$ of the sampling period are formed and shown in Figs. 3.27 (c) and (d), respectively. The amplitude and phase angle of $H_{1,1}(s)$ from the proposed methodology are calculated and shown in Figs. 3.27 (a) and (b), respectively, which compare well with those of the analytical one. Note that frequency resolutions of $H_{1,1}(s)$ in Eq. (3.29) and from the proposed methodology are 0.125 Hz, and that in Eq. (3.26) using $y_1(t)$ and $f(t)$ of the whole sampling period is 0.03125 Hz; numbers of spectral lines in the former two FRFs is a fourth of that in the latter. The frequency resolutions here differ because that of a FRF depends on durations of response and excitation series. With a certain sampling frequency, the longer the durations of response and excitation series, the higher the frequency resolution of the FRF and the more the spectral lines needed for DFTs. The conventional coherence function associated with $H_{1,1}(f)$ in Eq. (3.29) using

$y_1(t)$ and $f(t)$ of the first three sub-sampling periods and the extended coherence function associated with $H_{1,1}(f)$ from the proposed methodology in Eq. (3.37) are shown in Figs. 3.28 (a) and (b), respectively, and the fitting index fit associated with the extended coherence function is 99.999%.

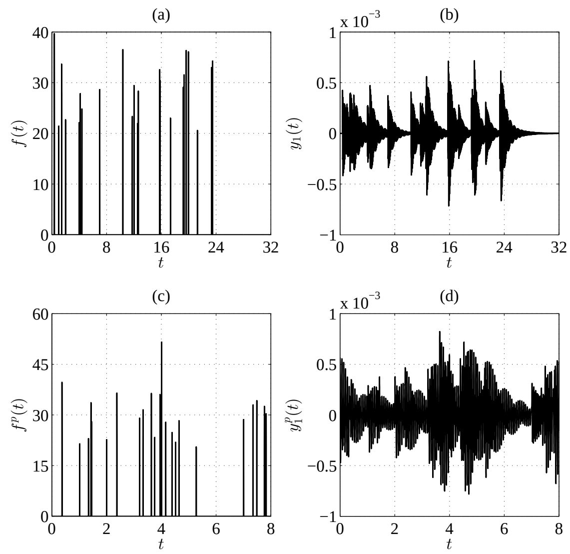

Figure 3.26: (a) Random impact series, (b) the response of m_1 in Fig. 3.25 of one sampling period, (c) the pseudo-periodic excitation series, and (d) the pseudo-periodic response series of m_1 in Fig. 3.25.

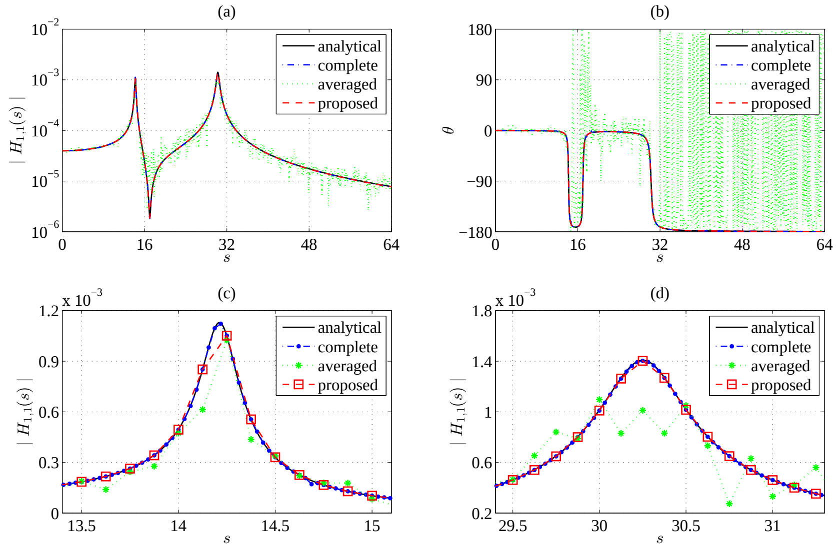

Figure 3.27: (a) Comparison of amplitudes of the analytical $H_{1,1}(s)$ (analytical), $H_{1,1}(s)$ in Eq. (3.26) using $y_1(t)$ and $f(t)$ of the whole sampling period (complete), $H_{1,1}(s)$ in Eq. (3.29) using $y_1(t)$ and $f(t)$ of the first three sub-sampling periods (averaged), and $H_{1,1}(s)$ from the proposed methodology (proposed); (b) comparison of their phase angles; (c) an enlarged view of amplitudes of the above four $H_{1,1}(s)$ in the neighborhood of the first natural frequency of the system; and (d) an enlarged view of amplitudes of the four $H_{1,1}(s)$ in the neighborhood of the second natural frequency of the system.

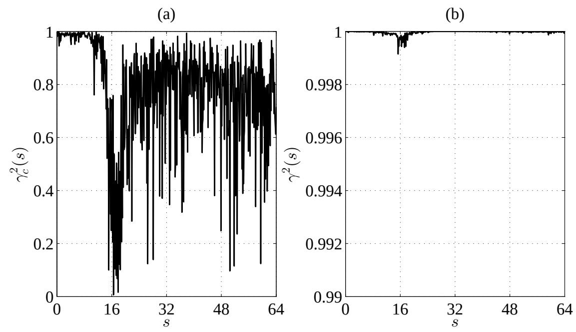

Figure 3.28: (a) Conventional coherence function associated with $H_{1,1}(s)$ in Eq. (3.29) using $y_1(t)$ and $f(t)$ of the first three sub-sampling periods, and (b) the extended coherence function associated with $H_{1,1}(s)$ from the proposed methodology.

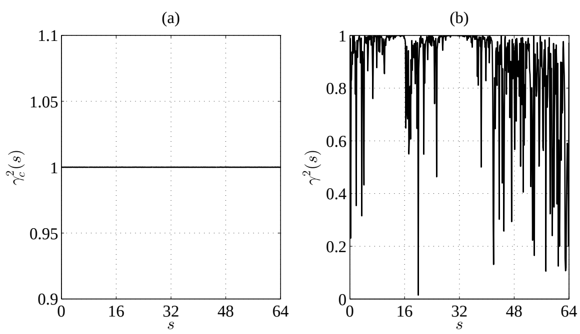

Figure 3.29: (a) Conventional coherence function associated with $H_{1,1}(s)$ in Eq. (3.29) using $y_1(t)$ and $f(t)$ of the first sampling period, and (b) the extended coherence function of $H_{1,1}(s)$ from the proposed methodology using $y_1(t)$ and $f(t)$ of the first sampling period.

IRFs associated with aforementioned FRFs are shown in Fig. 3.30. It can be seen from Fig. 3.30 that the IRFs associated with $H_{1,1}(s)$ in Eq. (3.26) using $y_1(t)$ and $f(t)$ of the whole sampling period and that from the proposed methodology agree well with the IRF associated with the analytical FRF throughout the sub-sampling period. The IRF associated with $H_{1,1}$ in Eq. (3.29) using $y_1(t)$ and $f(t)$ of the first three sub-sampling periods agrees well with that associated with the analytical FRF at the beginning of the sub-sampling period. However, there is larger error after the first second of the sub-sampling period, and the IRF does not decay to zero at the end of the sub-sampling period while the other three almost do. The response $y_1(t)$ and those calculated by convolution between $f(t)$ and the IRFs from different methods are shown in Fig. 3.31. Responses after impacts at $t = 10.4$ s and $t = 15.8$ s are shown in Figs. 3.31 (a) and (b), respectively. Responses calculated by convolution between $f(t)$ and the IRF associated with $H_{1,1}(s)$ in Eq. (3.26) using $y_1(t)$ and $f(t)$ of the whole sampling period and that from the proposed methodology agree well with the actual one, but the response calculated by convolution between $f(t)$ and the IRF associated with $H_{1,1}(s)$ in Eq. (3.29) using $y_1(t)$ and $f(t)$ of the first three sub-sampling periods deviates a little from the actual one. The responses between $t = 28$ s and $t = 32$ s from different methods are shown in Fig. 3.31 (c); that calculated by convolution between $f(t)$ and the IRF associated with $H_{1,1}(s)$ in Eq. (3.29) using $y_1(t)$ and $f(t)$ of the first three sub-sampling periods significantly deviates from the actual one.

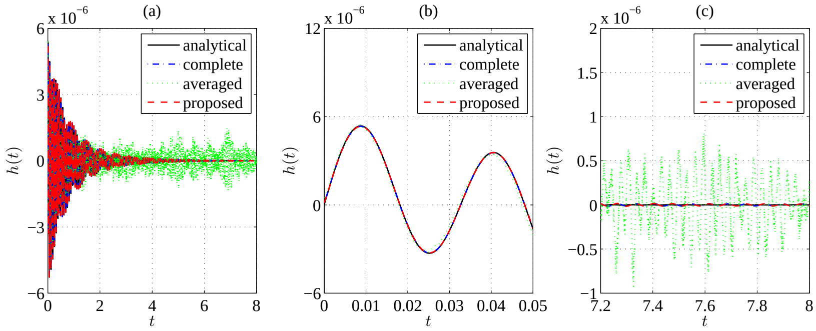

Figure 3.30: (a) Comparison of IRFs from the analytical $H_{1,1}(s)$ (analytical), $H_{1,1}(s)$ in Eq. (3.29) using $y_1(t)$ and $f(t)$ of the whole sampling period (complete), $H_{1,1}(s)$ in Eq. (3.29) using $y_1(t)$ and $f(t)$ of the first three sub-sampling periods (averaged), and $H_{1,1}(s)$ from the proposed methodology (proposed); (b) an enlarged view of the IRFs in the first 0.05 second; and (c) an enlarged view of the IRFs between $t = 7.2$ s and $t = 8$ s.

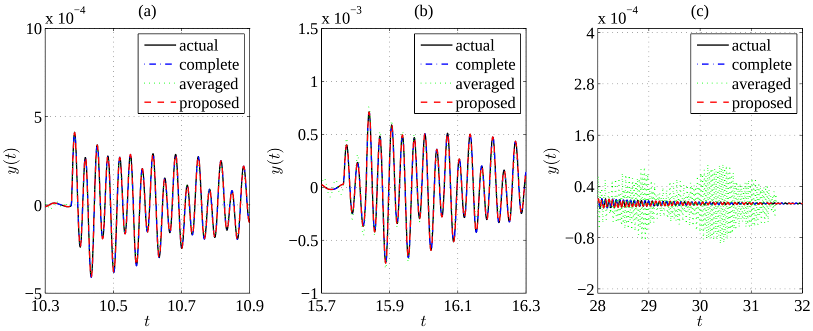

Figure 3.31: Enlarged views of the actual $y_1(t)$ (actual) and calculated ones by convolution between $f(t)$ and IRFs associated with $H_{1,1}(s)$ in Eq. (3.26) using $y_1(t)$ and $f(t)$ of the whole sampling period (complete), $H_{1,1}(s)$ in Eq. (3.29) using $y_1(t)$ and $f(t)$ of the first three sub-sampling periods (averaged), and $H_{1,1}(s)$ from the proposed methodology (proposed) in different time intervals: (a) between $t = 10.3$ s and $t = 10.9$ s, (b) between $t = 15.7$ s and $t = 16.3$ s, and (c) between $t = 28$ s and $t = 32$ s.

Responses of the two masses under zero-mean white-noise excitation with a standard deviation of 100 N are calculated in five sampling periods, and white noise is added to the responses with a SNR of 70 db to simulate measurement noise. Each sampling period has two sub-sampling periods, and the duration of one sub-sampling period is eight seconds. The excitation $f(t)$ and response $y_1(t)$ are shown in Figs. 3.32 (a) and (b), respectively. The response $y_1(t)$ of each sampling period cannot be considered to be completely measured, since it has not decayed to zero at the end of the sampling period due to the artificially added measurement noise. The pseudo-periodic excitation and response series corresponding to $y_1(t)$ and $f(t)$

of the first sampling period are shown in Figs. 3.32 (c) and (d), respectively.

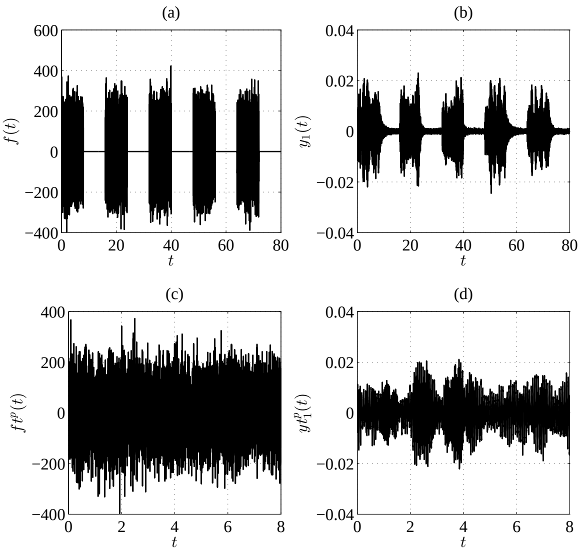

Figure 3.32: (a) Zero-mean white-noise excitation, (b) the response of m_1 in Fig. 3.25 of five sampling periods, (c) the pseudo-periodic excitation of the first sampling period, and (d) the pseudo-periodic response of m_1 in Fig. 3.25 of the first sampling period.

The amplitude and phase angle of $H_{1,1}(s)$ in Eq. (3.29) and from the proposed methodology using $y_1(t)$ and $f(t)$ of the first sampling period are shown in Figs. 3.33 (a) and (b), respectively, which compare well with those of the analytical one in neighborhoods of natural frequencies, as shown in Figs. 3.33 (c) and (d), except at some frequencies where $H_{1,1}(s)$ has low amplitudes due to the measurement noise. Note that the number of spectral lines in the latter is half of that in the former. With $y_1(t)$ and $f(t)$ of the first sampling period, the conventional coherence function associated with $H_{1,1}(s)$ in Eq. (3.29) and the extended coherence function associated with $H_{1,1}(s)$ from the proposed methodology in Eq. (3.37) are shown in Figs. 3.29 (a) and (b), respectively. While there are inaccuracies of $H_{1,1}(s)$ in Eq. (3.29) due to the measurement noise, the conventional coherence function has a value of one at all frequencies. The extended coherence function has low values at frequencies where $H_{1,1}(s)$ from the proposed methodology deviates from the analytical one, and it has values close to one at frequencies where $H_{1,1}(s)$ from the proposed methodology compares well with the analytical one. The fitting index fit associated with $H_{1,1}(s)$ from the proposed methodology is 99.37%.

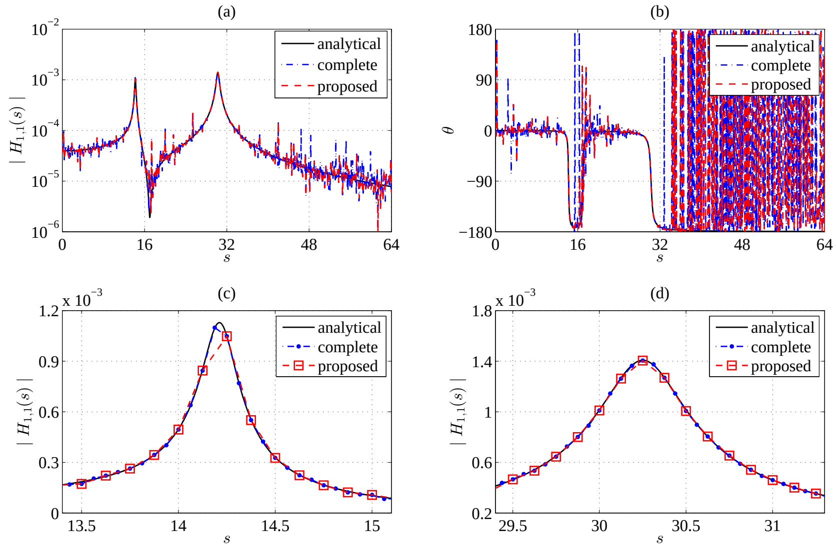

Figure 3.33: (a) Comparison of amplitudes of the analytical $H_{1,1}(s)$ (analytical), $H_{1,1}(s)$ in Eq. (3.26) using $y_1(t)$ and $f(t)$ of the first sampling period (complete), and $H_{1,1}(s)$ from the proposed methodology using $y_1(t)$ and $f(t)$ of the first sampling period (proposed); (b) comparison of their phase angles; (c) an enlarged view of amplitudes of the above three $H_{1,1}(s)$ in the neighborhood of the first natural frequency of the system; and (d) an enlarged view of amplitudes of the three $H_{1,1}(s)$ in the neighborhood of the second natural frequency of the system.

Amplitudes and phase angles of $H_{1,1}(s)$ in Eq. (3.29) and from the proposed methodology using $y_1(t)$ and $f(t)$ of the first two and five sampling periods are shown in Figs. 3.34 and 3.35, respectively. The amplitude and phase of the former compare well with those of the analytical $H_{1,1}(s)$, except at some frequencies where $H_{1,1}(s)$ has low amplitudes due to the measurement noise, which is similar to $H_{1,1}(s)$ using

$y_1(t)$ and $f(t)$ of the first sampling period. The amplitude and phase of the latter compare well with those of the analytical $H_{1,1}(s)$ in a wider frequency range than those of the former. The conventional coherence function associated with $H_{1,1}(s)$ in Eq. (3.29) and the extended coherence function associated with $H_{1,1}(s)$ from the proposed methodology using $y_1(t)$ and $f(t)$ of the first two and five sampling periods are shown in Figs. 3.36 and 3.37, respectively. When the number of sampling periods is larger than one, meaningful conventional coherence function values can be obtained, and their values become more steady with a larger number of sampling periods, which is also the case for the extended coherence function. The fitting indices fit associated with $H_{1,1}(s)$ from the proposed methodology using the first two and five sampling periods are 99.76% and 99.77%, respectively.

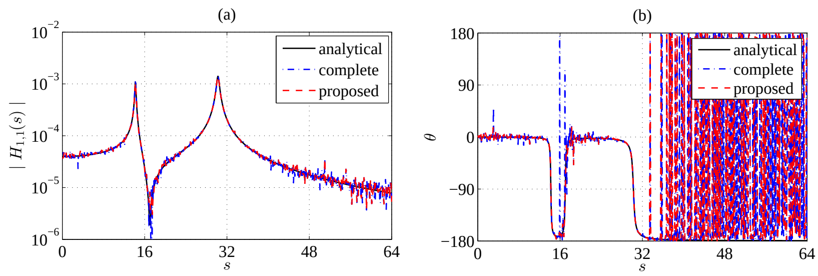

Figure 3.34: (a) Comparison of amplitudes of the analytical $H_{1,1}(s)$ (analytical), $H_{1,1}(s)$ in Eq. (3.29) using $y_1(t)$ and $f(t)$ of the first two sampling periods (complete), and $H_{1,1}(s)$ from the proposed methodology using $y_1(t)$ and $f(t)$ of the first two sampling periods (proposed); and (b) comparison of their phase angles.

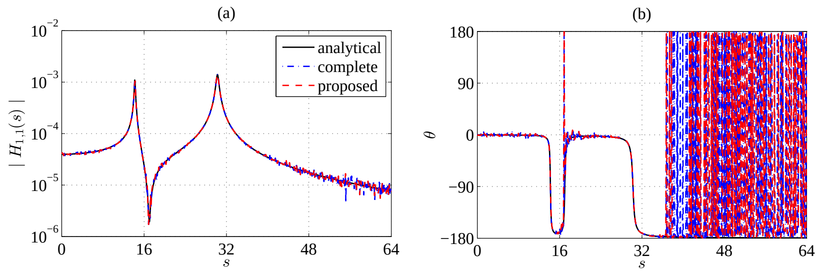

Figure 3.35: (a) Comparison of amplitudes of the analytical $H_{1,1}(s)$ (analytical), $H_{1,1}(s)$ in Eq. (3.29) using $y_1(t)$ and $f(t)$ of the first five sampling periods (complete), and $H_{1,1}(s)$ from the proposed methodology using $y_1(t)$ and $f(t)$ of the first five sampling periods (proposed); and (b) comparison of their phase angles.

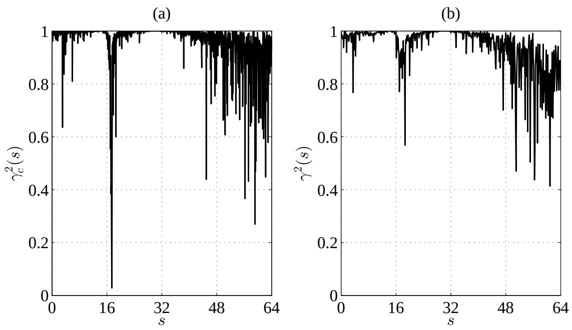

Figure 3.36: (a) Conventional coherence function associatd with $H_{1,1}(s)$ in Eq. (3.29) using $y_1(t)$ and $f(t)$ of the first two sampling periods, and (b) the extended coherence function of $H_{1,1}(s)$ from the proposed methodology using $y_1(t)$ and $f(t)$ of the first two sampling periods.

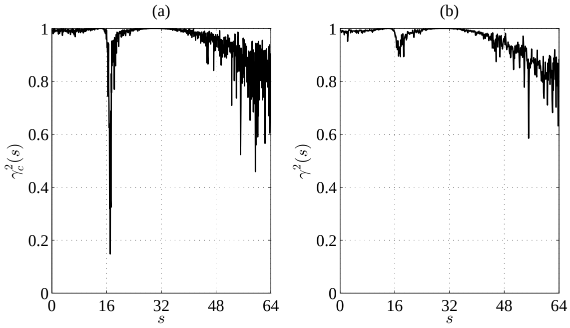

Figure 3.37: (a) Conventional coherence function associated with $H_{1,1}(s)$ in Eq. (3.29) using $y_1(t)$ and $f(t)$ of the first five sampling periods, and (b) the extended coherence function of $H_{1,1}(s)$ from the proposed methodology using $y_1(t)$ and $f(t)$ of the first five sampling periods.

IRFs associated with $H_{1,1}(s)$ in Eq. (3.29) and from the proposed methodology using $y_1(t)$ and $f(t)$ of the first and first five sampling periods are shown in Fig. 3.38 and 3.39, respectively. It can be seen from Fig. 3.38 that IRFs associated with $H_{1,1}(s)$ in Eq. (3.29) and from the proposed methodology compare well with that associated with the analytical $H_{1,1}(s)$ at the beginning of a sub-sampling period, and the former two IRFs deviate from the latter near the end of the sub-sampling period, where the latter has almost decayed to zero. Use of more sampling periods for $H_{1,1}(s)$ can reduce the deviation, as shown in Fig. 3.39, where the deviation of IRFs associated with $H_{1,1}(s)$ in Eq. (3.29) and from the proposed methodology using $y_1(t)$ and $f(t)$ of the first five sampling periods from that associated with the analytical $H_{1,1}(s)$ is much smaller.

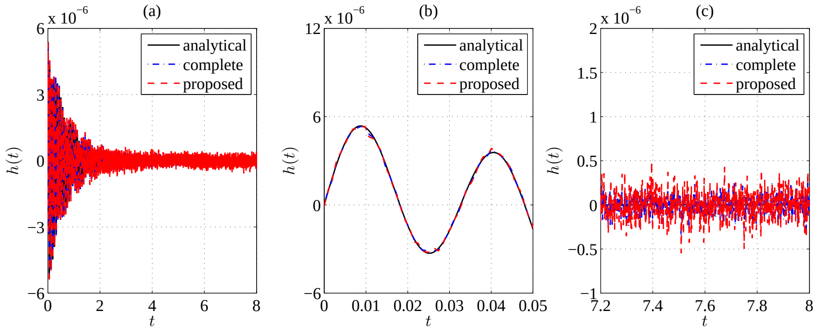

Figure 3.38: (a) Comparison of IRFs from the analytical $H_{1,1}(s)$ (analytical), $H_{1,1}(s)$ in Eq. (3.29) using $y_1(t)$ and $f(t)$ of the first sampling period (complete), and $H_{1,1}(s)$ from the proposed methodology using $y_1(t)$ and $f(t)$ of the first sampling period (proposed); (b) an enlarged view of the IRFs in the first 0.05 second; and (c) an enlarged view of the IRFs between $t = 7.2$ s and $t = 8$ s.

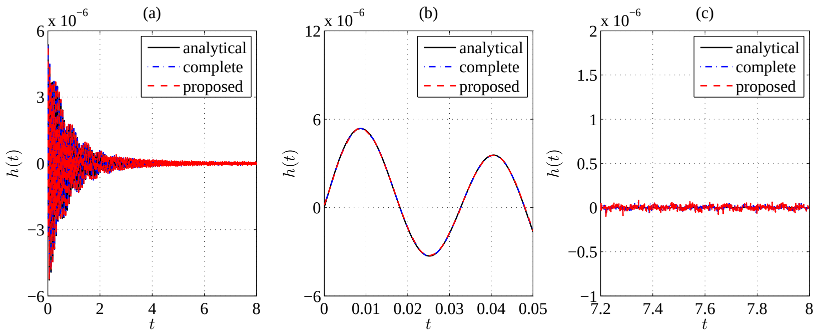

Figure 3.39: (a) Comparison of IRFs from the analytical $H_{1,1}(s)$ (analytical), $H_{1,1}(s)$ in Eq. (3.29) using $y_1(t)$ and $f(t)$ of the first five sampling periods (complete), and $H_{1,1}(s)$ from the proposed methodology using $y_1(t)$ and $f(t)$ of the first five sampling periods (proposed); (b) an enlarged view of the IRFs in the first 0.05 second; and (c) an enlarged view of the IRFs between $t = 7.2$ s and $t = 8$ s.

3.2.3.2 Experimental Example

EMA was conducted on an aluminum plate to measure a FRF associated with its out-of-plane vibration modes and its associated IRF. The plate had a length of 608 mm, width of 612 mm, and thickness of 4.3 mm. The test setup is shown in Fig. 3.40: the plate was hung using a nylon cord to simulate its free boundary conditions, and a PCB impact hammer and a PCB accelerometer were used to manually generate a random impact series, denoted by $f(t)$, at an excitation point and measure the response of a measurement point in the form of acceleration, denoted by $\ddot{z}(t)$, respectively. The hammer and accelerometer were connected to a LMS spectrum analyzer with the software LMS Test.Lab Rev. 9b [77]. Measured $f(t)$ and $\ddot{z}(t)$ of five sampling periods were obtained in the measurement period, and the measured frequency range was from 0 to 512 Hz with a sampling frequency of 1024 Hz. There were three sub-sampling periods in one sampling period, and the duration of one sub-sampling period was 32 seconds. The duration of a sampling period and that of the measurement period were 32×3 and $32 \times 3 \times 5$ seconds, respectively. Time histories of $f(t)$ and $\ddot{z}(t)$ of the five sampling periods are shown in Figs. 3.41 (a) and (b), respectively.

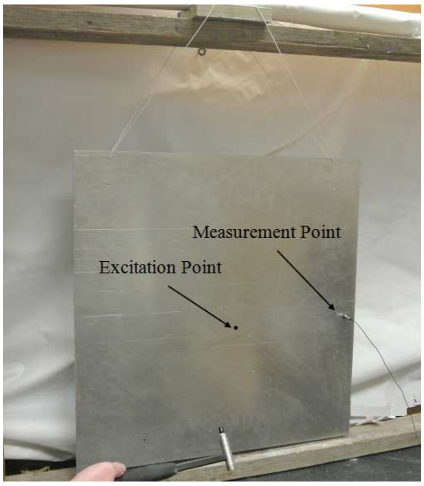

Figure 3.40: Test setup of EMA on an aluminum plate.

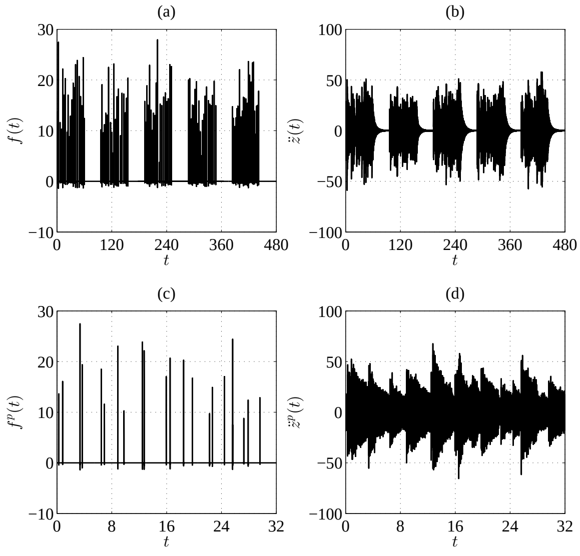

Figure 3.41: (a) Random impact series manually generated at the excitation point on the plate in Fig. 3.40, (b) the response of the measurement point on the plate in Fig. 3.40, (c) the pseudo-periodic excitation of the first sampling period, and (d) the pseudo-periodic response of the measurement point of the first sampling period.

FRFs in Eq. (3.29) and from the proposed methodology using $\ddot{z}(t)$ and $f(t)$ of the first, first two, and first five sampling periods were shown in Figs. 3.42 through 3.44, respectively. Note that the number of spectral lines in the latter is a third of that in the former. A FRF from a single impact test with the same excitation and measurement points as those in Fig. 3.40 was measured, which served as a benchmark FRF for comparison purposes. It can be seen that FRFs in Eq. (3.29) and from the proposed methodology using $\ddot{z}(t)$ and $f(t)$ of more sampling periods compared better with the benchmark one. For same numbers of sampling periods, FRFs from the proposed methodology are almost identical to those in Eq. (3.29), but the latter requires more spectral lines for DFT calculation. The conventional and extended coherence functions associated with the FRFs in Eq. (3.29) and from the proposed methodology, respectively, using $\ddot{z}(t)$ and $f(t)$ of the first sampling period were shown in Figs. 3.45 (a) and (b), respectively. The extended coherence function had meaningful values, but the conventional one had a value of one at all frequencies. The fitting index fit associated with the FRF from the proposed methodology using $\ddot{z}(t)$ and $f(t)$ of the first sampling period was 88.18%. Note that values of the extended coherence function at some frequencies and fit associated with the FRF from the proposed methodology were relatively low mainly because the random impact series was manually generated and points that were impacted on the plate could slightly deviate from the assigned excitation point in Fig. 3.40. Use of a random impact device can provide a random impact series with consistent impacted points and improve values of the extended coherence function and fit. The conventional and extended coherence functions using $\ddot{z}(t)$ and $f(t)$ of the first two and five sampling periods are shown in Figs. 3.46 and 3.47, respectively, and fit associated with the first two and five sampling periods were 96.97% and 97.24%, respectively, which indicated that the measured FRFs using $\ddot{z}(t)$ and $f(t)$ of more sampling periods were more accurate. The simulated boundary conditions could be considered to be free, since the highest natural frequency associated with rigid-body modes was 4.53 Hz, which was about 10% of the natural frequency of the first out-of-plane mode of the plate (44.5 Hz).

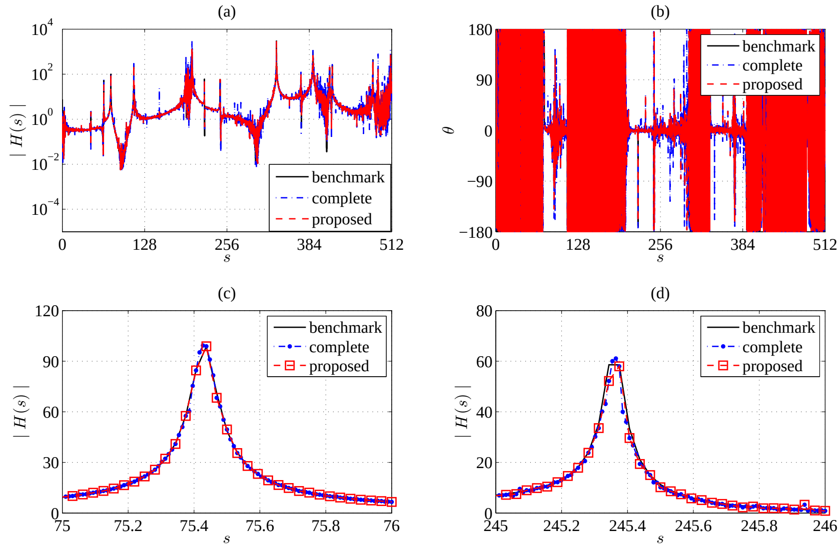

Figure 3.42: (a) Comparison of amplitudes of a FRF from a single impact test (benchmark), that in Eq. (3.29) using $\ddot{z}(t)$ and $f(t)$ of the first sampling period (complete), and that from the proposed methodology using $\ddot{z}(t)$ and $f(t)$ of the first sampling period (proposed); (b) comparison of their phase angles; (c) an enlarged view of amplitudes of the FRFs between 75 and 76 Hz; and (d) an enlarged view of amplitudes of the FRFs between 245 and 246 Hz.

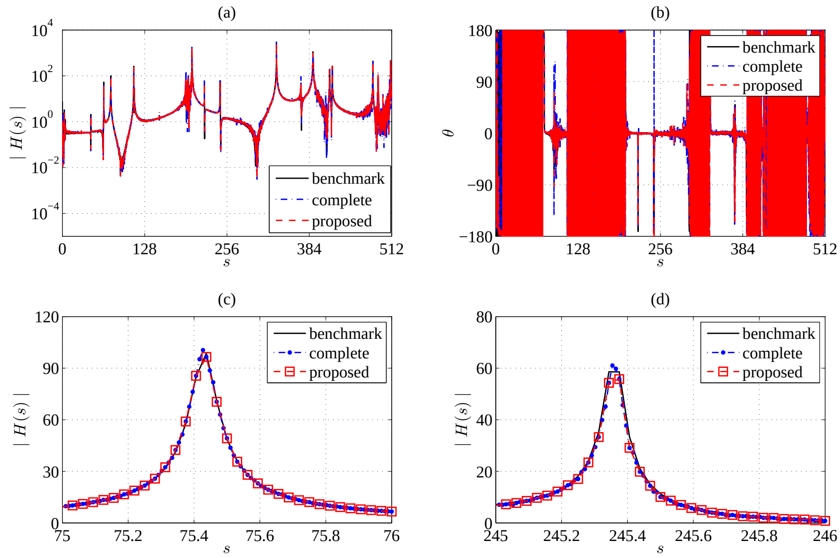

Figure 3.43: (a) Comparison of amplitudes of a FRF from a single impact test (benchmark), that in Eq. (3.29) using $\ddot{z}(t)$ and $f(t)$ of the first two sampling periods (complete), and that from the proposed methodology using $\ddot{z}(t)$ and $f(t)$ of the first two sampling periods (proposed); (b) comparison of their phase angles; (c) an enlarged view of amplitudes of the FRFs between 75 and 76 Hz, and (d) an enlarged view of amplitudes of the FRFs between 245 and 246 Hz.

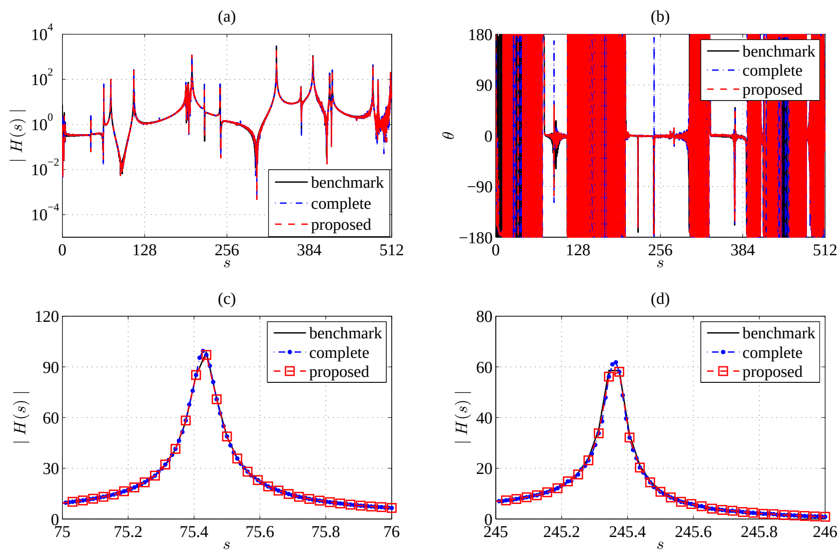

Figure 3.44: (a) Comparison of amplitudes of a FRF from a single impact test (benchmark), that in Eq. (3.29) using $\ddot{z}(t)$ and $f(t)$ of the first five sampling periods (complete), and that from the proposed methodology using $\ddot{z}(t)$ and $f(t)$ of the first five sampling periods (proposed); (b) comparison of their phase angles; (c) an enlarged view of amplitudes of the FRFs between 75 and 76 Hz, and (d) an enlarged view of amplitudes of the FRFs between 245 and 246 Hz.

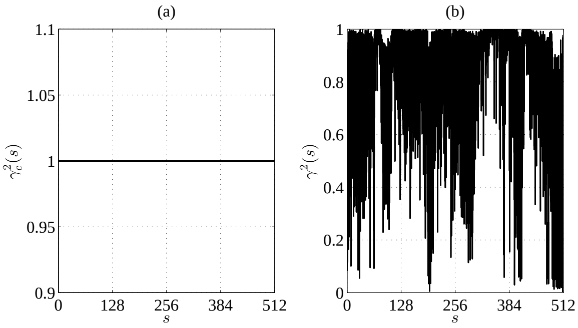

Figure 3.45: (a) Conventional coherence function associated with the FRF in Eq. (3.29) using $\ddot{z}(t)$ and $f(t)$ of the first sampling period, and (b) the extended coherence function associated with the FRF from the proposed methodology using $\ddot{z}(t)$ and $f(t)$ of the first sampling period.

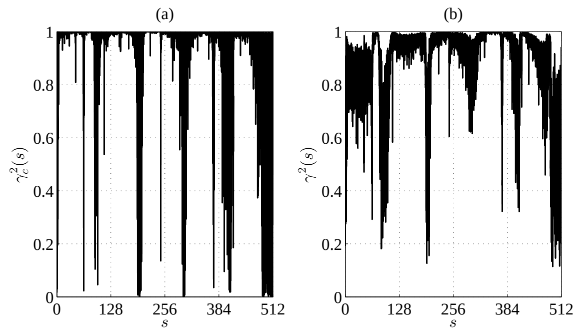

Figure 3.46: (a) Conventional coherence function associated with the FRF in Eq. (3.29) using $\ddot{z}(t)$ and $f(t)$ of the first two sampling periods, and (b) the extended coherence function associated with the FRF from the proposed methodology using $\ddot{z}(t)$ and $f(t)$ of the first two sampling periods.

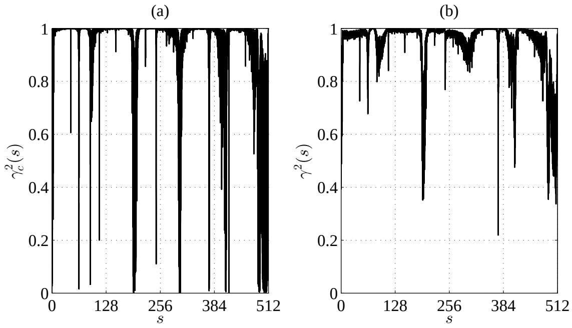

Figure 3.47: (a) Conventional coherence function associated with the FRF in Eq. (3.29) using $\ddot{z}(t)$ and $f(t)$ of the first five sampling periods, and (b) the extended coherence function associated with the FRF from the proposed methodology using $\ddot{z}(t)$ and $f(t)$ of the first five sampling periods.

IRFs associated with the FRFs in Eq. (3.29) and from the proposed methodology using $\ddot{z}(t)$ and $f(t)$ of the first and first five sampling periods were calculated and compared with that associated with the benchmark FRFs in different time intervals in Figs. 3.48 and 3.49, respectively. It can be seen from Fig. 3.48 that the IRFs associated with the FRFs in Eq. (3.29) and from the proposed methodology agreed well with that associated with the benchmark FRF at the beginning of the sub-sampling period, and the former two IRFs deviated from the latter near the end of the sub-sampling period, where the latter had almost decayed to zero. The IRFs associated with the FRFs in Eq. (3.29) and from the proposed methodology that use $\ddot{z}(t)$ and $f(t)$ of the first five sampling periods compared better with that associated with the benchmark FRF. Measured $\ddot{z}(t)$ and those obtained by convolution between $f(t)$ and the IRFs from the two methodologies using $\ddot{z}(t)$ and $f(t)$ of the first five sampling periods are shown in Fig. 3.50. The measured and calculated $\ddot{z}(t)$ after impacts at $t = 43.98$ s and $t = 220.22$ s are shown in Figs. 3.50 (a) and (b), respectively; those between $t = 257.68$ s and $t = 257.74$ s are shown in Fig. 3.50 (c). It can be seen that the calculated $\ddot{z}(t)$ associated with the FRFs in Eq. (3.29) and from the proposed methodology compared well with the measured one.

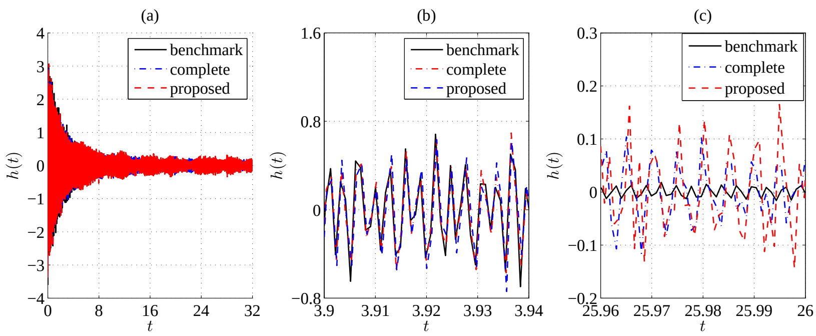

Figure 3.48: (a) Comparison of IRFs associated with a FRF from a single impact test (benchmark), that in Eq. (3.29) using $\ddot{z}(t)$ and $f(t)$ of the first sampling period (complete), and that from the proposed methodology using $\ddot{z}(t)$ and $f(t)$ of the first sampling period (proposed); (b) an enlarged view of the IRFs between $t = 3.9$ s and $t = 3.94$ s; and (c) an enlarged view of the IRFs between $t = 25.96$ s and $t = 26$ s.

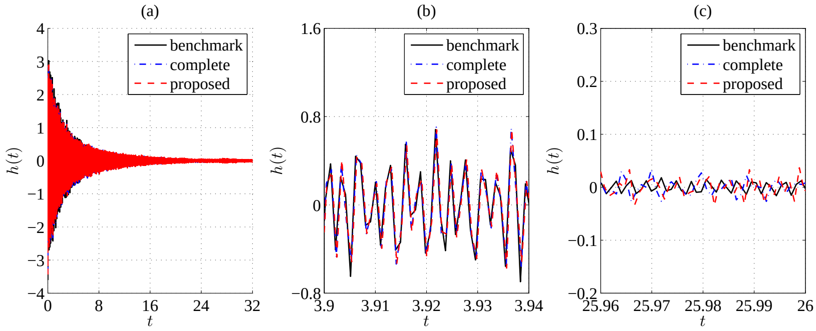

Figure 3.49: (a) Comparison of IRFs associated with a FRF from a single impact test (benchmark), that in Eq. (3.29) using $\ddot{z}(t)$ and $f(t)$ of the first five sampling periods (complete), and that from the proposed methodology using $\ddot{z}(t)$ and $f(t)$ of the first five sampling periods (proposed); (b) an enlarged view of the IRFs between $t = 3.9$ s and $t = 3.94$ s; and (c) an enlarged view of the IRFs between $t = 25.96$ s and $t = 26$ s.

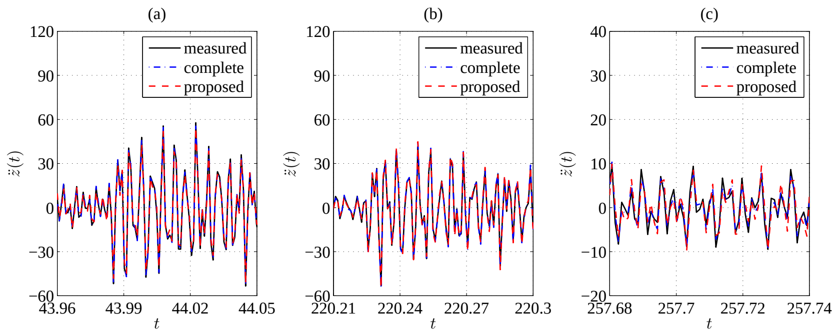

Figure 3.50: Enlarged views of the measured $\ddot{z}(t)$ (measured) and calculated ones by convolution between $f(t)$ and IRFs associated with the FRFs in Eq. (3.29) using $\ddot{z}(t)$ and $f(t)$ of the first five sampling periods (complete) and from the proposed methodology using $\ddot{z}(t)$ and $f(t)$ of the first five sampling periods (proposed) in different time intervals: (a) between $t = 43.96$ s and $t = 44.05$ s, (b) between $t = 220.21$ s and $t = 220.30$ s, and (c) between $t = 257.68$ s and $t = 257.71$ s.

3.2.4 Conclusion

An efficient and accurate methodology for calculating discrete FRFs and IRFs is proposed. Excitation and response measurements in the proposed methodology are similar to those in EMA using burst random excitation. The methodology is computationally efficient, since matrix inversion can be avoided and calculation time can be greatly shortened due to use of the FFT and IFFT. Data lengths of excitation and response series in calculation of FRFs and associated IRFs in the proposed methodology are shortened by a factor of the number of sub-sampling periods in one sampling period due to use of pseudo-periodic excitation and response series;

fewer spectral lines are needed in calculation of associated DFTs, and accuracies of resulting FRFs and IRFs from the proposed methodology can be maintained, compared with those by directly applying the DFT to excitation and response series, which need more spectral lines. The relationship between an IRF from the proposed methodology and that from the LS method is shown. The linear equation associated with the proposed method has a smaller number of rows than that associated with the LS method, and IRFs from the two linear equations are very close to each other in one sub-sampling period. Meaningful coherence function values associated with FRFs from the proposed methodology can be obtained using the extended coherence function even when response and excitation series of only one sampling period are available. FRFs and IRFs from the proposed methodology in the numerical simulation are as accurate as those directly using completely measured excitation and response series. The FRF and its associated IRF from the proposed methodology in the experimental example agreed well with the benchmark ones from a single impact test. Excitation and response series of more sampling periods can lead to more accurate FRF and IRF estimations from the proposed methodology, based on the extended coherence function and fitting index.

Chapter 4

STRUCTURAL DAMAGE IDENTIFICATION FOR BEAM AND PLATE STRUCTURES

4.1 Identification of Embedded Horizontal Cracks in Beams Using Measured Mode Shapes

4.1.1 Introduction

Vibration-based damage detection has become one of major research topics in the application of structural dynamics in the past few decades. Various methodologies have been developed to detect, locate, and characterize damage in structures based on vibration measurements, since physical properties of a structure, such as mass, stiffness, and damping, directly determine modal characteristics of the structure, i.e., natural frequencies, MSs, and modal damping ratios [7]. One criterion to categorize the methodologies is whether a model of the structure being monitored is needed. If it is needed, the methodology is model-based; otherwise, it is non-model-based. Model-based methods are capable of detecting locations and extent of damage in structures with a minimum amount of measurements information [81, 82, 83].

Model-based methods could have problems due to inaccuracy of models, environmental and other non-stationary effects on measurements, and lack of measurement data in certain frequency ranges [81]. In practice, it is difficult to construct models of most existing structures with high accuracy. Hence, methods that only analyze measured MSs or ODSs of a structure without the aid of a model can be good alternatives to model-based methods to locate damage, and they are non-model-based ones [84]. Since MSs are not sensitive to damage of small extent, curvatures of MSs, referred to as CMSs, are used to locate damage [85]. A global trend of a CMS of a beam can be observed, and one needs to isolate the features caused by damage from the trend in order to localize the damage. Differences between CMSs of a damaged beam and those of an undamaged one are localized in a damage region and increase as the damage size increases [86]. A gapped-smoothing method was used to locate delamination in a composite beam by inspecting smoothnesses of CMSs [87], and the method was extended to use broad-band ODS data [88]; for each measurement point to be inspected, a gapped cubic polynomial fitting the CMSs or curvatures of ODSs at its four neighboring points was used to eliminate trends at the point, which is a local method and can be computationally inefficient for a dense measurement grid. The gapped-smoothing method was extended to locate damage in a beam using a global fitting method, where generic MSs were used to fit measured MSs of a damaged beam [89], and the global fitting method was extended to ODS data for damage detection on beams and plates [90]. However, the generic MSs require a priori knowledge of test structures that may not be available in practice. A crucial aspect of damage detection methods using CMSs is calculation of derivatives of MSs. Optimal spatial sampling intervals were proposed for CMSs to avoid undersampling and oversampling of MS measurements, both of which have adverse effects on damage detection quality [91]. A novel Laplacian scheme was developed and experimentally validated in Ref. [92] to locate a delamination zone in a composite beam using associated modal curvatures with multiple resolutions, where a local method was applied to eliminate trends of the resulting modal curvatures. Besides CMSs, wavelet transforms of MSs can also be used in damage detection, since they are sensitive to localized abnormalities in MSs and can be presented with multiple scales. Cracks were identified in beams using a "symmetrical 4" wavelet function; the position of a crack was accurately detected with the aid of a beam model [93]. Damage in the forms of cracks in beams and thickness reductions in plates was identified using CWT, which was manifested as peaks in associated CWT coefficients [94]. However, the selections of the wavelet functions there failed to reflect the physical meanings of the resulting CWTs of MSs. While CWTs of differences between MSs of a damaged beam and those of the associated undamaged one can be used to locate cracks with high sensitivities [95], MSs of an undamaged beam are not always available in practice.

Beams with horizontal embedded cracks are studied in this work; they are similar to composite beams with delaminations. Natural frequencies of beams and plates will decrease if delaminations occur; the larger a delamination, the larger the reductions of the natural frequencies [96]. Free vibration analysis of a laminated beam was studied using a layerwise theory in Ref. [97]. Effects of the lamination angle, location, and size, and the number of delaminations on natural frequencies of beams were addressed there. A generalized variational principle was used to formulate equations of motion and associated boundary conditions for the free vibration of a delaminated composite beam; the coupling effect of longitudinal and bending vibrations was shown to be significant for the calculated natural frequencies and MSs [98]. Modal tests were conducted in Ref. [99] using polyvinylidene fluoride film sensors and piezoceramic patches with sine sweep actuation; backpropagation neural network models were developed using results from the beam theory and used to predict a delamination size. A spatial wavelet analysis was used in Ref. [100] to process static deformation profiles of cantilever beams to numerically and experimentally locate delaminations; deformation profiles from dense measurements were smoothed before applying the spatial wavelet analysis.

In this work, two non-model-based methods are proposed to identify embedded horizontal cracks in beams without use of any a priori information of associated undamaged beams, if the beams are geometrically smooth and made of materials that have no stiffness discontinuities. CMSs are presented with multiple resolutions to alleviate adverse effects of measurement noise. The relationship between CWTs of MSs and CMSs is shown. MSs from polynomials of MS-dependent orders, which fit those of a damaged beam, can well approximate MSs of the associated undamaged one; the MSs of the damaged beam are virtually extended beforehand, beyond boundaries of the beam, in order to improve the approximation of the CMSs from the resulting polynomial fits to those of the associated undamaged one near the boundaries. Differences between MSs of the damaged beam and those from the resulting polynomial fits are used to yield two damage indices: the curvature damage index (CDI) and the CWT damage index (CWTDI) with a Gaussian wavelet function. Superior over the existing methods that locally eliminate trends in resulting

CMSs and CWTs of MSs, the proposed methods apply a global trend elimination technique that can greatly reduce computational costs, especially for cases where multiple resolutions and scales are used to calculate CMSs and CWTs of MSs with dense measurement grids, respectively; physical interpretations of CWTDIs are provided.

A uniform cantilever beam made of acrylonitrile butadiene styrene (ABS) with an embedded horizontal crack is constructed, and its natural frequencies and MSs are measured using non-contact OMA. The crack tips can be successfully located using the two proposed damage indices; they are located near peaks of CDIs and CWTDIs with the second-order Gaussian wavelet function, and valleys of CWTDIs with the third-order Gaussian wavelet function. While the proposed methods are used to identify embedded horizontal cracks in this work, they can be used to identify edge cracks, slant cracks, and delaminations, and extended to other types of structures, such as plate structures.

4.1.2 Crack Identification Using CDIs and CWTDIs

A FE model of a cantilever beam made of steel with a mass density $\rho = 7800$ kg/m^3, an elastic modulus $E = 210$ GPa, and Poisson's ratio $\mu = 0.3$, with an embedded horizontal crack, is constructed using commercial FE software. The dimensions of the beam and crack and the FE model of the damaged beam are shown in Figs. 4.1 (a) and (b), respectively. An analytical model of the undamaged beam with the same material properties and dimensions as the damaged one is also constructed for comparison purposes. MSs of the damaged and undamaged beams, denoted by f^d and f^u, respectively, are used to illustrate the proposed methods. The j-th MSs of the damaged and undamaged beams are denoted by $f^{d,j}$ and $f^{u,j}$, respectively, and the MSs are normalized so that their maximum absolute values are one. White noise is added to the MSs with a signal-to-noise ratio (SNR) of 60 to simulate measurement noise.

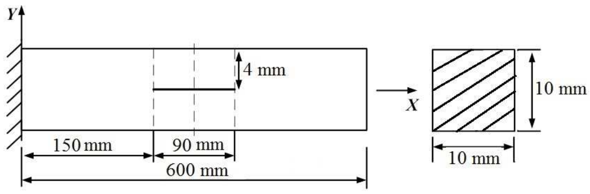

(a)

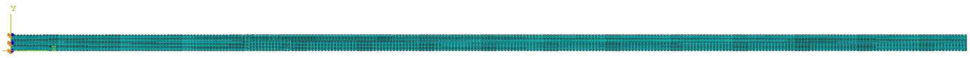

(b)

Figure 4.1: (a) Dimensions of a cantilever beam with an embedded horizontal crack, and (b) the FE model of the damaged beam.

4.1.2.1 CMS

A CMS is the second-order derivative of a MS. It can be used to identify damage because abnormalities in CMSs are localized in damage regions [86] and can be manifested by the gapped-smoothing method [87, 88]. Assuming the measurement points are equally spaced, the CMS at a measurement point i can be calculated from the MS, denoted by f, using the central finite difference scheme of second-order accuracy:

$$f_i'' = C_i = \frac{f_{i-1} - 2f_i + f_{i+1}}{h^2} \tag{4.1}$$

where a prime denotes first-order spatial differentiation, f_i is the MS at the measurement point i, and h is the distance between two neighbouring measurement points. The gapped-smoothing method assumes that the CMSs are smooth in undamaged regions and unsmooth elsewhere, which implies that the structure being inspected is geometrically smooth and made of materials that have no stiffness discontinuities; such an assumption applies throughout this work. A crucial aspect of the gapped-smoothing method is that the minimum size of identifiable damage is determined by the density of the measurement grid since the effects of damage on CMSs are localized. Hence, a dense measurement grid becomes necessary to identify damage of a small size. However, measurement noise of MSs will become dominant in the resulting CMSs with a dense measurement grid, since the difference between noise-free MSs at two neighbouring measurement points is small compared with that between noisy MSs at the two points. Figure 4.2(a) shows that measurement noise is amplified when the CMSs are calculated using Eq. (4.1), and they cannot be used to identify damage.

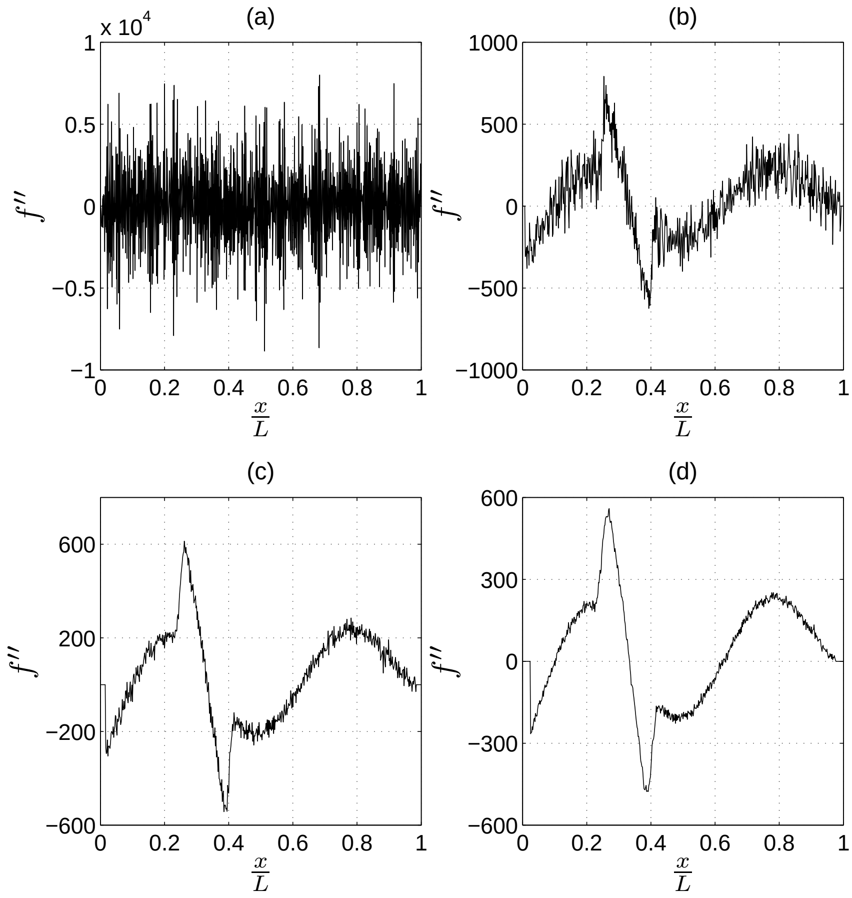

Figure 4.2: (a) CMS of the fourth mode of the damaged beam from Eq. (4.1), and those of the mode with different m values: (b) $m = 5$, (c) $m = 10$, and (d) $m = 15$.

In order to reduce the adverse effects of measurement noise, the central finite difference scheme in Eq. (4.1) is modified to be

$$f_i'' = C_i^m = \frac{f_{i-m} - 2f_i + f_{i+m}}{(mh)^2} \tag{4.2}$$

where m is the number of measurement points from point i to either end of the derivative interval, which determines the width of the derivative interval and the resolution of the resulting derivative. This formulation is similar to the *á trous* Laplacian operator in Ref. [92], and enables observation of CMSs with different resolutions: the lower the value of m, the higher the resolution of the resulting derivative. Note that Eq. (4.1) is the case with $m = 1$. Figures 4.2 (b) through (d) show that $\left(f^{d,4}\right)''$ can be obtained with a lower noise level with a larger m values. It can be seen from Figs. 4.2 (b) through (d) that while the CMSs at a same point slightly vary for different m, the singularities of the CMSs near the crack tips are retained. In practice, a suitable value of m can be obtained by increasing it from one until CMSs with a low noise level are observed.

4.1.2.2 CWT

A linear transformation is defined by

$$W_w f(u, s) = \int_{-\infty}^{+\infty} f(x) w^*_{u,s}(x) dx \tag{4.3}$$

where W_w denotes the linear transformation operator with the weight function

$$w_{u,s}(x) = \frac{1}{\sqrt{s}} w\left(\frac{x-u}{s}\right) \tag{4.4}$$

in which u and s are spatial and scale parameters of the weight function, respectively, and the superscript * denotes complex conjugation. In this work, the weight function is defined in the real domain, and the superscript * can be dropped. When the weight function is a wavelet function ψ, the transformation in Eq. (4.3) becomes a CWT [101]. The wavelet function ψ has a zero average, i.e.,

$$\int_{-\infty}^{+\infty} \psi(x)dx = 0 \quad (4.5)$$

and $W_\psi f(u,s)$ measures the variation of $f(x)$ in the neighbourhood centered at u with an interval size proportional to s. The L^2-norm of $\psi(x)$ is one, i.e.,

$$\|\psi\|_2 = \left(\int_{-\infty}^{+\infty} |\psi(x)|^2 \, dx\right)^{\frac{1}{2}} = 1 \quad (4.6)$$

The CWT can be considered as a convolution:

$$W_\psi f = \frac{1}{\sqrt{s}} \int_{-\infty}^{+\infty} f(x)\bar{\psi}(\frac{u-x}{s})dx = f \star \bar{\psi} \quad (4.7)$$

where an overbar denotes function reflection over the y-axis, i.e., $\bar{\psi}(x) = \psi(-x)$, and the symbol $\star$ denotes convolution.

In this work, a p-th-order ($p \geqslant 1$) Gaussian wavelet function, denoted by $g^p(x)$, is used as the wavelet function, since it is smooth and differentiable, and can capture local changes in a transformed function [102]. Gaussian wavelet functions are derived from the Gaussian function $g^0(x)$ with a unit L^2-norm:

$$g^0(x) = \sqrt[4]{\frac{2}{\pi}} e^{-x^2} \quad (4.8)$$

The p-th-order Gaussian wavelet function can be written as

$$g^p(x) = C_p \left[g^0(x)\right]^{(p)} \quad (4.9)$$

where C_p is a constant such that $g^p(x)$ has a unit L^2-norm. The relationship between $\bar{g}^q(x)$ and $\bar{g}^{p+q}(x)$ can be expressed by

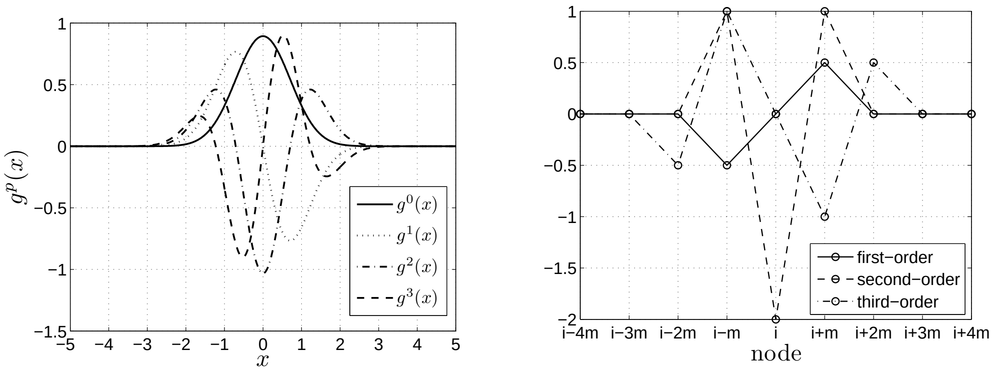

(a) (b)

Figure 4.3: (a) The Gaussian function $g^0(x)$ and the first- through third-order Gaussian wavelet functions, and (b) the finite difference coefficients of the central finite difference scheme of second-order accuracy for the first- through third-order derivatives.

$$\frac{d^p \bar{g}^q}{dx^p} = \frac{C_q}{C_{p+q}\,(-1)^p}\bar{g}^{p+q} \tag{4.10}$$

The Gaussian function $g^0(x)$ and the Gaussian wavelet functions of orders one through three are shown in Fig. 4.3(a).

Due to the commutative property of the convolution, i.e., $f \star \bar{\psi} = \bar{\psi} \star f$, a differentiation operation on $W_\psi f$ with respect to u can be expressed by

$$\frac{\partial^q}{\partial u^q} W_\psi f = f \star \bar{\psi}^{(q)} = \bar{\psi} \star f^{(q)} = f^{(q)} \star \bar{\psi} \tag{4.11}$$

Equation (4.11) shows that the differentiation operation on $\bar{\psi}$ in the CWT can be transferred onto f if $\bar{\psi}$ is differentiable. Hence, the variation of f'' can be measured without calculating f'':

$$W_\psi f'' = f'' \star \bar{\psi} = f \star \bar{\psi}'' \tag{4.12}$$

and the CWT can be used to inspect the variation of f'' and identify damage, which can reduce the adverse effects of measurement noise on $f(x)$. Similarly, when the $(p+q)$-th-order Gaussian wavelet function is used in the CWT, one has [102]

$$W_{g^{p+q}} f = f \star \bar{g}_{u,s}^{p+q} = \frac{C_q}{C_{p+q}(-s)^p} f^{(p)} \star \bar{g}_{u,s}^{q} = \frac{C_q}{C_{p+q} s^p} W_{(-1)^p g^q} f^{(p)} \tag{4.13}$$

When $q = 0$, Eq. (4.13) becomes

$$W_{g^p} f \;\; = \;\; = \frac{C_0}{C_p s^p} W_{(-1)^p g^0} f^{(p)} = \frac{C_0}{C_p s^p} W_{g^0} \left[(-1)^p f^{(p)} \right] \tag{4.14}$$

Equation (4.14) shows that the CWT of f with the p-th order Gaussian wavelet function has the same shape as the linear transformation of $(-1)^p f^{(p)}$ with the weight function g^0, and they differ by a factor $\frac{C_0}{C_p s^p}$. The linear transformation of f with the weight function g^0 is equivalent to applying a Gaussian filter g^0 to f, which smoothes the shape of f. Hence, $W_{g^p} f$ yields the smoothed shape of $(-1)^p f^{(p)}$. Figure 4.3(b) shows the finite difference coefficients of the central finite difference scheme of second-order accuracy for the first- through third-order derivatives. Note that the coefficients should be divided by $(mh)^k$, where k is the order of a derivative. It can be observed that the plot of the coefficients of the p-th-order derivative in Fig. 4.3(b) resembles that of $(-1)^p g^p(x)$ in Fig. 4.3(a); the latter is smoother than the former, and they have the same numbers of vanishing moments.

The CWTs of $f^{d,4}$ with wavelet functions $g^2(x)$ and $g^3(x)$ with different scales are shown in Figs. 4.5 and 4.4, respectively. In Figs. 4.5 (b) through (d), the shapes of the CWTs resemble those of the CMSs shown in Figs. 4.2 (b) through (d), where the two peaks are caused by the two crack tips. However, the peaks caused by the crack tips cannot be found in the case with the wavelet function $g^3(x)$, as shown in Fig. 4.4, where the CWT coefficients are zero near the crack tips, which can be explained by using Eq. (4.13):

$$W_{g^2} f = f \star \bar{g}^2_{u,s} = \frac{C_0}{C_2 s^2} f'' \star \bar{g}^0_{u,s} \tag{4.15}$$

$$W_{g^3} f = f \star \bar{g}^3_{u,s} = \frac{C_1}{C_3 s^2} f'' \star \bar{g}^1_{u,s} = -\frac{C_0}{C_3 s^3} f''' \star \bar{g}^0_{u,s} \tag{4.16}$$

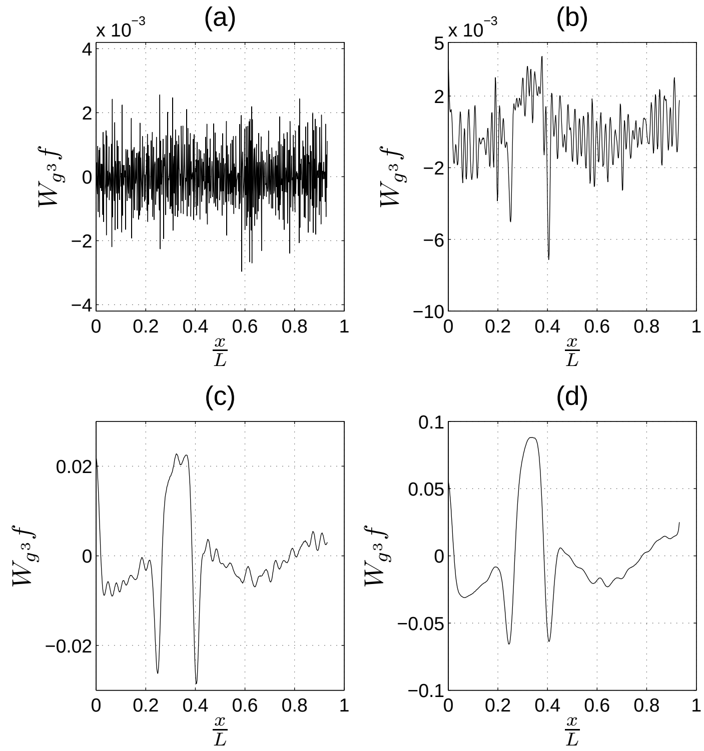

Figure 4.4: CWTs of the fourth measured MS of the damaged beam with the wavelet function $g^3(x)$ with different scales: (a) $s = 1$, (b) $s = 5$, (c) $s = 10$, and (d) $s = 15$.

The CWTs of f with wavelet functions $g^2_{u,s}(x)$ and $g^3_{u,s}(x)$ have the same shapes as the linear transformations of f'' and f''' with wavelet functions $g^0_{u,s}(x)$ and $-g^0_{u,s}(x)$, respectively. Since f''' is the derivative of f'', $f''' = 0$ at local extrema of f''. Hence, the crack tips are located in the neighbourhoods of zero values of the CWTs of f with the wavelet function $g^3(x)$, rather than their peak values.

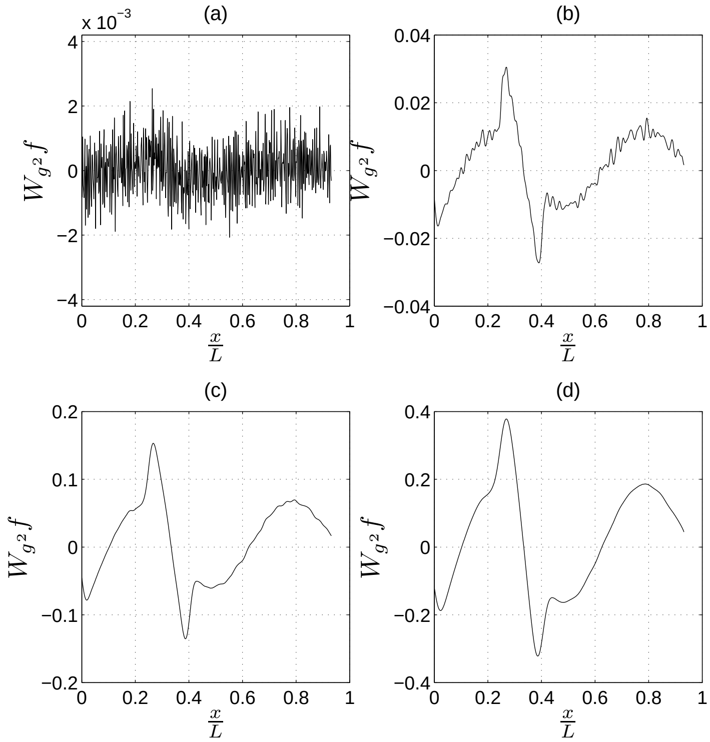

Figure 4.5: CWTs of the fourth measured MS of the damaged beam with the wavelet function $g^3(x)$ with different scales: (a) $s = 1$, (b) $s = 5$, (c) $s = 10$, and (d) $s = 15$.

4.1.2.3 Identification of an Embedded Horizontal Crack

When measured MSs of the associated undamaged beam are known a priori, an embedded horizontal crack can be identified using CMSs and CWTs of the measured MSs of the damaged and undamaged beams. The reason is that local features caused by the crack occur along with global trends of the CMSs and CWTs of the measured MSs of the damaged beam, and the measured MSs of the undamaged beam can provide references of the global trends to identify the crack. The gapped-smoothing method in Refs. [87, 103] can locally diminish the global trends in a point-wise way by calculating a damage index, which is the squared value of the difference between the CMS at a measurement point and the corresponding value calculated from a polynomial that fits the CMS at four neighbouring points of the measurement point. For each measurement point, a relatively large damage index indicates a high possibility of existence of damage. However, for a dense measurement grid, CMSs of a damaged beam can be locally smooth, and there may not be large differences between the CMSs and those from local polynomial fits, and measurement noise can affect the application of the method.

When MSs of both the damaged and undamaged beams are known, similar to the gapped-smoothing method, a CDI for a measured MS at a measurement point i with the resolution parameter m in Eq. (4.2) can be defined by

$$\delta_i^m = \left|\left(f_i^d\right)'' - \left(f_i^u\right)''\right|^2 = \left[\frac{\triangle_{d,u} f_{i+m} + \triangle_{d,u} f_{i-m} - 2\triangle_{d,u} f_i}{(mh)^2}\right]^2 \tag{4.17}$$

where $\triangle_{d,u} f_i = f_i^d - f_i^u$ is the difference between f^d and f^u at point i. Figure 4.6(a) shows the plots of $f^{u,4}$ and $f^{d,4}$. Figure 4.6(b) shows the plots of $(f^{u,4})''$ and $\left(f^{d,4}\right)''$ with $m = 15$; two extra peaks can be observed in $\left(f^{d,4}\right)''$ near the crack tips at $\frac{x}{L} = 0.25$ and $\frac{x}{L} = 0.40$, as opposed to $(f^{u,4})''$. The CDIs associated with $f^{d,4}$ are shown in Fig. 4.7; two peaks can be clearly observed in the neighbourhoods of the crack tips.

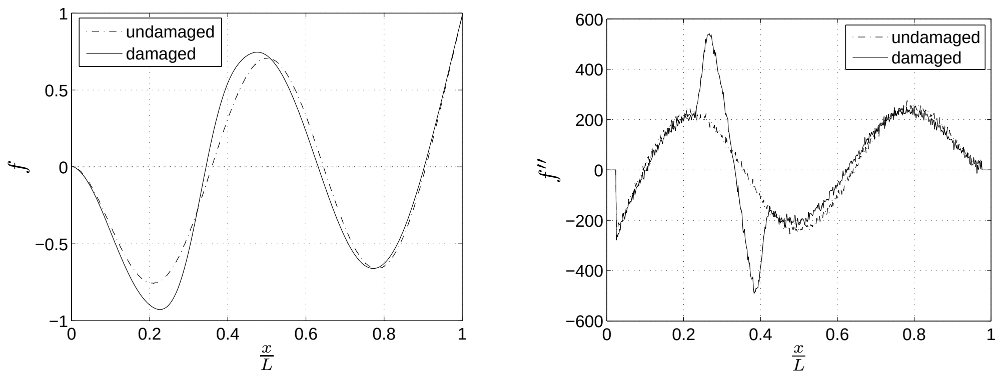

(a) (b)

Figure 4.6: (a) The fourth MSs of the undamaged and damaged beams, and (b) the associated CMSs with $m = 15$.

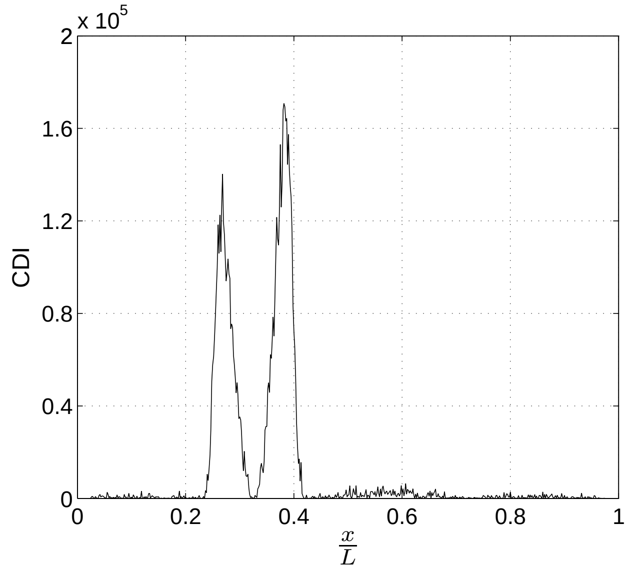

Figure 4.7: CDIs using the differences between the fourth MSs of the damaged and undamaged beams with $m = 15$

A CWTDI for a measured MS with wavelet function $\psi(x)$ with scale s at a measurement point i can be defined by

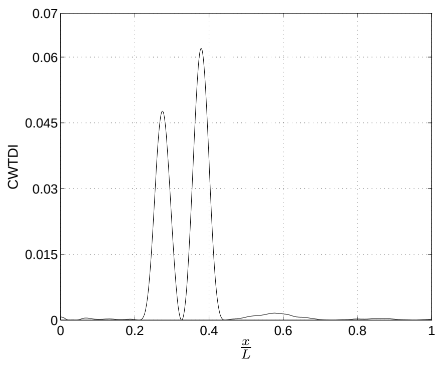

(a)

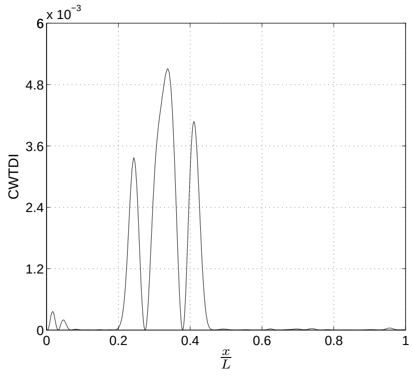

(b)

Figure 4.8: (a) CWTDIs with the wavelet function $g^2(x)$ with $s = 15$ using differences between the fourth MSs of the damaged and undamaged beams, and (b) those with the wavelet function $g^3(x)$ with $s = 15$ using differences between the fourth MSs of the damaged and undamaged beams.

$$\varpi_i^s = |W_\psi \triangle_{d,u} f(u_i, s)| \tag{4.18}$$

The plots of the CWTDIs for $f^{d,4}$ with the wavelet functions $g^2(x)$ and $g^3(x)$ with $s = 15$ are shown in Figs. 4.8(a) and (b), respectively, whose peaks and valleys are located near the crack tips, respectively. However, the two types of damage indices defined above require use of MSs of the associated undamaged beam f^u as baseline information, which are not always available in practice.

When MSs of the associated undamaged beam are not available, they can be constructed using polynomials that fit the MSs of the damaged beam, under the assumption that the presence of a crack in a beam does not cause prominent changes in its MSs in the neighbourhood of the crack, which is valid for a crack of a small size. The MSs of an undamaged beam corresponding to a damaged one are not measured in this work, and it is proposed that the j-th MS of the undamaged beam be obtained from a polynomial of order $n + k$ that fits the j-th MS of the damaged one:

$$f^{p,j}(x) = \sum_{i=0}^{n+k} a_i x^i \tag{4.19}$$

where n is the number of nodal points of the MS, k is a parameter that controls the level of approximation of the polynomial fit to the MS of the damaged beam, and a_i are coefficients of the polynomial. As shown in Table 4.1, modal assurance criterion (MAC) values in percent between the first four measured MSs of the undamaged and damaged beams are all above 97%, which indicates that they are almost identical to each other [1]; this validates the assumption on the effects of a small crack on MSs. Hence, a MS f^p from a polynomial that fits the MS of a damaged beam f^d can well approximate that of an undamaged one f^u. On one hand, a CMS $(f^p)''$ with a properly chosen value of k in Eq. (4.19) cannot capture local features of $\left(f^d\right)''$ in the neighbourhood of the crack, which are caused by the crack, even though f^p is constructed based on f^d. On the other hand, the resulting $(f^p)''$ can well approximate $(f^u)''$ since the former is as smooth as the latter without any local abnormalities. With different k values in Eq. (4.19), MAC values in percent between $f^{u,4}$ and $f^{p,4}$ and those between $(f^{u,4})''$ and $(f^{p,4})''$ are shown in Table 4.2(a); MAC values in percent between $f^{d,4}$ and $f^{p,4}$ and those between $\left(f^{d,4}\right)''$ and $(f^{p,4})''$ are shown in Table 4.2(b). When $k \geqslant 2$, the MAC values between $f^{u,4}$ and $f^{p,4}$ and those between $f^{d,4}$ and $f^{p,4}$ are all above 98%. However, the MAC values between $(f^{u,4})''$ and $(f^{p,4})''$ and those between $\left(f^{d,4}\right)''$ and $(f^{p,4})''$ are relatively low. Figures 4.9(a) and (b) show $f^{u,4}$, $f^{d,4}$, and $f^{p,4}$ from the polynomial fit with $k = 4$ and the associated CMSs, respectively. It can be seen that there are large discrepancies between $(f^{u,4})''$ and $\left(f^{d,4}\right)''$ in the boundary intervals $[0, 0.1]$ and $[0.9, 1]$. The reason is that the coefficients a_i of $f^p(x)$ are determined by solving the unconstrained least-squares problem:

$$\min \sum_{i=1}^{N} \left[f^p\left(x_i\right) - f^d\left(x_i\right)\right]^2 \tag{4.20}$$

where N is the number of measurement points, and there are no constraints applied on the boundaries. For MSs of a cantilever beam defined on $[0, 1]$, for instance, the boundary conditions that the fitting polynomials should satisfy are

$$\begin{cases} f^p\left(0\right) &= 0 \\ \left[f^p\right]'\left(0\right) &= 0 \\ \left[f^p\right]''\left(1\right) &= 0 \\ \left[f^p\right]'''\left(1\right) &= 0 \end{cases} \tag{4.21}$$

With the boundary conditions in Eq. (4.21), the least-squares problem in Eq. (4.20) becomes a constrained one, which can be solved by a numerical method [104]. However, the boundary conditions of a beam can be unknown or it can be difficult to accurately define them in practice; polynomials that can fit f^d well near the boundaries may not be constructed.

Table 4.2: (a) MAC values in percent between the fourth MS of the undamaged beam and those from polynomial fits with different k values, and MAC values in percent between the associated CMSs with $m = 15$; and (b) MAC values in percent between the fourth MS of the damaged beam and those from polynomial fits with different k values, and MAC values in percent between the associated CMSs with $m = 15$.

(a)

k	0	1	2	3	4	5	6
MS	87	86	99	98	98	98	98
CMS	15	13	68	69	82	79	70

(b)

k	0	1	2	3	4	5	6
MS	83	84	98	99	99	100	100
CMS	9	7	51	55	67	72	66

Table 4.1: MAC values in percent between the first four measured MSs of the damaged and undamaged beams, and those between the associated CMSs with $m = 15$.

mode	1	2	3	4
MS	100	100	100	97
CMS	94	94	83	85

To eliminate discrepancies between CMSs of a damaged beam and those from corresponding polynomial fits near boundaries without any a priori knowledge of the boundary conditions, it is proposed that MSs of the beam be extended to virtual

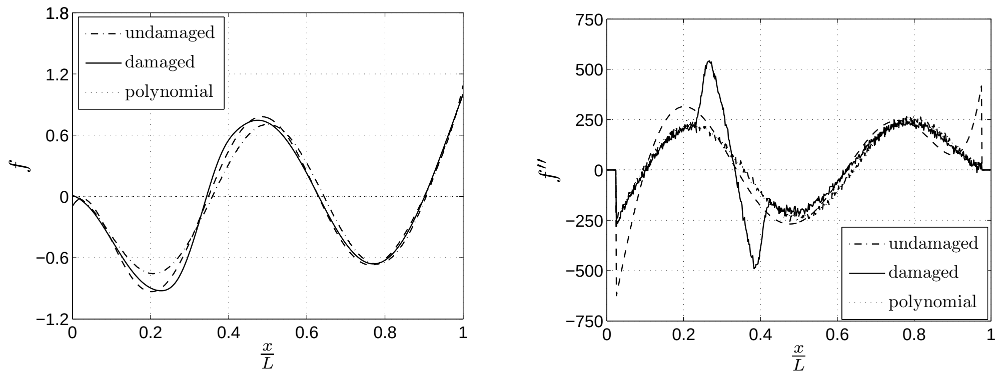

(a) (b)

Figure 4.9: (a) The fourth MSs of the undamaged and damaged beams and that from the polynomial fit; and (b) the associated CMSs with m=15.

intervals $[-0.2, 0]$ and $[1, 1.2]$, which are of twice the length of the boundary intervals indicated above, and the extended portions of the MSs on $[-0.2, 0]$ and $[1, 1.2]$ be obtained using polynomials of order three that fit the MSs in the boundary intervals $[0, 0.1]$ and $[0.9, 1]$, respectively. The extended MSs are obtained by correspondingly stitching the two extended portions onto the boundaries of the original MSs. With construction of the extended MSs, discrepancies between CMSs of the damaged beam and those from the corresponding polynomial fits are transferred to the virtually extended portions. The polynomial that fits the j-th extended MS in $[-0.2, 1.2]$ can be obtained, and the MS from the polynomial fit in $[0, 1]$ can be extracted and is denoted by $\widetilde{f^{p,j}}$, which can be used as the j-th MS of the associated undamaged beam. With different k values, MAC values in percent between $f^{u,4}$ and $\widetilde{f^{p,4}}$ and those between $(f^{u,4})''$ and $\left(\widetilde{f^{p,4}}\right)''$ are shown in Table 4.3(a), and MAC values in percent between $f^{d,4}$ and $\widetilde{f^{p,4}}$ and those between $\left(f^{d,4}\right)''$ and $\left(\widetilde{f^{p,4}}\right)''$ are shown in

Table 4.3(b). When $k \geqslant 4$, the MAC values between $f^{u,4}$ and $\widetilde{f^{p,4}}$ and those between $(f^{u,4})''$ and $\left(\widetilde{f^{p,4}}\right)''$ are all above 98% and 92%, respectively, indicating that the resulting $\widetilde{f^{p,4}}$ and $\left(\widetilde{f^{p,4}}\right)''$ can well approximate $f^{u,4}$ and $(f^{u,4})''$ in $[0,1]$, respectively. A proper k value for a certain MS is proposed to be two plus the least k value with which the MAC value between the MS to be fitted and that from the corresponding polynomial fit is above 90%. Two is added here in order to preserve the smoothness of the CMSs from the corresponding polynomial fits, since calculation of a curvature incurs second-order differentiation, which reduces the orders of the polynomial fits by two. Since the MAC value between $f^{d,4}$ and $\widetilde{f^{p,4}}$ with $k = 4$ is above 90%, the optimal k value for the polynomial fit is chosen to be six. The extended $f^{u,4}$, $f^{d,4}$, and $f^{p,4}$, and the associated CMSs are shown in Figs. 4.10(a) and (b), respectively. The MAC value between $\left(f^{d,4}\right)''$ and $\left(\widetilde{f^{p,4}}\right)''$ with $k = 4$ is 76%; such a low value is mainly attributed to the presence of the crack, and the MAC value between $(f^{u,4})''$ and $\left(\widetilde{f^{p,4}}\right)''$ is 99%.

Combined with the above approximation technique for MSs of an undamaged beam, the proposed methods can identify a crack, including one near a boundary. The CDIs of the damaged beam using the differences between $f^{d,4}$ and $\widetilde{f^{p,4}}$, denoted by $\triangle_{d,p}f$, are shown in Fig. 4.11, where the crack tips can be located near the peaks of the CDIs. The CWTDIs using $\triangle_{d,p}f$ with wavelet functions $g^2(x)$ and $g^3(x)$ with $s = 15$ are shown in Figs. 4.12(a) and (b), respectively, where the crack tips can be located near the peaks and valleys of the CWTDIs, respectively.

Table 4.3: (a) MAC values in percent between the fourth MS of the undamaged beam and those from polynomials that fit the fourth extended MS of the damaged beam shown in Fig. 4.1 with different k values, and MAC values in percent between the associated CMSs with $m = 15$; and (b) MAC values in percent between the fourth MS of the damaged beam and those from polynomials that fit the fourth extended MS of the damaged beam with different k values, and MAC values in percent between the associated CMSs with $m = 15$.

(a)

k	0	1	2	3	4	5	6
MS	8	12	89	89	99	98	99
CMS	7	9	62	64	95	93	96

(b)

k	0	1	2	3	4	5	6
MS	9	12	86	86	97	98	99
CMS	4	6	40	43	70	71	76

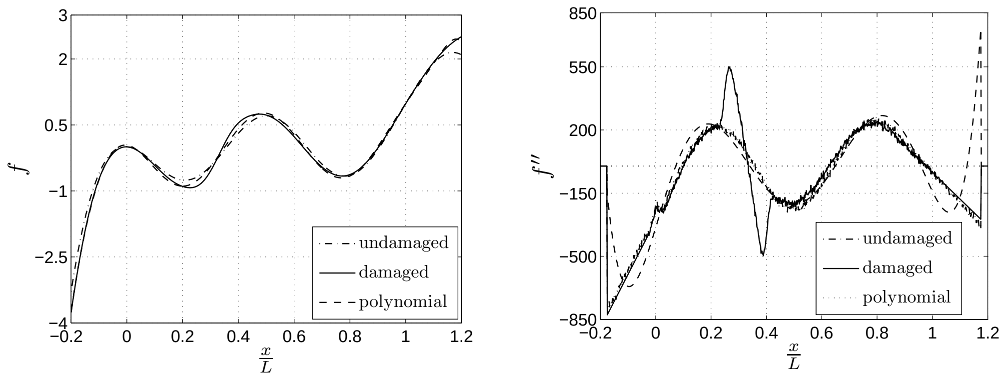

(a) (b)

Figure 4.10: (a) The fourth extended MSs of the undamaged and damaged beams and that from the polynomial fit; and (b) the associated CMSs with m=15.

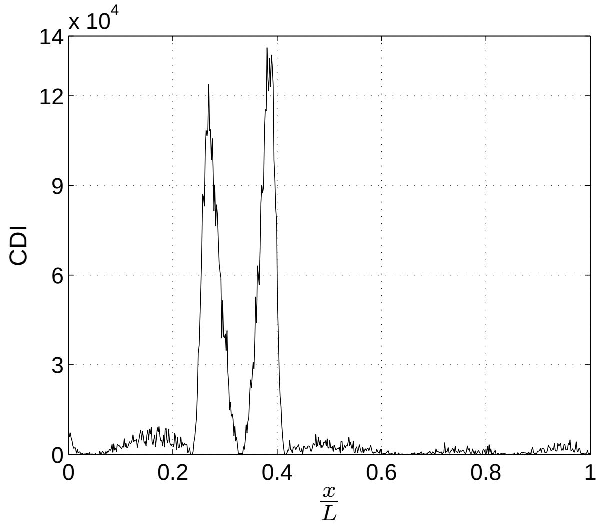

Figure 4.11: CDIs using the differences between the fourth MS of the damaged beam and that from the polynomial fit with $m = 15$.

In order to validate the robustness of the proposed methods on identifying a crack near a boundary, the crack in the damaged beam in Fig. 4.1 is translated to the position where its left tip is 30 mm away from the fixed end of the beam,

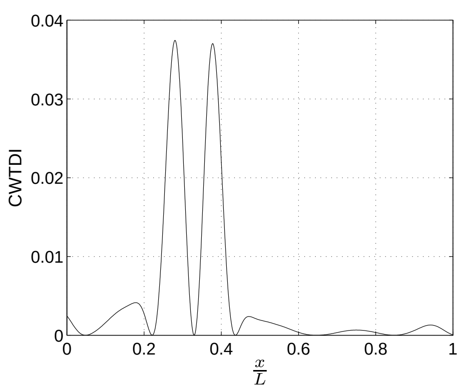

(a)

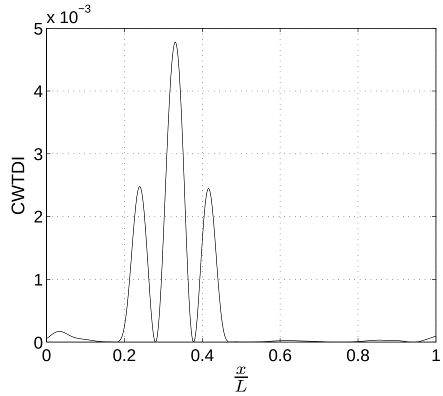

(b)

Figure 4.12: (a) CWTDIs with the wavelet function $g^2(x)$ with $s = 15$ using the differences between the fourth MS of the damaged beam and that from the polynomial fit, and (b) those with the wavelet function $g^3(x)$ with $s = 15$ using the differences in (a).

and its vertical position and length remain unchanged. A FE model of the beam is constructed, from which its fourth MS is calculated and used to identify the crack. The fourth MS of the associated undamaged beam can be obtained from polynomial fits with different k values. MAC values in percent between the fourth MS of the damaged beam and those from the polynomial fits and MAC values in percent between the associated CMSs are shown in Table 4.4; the optimal k value is chosen to be six for this MS, according to the proposed criterion. The extended $f^{u,4}$, $f^{d,4}$, and $\widetilde{f^{p,4}}$, and the associated CMSs are shown in Figs. 4.13(a) and (b), respectively. The associated CDIs with $m = 15$ and CWTDIs with wavelet functions $g^2(x)$ and $g^3(x)$ with $s = 15$ are shown in Figs. 4.14 and 4.15(a) and (b), respectively, from which the crack tips can be located near the peaks of the CDIs, and the peaks and

Table 4.4: (a) MAC values in percent between the fourth MS of the undamaged beam and those from polynomials that fit the fourth extended MS of a damaged beam with a crack near the fixed boundary with different k values, and MAC values in percent between the associated CMSs with $m = 15$; and (b) MAC values in percent between the fourth MS of the damaged beam and those from polynomials that fit the fourth extended MS of the damaged beam with different k values, and MAC values in percent between the associated CMSs with $m = 15$.

(a)

k	0	1	2	3	4	5	6
MS	17	23	89	87	98	97	98
CMS	10	12	58	57	94	92	97

(b)

k	0	1	2	3	4	5	6
MS	21	25	89	89	94	99	100
CMS	8	9	47	47	81	83	87

valleys of the CWTDIs, respectively. Since the effects of a small crack on MSs are local and negligible, multiple small cracks that simultaneously occur without any overlap along the length of a beam would not cause prominent local changes in MSs either. Hence CDIs and CWTDIs combined with the approximation technique for MSs of an undamaged beam can also be used to identify multiple small cracks in a beam.

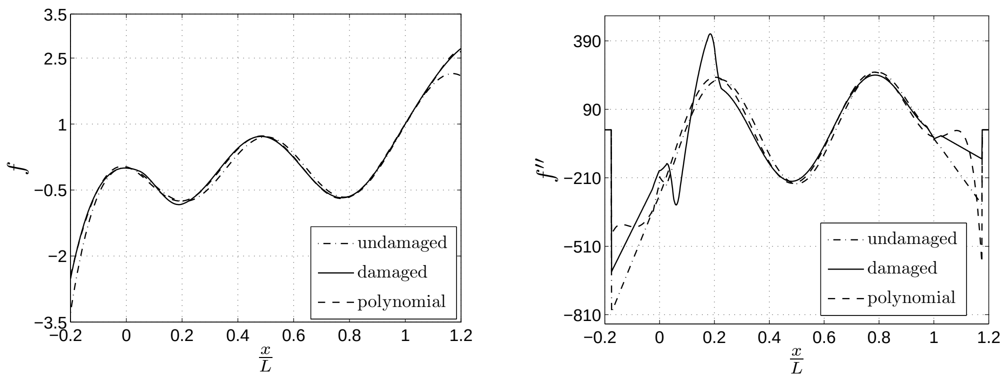

(a)

(b)

Figure 4.13: (a) The fourth extended MSs of the undamaged and damaged beams and that from the polynomial fit; and (b) the associated CMSs with $m = 15$.

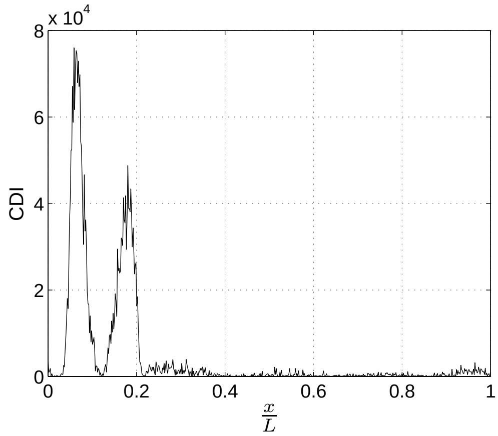

Figure 4.14: CDIs using differences between the fourth MS of the damaged beam with a crack near the fixed boundary and that from the polynomial fit with $m = 15$.

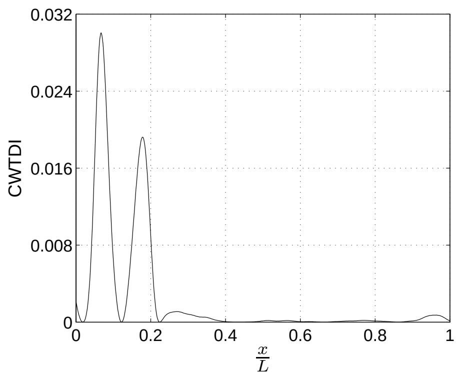

(a)

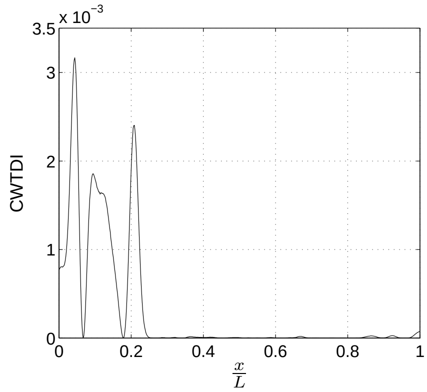

(b)

Figure 4.15: (a) CWTDIs with the wavelet function $g^2(x)$ with $s = 15$ using differences between the fourth MS of the damaged beam with a crack near the fixed boundary and that from the polynomial fit the fourth, and (b) those with the wavelet function $g^3(x)$ with $s = 15$ using the differences in (a).

4.1.2.4 Denoising of MSs

The above crack identification methods rely on MS measurement quality, which is usually subject to measurement noise that can deteriorate the resulting CMSs and CWTs of MSs, as shown in Figs. 4.2(a) and 4.5(a), respectively. Suitable values of the resolution parameter m for a CMS and of the scale s for a CWT can alleviate the adverse effects of measurement noise. Since the noise level of a measured MS is usually unknown, one needs to progressively test different values of m and s from smaller ones to larger ones in order to get the suitable ones, with which global trends of the resulting CMS and CWT of a MS are clear and they would not drastically change even with higher values of m and s, respectively. A numerical smoothing technique, which is local regression using weighted linear least squares and a second-

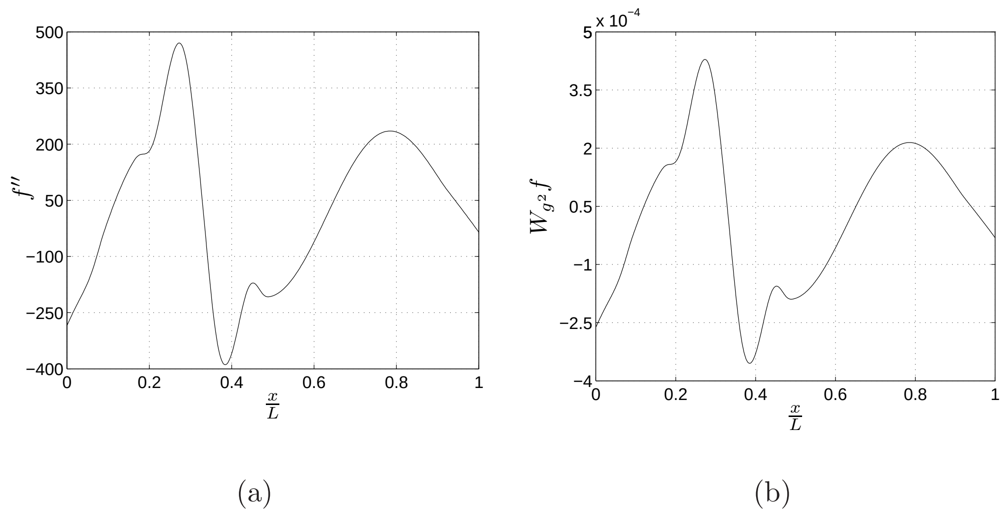

Figure 4.16: (a) Curvature of the denoised fourth MS of the damaged beam with $m = 1$, and (b) the CWT with the wavelet function $g^2(x)$ with $s = 1$ of the denoised fourth MS the damaged beam.

order polynomial model, is applied to directly reduce measurement noise in MSs, and it is performed using the Matlab function "smooth". The method calculates a weighted quadratic least square on every measurement point within an interval that consists of a certain number of its neighbouring points, which is 15% of the total number of measurement points herein. The CMS with $m = 1$ and CWT with the wavelet function $g^2(x)$ with $s = 1$ of the denoised fourth MS of the damaged beam shown in Fig. 4.1 are shown in Figs. 4.16(a) and (b), respectively, where the CMS and CWT of the MS have a lower noise level and are smooth, and their shapes are similar to the CMSs and CWTs of MSs before denoising with higher values of m and s as shown in Figs. 4.2(b) through (d) and Figs. 4.5(b) through (d), respectively.

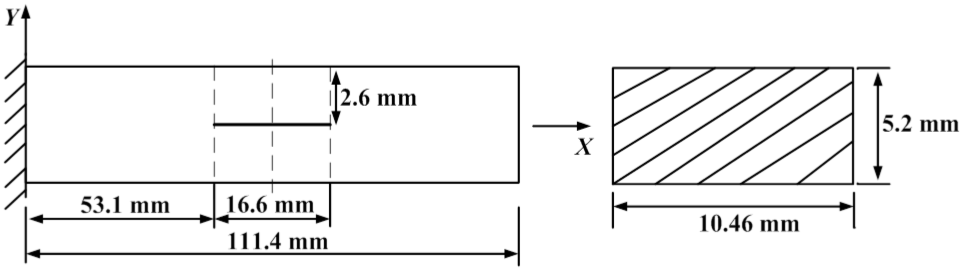

(a)

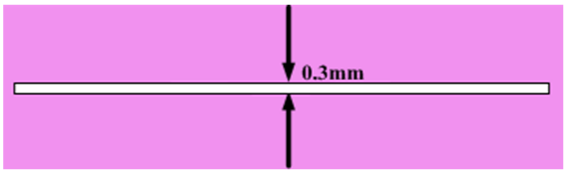

(b)

Figure 4.17: (a) Dimensions of the uniform ABS cantilever beam with an embedded horizontal crack, and (b) an enlarged view of the crack region.

4.1.3 Experimental Investigation

4.1.3.1 Modal Analysis and Model Validation

A uniform ABS cantilever beam of length 114.4 mm, height 5.2 mm, and width 10.5 mm with an embedded horizontal crack was made by a 3D printer, as shown in Fig. 4.17(a); the shape of the crack was a rectangle, and its length, width, and height were 16.6 mm, 10.5 mm, and 0.3 mm, respectively, as shown in Fig. 4.17(b). The distance between the left tip of the crack and the fixed end of the beam was 53.1 mm, and that between the top surface crack and that of the beam was 2.6 mm.

In order to get precise natural frequency and MS measurements of the beam without incurring unwanted mass loading, OMA with non-contact excitations and measurements was performed [105]; the experimental setup is shown in Fig. 4.18(a).

To create a fixed boundary for the beam, a bench vice was used to firmly clamp two flat metal plates, and the fixed end of the beam was clamped between the two plates. An electric speaker with a wood fixture faced the beam and generated acoustic excitations onto the beam surface. Two laser vibrometers were used to measure the responses of the beam: Laser 1 shown in Fig. 4.18(a) was a Polytec PSV-500 scanning laser vibrometer that measured velocities of measurement points on the beam, and Laser 2 was a Polytec OFV-353 single-point laser vibrometer that measured the velocity of a fixed reference point on the beam. There were totally 129 evenly distributed measurement points along the length of the beam, and a retro-reflective tape was attached on the beam surface to enhance laser reflection that directly determined SNRs of laser measurements. Acoustic excitations in the form of a burst chirp were used to excite the beam, and cross power spectral densities between the velocities of the measurement points and that of the reference point were calculated, from which the first four natural frequencies and MSs of the beam were obtained using Operational PolyMax of LMS Test.Lab Rev. 9b. In this test, two speakers of different sizes were used to excite the beam in two different frequency ranges. A Polk MM2084 speaker and a Fostex FE126En speaker were used to produce broad-band acoustic excitations with frequencies ranging from 10 to 150 Hz for mode one and from 500 to 3800 Hz for modes two through four. In order to enhance the excitation for the mode one, a wood box that concentrates the acoustic excitation of the low-frequency speaker onto the beam was built, as shown in Fig. 4.18(b). The box had a narrow open slot whose dimensions were slightly larger than those of the beam, and there was no contact between the wood box and the beam

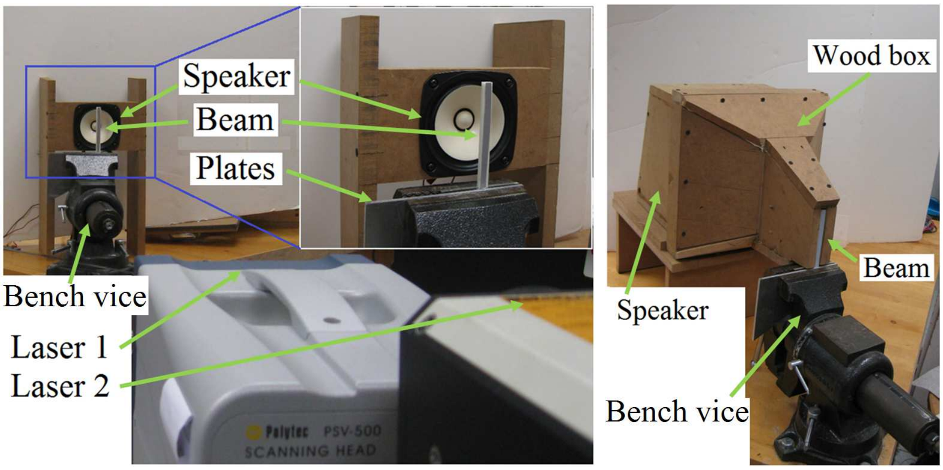

(a) (b)

Figure 4.18: (a) Experimental setup of OMA, and (b) a wood box used for the low-frequency excitation.

nor the bench vice throughout the tests.

In order to validate the measured natural frequencies and MSs and the rigidity of the fixed boundary, a FE model of the damaged beam was needed for comparison purposes, but the elastic modulus of the ABS was unknown. EMA was conducted to acquire the elastic modulus of the ABS; the experimental setup is shown in Fig. 4.19. An undamaged ABS beam of length 160.1 mm, height 5.2 mm, and width 10.5 mm was made, and it was placed on foams to simulate free boundary conditions. The roving hammer technique was applied, and the beam was excited at 17 evenly distributed points along the length of the beam using a PCB 086-D80 miniature impact hammer. The excitation was in the form of a single impact, and the direction of the impact was perpendicular to the surface of the beam. The responses of the beam were measured using the single-point laser vibrometer, and the impact and response data were collected using a LMS 36-channel spectrum analyser. The frequency resolution of the data was 1.56 Hz, and five tests were averaged to ensure repeatable results with a good coherence at each measurement point. The first four elastic modes of the beam were measured, and the measured natural frequencies are shown in Table 4.5. The simulated free boundary conditions were valid, since the highest natural frequency of the rigid body modes was 31.7 Hz, which was about 10.4% of the natural frequency of the first elastic mode [1]. The mass density of the beam was measured to be 1000 kg/m^3. The natural frequency of the i-th elastic mode of the undamaged beam can be calculated by [54]

$$\omega_i = (\beta_i L)^2 \sqrt{\frac{EI}{\rho L^4}} \tag{4.22}$$

where E is the elastic modulus of the ABS, I is the area moment of inertia of the cross-section of the beam, ρ is the mass per unit length of the beam, and β_i is the i-th positive root of the characteristic equation:

$$cos\,(\beta L)\,cosh\,(\beta L) = 1 \tag{4.23}$$

The elastic modulus was updated to be 2.10 GPa so that the maximum error between the calculated and measured natural frequencies is 0.85%, as shown in Table 4.5.

Table 4.5: Comparison between the calculated natural frequencies of the undamaged ABS beam with simulated free boundary conditions from the FE model using the updated elastic modulus of the ABS and the measured ones by EMA

Mode	Calculated Frequency (Hz)	Measured Frequency (Hz)	Error (%)
1	302.47	305.05	-0.85
2	833.77	836.49	-0.32
3	1634.52	1631.36	0.19
4	2701.95	2679.06	0.85

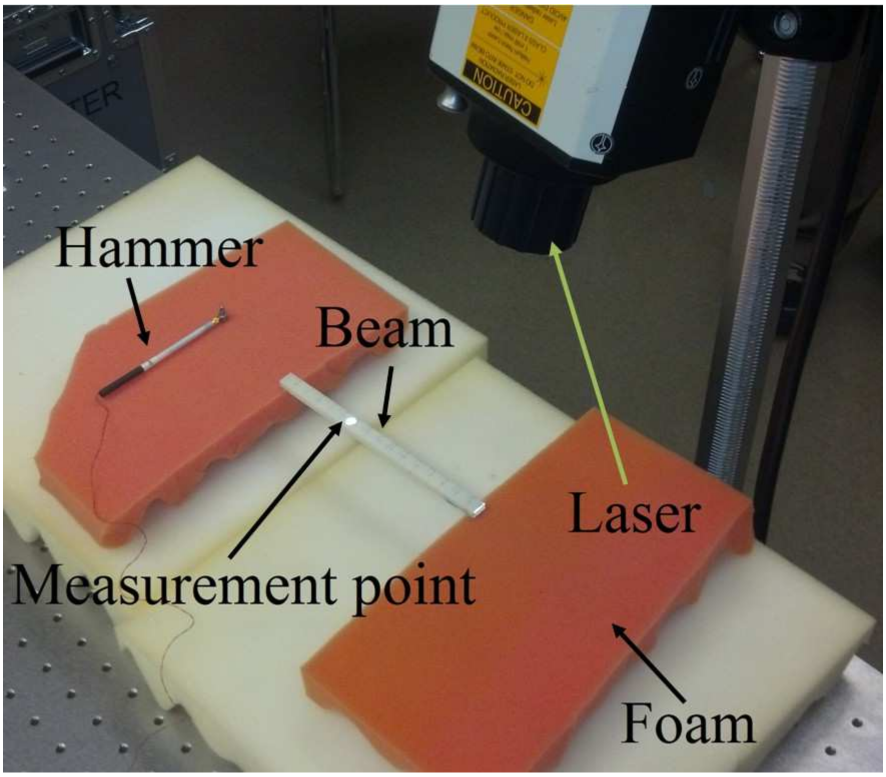

Figure 4.19: Experimental setup of EMA for an undamaged ABS beam

With the updated elastic modulus of the ABS, the FE model of the damaged beam was constructed. The first four calculated and measured natural frequencies of the damaged beam are shown in Table 4.6. The largest error between the calculated and measured natural frequencies is 1.72%. The fixed boundary of the damaged beam is also validated by the small natural frequency errors. White noise was added to the calculated MSs from the FE model with a SNR of 60 to simulate measurement noise. The first four calculated and measured MSs were normalized so that their maximum absolute values were one, as shown in Fig. 4.20, and the MAC matrix in percent between the calculated and measured MSs is shown in Table 4.7; the diagonal entries are all over 93%.

Table 4.6: Comparison between the measured natural frequencies of the damaged ABS cantilever beam by OMA and the calculated ones from the FE model

Mode	Measured Frequency (Hz)	Calculated Frequency (Hz)	Error (%)
1	97.79	97.14	0.67
2	611.10	615.00	-0.63
3	1604.00	1608.00	-0.25
4	3124.20	3179.00	-1.72

Table 4.7: Entries of the MAC matrix in percent between the first four measured MSs of the damaged beam and the calculated ones from the FE model; the horizontal and vertical mode numbers correspond to the calculated and measured modes, respectively.

Mode	1	2	3	4
1	100	0	0	0
2	0	100	0	0
3	4	1	93	0
4	0	0	0	99

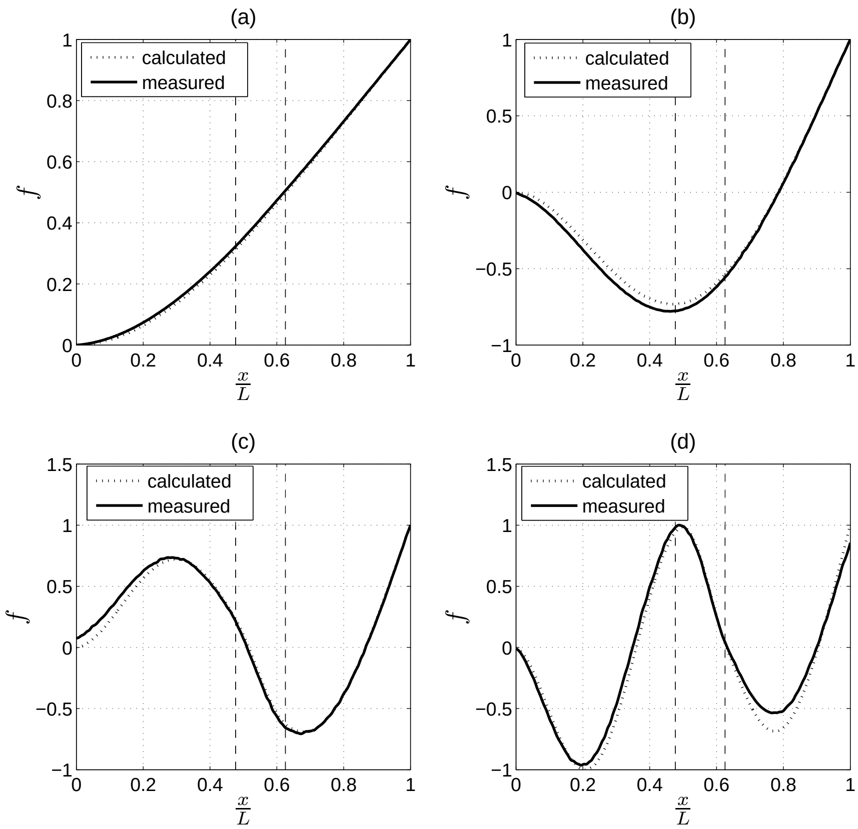

Figure 4.20: The first four measured MSs of the damaged beam and the calculated ones from the FE model, with the dashed lines indicating the locations of the crack tips.

4.1.3.2 Crack Identification Results

The first four MSs from the FE model are denoised using the technique in Sec. 2.4. Tables 4.8(a) through (d) show MAC values in percent between the first four MSs from the FE model and those from the polynomial fits with different k values, which are obtained using the approximation technique for MSs of the associated undamaged beam described in Sec. 2.3; MAC values in percent between the associated CMSs are also shown. The optimal k values for modes one through four are chosen to be two, three, four, and six, respectively. Figures 4.21(a) through (d) show the resulting CDIs with resolution up to 20 for the first four modes of the damaged beam from the FE model; two ridges can be observed in the CDIs for each mode, from which the crack tips can be correspondingly located. In Fig. 4.21(a), the right crack tip at $\frac{x}{L} = 0.61$ can be more clearly located than the left one at $\frac{x}{L} = 0.46$; in Fig. 4.21(b), the ridges corresponding to the two crack tips are both weak. The reason is that the CMS of mode two, shown in Fig. 4.22(b), is insensitive to the crack, since its abnormalities caused by the crack are weaker than those of the CMSs of the three other modes, as shown in Figs. 4.22(a), (c), and (d). It can also be observed from Fig. 4.22 that modes three and four are more sensitive to the crack. Hence, the CDIs for modes three and four can be used to more clearly identify the crack than those for modes one and two, as shown in Figs. 4.21(c) and (d).

Table 4.8: MAC values in percent between the first four calculated MSs of the damaged beam shown in Fig. 4.17 from the FE model and those from polynomial fits with different k values, and MAC values in percent between the associated CMSs; (a) through (d) correspond to modes one through four, respectively.

(a)

k	0	1	2
MS	98	100	100
CMS	0	60	98

(b)

k	0	1	2	3
MS	85	93	100	100
CMS	19	36	98	98

(c)

k	0	1	2	3	4
MS	52	66	97	97	100
CMS	14	18	73	73	85

(d)

k	0	1	2	3	4	5	6
MS	11	14	87	87	97	98	99
CMS	8	5	52	52	82	83	89

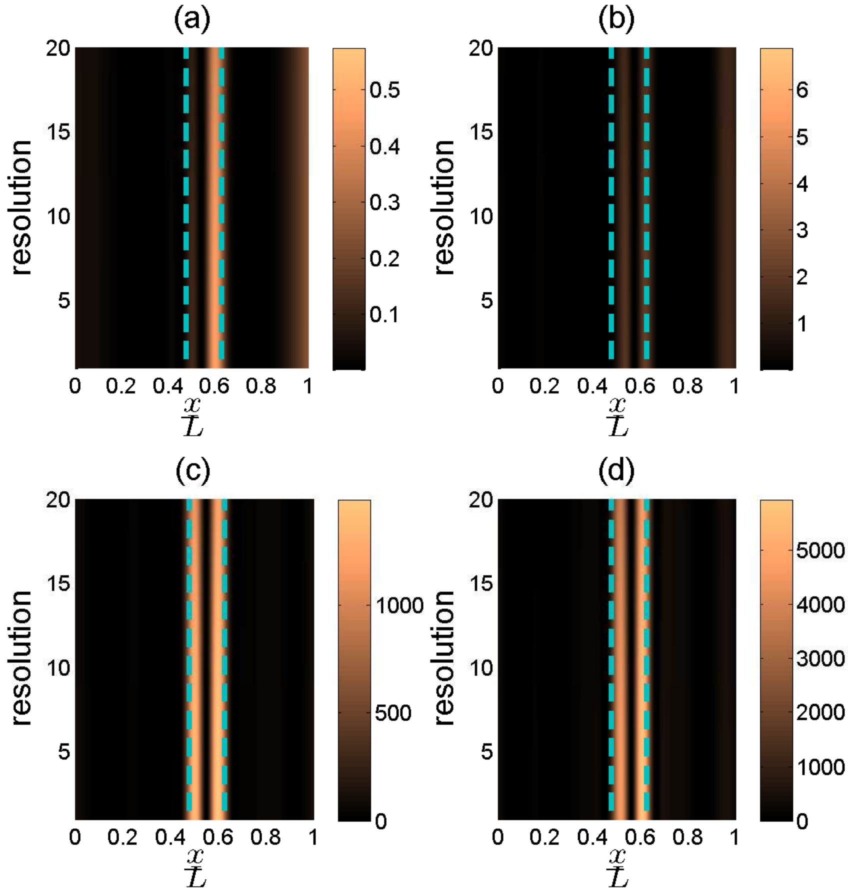

Figure 4.21: Numerical crack identification by tracking the ridges of the CDIs with resolution up to 20. The locations of the crack tips are indicated by dashed lines; the CDIs associated with modes one through four are shown in (a) through (d), respectively.

Figures 4.23 and 4.24 show the CWTDIs with wavelet functions $g^2(x)$ and $g^3(x)$ with scale up to 50 for the first four MSs of the damaged beam from the FE model, respectively. Similar to the results for the CDIs, relatively high CWTDIs with the wavelet function $g^2(x)$ can be more clearly observed from modes three and four near the crack tips than from modes one and two, as shown in Fig. 4.23, since

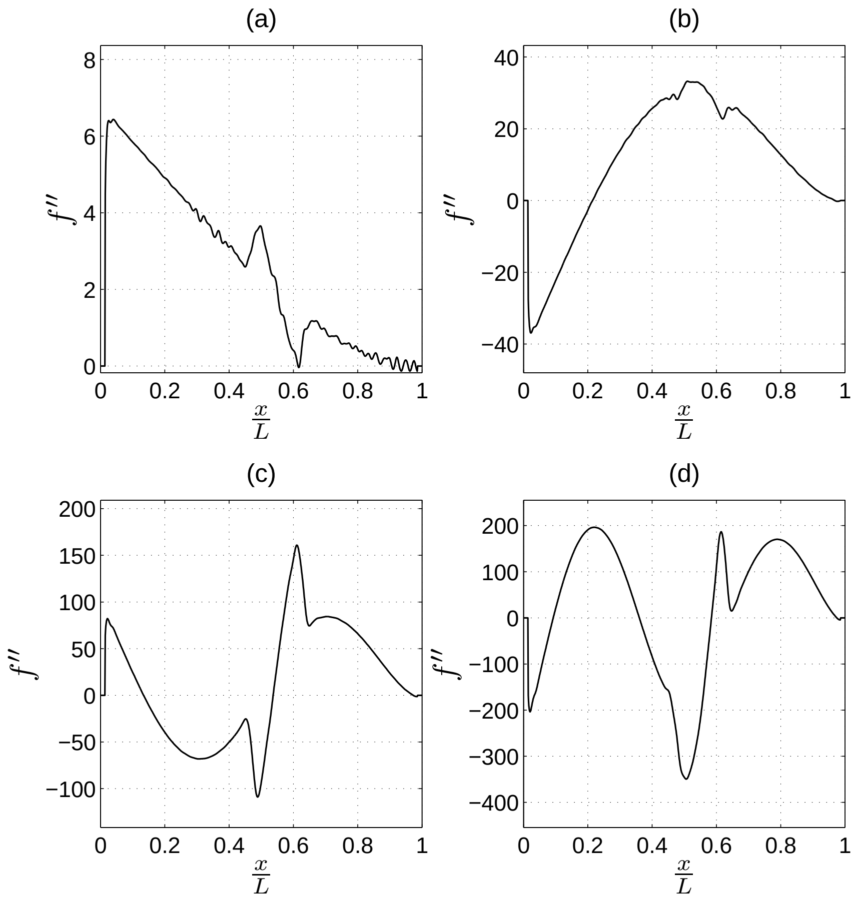

Figure 4.22: CMSs of the first four modes of the damaged ABS beam shown in Fig. 4.17 with $m = 15$

modes three and four are more sensitive to the crack. With the CWTDIs with the wavelet function $g^3(x)$, the crack tips can be located near the valleys of modes one through four, as shown in Figs. 4.24(a) through (d), respectively. The crack tips can be more clearly and accurately located near the valleys of modes one, three, and four than of mode two.

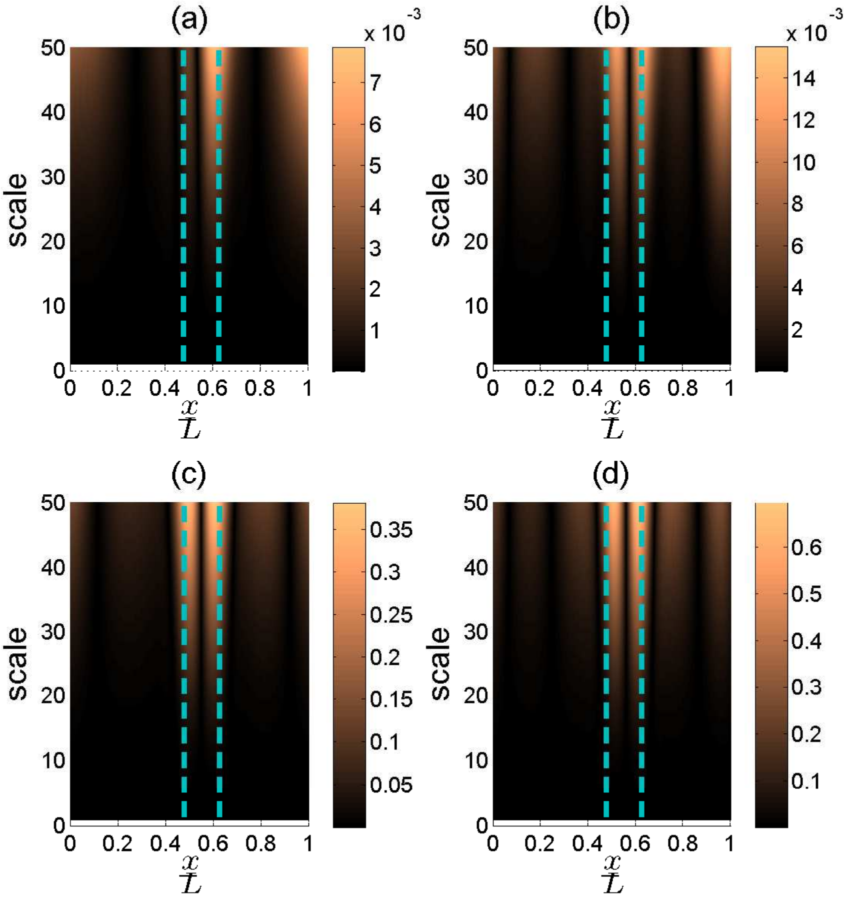

Figure 4.23: Numerical crack identification by tracking the peaks of the CWTDIs with the wavelet function $g^2(x)$ with scale up to 50. The locations of the crack tips are indicated by dashed lines; the CWTDIs associated with modes one through four are shown in (a) through (d), respectively.

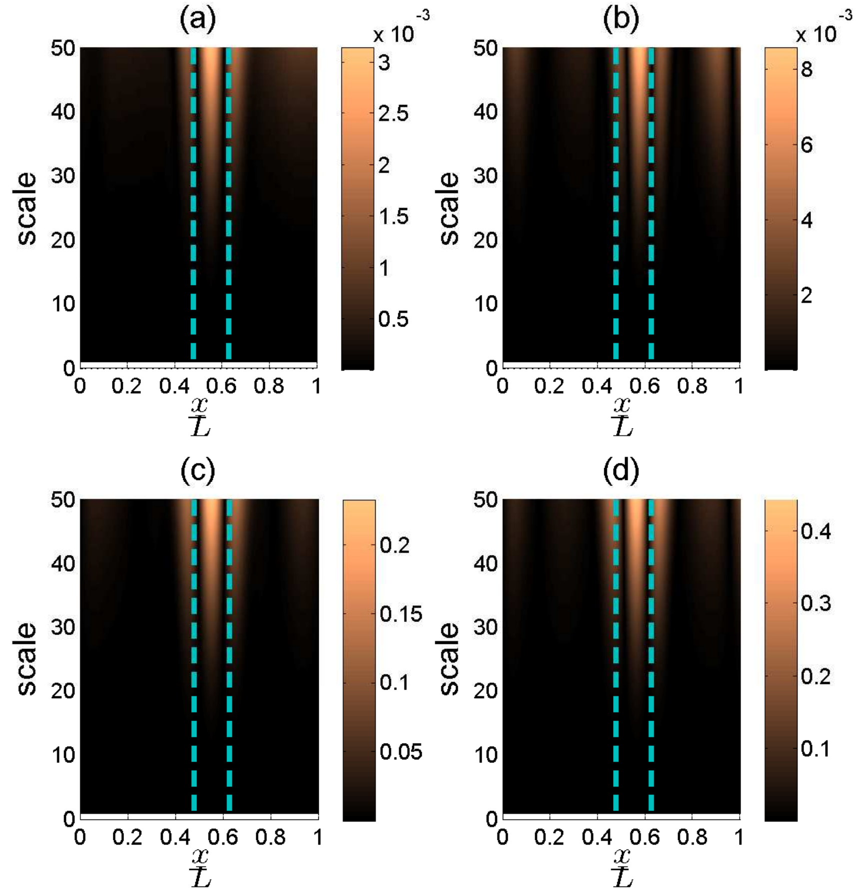

Figure 4.24: Numerical crack identification by tracking the valleys of the CWTDIs with the wavelet function $g^3(x)$ with scale up to 50. The locations of the crack tips are indicated by dashed lines; the CWTDIs associated with modes one through four are shown in (a) through (d), respectively.

The experimentally measured MSs were then used to identify the crack in the damaged ABS beam. Since an experimentally measured MS is complex, one needs two polynomials to fit its real and imaginary parts in order to approximate the MS of the associated undamaged beam. Hence, a CDI for a complex MS at measurement point i is defined by

$$\delta_i^m = \left| \left(f_{i,real}^d \right)'' - \left(\widetilde{f_{i,real}^p} \right)'' \right|^2 + \left| \left(f_{i,imag}^d \right)'' - \left(\widetilde{f_{i,imag}^p} \right)'' \right|^2 \tag{4.24}$$

where $f_{i,real}^d$ and $f_{i,imag}^d$ are the real and imaginary parts of the MS of the damaged beam at point i, respectively, and $\widetilde{f_{i,real}^p}$ and $\widetilde{f_{i,imag}^p}$ are the real and imaginary parts of the MS from the polynomials that fit $f_{i,real}^d$ and $f_{i,imag}^d$ at measurement point i, respectively. A CWTDI for a complex MS at point i is defined by

$$\varpi_i^s = |W_\psi \triangle_{d,p,real} f_i(x,s)| + |W_\psi \triangle_{d,p,imag} f_i(x,s)| \tag{4.25}$$

where $\triangle_{d,p,real} f_i = f_{i,real}^d - \widetilde{f_{i,real}^p}$ and $\triangle_{d,p,imag} f_i = f_{i,imag}^d - \widetilde{f_{i,imag}^p}$. In order to smooth the transition of the experimentally measured MSs from one measurement point to another, two cubic spline interpolations were used to obtain the real and imaginary parts of each MS using 1025 evenly distributed points along the length of the beam; the resulting data were then denoised using the technique in Sec. 2.4. Tables 4.9(a) through (d) show MAC values in percent between the first four measured MSs of the damaged beam and those from the polynomial fits and MAC values in percent between the associated CMSs, respectively; the optimal k values for modes one through four are chosen to be two, two, five, and six, respectively.

Figures 4.25(a) through (d) show the CDIs for the experimentally measured MSs of the damaged beam with resolution up to 20. Similar to the results from the FE model, two prominent ridges can be clearly observed in the CDIs for modes three and four, as shown in Figs. 4.25(c) and (d), respectively. The right crack tip can be more clearly located than the left one from mode one, as shown in Fig. 4.25(a);

Table 4.9: MAC values in percent between the first four experimentally measured MSs of the damaged beam shown in Fig. 4.17 and those from polynomial fits with different k values, and MAC values in percent between the associated CMSs; (a) through (d) correspond to modes one through four, respectively.

(a)

k	0	1	2
MS	98	100	100
CMS	0	61	97

(b)

k	0	1	2
MS	92	95	100
CMS	29	39	95

(c)

k	0	1	2	3	4	5
MS	62	75	89	94	97	99
CMS	29	31	69	69	84	84

(d)

k	0	1	2	3	4	5	6
MS	47	48	86	87	97	98	99
CMS	25	25	75	75	92	93	96

in Fig. 4.25(b), the crack tips cannot be identified due to measurement noise and, more importantly, the fact that mode two is insensitive to the crack. Figures 4.26 and 4.27 show the CWTDIs with wavelet functions $g^2(x)$ and $g^3(x)$ with scale up to 50 for the first four measured MSs of the damaged beam, respectively. Similar to the simulation results, the crack tips can be located near the peaks and valleys of the CWTDIs with wavelet functions $g^2(x)$ and $g^3(x)$, respectively, from modes one, three, and four; the crack cannot be identified from mode two.

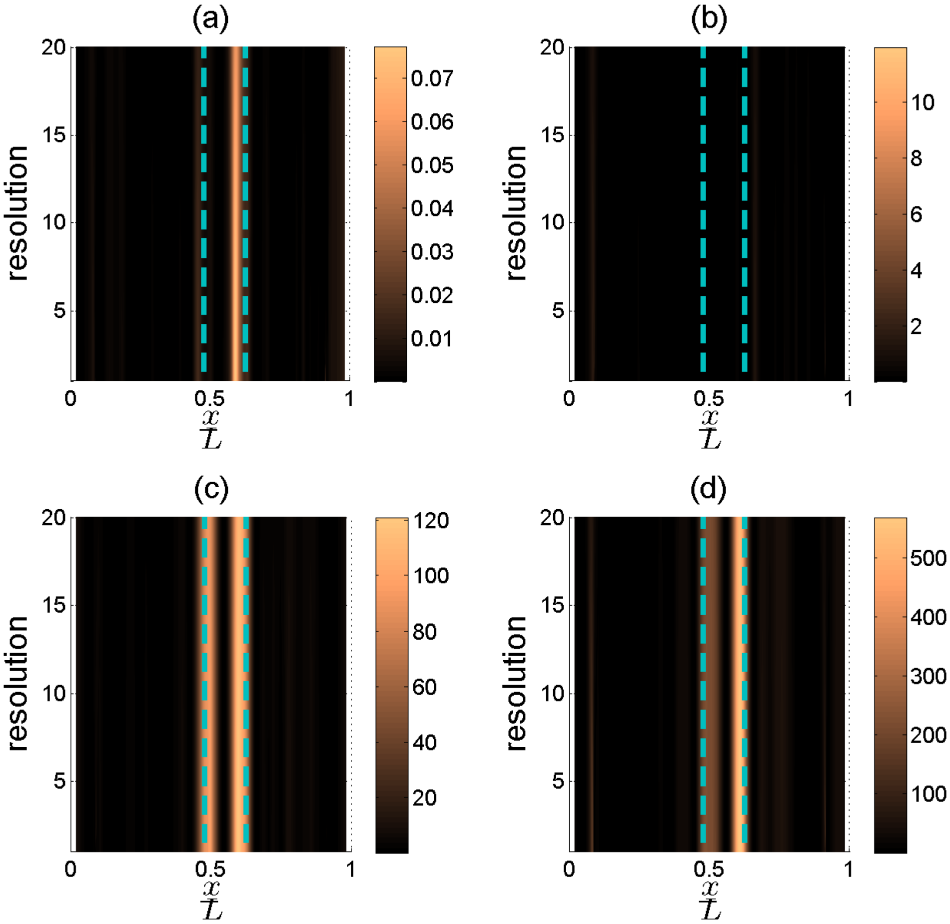

Figure 4.25: Experimental crack identification by tracking the ridges of the CDIs with resolution up to 20. The locations of the crack tips are indicated by dashed lines; the CDIs associated with modes one through four are shown in (a) through (d), respectively.

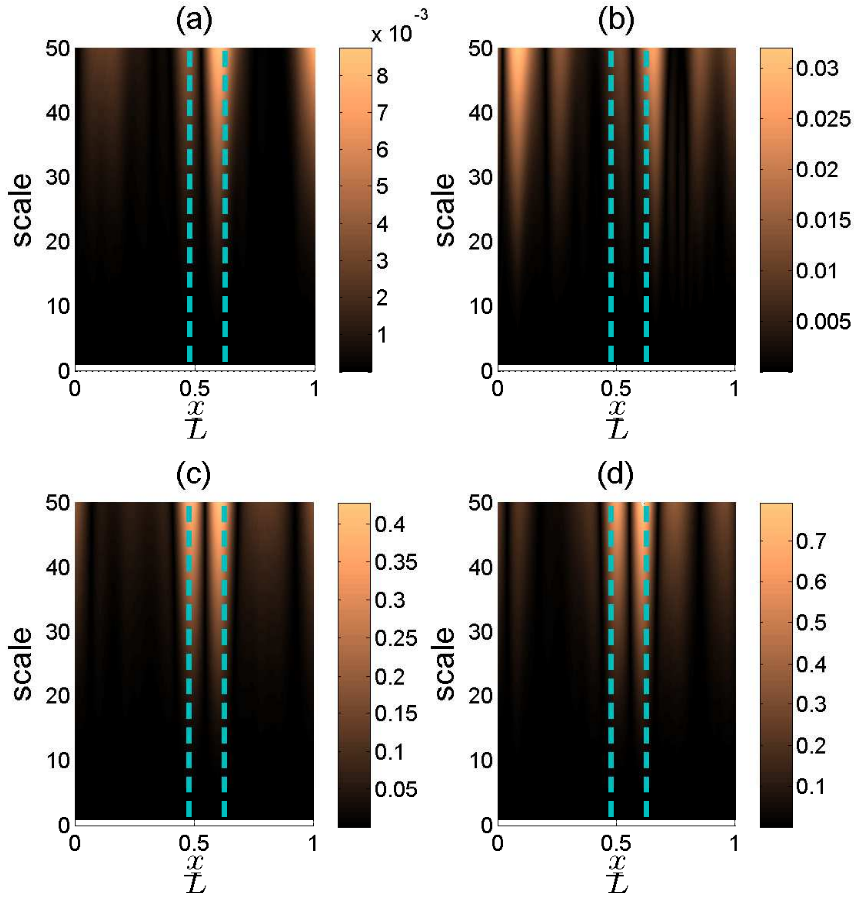

Figure 4.26: Experimental crack identification by tracking the peaks of the CWTDIs with the wavelet function $g^2(x)$ with scale up to 50. The locations of the crack tips are indicated by dashed lines; the CWTDIs associated with modes one through four are shown in (a) through (d), respectively.

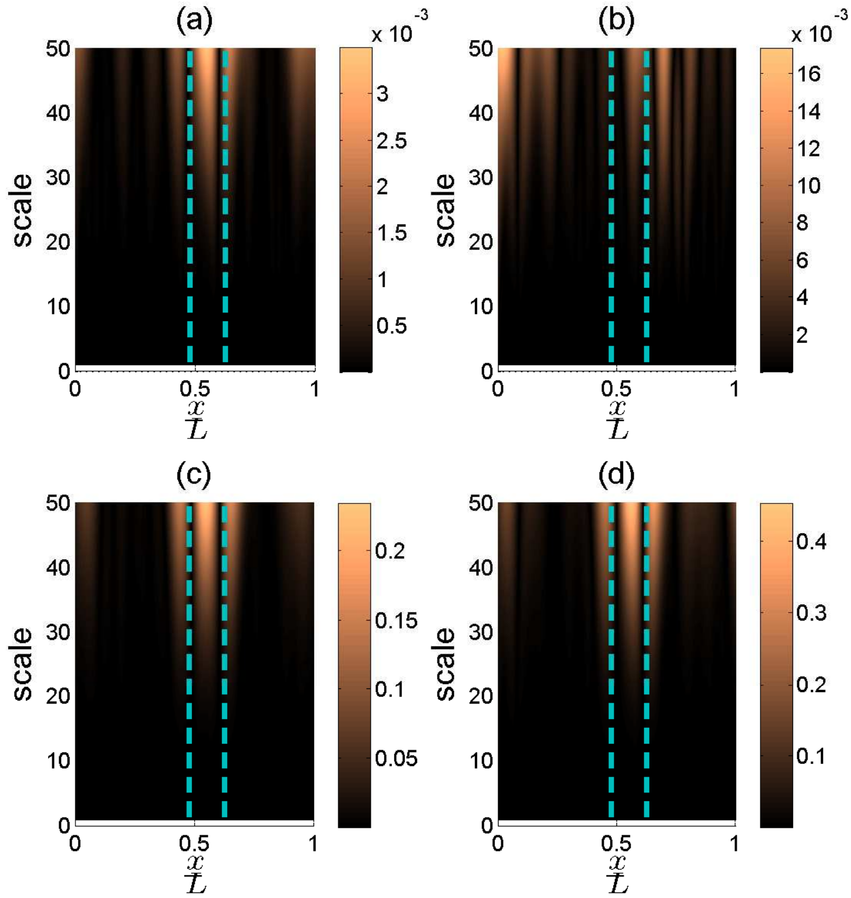

Figure 4.27: Experimental crack identification by tracking the valleys of the CWT-DIs with the wavelet function $g^3(x)$ with scale up to 50. The locations of the crack tips are indicated by dashed lines; the CWTDIs associated with modes one through four are shown in (a) through (d), respectively.

4.1.4 Conclusion

Two new non-model-based methods are developed to identify embedded horizontal cracks in beams without use of any a priori information of associated undamaged beams, if the beams are geometrically smooth and made of materials that have no stiffness discontinuities. Differences between measured MSs of a damaged beam with an embedder horizontal crack and those from polynomials that fit the MSs of the damaged beam are converted to CDIs and CWTDIs, which are used to locate the crack tips. MSs from polynomials that fit the MSs of a damaged beam can well approximate those of the associated undamaged beam, provided that the measured MSs of the damaged beam are extended beyond boundaries of the beam and the orders of the polynomials are properly chosen; the MSs from the polynomials can be used to eliminate trends of associated CMSs and CWTs of MSs. CDIs for a MS are presented with multiple resolutions to alleviate adverse effects of measurement noise, and crack tips can be located near peaks of the CDIs. It is shown that the CWT of a MS with the n-th-order Gaussian wavelet function resembles that of the n-th-order derivative of the MS. Crack tips can be located near peaks and valleys of CWTDIs with multiple scales using second- and third-order Gaussian wavelet functions, respectively, which are based on the physical interpretations of CWTs of MSs. The proposed methods are numerically and experimentally applied to a uniform ABS cantilever beam with an embedded horizontal crack; non-contact OMA with acoustic excitations and measurements by two laser vibrometers was conducted to measure the MSs of the beam. The proposed methods can also be used to identify other types of damage, such as edge cracks, slant cracks, and delaminations, in beams, and extended to identify damage in other types of structures.

4.2 Damage Identification of Plates Using Measured Mode Shapes

4.2.1 Introduction

Vibration-based damage detection has been a major research topic of structural dynamics in the past few decades. Measured modal characteristics of a structure, such as natural frequencies and MSs, are processed in various methods for detecting, locating and characterizing damage in the structure, since modal characteristics are related to physical properties of the structure, such as mass, stiffness and damping, which can change due to occurrence of damage [7]. Various methods that use measured MSs to identify damage in a structure have been proposed and investigated. Effects of damage on MSs are mainly local abrupt changes in the neighborhood of damage and the effects can be manifested and observed in curvature CMSs associated with the MSs. Based on a gapped smoothing method [88] for one-dimensional structures, such as beams, a two-dimensional gapped smoothing method was proposed to identify damage in two-dimensional structures using measured CMSs or curvatures of operating deflection shapes (CODSs).[106] An advantage of the gapped smoothing methods is that MSs of associated undamaged structures are not needed. However, one needs to conduct point-by-point calculation of curvatures to obtain a CMS or CODS; for each measurement point, a gapped polynomial that fit curvatures near the point is constructed to yield a fitted curvature to eliminate the global trend of the CMS or CODS at the point. Hence a gapped smoothing method is a local method and could be computationally inefficient, especially when the measurement grid is large and dense. Global fitting methods were proposed to identify damage by comparing CMSs [89] or CODSs [90] associated with damaged and undamaged beams and plates. They have the same advantage as that of the gapped smoothing methods. However, generic MSs of undamaged structures are needed, which can be unavailable in practice. Use of curvatures of frequency-shift surfaces to identify damage in plates was proposed.[107] The method was shown to have better results than the gapped smoothing method for plates. Use of mean CMSs was proposed to identify damage in plates,[108] where a two-dimensional wavelet transform was used to alleviate adverse effects of measurement noise on calculating mean CMSs and a Teager energy operator was used to manifest effects of damage in transformed mean CMSs. Curvatures of uniform-load surfaces were shown to be sensitive to existence of damage and were used to identify damage in plates;[109] the method used natural frequencies and MSs of first few modes of damaged and undamaged plates. A simplified gapped smoothing method, a generalized fractal dimension method and a strain energy method were used to process CMSs and curvatures of uniform-load surfaces to detect delamination in a composite plate.[110] A two-dimensional polynomial annihilation edge detection method was proposed for detection and localization of damage in plates;[111] it was extended from a method for beams to detect discontinuities in piecewise smooth functions and their derivatives.[84]

In this work, a new non-model-based method is proposed to identify damage in plates, where MSs of undamaged plates are not used. A MS of a pseudo-undamaged plate is constructed using a polynomial that fits the corresponding MS of a damaged plate, and differences between the MSs of the pseudo-undamaged and damaged plates are processed to yield MS damage indices (MSDIs) at each measurement point. Damage can be identified near regions with consistently high values of MSDIs. Use of a MS of an undamaged plate and that of a pseudo-undamaged plate from a polynomial fit is compared with respect to effectiveness of damage identification. Effectiveness and robustness of the proposed method on different MSs for damage of different positions and areas are numerically investigated; effects of crucial factors that determine effectiveness of the proposed method are also numerically investigated. MSs of an aluminum plate with damage in the form of a machined thickness reduction area were measured to experimentally validate the proposed methodology.

4.2.2 Methodology

A finite element (FE) model of a damaged rectangular steel plate that has a length of 300 mm, a width of 400 mm and a thickness of 2 mm is constructed with free boundary conditions; the model has a total of 150×200 plate elements. The damage is in the form of a rectangular thickness reduction area, and its position and area are shown in Fig. 4.56(a); the depth of the damage is 0.2 mm. The mass density, elastic modulus and Poisson's ratio of the plate are 7850 kg/m^3, 200 GPa and 0.3, respectively. A FE model of an undamaged plate with the same dimensions, boundary conditions and material properties as those of the damaged plate is constructed. Natural frequencies of the damaged and undamaged plates are different due to the damage; the maximum natural frequency change in percentage for the first 40 elastic modes is 0.28%, which occurs at the 6th elastic mode. Undamped

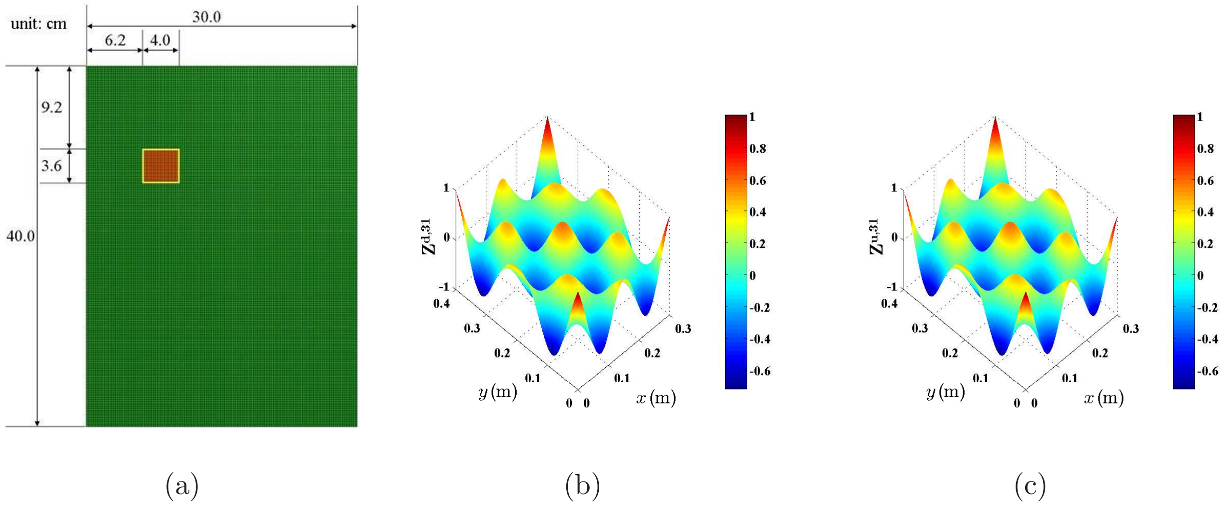

Figure 4.28: (a) FE model of a rectangular steel plate with damage in the form of a rectangular thickness reduction area, (b) the MS of the 31st elastic mode of the damaged plate and (c) that of the 31st elastic mode of an undamaged plate with the same dimensions, boundary conditions and material properties as the damaged one.

MSs of the 31st elastic modes of the damaged and undamaged plates, denoted by $\mathbf{Z}^{d,31}$ and $\mathbf{Z}^{u,31}$, respectively, which are randomly selected, are used to illustrate the proposed method in this section. The two MSs have the same phase, and they are normalized so that their maximum absolute values are equal to one. Normalized $\mathbf{Z}^{d,31}$ and $\mathbf{Z}^{u,31}$ are shown in Figs. 4.56(b) and (c), respectively.

4.2.2.1 Effects of Damage on MSs

For a constant-thickness plate made of homogeneous material, one has

$$\begin{bmatrix} M_{xx} \\ M_{yy} \\ M_{xy} \end{bmatrix} = \frac{Eh^3}{12\left(\nu^2-1\right)} \begin{bmatrix} 1 & \nu & 0 \\ \nu & 1 & 0 \\ 0 & 0 & \nu-1 \end{bmatrix} \begin{bmatrix} \kappa_{xx} \\ \kappa_{yy} \\ \kappa_{xy} \end{bmatrix} \tag{4.26}$$

where M_{xx} and M_{yy} are bending moments per unit length acting on edges of a differential element parallel to y- and x- axes of a Cartesian coordinate system $O-xyz$, respectively; M_{xy} is the twisting moment with respect to x- and y- axes; h, E and ν are the thickness, Young's modulus and Poisson's ratio of the plate, respectively; κ_{xx} and κ_{yy} are curvatures with respect to x- and y- axes, respectively; and κ_{xy} is the twist with respect to x- and y- axes. Effects of damage on κ_{xx}, κ_{yy} and κ_{xy} are local in that damage causes changes to material properties and geometry of the plate in the neighborhood of the damage, which are directly related to MSs. Effects of damage could be localized by comparing MSs of damaged and undamaged plates.

The MAC value in percentage between $\mathbf{Z}^{d,31}$ and $\mathbf{Z}^{u,31}$ is 99.96%, which indicates that they are almost identical to each other.[1] The difference between $\mathbf{Z}^{d,31}$ and $\mathbf{Z}^{u,31}$ is shown in Fig. 4.29(a), where a steep peak can be observed in the damage region. But besides the peak in the damage region, there are several peaks outside the region, which are less steep than that in the region and there are abrupt changes in some regions near boundaries, as shown in Figs. 4.29(a) and (b). The reason is that the stiffness of the plate changes due to the damage and changes of MSs occur inside and outside the damage region. When MSs of the damaged and undamaged plates are normalized so that their maximum absolute values are equal to one, differences of the MSs outside the damage region can be larger than those inside the region, and the effects of the damage cannot be isolated by directly comparing the two MSs. When $\mathbf{Z}^{u,31}$ is scaled so that its maximum absolute value is 0.975, the difference between scaled $\mathbf{Z}^{u,31}$ and $\mathbf{Z}^{d,31}$ can be used to identify the damage, as shown in Fig. 4.29(c). Effects of the damage on $\mathbf{Z}^{d,31}$ can be isolated since the peaks that are not in the damage region in Fig. 4.29(a) are much lower than that in the region, as show in Figs. 4.29(c) and (d). However, since whether damage exists or not is unknown a priori in practice, there is no guarantee that a MS of a damaged plate can be properly scaled so that the damage can be clearly identified by comparing the MS with that of an undamaged plate, and MSs of an undamaged plate are usually unavailable.

4.2.2.2 Construction of MSs of Pseudo-undamaged Plates

While one cannot easily identify damage by directly comparing MSs of damaged and undamaged plates, one can construct MSs of pseudo-undamaged plates using polynomial fits, which can approximate MSs of the damaged plate as if the plate had no damage, and one can easily identify damage by comparing MSs of the damaged and pseudo-undamaged plates. Assuming that existence of relatively small damage in a plate does not cause prominent changes in its MSs in the neighborhood of the damage, one can construct MSs of the associated pseudo-undamaged plate

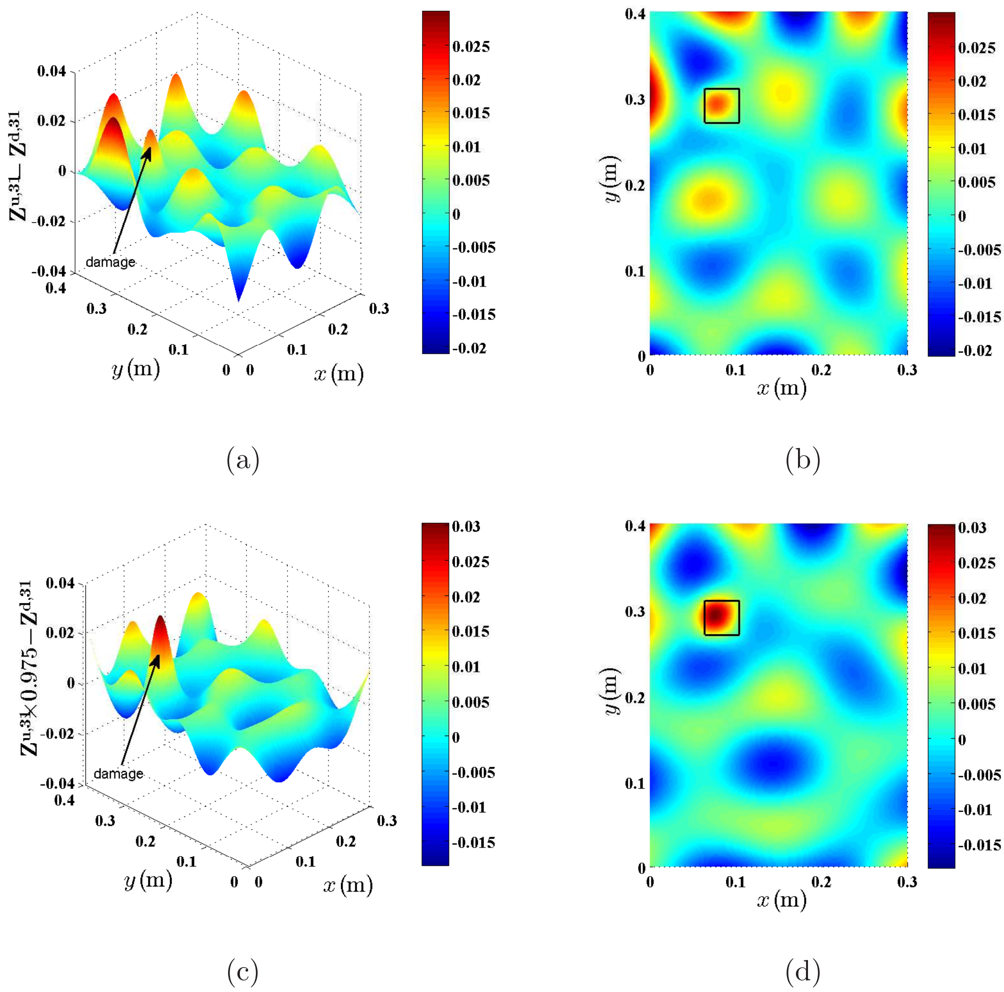

Figure 4.29: (a) Difference between $\mathbf{Z}^{d,31}$ and $\mathbf{Z}^{u,31}$, (b) the top view of (a) where damage is outlined by solid lines, (c) the difference between $\mathbf{Z}^{d,31}$ and $\mathbf{Z}^{u,31} \times 0.975$ and (d) the top view of (c) where damage is outlined by solid lines.

using polynomials that fit the corresponding MSs of the damaged plate, provided that the undamaged plate is geometrically smooth and made of materials that have no stiffness and mass discontinuities. Since the MAC value in percentage between $\mathbf{Z}^{d,31}$ and $\mathbf{Z}^{u,31}$ is 99.96%, the assumption on the existence of relatively small damage is validated. A similar technique has been proposed to approximate MSs of an undamaged beam using polynomials that fit the corresponding MSs of the damaged one.[9] MSs of an undamaged plate corresponding to those of a damaged one are not measured in this work, and it is proposed that a MS of the pseudo-undamaged plate be obtained from a polynomial with a properly determined order that fits the corresponding MS of the damaged plate:

$$z^p\left(x,y\right)=\sum_{k=0}^{n}\sum_{i=0}^{k}a_{i,k-i}x^iy^{k-i} \tag{4.27}$$

where n is the order of the polynomial, which controls the level of approximation of the polynomial fit to the MS of the damaged plate, (x,y) are x and y coordinates of a point on an undeformed plate, and $a_{i,k-i}$ are coefficients of the polynomial that can be obtained by solving a linear equation

$$\mathbf{Va}=\mathbf{z} \tag{4.28}$$

in which $\mathbf{V}$ is the $N \times \left(\sum_{p=1}^{n+1} p\right)$-dimensional bivariate Vandermonde matrix with N being the dimension of $\mathbf{z}$, which can be expressed by

$$\mathbf{V} = \begin{bmatrix} 1 & x_1 & y_1 & \dots & x_1^n & \dots & x_1^i y_1^{n-i} & \dots & y_1^n \\ 1 & x_2 & y_2 & \dots & x_2^n & \dots & x_2^i y_2^{n-i} & \dots & y_2^n \\ \vdots & \vdots & \vdots & \ddots & \vdots & \ddots & \vdots & \ddots & \vdots \\ 1 & x_N & y_N & \dots & x_N^n & \dots & x_N^i y_N^{n-i} & \dots & y_N^n \end{bmatrix} \tag{4.29}$$

$\mathbf{a}$ is the $\left(\sum_{p=1}^{n+1} p\right)$-dimensional coefficient vector, which can be expressed by

$$\mathbf{a} = \begin{bmatrix} a_{0,0} & a_{1,0} & a_{0,1} & \dots & a_{n,0} & \dots & a_{i,n-i} & \dots & a_{0,n} \end{bmatrix}^{\mathrm{T}} \tag{4.30}$$

and $\mathbf{z}$ is the MS vector of the damaged plate to be fit. Solving Eq. (4.57) for the coefficient vector is equivalent to solving an unconstrained least-squares problem $\min \frac{1}{2} \left\| \mathbf{V}\mathbf{a}^* - \mathbf{z} \right\|^2$ for an optimal minimizer $\mathbf{a}^*$,[112] which is usually an over-determined problem, i.e., $N > \sum_{p=1}^{n+1} p$. A solution can be obtained using the singular-value decomposition (SVD) of $\mathbf{V}$,[112] which gives

$$\mathbf{V} = \mathbf{U} \begin{bmatrix} S \\ 0 \end{bmatrix} \mathbf{W}^{\mathrm{T}} \tag{4.31}$$

where $\mathbf{U}$ and $\mathbf{W}$ are $N \times N$ and $\left(\sum_{p=1}^{n+1} p\right) \times \left(\sum_{p=1}^{n+1} p\right)$ orthogonal matrices, respectively, and $\mathbf{S}$ is a $\left(\sum_{p=1}^{n+1} p\right) \times \left(\sum_{p=1}^{n+1} p\right)$ diagonal matrix. An optimal minimizer $\mathbf{a}^*$ based on the SVD of $\mathbf{V}$ can be obtained by

$$\mathbf{a}^* = \mathbf{W}\mathbf{S}^{-1}\mathbf{U}_{\mathbf{1}}^{\mathrm{T}}\mathbf{z} \tag{4.32}$$

where $\mathbf{U}_1$ is the first $\sum_{p=1}^{n+1} p$ columns of $\mathbf{U}$. When n in Eq. (4.56) becomes a large value, $\mathbf{S}$ can be ill-conditioned, which can result in a low level of approximation of the associated polynomial fit. To avoid ill-conditioning of $\mathbf{S}$, it is proposed that x and y in Eq. (4.56) be normalized using the "center and scale" technique [113] before formulation of the linear equation in Eq. (4.57). Normalized coordinates $\tilde{x}$ and $\tilde{y}$ can be expressed by

$$\begin{cases} \tilde{x} = \frac{2x-2\bar{x}}{l_1} \\ \tilde{y} = \frac{2y-2\bar{y}}{l_2} \end{cases} \tag{4.33}$$

where $\bar{x}$ and $\bar{y}$ are x and y coordinates of the center point of the plate, respectively, and l_1 and l_2 are lengths of the plate along x- and y-axes, respectively.

An increase of n in the polynomial fit in Eq. (4.56) can improve the level of approximation of the resulting MS to that to be fit. To quantify the level of approximation, a fitting index fit in percentage, defined by

$$fit\,(n) = \frac{\mathrm{RMS}\,(\mathbf{z})}{\mathrm{RMS}\,(\mathbf{z}) + \mathrm{RMS}\,(\mathbf{e})} \times 100\% \tag{4.34}$$

is proposed, where $\mathrm{RMS}\,(\cdot)$ denotes the root-mean-square value of a vector and $\mathbf{e}$ is the error vector between the MS to be fit and the corresponding one from the current polynomial fit, i.e., $\mathbf{e} = \mathbf{z} - \mathbf{V}\mathbf{a}^*$. When the fitting index is close to 100%, the MS from the current polynomial fit is almost completely identical to $\mathbf{z}$; the lower the fitting index, the lower the level of approximation of the MS from the current polynomial fit. Fitting indices fit associated with $\mathbf{Z}^{d,31}$ for different n are shown in Fig. 4.63(a). It can be seen in Fig. 4.63(b) that fit converges to a certain value as n increases. To determine the proper order of a polynomial fit, a convergence index con for the polynomial fit with $n \geqslant 3$ is defined based on fit, which can be expressed by

$$con\,(n) = fit\,(n) - fit\,(n-2) \tag{4.35}$$

Convergence indices con associated with $\mathbf{Z}^{d,31}$ for different n are shown in Fig. 4.63(c). It can be seen that when n is larger than a certain value, con starts to decrease. When con is sufficiently small after its start of decrease, there is no significant improvement in the level of approximation of the polynomial fit. To determine a proper value of n, it is proposed that the value be the smallest one with which con is smaller than a prescribed threshold value. In this work, the prescribed threshold value for con is 0.50%. Hence the proper value of n associated with $\mathbf{Z}^{d,31}$ is determined to be 18, with which $con = 0.09\%$, as shown in Fig. 4.63(d). The difference between $\mathbf{Z}^{d,31}$ and the MS of the associated pseudo-undamaged plate from the polynomial fit with $n = 18$, denoted by $\mathbf{Z}^{p,31}$, is shown in Fig. 4.31, where abrupt changes can only be observed in and near the damage region.

4.2.2.3 MSDIs

The difference between a MS of a damaged plate and that of the associated pseudo-undamaged plate from a polynomial fit with a properly determined order can be processed for identifying the damage using a MSDI defined by

$$\delta\,(\mathbf{p}) = \left[\mathbf{Z}^{d,j}\,(\mathbf{p}) - \mathbf{Z}^{p,j}\,(\mathbf{p})\right]^2 \tag{4.36}$$

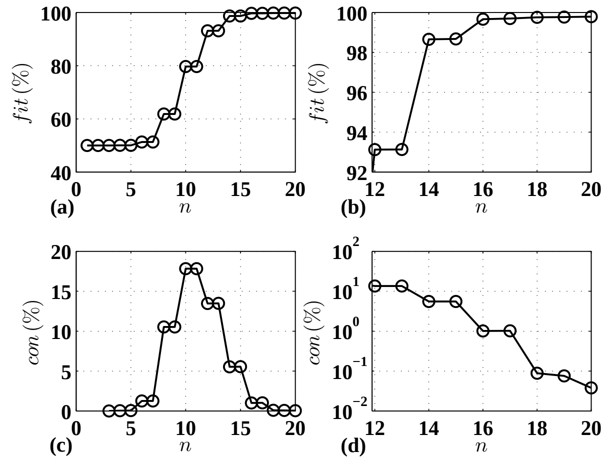

Figure 4.30: (a) Fitting index fit associated with $\mathbf{Z}^{d,31}$, (b) an enlarged view of fit, (c) con associated with $\mathbf{Z}^{d,31}$ and (d) an enlarged view of con.

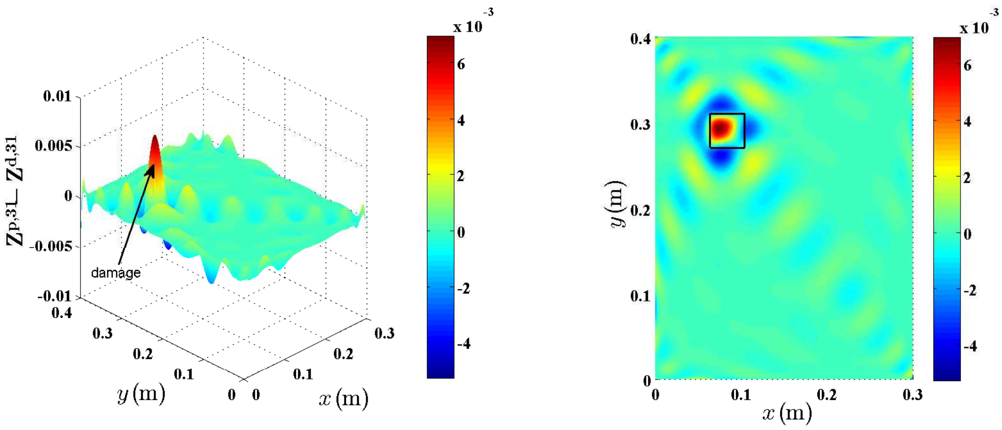

(a) (b)

Figure 4.31: (a) Difference between $\mathbf{Z}^{d,31}$ and $\mathbf{Z}^{p,31}$ and (b) the top view of (a) where the damage is outlined by solid lines.

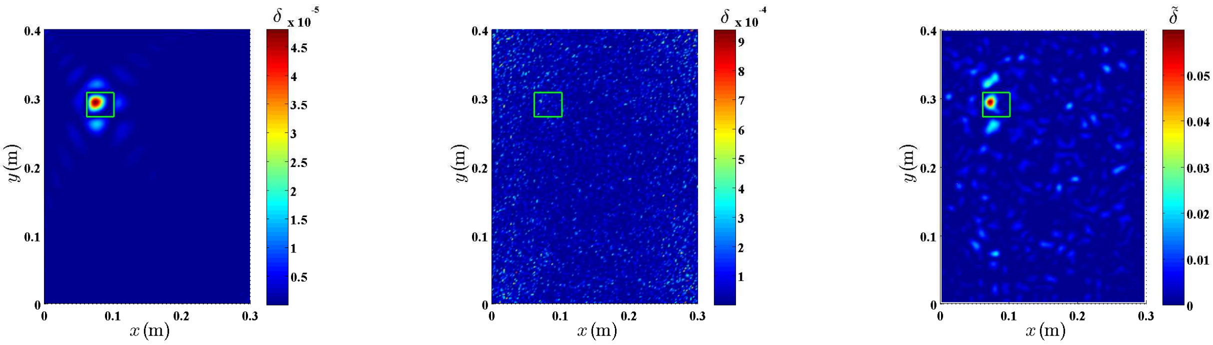

(a) (b) (c)

Figure 4.32: (a) MSDIs using the difference between noise-free $\mathbf{Z}^{d,31}$ and associated $\mathbf{Z}^{p,31}$, (b) MSDIs using the difference between $\mathbf{Z}^{d,31}$ with measurement noise and associated $\mathbf{Z}^{p,31}$ and (c) weighted MSDIs with $M_w = 7$ using the difference between $\mathbf{Z}^{d,31}$ with measurement noise and associated $\mathbf{Z}^{p,31}$; the damage is outlined by solid lines. SNRs of the MSs used in (b) and (c) are 40 db.

where $\mathbf{Z}^{p,j}$ is the MS of the pseudo-undamaged plate from a polynomial that fits $\mathbf{Z}^{d,j}$ with a properly determined order. MSDIs associated with noise-free $\mathbf{Z}^{d,31}$ and $\mathbf{Z}^{p,31}$ are shown in Fig. 4.32(a). It can be seen that the damage can be identified near regions with high values of MSDIs. Note that the density of a measurement grid of a MS determines the smallest size of identifiable damage. The denser the measurement grid, the smaller size of identifiable damage by MSDIs.

MSs are usually subject to measurement noise, and it can fuzz existence of damage in MSDIs, as shown in Fig. 4.32(b), where white noise is added to $\mathbf{Z}^{d,31}$ with a signal-to-noise ratio (SNR) of 40 db to simulate measurement noise; the damage can be hardly identified in the MSDIs. To manifest existence of damage in the proposed MSDIs, a two-dimensional discrete weight function is applied to the difference between the two MSs before calculating the MSDIs. The weight function for a mesh with square elements is expressed by

$$W_{M_w}(k_1, k_2) = e^{-4\left[\left(\frac{k_1}{M_w}\right)^2 + \left(\frac{k_2}{M_w}\right)^2\right]} \tag{4.37}$$

where M_w is the scale of the weight function, which is an integer; k_1 and k_2 are integer coordinates associated with x- and y-axes of the weight function, respectively, with $k_1,\ k_2 \in [-M_w, M_w]$. For a mesh with non-square elements, one can interpolate a MS on a mesh with square elements so that the weight function can have equal weights along x- and y-axes. An interpolation can also be conducted to obtain a MS on a finer mesh with better spatial resolution in resulting MSDIs. Weighted MSDIs $\tilde{\delta}(\mathbf{p})$ at a point $\mathbf{p}$ on a plate, based on the MSDI in Eq. (4.36), can be expressed by

$$\begin{aligned}\tilde{\delta}(\mathbf{p}) = \Big\{\textstyle\sum_{k_1=-M_w}^{M_w} \sum_{k_2=-M_w}^{M_w} \big[\big(\mathbf{Z}^{d,j}(\mathbf{p}_{k_1,k_2}) - \\ \mathbf{Z}^{p,j}(\mathbf{p}_{k_1,k_2})\big) \times W_{M_w}(k_1, k_2)\big]\Big\}^2\end{aligned} \tag{4.38}$$

where $\mathbf{p}_{k_1,k_2}$ is a point with x and y coordinates $(x_{\mathbf{p}} + k_1 \Delta d, y_{\mathbf{p}} + k_2 \Delta d)$, in which $x_{\mathbf{p}}$ and $y_{\mathbf{p}}$ are x and y coordinates of $\mathbf{p}$, respectively, and Δd is the side length of an element of the mesh. Weighted MSDI with $M_w = 7$ associated with $\mathbf{Z}^{d,31}$ are shown in Fig. 4.32(c). It can be seen that the weighted MSDIs are qualitatively similar to those associated with noise-free $\mathbf{Z}^{d,31}$, and the damage can be identified near regions with high values of the weighted MSDIs. Note that estimation of a damage depth cannot be achieved by MSDIs and weighted MSDIs since it requires use of an accurate model of a plate that is usually unavailable in practice.

4.2.3 Numerical Investigation

In this section, effects of SNRs in MSs on the proposed damage identification method and effectiveness of the methodology with use of different MSs are numerically investigated. The methodology is also numerically applied to identify small-sized damage with different M_w in Eq. (4.38) and using polynomial fits with different orders.

The method is applied to the plate shown in Fig. 4.56(a) to identify its damage using its normalized MSs of the 2nd, 12th, 25th, 27th and 28th elastic modes, denoted by $\mathbf{Z}^{d,2}$, $\mathbf{Z}^{d,12}$, $\mathbf{Z}^{d,25}$, $\mathbf{Z}^{d,27}$ and $\mathbf{Z}^{d,28}$, respectively, as shown in Fig. 4.33. White noise is added to the five MSs with a SNR of 40 db to simulate measurement noise. Fitting indices fit and convergence indices con associated with $\mathbf{Z}^{d,2}$, $\mathbf{Z}^{d,12}$, $\mathbf{Z}^{d,25}$, $\mathbf{Z}^{d,27}$ and $\mathbf{Z}^{d,28}$ for different n are shown in Figs. 4.34 through 4.38, respectively. Proper orders for polynomial fits associated with $\mathbf{Z}^{d,2}$, $\mathbf{Z}^{d,12}$, $\mathbf{Z}^{d,25}$, $\mathbf{Z}^{d,27}$ and $\mathbf{Z}^{d,28}$ are determined to be 8, 15, 17, 17 and 18, respectively. MSDIs from Eq. (4.36) associated with $\mathbf{Z}^{d,2}$, $\mathbf{Z}^{d,12}$, $\mathbf{Z}^{d,25}$, $\mathbf{Z}^{d,27}$ and $\mathbf{Z}^{d,28}$ are shown in Figs. 4.39(a), 4.40(a), 4.41(a), 4.42(a) and 4.43(a), respectively, and it can be seen that the damage can be hardly identified in the MSDIs due to measurement noise.

Weighted MSDIs from Eq. (4.38) with $M_w = 7$ associated with $\mathbf{Z}^{d,2}$, $\mathbf{Z}^{d,12}$, $\mathbf{Z}^{d,25}$, $\mathbf{Z}^{d,27}$ and $\mathbf{Z}^{d,28}$ are shown in Figs. 4.39(b), 4.40(b), 4.41(b), 4.42(b) and 4.43(b), respectively. Effects of the damage in $\mathbf{Z}^{d,25}$, $\mathbf{Z}^{d,27}$ and $\mathbf{Z}^{d,28}$ are manifested due to use of the weight function in Eq. (4.65), and the damage can be identified in the associated weighted MSDIs. However, the damage cannot be identified in the weighted MSDIs associated with $\mathbf{Z}^{d,2}$ and $\mathbf{Z}^{d,12}$ due to measurement noise. For comparison purposes, MSDIs associated with noise-free MSs $\mathbf{Z}^{d,2}$, $\mathbf{Z}^{d,12}$, $\mathbf{Z}^{d,25}$, $\mathbf{Z}^{d,27}$ and $\mathbf{Z}^{d,28}$ are calculated and shown in Figs. 4.39(c), 4.40(c), 4.41(c), 4.42(c) and 4.43(c), respectively. It can be seen that values of the MSDIs associated with noise-free $\mathbf{Z}^{d,2}$ and $\mathbf{Z}^{d,12}$ are relatively low compared with those associated with $\mathbf{Z}^{d,25}$, $\mathbf{Z}^{d,27}$, $\mathbf{Z}^{d,28}$ and $\mathbf{Z}^{d,31}$ in the damage region. Hence MSDIs associated with $\mathbf{Z}^{d,2}$ and $\mathbf{Z}^{d,12}$ are less sensitive to the damage and more vulnerable to measurement noise compared with the other four. The SNRs of $\mathbf{Z}^{d,2}$ and $\mathbf{Z}^{d,12}$ are then increased to 50 db. MSDIs from Eq. (4.36) and weighted MSDIs from Eq. (4.38) with $M_w = 7$ associated with $\mathbf{Z}^{d,2}$ and $\mathbf{Z}^{d,12}$ are calculated. While the damage cannot be identified in the MSDIs associated with the two MSs, as shown in Figs. 4.44(a) and 4.45(a), it can be in the weighted MSDIs associated with the two MSs, as shown in Figs. 4.44(b) and 4.45(b). Damage can become unidentifiable especially when there is relatively large measurement noise, and whether the damage can be identified in weighted MSDIs associated with MSs with measurement noise or not also depends on selection of MSs, since some MSs are more vulnerable to measurement noise as shown above. Hence one needs to use weighted MSDIs associated with different MSs to identify damage.

Based on the MSDIs associated with $\mathbf{Z}^{d,2}$, $\mathbf{Z}^{d,12}$, $\mathbf{Z}^{d,25}$, $\mathbf{Z}^{d,27}$, $\mathbf{Z}^{d,28}$ and $\mathbf{Z}^{d,31}$, it can be observed that use of MSDIs associated with one single elastic mode can identify the damage but it cannot yield accurate and complete estimation of the damage position and area; use of MSDIs associated with some of the MSs can. The reason is that each MS has portions that can be sensitive or insensitive to certain portions of the damage due to its relatively large area. In this case, left and right edges of the damage can be identified in the MSDIs associated with $\mathbf{Z}^{d,27}$, while top and bottom edges can be identified in the MSDIs associated with $\mathbf{Z}^{d,28}$. Hence the damage position and area can be accurately and completely estimated if the MSDIs associated with $\mathbf{Z}^{d,27}$ and $\mathbf{Z}^{d,28}$ are used. A similar observation can be made that the MSDIs associated with $\mathbf{Z}^{d,2}$, $\mathbf{Z}^{d,12}$, $\mathbf{Z}^{d,25}$ and $\mathbf{Z}^{d,31}$ indicate the lower, upper right, lower left and upper left portions of the damage, respectively, and the damage position and area can also be accurately and completely estimated if the MSDIs associated with $\mathbf{Z}^{d,2}$, $\mathbf{Z}^{d,12}$ and $\mathbf{Z}^{d,31}$ are used. Hence a damage position and area can be completely and accurately estimated using MSDIs associated with MSs of multiple elastic modes, but one cannot ensure that in practice since the damage position and area are unknown a priori.

A small-sized damage is then introduced to an undamaged steel plate with the same dimensions, boundary conditions and material properties as those of the damaged plate in Fig. 4.56(a). The damage is in the form of thickness reduction and its depth is 0.2 mm; the damage position and area are shown in Fig. 4.46(a). MSs of the 27th and 28th elastic modes of the damaged plate shown in Figs. 4.46(b) and (c), respectively, are used to identify the damage, and white noise is added to the MSs with a SNR of 40 db to simulate measurement noise. Proper orders for polynomial fits associated with the MSs of the 27th and 28th elastic modes are 17 and 18, respectively. MSDIs from Eq. (4.36) associated with the MSs of the 27th and 28th elastic modes are shown in Figs. 4.47(a) and 4.48(a), respectively, and the damage can be hardly identified in the MSDIs due to measurement noise. MSDIs

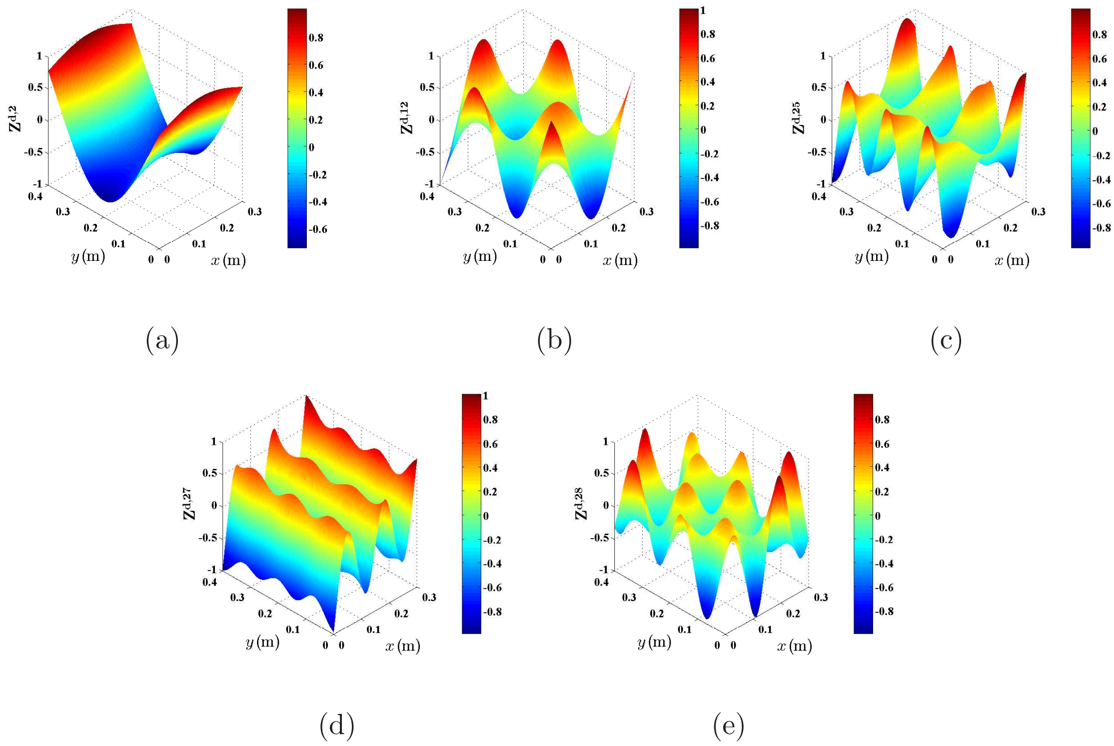

Figure 4.33: MSs of the (a) 2nd, (b) 12th, (c) 25th, (d) 27th and (e) 28th elastic modes of the damaged plate in Fig. 4.56(a).

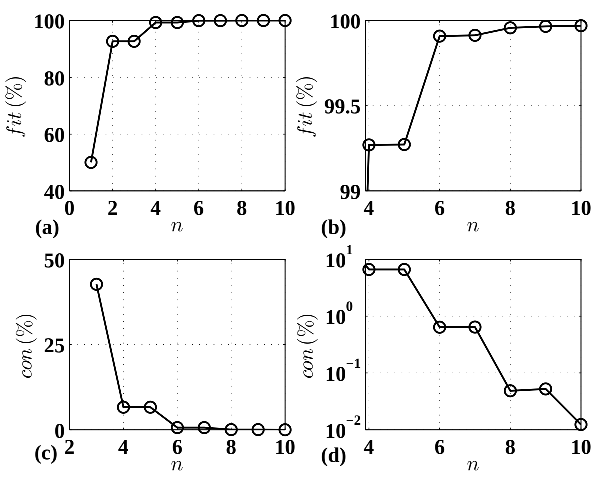

Figure 4.34: (a) Fitting index fit associated with $\mathbf{Z}^{d,2}$, (b) an enlarged view of fit, (c) con associated with $\mathbf{Z}^{d,2}$ and (d) an enlarged view of con.

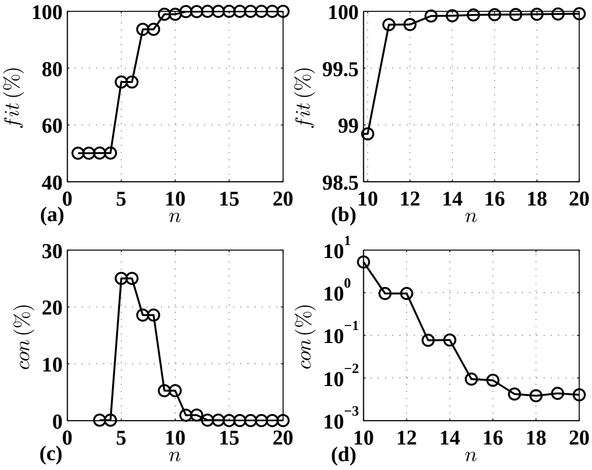

Figure 4.35: (a) Fitting index fit associated with $\mathbf{Z}^{d,12}$, (b) an enlarged view of fit, (c) con associated with $\mathbf{Z}^{d,12}$ and (d) an enlarged view of con.

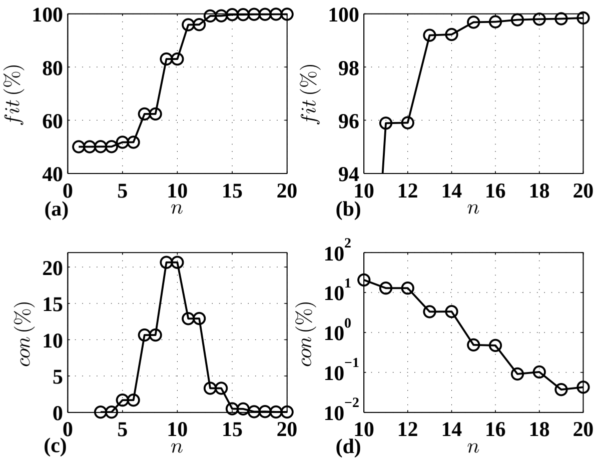

Figure 4.36: (a) Fitting index fit associated with $\mathbf{Z}^{d,25}$, (b) an enlarged view of fit, (c) con associated with $\mathbf{Z}^{d,25}$ and (d) an enlarged view of con.

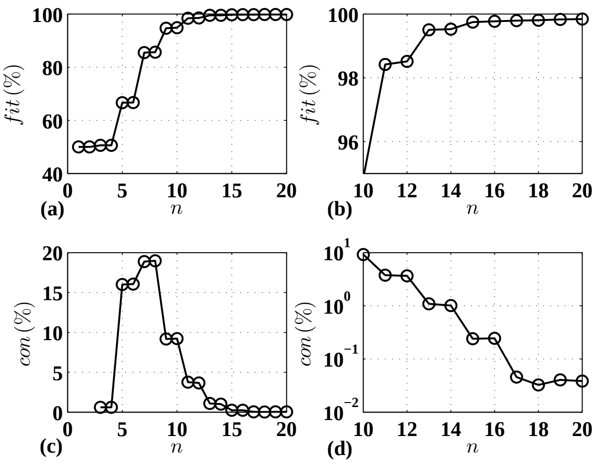

Figure 4.37: (a) Fitting index fit associated with $\mathbf{Z}^{d,27}$, (b) an enlarged view of fit, (c) con associated with $\mathbf{Z}^{d,27}$ and (d) an enlarged view of con.

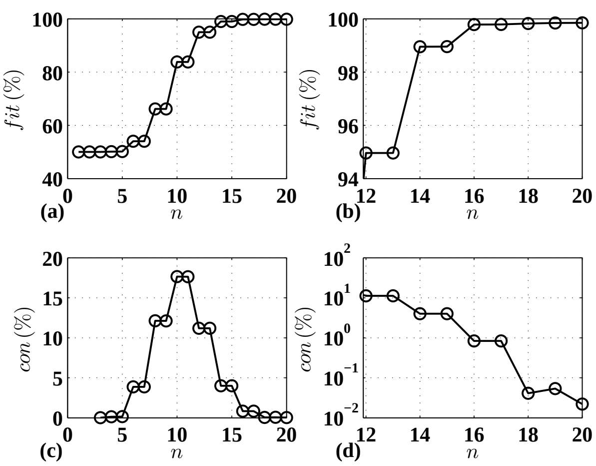

Figure 4.38: (a) Fitting index fit associated with $\mathbf{Z}^{d,28}$, (b) an enlarged view of fit, (c) con associated with $\mathbf{Z}^{d,28}$ and (d) an enlarged view of con.

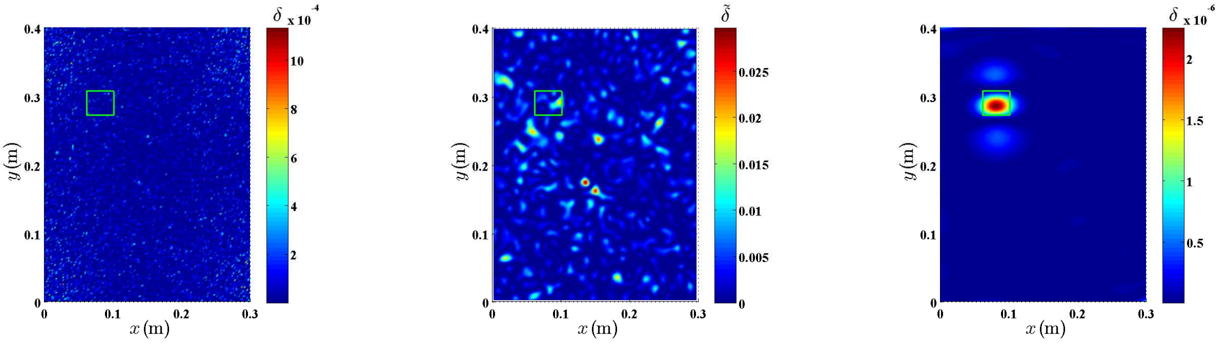

(a) (b) (c)

Figure 4.39: (a) MSDIs using the difference between $\mathbf{Z}^{d,2}$ with measurement noise and associated $\mathbf{Z}^{p,2}$, (b) weighted MSDIs with $M_w = 7$ using the difference between $\mathbf{Z}^{d,2}$ with measurement noise and associated $\mathbf{Z}^{p,2}$ and (c) MSDIs using the difference between noise-free $\mathbf{Z}^{d,2}$ and associated $\mathbf{Z}^{p,2}$; the damage is outlined by solid lines. SNRs of the MSs used in (a) and (b) are 40 db.

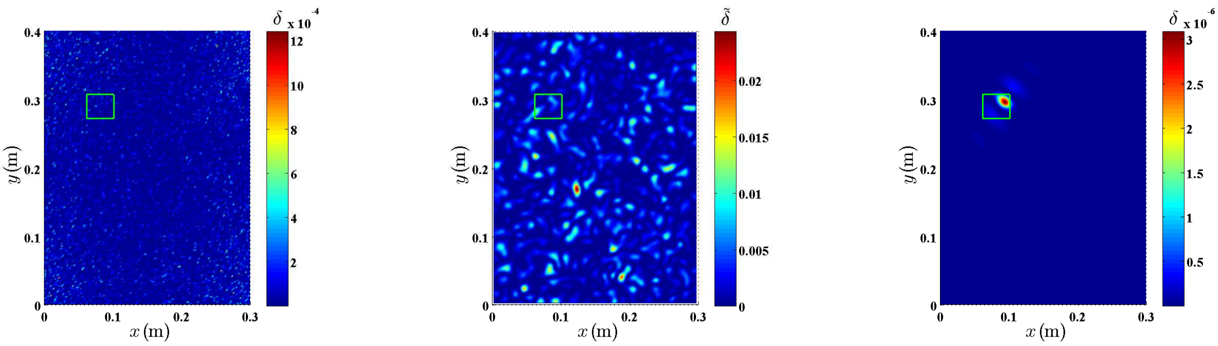

(a) (b) (c)

Figure 4.40: (a) MSDIs using the difference between $\mathbf{Z}^{d,12}$ with measurement noise and associated $\mathbf{Z}^{p,12}$, (b) weighted MSDIs with $M_w = 7$ using the difference between $\mathbf{Z}^{d,12}$ with measurement noise and associated $\mathbf{Z}^{p,12}$ and (c) MSDIs using the difference between noise-free $\mathbf{Z}^{d,12}$ and associated $\mathbf{Z}^{p,12}$; the damage is outlined by solid lines. SNRs of the MSs used in (a) and (b) are 40 db.

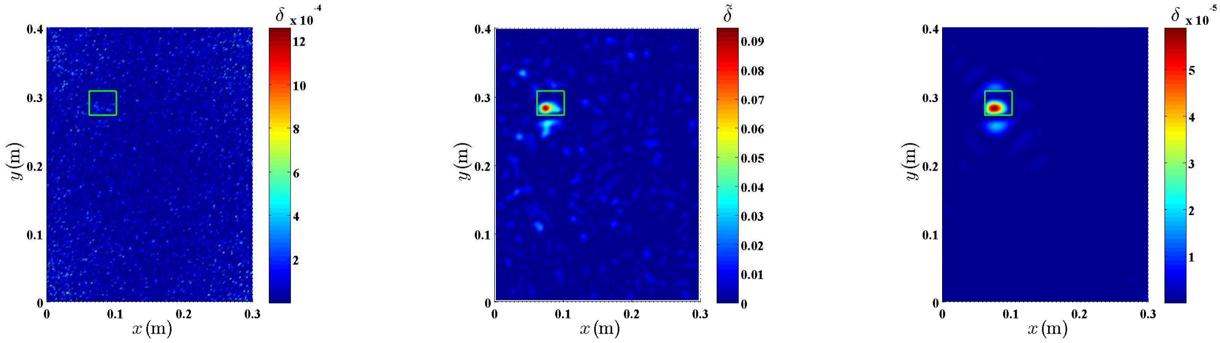

(a) (b) (c)

Figure 4.41: (a) MSDIs using the difference between $\mathbf{Z}^{d,25}$ with measurement noise and associated $\mathbf{Z}^{p,25}$, (b) weighted MSDIs with $M_w = 7$ using the difference between $\mathbf{Z}^{d,25}$ with measurement noise and associated $\mathbf{Z}^{p,25}$ and (c) MSDIs using the difference between noise-free $\mathbf{Z}^{d,25}$ and associated $\mathbf{Z}^{p,25}$; the damage is outlined by solid lines. SNRs of the MSs used in (a) and (b) are 40 db.

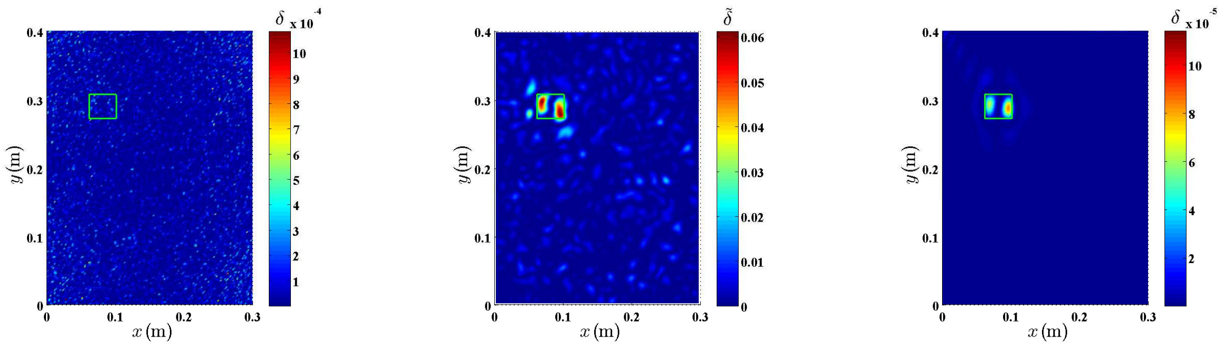

(a) (b) (c)

Figure 4.42: (a) MSDIs using the difference between $\mathbf{Z}^{d,27}$ with measurement noise and associated $\mathbf{Z}^{p,27}$, (b) weighted MSDIs with $M_w = 7$ using the difference between $\mathbf{Z}^{d,27}$ with measurement noise and associated $\mathbf{Z}^{p,27}$ and (c) MSDIs using the difference between noise-free $\mathbf{Z}^{d,27}$ and associated $\mathbf{Z}^{p,27}$; the damage is outlined by solid lines. SNRs of the MSs used in (a) and (b) are 40 db.

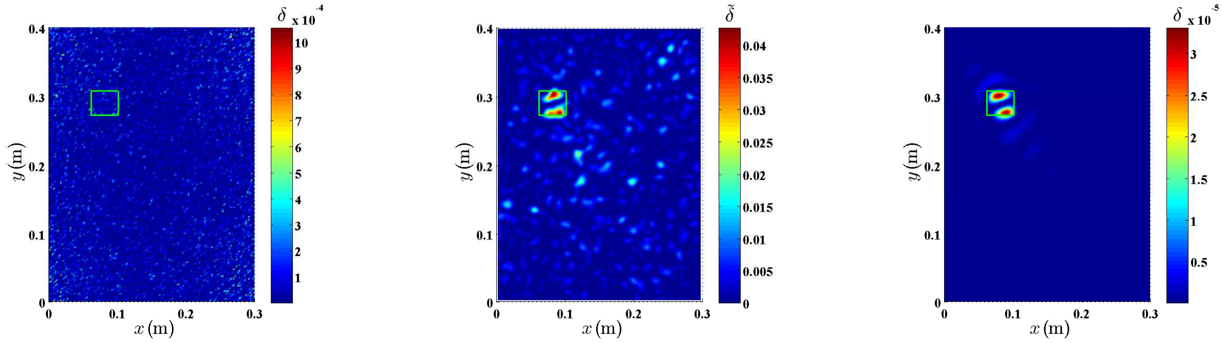

(a) (b) (c)

Figure 4.43: (a) MSDIs using the difference between $\mathbf{Z}^{d,28}$ with measurement noise and associated $\mathbf{Z}^{p,28}$, (b) weighted MSDIs with $M_w = 7$ using the difference between $\mathbf{Z}^{d,28}$ with measurement noise and associated $\mathbf{Z}^{p,28}$ and (c) MSDIs using the difference between noise-free $\mathbf{Z}^{d,28}$ and associated $\mathbf{Z}^{p,28}$; the damage is outlined by solid lines. SNRs of the MSs used in (a) and (b) are 40 db.

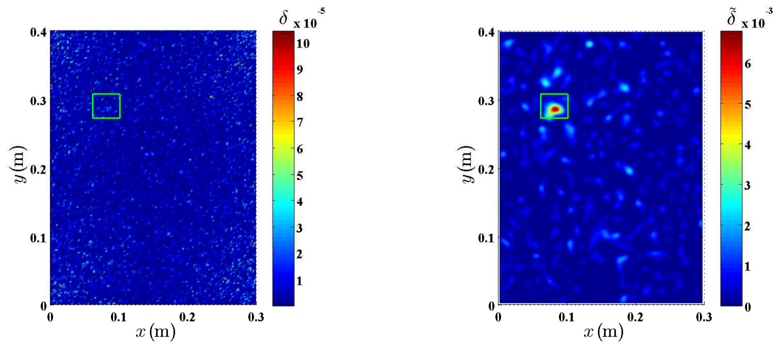

(a) (b)

Figure 4.44: (a) MSDIs using the difference between $\mathbf{Z}^{d,2}$ with measurement noise and associated $\mathbf{Z}^{p,2}$ and (b) weighted MSDIs with $M_w = 7$ using the difference between $\mathbf{Z}^{d,2}$ with measurement noise and associated $\mathbf{Z}^{p,2}$; the damage is outlined by solid lines. SNRs of the MSs used in (a) and (b) are 50 db.

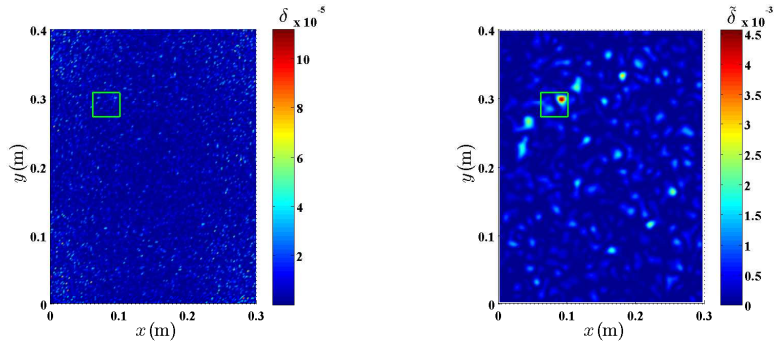

(a) (b)

Figure 4.45: (a) MSDIs using the difference between $\mathbf{Z}^{d,12}$ with measurement noise and associated $\mathbf{Z}^{p,12}$ and (b) weighted MSDIs with $M_w = 7$ using the difference between $\mathbf{Z}^{d,12}$ with measurement noise and associated $\mathbf{Z}^{p,12}$; the damage is outlined by solid lines. SNRs of the MSs used in (a) and (b) are 50 db.

associated with noise-free MSs of the 27th and 28th elastic modes are shown in Figs. 4.47(b) and 4.48(b), respectively, where the damage can be clearly identified.

Weighted MSDIs from Eq. (4.38) with $M_w = 3$ associated with the MSs of the 27th and 28th elastic modes are shown in Figs. 4.47(c) and 4.48(c), respectively. The damage position and area can be identified in the former, since relatively high values of MSDIs exist in the damage region; those cannot be in the latter. The scale of the weigh function in Eq. (4.65) is then increased to 7, weighted MSDIs associated with the MSs of the 27th and 28th elastic modes are shown in Figs. 4.47(d) and 4.48(d), respectively. Similarly, the damage position and area can be identified in the former, and those cannot be in the latter. It can be observed that effects of measurement noise on damage identification can be lowered with a higher M_n in the weighted MSDI in Eq. (4.38) since the weighted MSDIs with $M_w = 7$

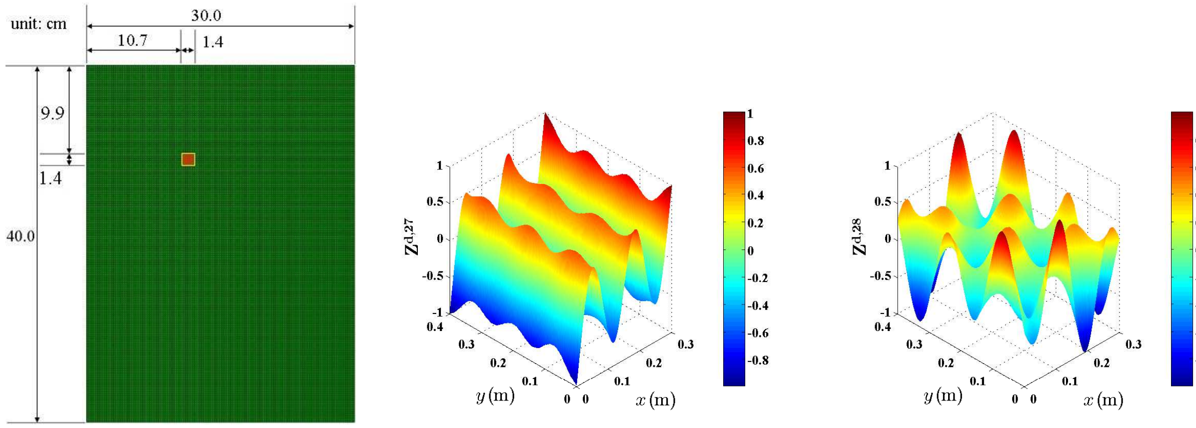

(a) (b) (c)

Figure 4.46: (a) FE model of a plate with damage in the form of a thickness reduction area and MSs of the (b) 27th and (c) 28th elastic modes of the damaged plate in (a).

in Fig. 4.47(d) are less fuzzy. However, a guideline to determine an optimal M_n would not exist. The reason is that whether damage exist in a plate or not and the position and area of the damage are unknown a priori in practice. Hence one needs to calculate weighted MSDIs with progressively increasing scales to identify damage. The scale of a weighted MSDI in Eq. (4.38) is analogous to the scale parameter in a continuous wavelet transform (CWT). The higher the scale parameter in the CWT, the smoother the CWT. In other words, adverse effects of noise in the CWT can be lowered by increasing its scale parameter. More details on the scale parameter in a CWT for damage identification are provided in Ref. 11.

Another observation can be made that the MS of the 27th elastic mode is sensitive to the damage but that of the 28th elastic mode is not. It can be validated by comparing MSDIs associated with the noise-free MSs. The MSDIs associated

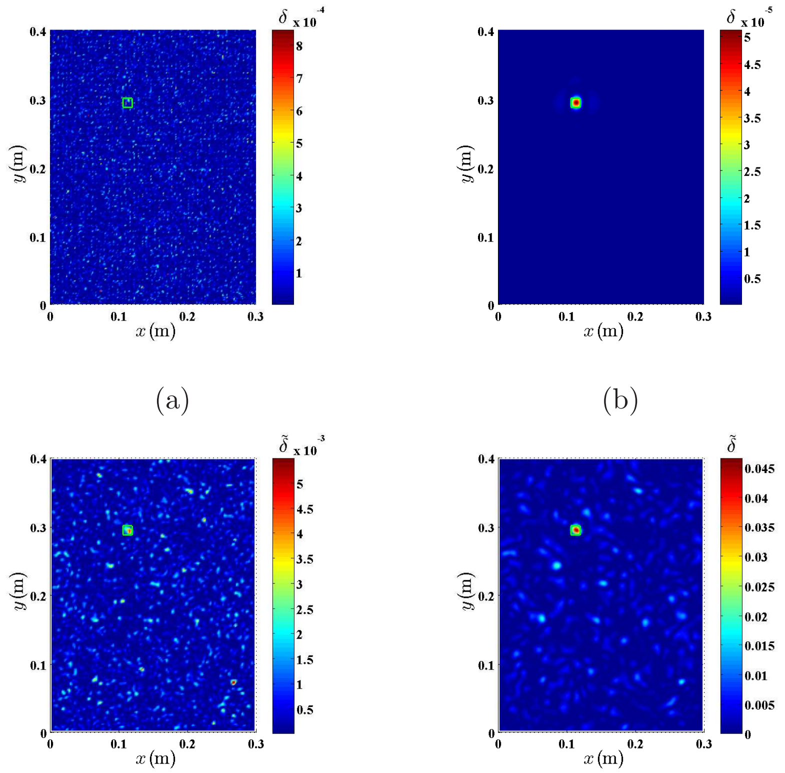

(a) (b) (c) (d)

Figure 4.47: (a) MSDIs using the difference between the MS of the 27th elastic mode of the damaged plate in Fig. 4.46(a) with measurement noise and that of the associated pseudo-undamaged plate, (b) MSDIs using the difference between the noise-free MS of the 27th elastic mode of the damaged plate and that of the associated pseudo-undamaged plate, (c) weighted MSDIs with $M_w = 3$ using the difference between the MS of the 27th elastic mode of the damaged plate with measurement noise and that of the associated pseudo-undamaged plate and (d) weighted MSDIs with $M_w = 7$ using the difference between the MS of the 27th elastic mode of the damaged plate with measurement noise and that of the associated pseudo-undamaged plate; the damage is outlined by solid lines. SNRs of the MSs used in (a), (c) and (d) are 40 db.

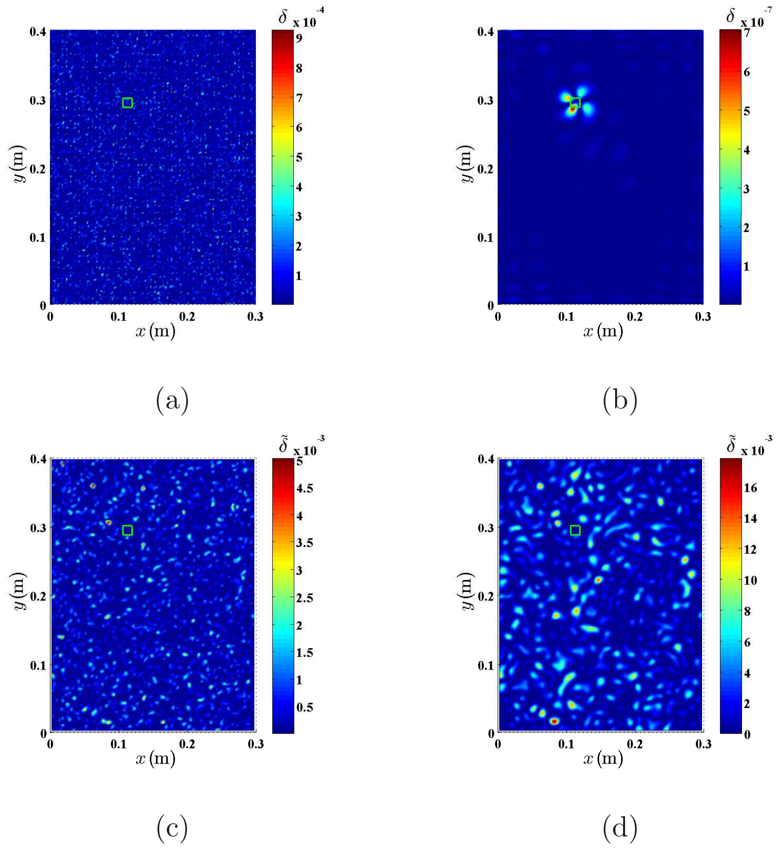

Figure 4.48: (a) MSDIs using the difference between the MS of the 28th elastic mode of the damaged plate in Fig. 4.46(a) with measurement noise and that of the associated pseudo-undamaged plate, (b) MSDIs using the difference between the noise-free MS of the 28th elastic mode of the damaged plate and that of the associated pseudo-undamaged plate, (c) weighted MSDIs with $M_w = 3$ using the difference between the MS of the 28th elastic mode of the damaged plate with measurement noise and that of the associated pseudo-undamaged plate and (d) weighted MSDIs with $M_w = 7$ using the difference between the MS of the 28th elastic mode of the damaged plate with measurement noise and that of the associated pseudo-undamaged plate; the damage is outlined by solid lines. SNRs of the MSs used in (a), (c) and (d) are 40 db.

with the noise-free MS of the 27th elastic mode can yield accurate estimation of the damage position and area, which indicates that this mode is sensitive to the whole damage. Four corners of the damage can be identified in the MSDIs associated with the noise-free MS of the 28th elastic mode, which indicates that this mode is sensitive to the corners of the damage. However, values of the MSDIs associated with the MS of the 28th elastic mode are relatively low compared with those associated with the MS of the 27th elastic mode in the damage region; hence MSDIs associated with the MS of the 28th elastic mode are less senstive to the damage and more vulnerable to measurement noise compared with those associated with the MS of the 27th elastic mode.

When orders for polynomials that fit the noise-free MS of the 27th elastic mode of the damaged plate are 11 and 14, MSs of associated pseudo-undamaged plates are calculated and shown in Figs. 4.49(a) and (b), respectively. MAC values in percentage between the MS from the polynomial fit with $n = 11$ and that to be fit and between the MS from the polynomial fit with $n = 14$ and that to be fit are 99.979% and 99.998%, respectively, which indicates that the two MSs of the pseudo-undamaged plates both well approximate that to be fit. However, the damage cannot be identified in MSDIs using differences between the noise-free MS of the 27th elastic mode of the damaged plate and the MSs from the polynomial fits with $n = 11$ and $n = 14$, as shown in Fig. 4.49(c) and (d), respectively. When the order for a polynomial that fits the noise-free MS of the 27th elastic mode of the damaged plate is 27, the MS of the associated pseudo-undamaged plate is calculated and shown in Figs. 4.49(e). The MAC value in percentage between the MS from the polynomial fit with $n = 27$ and that to be fit is close to 100.00%. The damage can be clearly identified in MSDIs using the difference between the two MSs, as shown in Fig. 4.49(f). It can be seen that the damage can be unidentifiable when the order for a polynomial fit is smaller than its proper value, since it underfits the MS to be fit and effects of the damage cannot be manifested in associated MSDIs. However, when the order is larger than its proper value, damage can still be identified in associated MSDIs due to two facts. One is that the associated fitting index converges when the order is sufficiently large, i.e., increasing the order cannot change the level of approximation of a polynomial fit much. The other is that effects of damage on a MS is assumed to be small and cannot be included in a polynomial fit unless its order is unreasonably large, which can lead to numerical issues in solving the equation in Eq. (4.57).

4.2.4 Experimental Investigation

4.2.4.1 Experimental Setup

A rectangular damaged aluminum plate that had a length of 500.00 mm, a width of 400.00 mm and a thickness of 4.75 mm was constructed; its dimensions are shown in Fig. 4.76(a). The plate was hung using two nylon cords to simulate free boundary conditions, as shown in Fig. 4.76(b). The damage was a square, machined thickness reduction area, which had a side length of 40.00 mm and a depth of 0.5 mm; the depth was about 10% of the thickness of the undamaged portion of the plate, as shown in Fig. 4.76(c). In order to validate the simulated free boundary

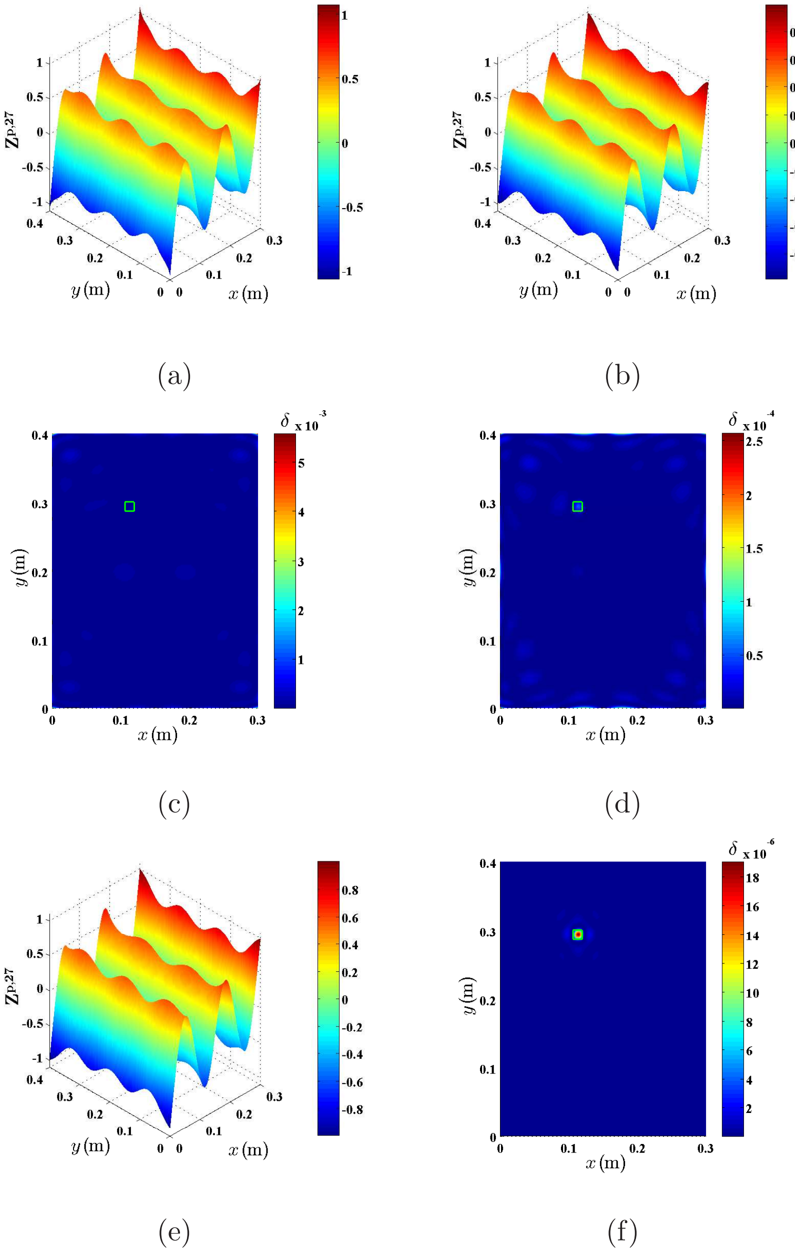

Figure 4.49: (a) MS of a pseudo-undamaged plate from a polynomial that fits the MS of the 27th elastic mode of the damaged plate in Fig. 4.46(a) with $n = 11$, (b) the MS of a pseudo-undamaged plate from a polynomial that fits the MS of the 27th elastic mode of the damaged plate with $n = 14$, (c) MSDIs using the difference between the MS of the 27th elastic mode of the damaged plate and that in (a), (d) MSDIs using the difference between the MS of the 27th elastic mode of the damaged plate and that in (b), (e) the MS of a pseudo-undamaged plate from a polynomial that fits the MS of the 27th elastic mode of the damaged plate with $n = 27$ and (f) MSDIs using the difference between the MS of the 27th elastic mode of the damaged plate and that in (e).

conditions of the plate, an EMA was performed, where a PCB 086-D80 miniature impact hammer and a Polytec PSV-500 scanning laser Doppler vibrometer (SLDV) were used to excite the plate and measure its response, respectively (Fig. 4.76(b)). In EMA, a fixed excitation point was impacted using the hammer, and the response of a measurement point was measured to yield five FRFs from five different impacts, which were averaged and analyzed using PolyMax of LMS Test.Lab Rev.9b to obtain natural frequencies of the plate. The lowest measured elastic natural frequency of the plate was 76.5 Hz. Since the highest measured natural frequency of rigid-body modes of the plate in the setup was 2.1 Hz, which was much less than 10% of its lowest measured elastic natural frequency, the simulated free boundary conditions were validated.[1] A rectangular measurement area was assigned on a surface of the plate for MS measurements; the surface was opposite to the damaged one, and the area had a length of 488.1 mm and a width of 395.9 mm, as shown in Fig. 4.76(d). The rectangular area is slightly smaller than that of the plate in that there were two holes drilled on two top corners of the plate for hanging and clearances between edges of the plate and the rectangular measurement area were reserved to prevent the laser of the SLDV from reaching edges of the plate and the two holes. The measurement area was sprayed with spot checker to enhance laser reflection that directly determined SNRs of laser measurements.

In order to accurately measure MSs of the damaged plate without incurring unwanted mass loading, non-contact excitation and measurements were performed,[114] as shown in Figs. 4.76(b) and (e): an electric speaker with a wood box faced the damaged surface of the plate and generated acoustic excitation onto it, and the

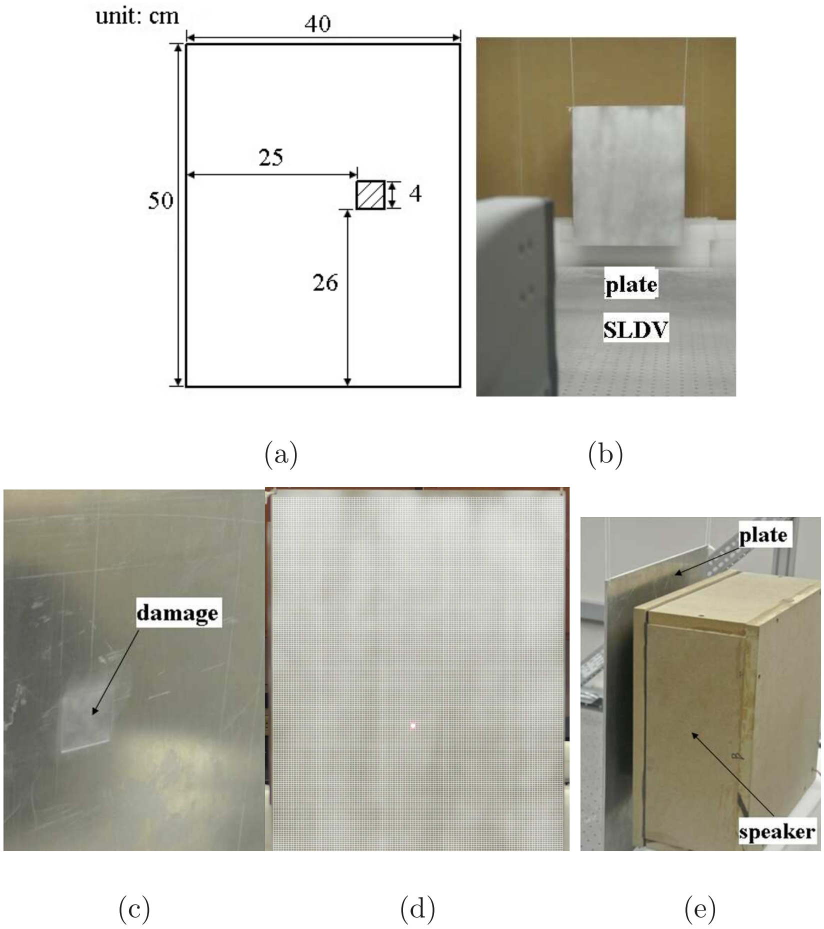

Figure 4.50: (a) Dimensions of the damaged plate, (b) the test setup for response measurements of the measurement surface, (c) the damaged surface of the plate, (d) the measurement grid on the measurement surface and (e) the electric speaker facing the damaged surface.

SLDV measured velocities of measurement points in the measurement area. There were a total of 115×177 measurement points in the measurement grid, whose elements were rectangular and had a length of 3.44 mm and a width of 2.76 mm, as shown in Fig. 4.76(d). Acoustic excitation in the form of a sine wave was used to excite the plate, and velocities of the measurement points were measured using the "FastScan" mode of the SLDV system, where the bandwidth was equal to an excitation frequency and 80 averages were used for each measurement point. The 24th and 25th MSs of the damaged plate at natural frequencies of 1349 Hz and 1405 Hz, denoted by $\mathbf{Z}^{exp,1}$ and $\mathbf{Z}^{exp,2}$, respectively, were measured with excitation frequencies of 1349 Hz and 1405 Hz, respectively, to experimentally validate the proposed methodology; the measurement time of each MS was about 23 minutes. In order to transform the current measurement grid to one with square elements and increase the spatial resolution of MSDIs, $\mathbf{Z}^{exp,1}$ and $\mathbf{Z}^{exp,2}$ were interpolated using the MATLAB function "griddata" with the option "natural" on a measurement grid with 199×245 measurement points, which had square elements with a side length of 1.99 mm, as shown in Fig. 4.77(a) and (b), respectively. For simplicity, the interpolated $\mathbf{Z}^{exp,1}$ and $\mathbf{Z}^{exp,2}$ are hereafter denoted by $\mathbf{Z}^{exp,1}$ and $\mathbf{Z}^{exp,2}$, respectively.

4.2.4.2 Experimental Damage Identification Results

To determine proper orders for polynomials to fit $\mathbf{Z}^{exp,1}$ and $\mathbf{Z}^{exp,2}$, fit associated with $\mathbf{Z}^{exp,1}$ and $\mathbf{Z}^{exp,2}$ for different n were calculated and shown in Figs. 4.81(a) and 4.53(a), respectively. Similar to the numerical examples in Secs. 2 and 3, fit

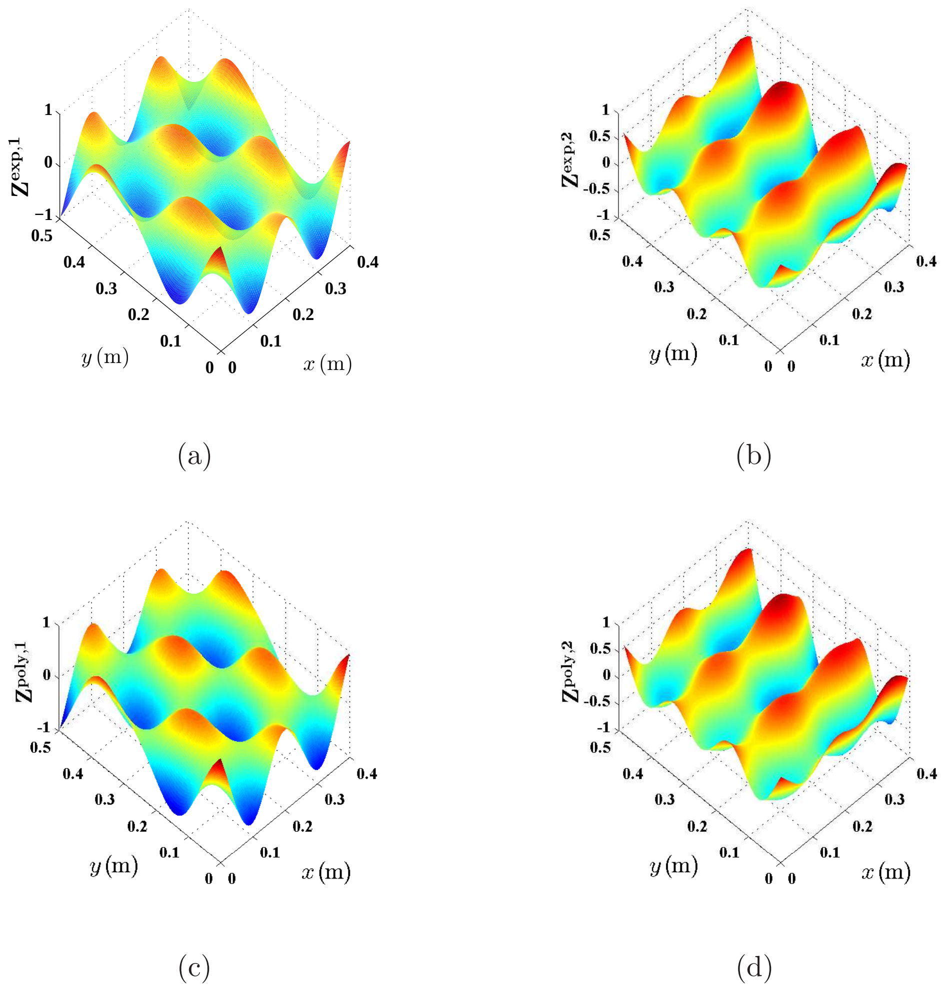

Figure 4.51: (a) Measured $\mathbf{Z}^{exp,1}$ of the damaged plate at the natural frequency of 1349 Hz, (b) $\mathbf{Z}^{exp,2}$ of the damaged plate at the natural frequency of 1405 Hz, (c) the MS of the associated pseudo-undamaged plate from a polynomial that fits $\mathbf{Z}^{exp,1}$ with $n = 15$ and (d) that of the associated pseudo-undamaged plate from a polynomial that fits $\mathbf{Z}^{exp,2}$ with $n = 16$.

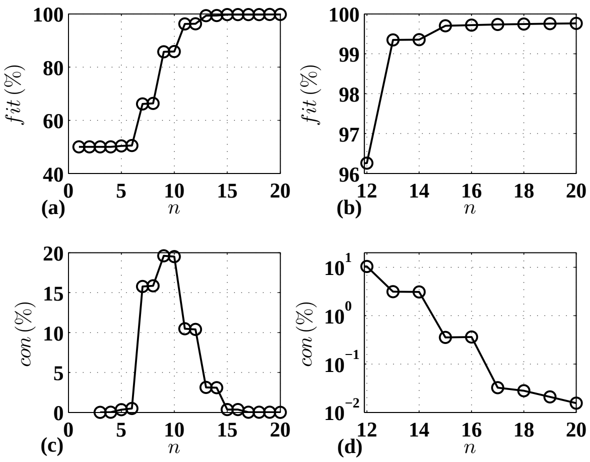

Figure 4.52: (a) Fitting indices fit associated with $\mathbf{Z}^{exp,1}$, (b) an enlarged view of fit, (c) the convergence indices con associated with $\mathbf{Z}^{exp,1}$ and (d) an enlarged view of con.

associated with the two MSs converged to certain values as n increased, as shown in Figs. 4.81(b) and 4.53(b). Associated con for different n were calculated and shown in Figs. 4.81(c) and 4.53(c). The proper orders of the polynomials to fit $\mathbf{Z}^{exp,1}$ and $\mathbf{Z}^{exp,2}$ were determined to be 15 and 16, respectively, since $con = 0.35\%$ for $\mathbf{Z}^{exp,1}$ and $con = 0.13\%$ for $\mathbf{Z}^{exp,2}$, which were lower than the prescribed threshold value, as shown in Figs. 4.81(d) and 4.53(d), respectively. MSs of the associated pseudo-undamaged plate from the polynomials that fit $\mathbf{Z}^{exp,1}$ and $\mathbf{Z}^{exp,2}$ are shown in Figs. 4.77(c) and (d), respectively; MAC values between $\mathbf{Z}^{exp,1}$ and the MS from the associated polynomial and between $\mathbf{Z}^{exp,2}$ and that from the associated polynomial were both 99.99%.

MSDIs associated with $\mathbf{Z}^{exp,1}$ and $\mathbf{Z}^{exp,2}$ are shown in Figs. 4.54(a) and (b), respectively; high values of MSDIs could be observed in the damage region while

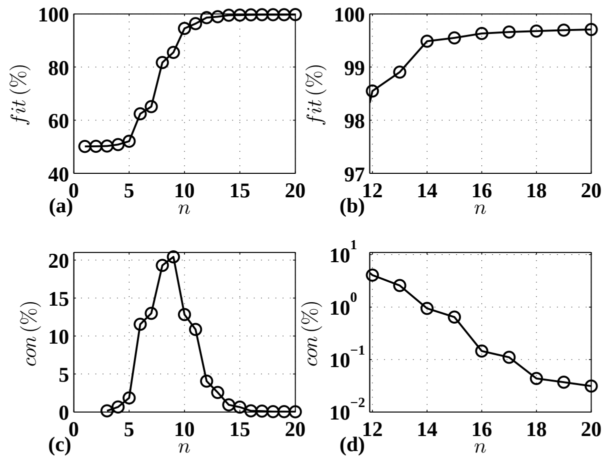

Figure 4.53: (a) Fitting indices fit associated with $\mathbf{Z}^{exp,2}$, (b) an enlarged view of fit, (c) the convergence indices con associated with $\mathbf{Z}^{exp,2}$ and (d) an enlarged view of con.

some regions with lower values of MSDIs could also be observed outside the region, which were caused by measurement noise. Weighted MSDIs with $M_w = 7$ associated with $\mathbf{Z}^{exp,1}$ and $\mathbf{Z}^{exp,2}$ are shown in Figs. 4.54(c) and (d), respectively; high values of MSDIs could be observed in the damage region and smaller regions with lower values of weighted MSDIs could be observed due to use of the weight function. One could identify the damage near regions with consistently high values of MSDIs.

MSDIs associated with uninterpolated $\mathbf{Z}^{exp,1}$ and $\mathbf{Z}^{exp,2}$ are shown in Figs. 4.55(a) and (b), respectively. Similar to Figs. 4.54(a) and (b), high values of MSDIs could be observed in the damage region while some regions with lower values of MSDIs that were caused by measurement noise could be observed outside the region. However, one cannot properly calculate weighted MSDIs to alleviate effects of measurement noise in that the elements of the measurement grid of uninterpolated

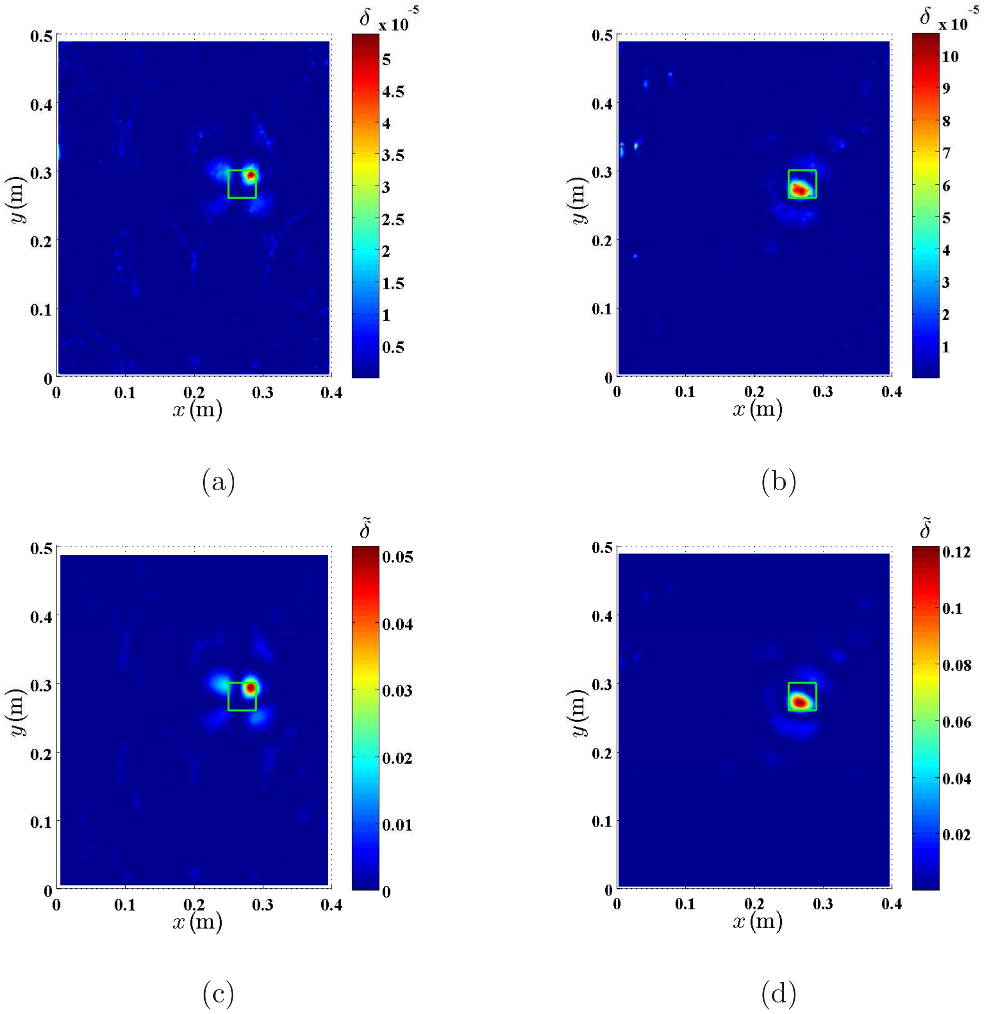

Figure 4.54: (a) MSDIs associated with $\mathbf{Z}^{exp,1}$, (b) those associated with $\mathbf{Z}^{exp,2}$, (c) weighted MSDIs with $M_w = 7$ associated with $\mathbf{Z}^{exp,1}$ and (d) those associated with $\mathbf{Z}^{exp,2}$.

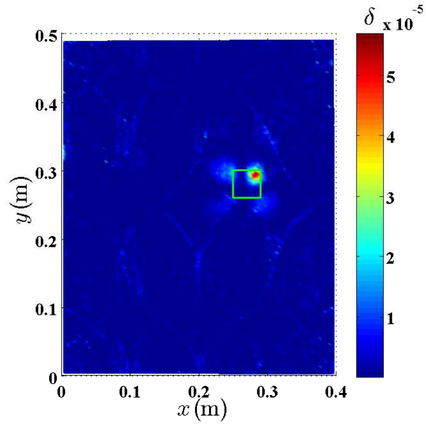

(a)

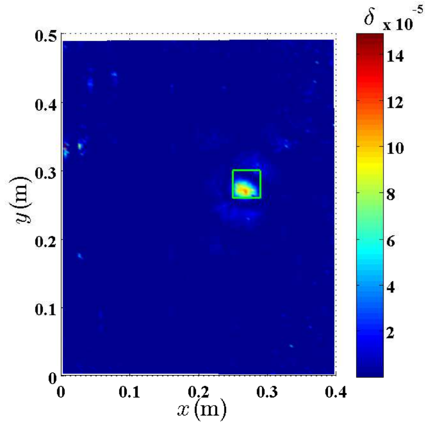

(b)

Figure 4.55: (a) MSDIs associated with uninterpolated $\mathbf{Z}^{exp,1}$ and (b) those associated with uninterpolated $\mathbf{Z}^{exp,2}$.

$\mathbf{Z}^{exp,1}$ and $\mathbf{Z}^{exp,2}$ were rectangular and spatial weights in x- and y-axes of the weight function in Eq. (4.65) would be different, which violates its definition. The weights would be the same only when elements of a measurement grid are square. Hence it is recommended that an interpolation operation be conducted to transform a measurement grid with non-square elements to one with square elements.

4.2.5 Conclusion

A new non-model-based plate damage identification method using measured MSs is proposed. The method can be applied to a damaged plate without use of MSs of the associated undamaged plate, if the undamaged plate is geometrically smooth and made of materials that have no stiffness and mass discontinuities. Use of differences between MSs of a damaged plate and those of an associated pseudo-undamaged plate from polynomials that fit the MSs of the damaged plate is shown to be better than that between MSs of a damaged plate and those of an associated undamaged plate with respect to effectiveness of damage identification. A proper order of a polynomial fit can be determined as proposed; a polynomial fit with an order lower than the proper order for MSDIs cannot be used to identify damage and that with an order reasonably higher than the proper order can be. MSDIs associated with a MS can be used to identify damage or portions of the damage, and whether damage can be identified in MSDIs associated with a MS or not depends on the MS itself, since the MS can be insensitive to the damage and vulnerable to measurement noise. Adverse effects of measurement noise on MSDIs can be alleviated using the weight function, and one needs to progressively increase the scale of the function to lower the adverse effects and identify damage. The proposed methodology was experimentally applied to a plate with damage in the form of a machined thickness reduction area. The damage was successfully identified near regions with consistently high values of MSDIs associated with MSs of different modes.

4.3 Damage Identification of Plates Using Principal, Mean and Gaussian Curvature Mode Shapes

4.3.1 Introduction

Vibration-based damage detection has been a major research topic of structural dynamics in the past few decades. Measured modal characteristics, such as natural frequencies and mode shapes, are processed in various methods for detecting, locating and characterizing damage in structures, since modal characteristics are related to physical properties of structures, such as mass, stiffness and damping, which can change due to damage. A method can be categorized as a model-based or non-model-based method; the difference between them is that the former requires use of an accurate model of a structure and the latter does not. A method that only requires a minimum amount of measured natural frequencies was developed to accurately detect locations and extent of damage in such structures as lightening masts [82, 83], space frames [115] and pipelines [116]. It is model-based and requires an accurate physics-based model of a structure, and effectiveness of the method highly depend on accuracy of the model of the structure. However, it can be difficult to construct models of most structures that can accurately predict their natural frequencies before and after occurrence of damage.

Methods that use measured mode shapes to identify damage in a structure can be good alternatives. While effects of damage on natural frequencies are global, those on mode shapes are local; abrupt changes in mode shapes in the neighborhood of damage can be observed. A two-dimensional gapped smoothing method was developed based on a one-dimensional gapped smoothing method [88]. Curvature mode shapes (CMSs) and curvatures of operating deflection shapes were used in the two-dimensional method to identify damage in plates [106], where mode shapes of an undamaged plate were not needed. A gapped polynomial fitting the curvatures was used to eliminate global trends of CMSs and curvatures of operating deflection shapes at each measurement point. A method that used curvatures of frequency-shift surfaces of plates to identify damage was proposed in Ref. [107]; curvatures of frequency-shift surfaces of associated undamaged plates could be obtained using a technique of locally weighted regression. It was shown to be better than the two-dimensional gapped smoothing method, since a frequency-shift surface contained information of a squared mode shape. A CMS-based method was proposed in Ref. [108], where a CMS of a plate based on an average curvature was calculated using a wavelet transform to alleviate adverse effects of measurement noise on the CMS and a Teager energy operator was applied to the CMS at each measurement point to eliminate the global trend of the transformed CMS. The mode shape-based methods mentioned above are local ones, and their common disadvantage is that they can be computationally inefficient, especially for a large and dense measurement grid, since the global trend of a curvature is locally eliminated in a point-by-point manner. A simplified gapped smoothing method, a generalized fractal dimension method and a strain energy method were used to detect delamination in a composite plate [110], and the methods there are also local ones and can be computationally inefficient. Changes in curvatures of uniform-load surfaces were used to identify damage in plates; the curvatures were shown to be sensitive to presence of local damage, even with truncated, incomplete and noisy measurements [109]. The method in Ref. [109] used natural frequencies and mode shapes of the first few modes of damaged and undamaged plates, but those of undamaged plates can be unavailable in practice. Mean and Gaussian curvature shapes of three-dimensional digital models of structures obtained by a terrestrial laser scanner were used to identify mass loss of concrete via piecewise comparisons of distributions of the curvature shapes [117]. A limitation of the method is that only surface damage can be identified. Besides curvature-based methods, wavelet transform-based methods have been widely studied to identify damage in plates [118, 119, 120]. Gabor wavelets were used to identify damage in a rectangular plate [118]; effects of various wavelets on identifying damage, such as Haar, Daubechies, Gaussian and Coiflet wavelets, were studied and compared in Ref. [119]. Depths of cracks in plates could be detected using a wavelet transform-based method with the aid of models of undamaged plates [120]. However, whether damage can be identified using a wavelet transform-based method depends on the type and parameters of an applied wavelet. Changes in the strain energy of a structure have been used to identify damage; the method was extended from the one for beams [121], which require mode shapes of damaged and undamaged structures. A two-dimensional polynomial annihilation edge detection method was proposed for detection and localization of damage in plates [111]; it was extended from the one for beams, which can detect discontinuities in piecewise smooth functions and their derivatives [84]. The limitation of the method is that only edges of damage could be identified.

A non-model-based method based on principal, mean and Gaussian CMSs is proposed in this work to identify damage in plates. Theoretical bases of principal CMSs of a plate are shown. A multi-scale discrete differential-geometry scheme is proposed to calculate principal, mean and Gaussian CMSs associated with a mode shape of a plate, which can alleviate adverse effects of measurement noise on calculating the CMSs. Principal CMSs are directly related to principal stresses of a deformed plate, and mean and Gaussian CMSs can quantify differential-geometry features of a mode shape of the plate. Differences between principal, mean and

Gaussian CMSs of a damaged plate and those of the associated undamaged one are used to yield four curvature damage indices (CDIs), including Maximum-CDI, Minimum-CDI, Mean-CDI and Gaussian-CDI. Global trends of the CMSs are eliminated in a global manner and can be computationally more efficient than the local methods. A mode shape from a polynomial of a properly determined order that fits a mode shape of a damaged plate can be used to approximate the corresponding mode shape of the associated undamaged one, provided that the undamaged plate has a smooth geometry and is made of material that has no stiffness and mass discontinuities. Fitting and convergence indices are introduced to assist determination of the proper order of the polynomial fit. A weight function is applied to the proposed CDIs to alleviate adverse effects of measurement noise on the CDIs and manifest existence of damage in the CDIs. The applicability and robustness of the proposed method to a mode shape of a low elastic mode on a coarse measurement grid are numerically investigated. An aluminum plate with damage in the form of a machined thickness reduction area was constructed, and a mode shape of the damaged plate was measured using non-contact excitation and measurement to investigate effectiveness of the proposed method. The mode shape associated with the same mode as that of the measured mode shape from a finite element model of the damaged plate was used to numerically verify the experimental damage identification results.

4.3.2 Methodology

A finite element model of a damaged rectangular steel plate that has a length of 0.3 m, a width of 0.4 m and a thickness of 0.002 m is constructed using commercial finite element software ABAQUS; the model has a total of 150×200 square plate elements. The damage is in the form of a thickness reduction area, and its position and dimensions are shown in Fig. 4.56(a); the depth of the thickness reduction area is 0.0002 m. The mass density, elastic modulus and Poisson's ratio of the plate are 7850 kg/m^3, 200 GPa and 0.3, respectively. A finite element model of an undamaged plate of the same dimensions and material properties as those of the damaged plate is also constructed, which has the same number of square plate elements as that of the damaged one. To demonstrate the proposed method, undamped mode shapes of the damaged and undamaged plates associated with their 23-rd elastic modes are calculated and denoted by $\mathbf{Z}^{d,23}$ and $\mathbf{Z}^{u,23}$, respectively; $\mathbf{Z}^{d,23}$ and $\mathbf{Z}^{u,23}$ are in the same phase, and they are normalized so that their maximum absolute values are equal to one. Mode shapes $\mathbf{Z}^{d,23}$ and $\mathbf{Z}^{u,23}$ are shown in Figs. 4.56(b) and (c), respectively.

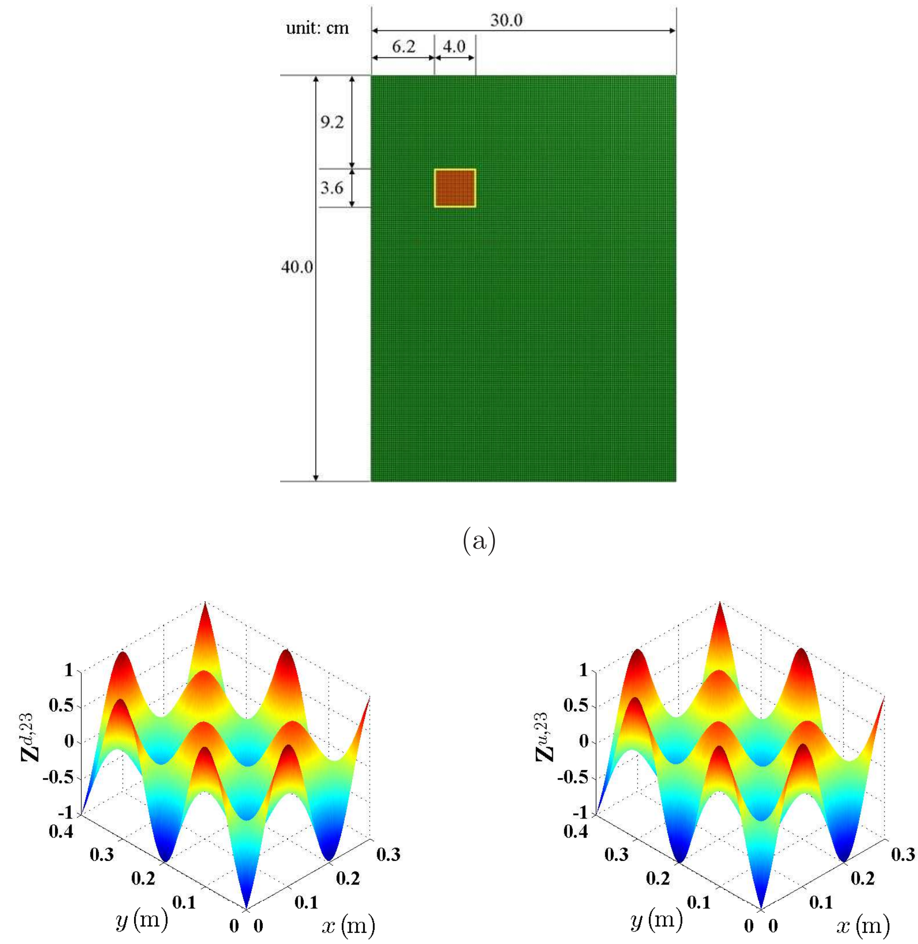

(a)

(b) (c)

Figure 4.56: (a) Finite element model of a plate with damage in the form of a thickness reduction area, (b) the 23-rd mode shape of the damaged plate and (c) the 23-rd mode shape of an undamaged plate of the same dimensions and material properties as the damaged one.

4.3.2.1 Principal CMSs of Plates

While the curvature at a point on a mode shape of a one-dimensional structure, such as a beam, is defined along the length of the structure, that on a mode shape of a plate is defined on a unit vector tangent to the mode shape at the point, and its value depends on not only the mode shape but the unit vector. The curvature at a point $\mathbf{p}$ on a mode shape $\mathbf{Z}$ shown in Fig. 4.57 with respect to a unit vector $\mathbf{v}$ tangent to $\mathbf{Z}$ at $\mathbf{p}$ is defined by [122]

$$\kappa_{\mathbf{Z},\mathbf{p}}(\mathbf{v}) = -(\nabla_{\mathbf{v}}\mathbf{n}) \cdot \mathbf{v} \tag{4.39}$$

where $\mathbf{n}$ is a unit normal vector field in the neighborhood of $\mathbf{p}$ on $\mathbf{Z}$, and $\nabla_{\mathbf{v}}\mathbf{n}$ is the covariant derivative of $\mathbf{n}$ with respect to $\mathbf{v}$, which can be defined by

$$\nabla_{\mathbf{v}}\mathbf{n} = \frac{\mathrm{d}}{\mathrm{d}t}\mathbf{n}(\mathbf{p} + t\mathbf{v})\Big|_{t=0} \tag{4.40}$$

The geometric meaning of the curvature is that it quantifies the bending rate of a curve σ on $\mathbf{Z}$ with respect to $\mathbf{n}$; σ is obtained by intersecting $\mathbf{Z}$ with a plane that is determined by $\mathbf{n}$ and $\mathbf{v}$, as shown in Fig. 4.57. When $\mathbf{p}$ is an umbilic point, $\kappa_{\mathbf{Z},\mathbf{p}}$ is equal to one value with any $\mathbf{v}$. Examples of surfaces that consist of umbilic points are planes and spheres. More commonly for a mode shape, when $\mathbf{p}$ is a nonumbilic point, there are two orthogonal principal directions, along which $\kappa_{\mathbf{Z},\mathbf{p}}$ attains its maximum and minimum values, denoted by $\kappa_{\mathbf{Z},\mathbf{p}}^{\max}$ and $\kappa_{\mathbf{Z},\mathbf{p}}^{\min}$, respectively; the two curvatures, i.e., the maximum and minimum curvatures, are termed as principal curvatures. Shapes that are formed by maximum and minimum curvatures associated with a mode shape are termed as maximum and minimum CMSs, respectively, and they are principal CMSs.

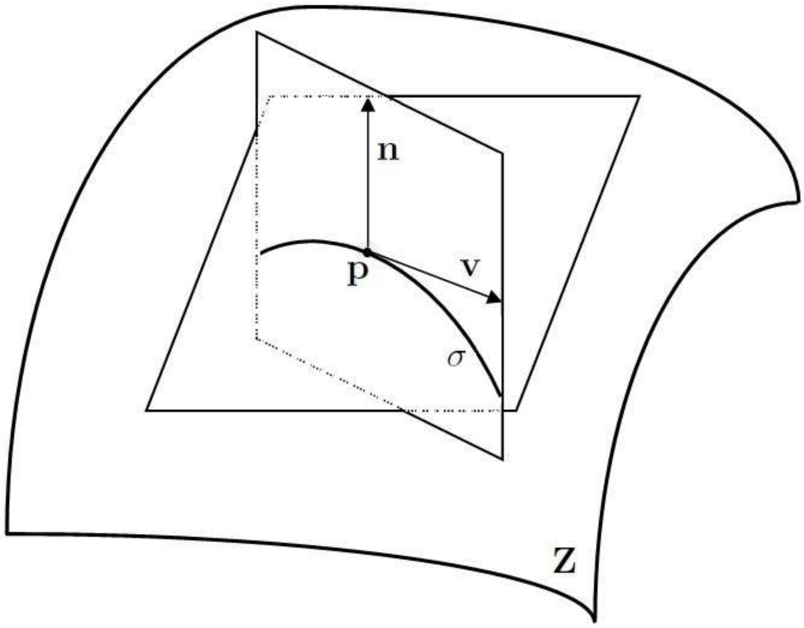

Figure 4.57: Point $\mathbf{p}$ on a mode shape $\mathbf{Z}$, a unit normal vector $\mathbf{n}$ associated with $\mathbf{p}$, a unit tangent vector $\mathbf{v}$ associated with $\mathbf{p}$, and a curve σ obtained by intersecting $\mathbf{Z}$ with the plane determined by $\mathbf{n}$ and $\mathbf{v}$.

For a constant-thickness plate made of homogeneous material, one has [123]

$$\begin{bmatrix} M_{xx} \\ M_{yy} \\ M_{xy} \end{bmatrix} = \frac{Eh^3}{12\left(\nu^2-1\right)} \begin{bmatrix} 1 & \nu & 0 \\ \nu & 1 & 0 \\ 0 & 0 & \nu-1 \end{bmatrix} \begin{bmatrix} \kappa_{xx} \\ \kappa_{yy} \\ \kappa_{xy} \end{bmatrix} \tag{4.41}$$

where M_{xx} and M_{yy} are bending moments per unit length acting on edges of a differential element parallel to y- and x-axes of a global three-dimensional Cartesian coordinate $O-xyz$, respectively; M_{xy} is the twisting moment with respect to x- and y-axes; E, h and ν are the Young's modulus, thickness and Poisson's ratio of the plate, respectively; κ_{xx} and κ_{yy} are curvatures with respect to x- and y-axes, respectively; and κ_{xy} is the twist with respect to x- and y-axes. For a point $\mathbf{p}$ on the plate, a local Cartesian coordinate $\mathbf{p} - x'y'z'$ can be defined, where x'- and y'-axes are along principal directions associated with the maximum and minimum curvatures of $\mathbf{p}$ on $\mathbf{Z}$, respectively. In this case, associated $M_{x'y'}$ and $\kappa_{x'y'}$ vanish, and one has

$$\begin{cases} \kappa_{\mathbf{Z},\mathbf{p}}^{\mathrm{Max}} = -\frac{12}{Eh^3}\left(M_{x'x'} - \nu M_{y'y'}\right) \\ \kappa_{\mathbf{Z},\mathbf{p}}^{\mathrm{Min}} = -\frac{12}{Eh^3}\left(M_{y'y'} - \nu M_{x'x'}\right) \end{cases} \tag{4.42}$$

Principal curvatures can be used to construct a quadratic approximation of $\mathbf{Z}$ near $\mathbf{p}$. When $\mathbf{v}$ in Eq. (4.39) is not on a principal direction, $\kappa_{\mathbf{Z},\mathbf{p}}$ can be expressed by [122]

$$\kappa_{\mathbf{Z},\mathbf{p}}\left(\mathbf{v}\right) = \kappa_{\mathbf{Z},\mathbf{p}}^{\mathrm{Max}} \cos^2\vartheta_1 + \kappa_{\mathbf{Z},\mathbf{p}}^{\mathrm{Min}} \cos^2\vartheta_2 \tag{4.43}$$

where ϑ_1 and ϑ_2 are angles between $\mathbf{v}$ and principal directions associated with the maximum and minimum curvatures, respectively. Hence, principal curvatures can be considered to be properties of $\mathbf{Z}$ at $\mathbf{p}$ that are independent of $\mathbf{v}$.

4.3.2.2 Multi-scale Discrete Differential-geometry Scheme

When $\mathbf{Z}$ can be analytically expressed, principal CMSs can be calculated using a well-established analytical method [122]. When $\mathbf{Z}$ cannot be analytically expressed and is presented in a discrete form, a numerical scheme is needed to calculate discrete principal CMSs associated with $\mathbf{Z}$. For a one-dimensional structure, a discrete CMS can be accurately calculated using a finite difference scheme. Discrete principal CMSs associated with $\mathbf{Z}$ cannot be easily calculated in that $\kappa_{\mathbf{Z},\mathbf{p}}$ depends on $\mathbf{v}$, as shown in Eq. (4.39), and there are an infinite number of $\mathbf{v}$ that can be defined at $\mathbf{p}$. One can perform a one-dimensional finite difference scheme at $\mathbf{p}$ with respect to different $\mathbf{v}$ to calculate curvatures and find principal curvatures as the maximum and minimum values among resulting curvatures, but it can be computationally inefficient.

To efficiently and accurately calculate principal CMSs associated with $\mathbf{Z}$, two operators in Ref. [124] for shapes with a triangulated mesh are introduced; they can be used to calculate its mean and Gaussian curvatures at a point $\mathbf{p}$, denoted by $H_{\mathbf{Z},\mathbf{p}}$ and $G_{\mathbf{Z},\mathbf{p}}$, respectively. Mean and Gaussian curvatures of $\mathbf{Z}$ at $\mathbf{p}$ are the average and product of two principal curvatures of $\mathbf{Z}$ at $\mathbf{p}$, respectively, which can be expressed by

$$H_{\mathbf{Z},\mathbf{p}} = \frac{\kappa_{\mathbf{Z},\mathbf{p}}^{\mathrm{Max}} + \kappa_{\mathbf{Z},\mathbf{p}}^{\mathrm{Min}}}{2} \tag{4.44}$$

and

$$G_{\mathbf{Z},\mathbf{p}} = \kappa_{\mathbf{Z},\mathbf{p}}^{\mathrm{Max}} \times \kappa_{\mathbf{Z},\mathbf{p}}^{\mathrm{Min}} \tag{4.45}$$

Shapes that are formed by mean and Gaussian curvatures associated with a mode shape are termed as mean and Gaussian CMSs, respectively. In the operators for mean and Gaussian curvatures of $\mathbf{p}$ on $\mathbf{Z}$ with a triangulated mesh, a new surface area $A_{\mathbf{P}}$ is calculated for a one-ring neighborhood associated with $\mathbf{p}$, which is formed by all triangulated elements of the mesh consisting of $\mathbf{p}$, as shown in Fig. 4.58(a). The pseudo-code for calculating $A_{\mathbf{P}}$ is shown in Fig. 4.59, where the Voronoi area of an acute triangle $\triangle\mathbf{pqr}$ shown in Fig. 4.58(b) can be expressed by

$$A_{\text{Voronoi}} = \frac{1}{8}\left(|\mathbf{pr}|^2 \cot\angle\mathbf{q} + |\mathbf{pq}|^2 \cot\angle\mathbf{r}\right) \tag{4.46}$$

and A is the area of a triangle in the one-ring neighborhood. Mean and Gaussian curvatures of $\mathbf{p}$ on $\mathbf{Z}$ can be calculated by

$$H_{\mathbf{Z},\mathbf{p}} = \frac{1}{4A_{\mathbf{P}}}\left[\sum_{i\in N_1(\mathbf{p})} \left(\cot\alpha_i + \cot\beta_i\right)\left(\mathbf{p} - \mathbf{q}_i\right)\right] \cdot \mathbf{n}\left(\mathbf{p}\right) \tag{4.47}$$

and

$$G_{\mathbf{Z},\mathbf{p}} = \frac{2\pi - \sum_{i\in N_1(\mathbf{p})} \theta_i}{A_{\mathbf{P}}} \tag{4.48}$$

where $N_1(\mathbf{p})$ is the number of points that are connected with $\mathbf{p}$ in the one-ring neighborhood, and θ_i is the angle associated with $\mathbf{q}_i$, as shown in Fig. 4.58(a). With calculated $H_{\mathbf{Z},\mathbf{p}}$ and $G_{\mathbf{Z},\mathbf{p}}$, principal curvatures at $\mathbf{p}$ can be calculated by

$$\kappa^{\text{Max}}_{\mathbf{Z},\mathbf{p}} = H_{\mathbf{Z},\mathbf{p}} + \sqrt{H^2_{\mathbf{Z},\mathbf{p}} - G_{\mathbf{Z},\mathbf{p}}} \tag{4.49}$$

and

$$\kappa^{\text{Min}}_{\mathbf{Z},\mathbf{p}} = H_{\mathbf{Z},\mathbf{p}} - \sqrt{H^2_{\mathbf{Z},\mathbf{p}} - G_{\mathbf{Z},\mathbf{p}}} \tag{4.50}$$

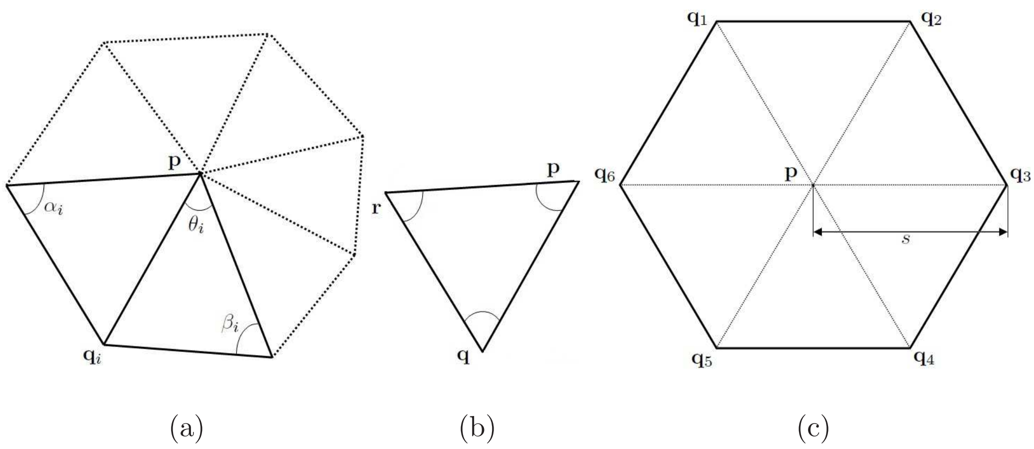

Figure 4.58: (a) One-ring neighborhood of a triangulated mesh associated with $\mathbf{p}$, (b) an acute triangle $\triangle\mathbf{pqr}$ and (c) a hexagonal one-ring neighborhood with a side length of s.

$A_{\mathbf{P}} = 0$

For each triangle in the one-ring neighborhood of $\mathbf{p}$

If the triangle is acute,

$A_{\mathbf{P}} = A_{\mathbf{P}} + A_{\text{Voronoi}}$

Else

If $\angle\mathbf{p}$ is obtuse

$A_{\mathbf{P}} = A_{\mathbf{P}} + \frac{A}{2}$

Else

$A_{\mathbf{P}} = A_{\mathbf{P}} + \frac{A}{4}$

Figure 4.59: Pseudo-code for calculating the new surface area $A_{\mathbf{p}}$ associated with $\mathbf{p}$.

Similar to calculating curvatures of a one-dimensional structure [125], those associated with a mode shape of a plate can be contaminated by measurement noise. To alleviate adverse effects of measurement noise on calculating curvatures of a plate, a multi-scale discrete differential-geometry scheme is proposed based on the operators introduced above, where a hexagonal one-ring neighborhood is constructed at each measurement point. The hexagonal one-ring neighborhood associated with $\mathbf{p}$ projected onto the undeformed plate is equilateral with a side length of s, as shown in Fig. 4.58(c). Since xy-coordinates of $\mathbf{q}_i$, where $i = 1, 2, \ldots, 6$, can be analytically obtained from the geometry of the hexagonal one-ring neighborhood, its z-coordinate can be obtained from interpolation based on $\mathbf{Z}$. CMSs of $\mathbf{p}$ can be obtained based on the hexagonal one-ring neighborhood, and s is considered as the scale of the scheme. For a measured mode shape with an unknown noise level, one needs to progressively test different values of s from smaller to larger ones. A proper value of s is the one with which the resulting CMS becomes smooth and has a clear global trend.

To illustrate adverse effects of measurement noise and the effectiveness of the scheme, white noise is added to $\mathbf{Z}^{d,23}$ with a signal-to-noise ratio of 60 db to simulate measurement noise. Maximum CMSs associated with $\mathbf{Z}^{d,23}$ from the scheme with $s = 0.002$ m, 0.005 m and 0.015 m are shown in Fig. 4.60(a) through (c), respectively; the maximum CMS associated with noise-free $\mathbf{Z}^{d,23}$ is shown in Fig. 4.60(d). It can be seen that measurement noise is amplified and becomes dominant in the resulting maximum CMS from the scheme with $s = 0.002$ m, since differences between the value of a noise-free $\mathbf{Z}^{d,23}$ at a point and those in the hexagonal one-ring neighborhood with a side length of s are small compared with those associated with $\mathbf{Z}^{d,23}$ with the measurement noise. Figures 4.60(b) and (c) show that maximum CMSs can be obtained with a lower noise level with a larger value of s. While maximum curvatures of $\mathbf{Z}^{d,23}$ at a point from the scheme with different values of s are different from those associated with noise-free $\mathbf{Z}^{d,23}$ at the point from the scheme with $s = 0.002$ m, global trends of the maximum CMSs are retained; the larger the value of s, the lower the noise level in the resulting maximum CMS, which is also the case for minimum, mean and Gaussian CMSs.

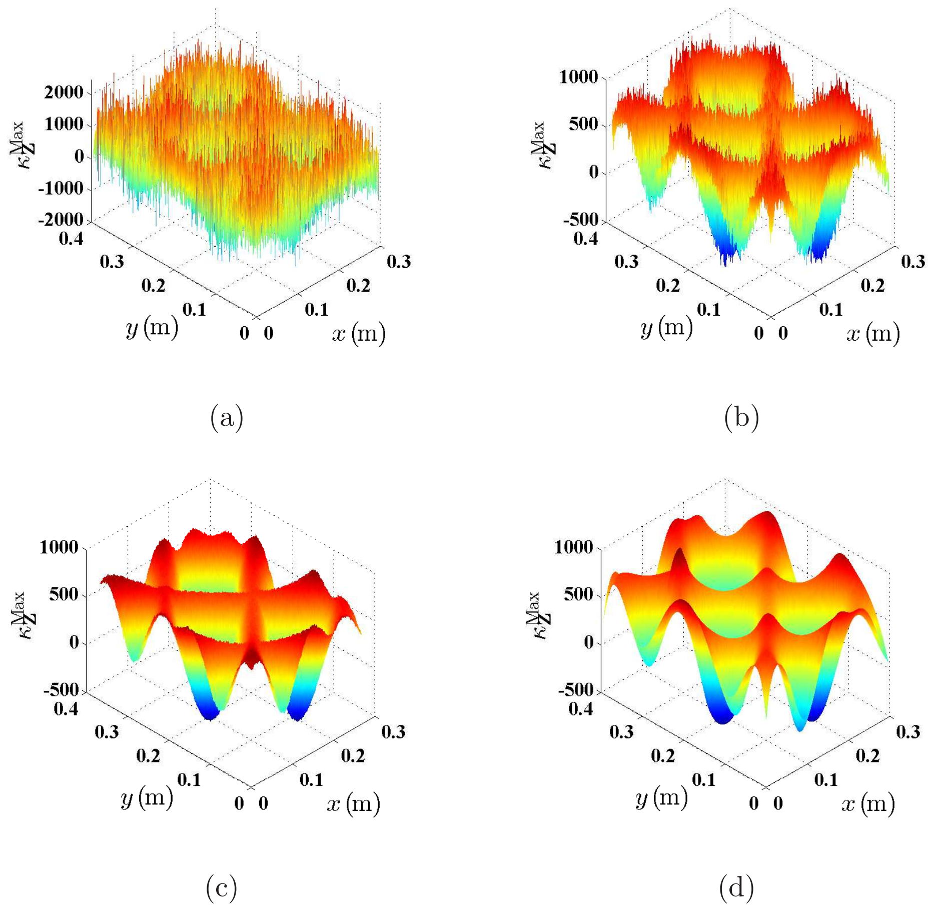

Figure 4.60: Maximum CMSs associated with $\mathbf{Z}^{d,23}$ with measurement noise from the scheme with (a) $s = 0.002$ m, (b) $s = 0.005$ m and (c) $s = 0.015$ m; (d) the maximum CMS associated with noise-free $\mathbf{Z}^{d,23}$ from the scheme with $s = 0.002$ m.

4.3.2.3 CMS-based Damage Indices

CMSs have been widely used to identify damage in beams, since the curvature at a point on a beam can be expressed by [86]

$$v'' = \frac{M}{EI} \tag{4.51}$$

where v'' is the curvature at the point, M is the bending moment applied at the point, and EI is the bending stiffness of the cross-section at the point. Since damage can introduce reduction in EI in its neighborhood, the magnitude of v'' increases in the neighborhood of the damage compared with that of the undamaged beam. Differences between v'' associated with the damaged and undamaged beams can be used for identifying the damage. When E in Eq. (4.42) changes in the neighborhood of damage in a plate, magnitudes of principal curvatures in the neighborhood of the damage would change, and so would those of mean and Gaussian curvatures. Hence, differences between principal, mean and Gaussian CMSs associated with the damaged and undamaged plates can be used for identifying damage in a plate. Four CDIs associated with a mode shape of a plate are proposed to identify damage; for each point on the plate, the CDIs are listed below:

1. **Maximum-CDI.** A Maximum-CDI denoted by $\delta^{\mathrm{Max}}(\mathbf{p})$ is defined by

$$\delta^{\mathrm{Max}}(\mathbf{p}) = \left(\kappa^{\mathrm{Max}}_{\mathbf{Z}^{d,j},\mathbf{p}} - \kappa^{\mathrm{Max}}_{\mathbf{Z}^{u,j},\mathbf{p}}\right)^2 \tag{4.52}$$

2. **Minimum-CDI.** A Minimum-CDI denoted by $\delta^{\mathrm{Min}}(\mathbf{p})$ is defined by

$$\delta^{\mathrm{Min}}(\mathbf{p}) = \left(\kappa^{\mathrm{Min}}_{\mathbf{Z}^{d,j},\mathbf{p}} - \kappa^{\mathrm{Min}}_{\mathbf{Z}^{u,j},\mathbf{p}}\right)^2 \tag{4.53}$$

3. **Mean-CDI.** A Mean-CDI denoted by $\delta^{\mathrm{Mean}}(\mathbf{p})$ is defined by

$$\delta^{\text{Mean}}(\mathbf{p}) = \left(H_{\mathbf{Z}^{d,j},\mathbf{p}} - H_{\mathbf{Z}^{u,j},\mathbf{p}}\right)^2 \tag{4.54}$$

4. **Gaussian-CDI.** A Gaussian-CDI denoted by $\delta^{\text{Gaussian}}(\mathbf{p})$ is defined by

$$\delta^{\text{Gaussian}}(\mathbf{p}) = \left(G_{\mathbf{Z}^{d,j},\mathbf{p}} - G_{\mathbf{Z}^{u,j},\mathbf{p}}\right)^2 \tag{4.55}$$

Maximum-CDIs, Minimum-CDIs, Mean-CDIs and Gaussian-CDIs associated with noise-free $\mathbf{Z}^{d,23}$ and $\mathbf{Z}^{u,23}$ with $s = 0.002$ m in the scheme are shown in Fig. 4.61(a) through (d), respectively. It can be seen that the damage can be identified near regions with consistently higher values of the CDIs.

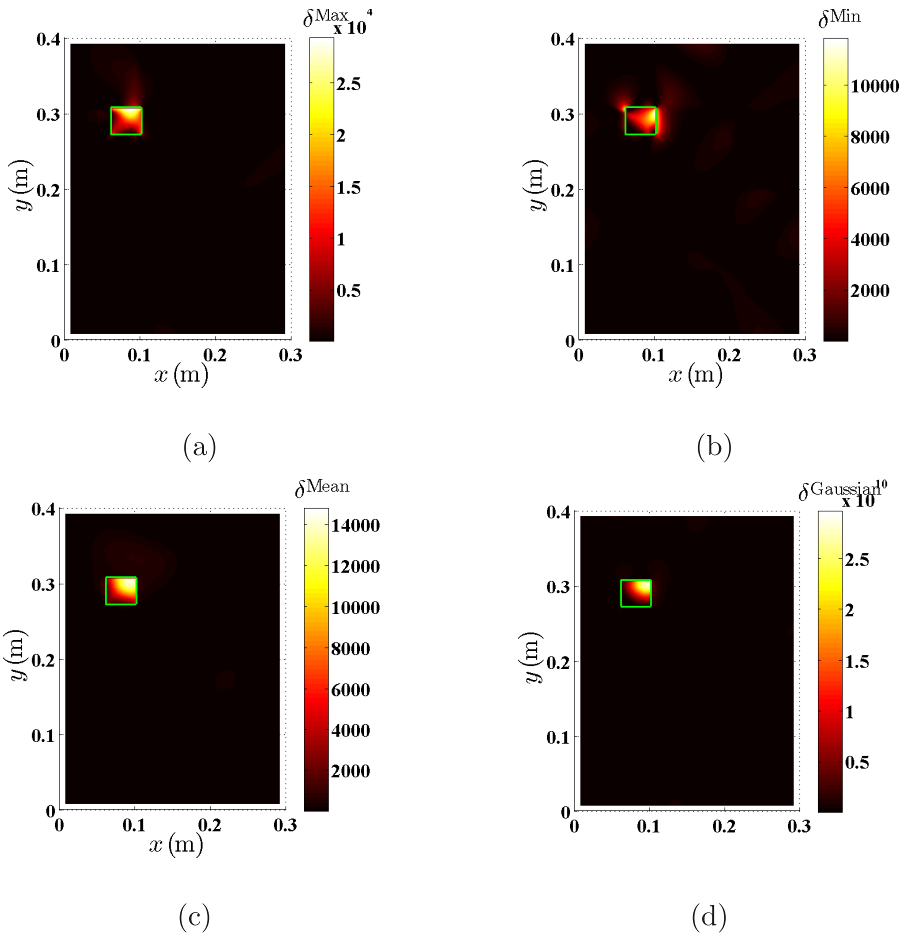

Figure 4.61: (a) Maximum-CDIs, (b) Minimum-CDIs, (c) Mean-CDIs and (d) Gaussian-CDIs associated with noise-free $\mathbf{Z}^{d,23}$ and $\mathbf{Z}^{u,23}$; $s = 0.002$ m in the scheme.

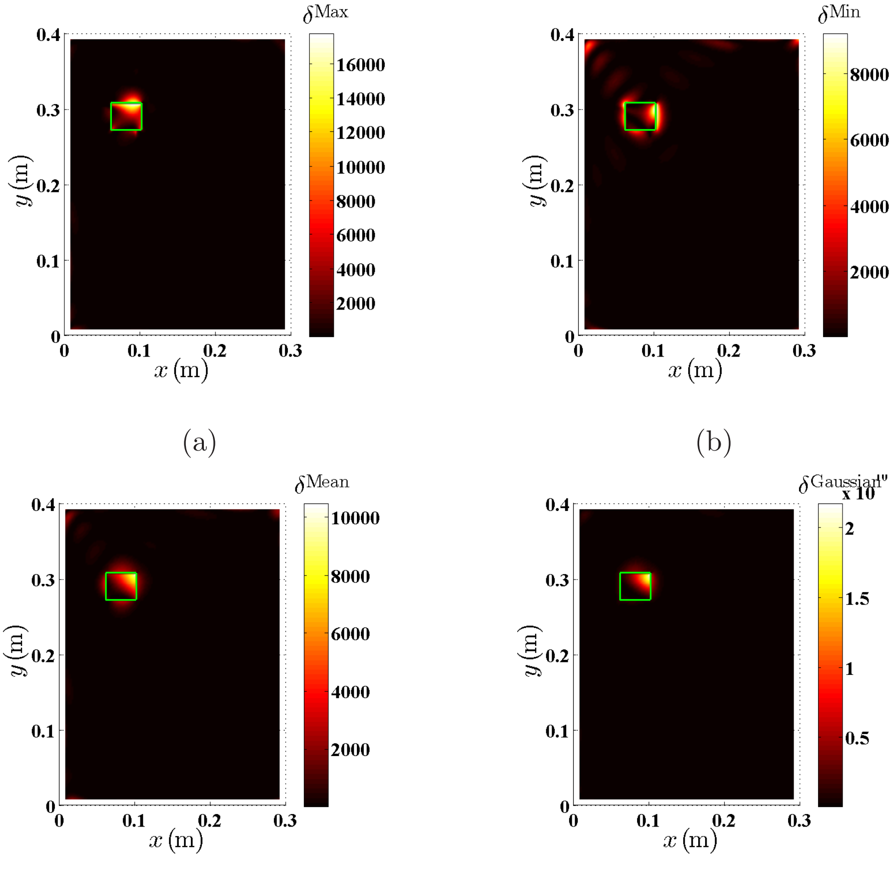

(a) (b)

(c) (d)

Figure 4.62: (a) Maximum-CDIs, (b) Minimum-CDIs, (c) Mean-CDIs and (d) Gaussian-CDIs associated with noise-free $\mathbf{Z}^{d,23}$ and the corresponding mode shape from the polynomial fit with $n = 15$; $s = 0.002$ m in the scheme.

4.3.2.4 Approximation of Mode Shapes of an Undamaged Plate

While the CDIs proposed above can be used to identify damage in a plate, they require use of mode shapes of an undamaged plate, which are usually unavailable in practice. Assuming that existence of relatively small damage in a plate does not cause prominent changes in its mode shapes in the neighborhood of the damage, one can approximate mode shapes of the associated undamaged plate using polynomials that fit the corresponding mode shapes of the damaged plate, provided that the undamaged plate is geometrically smooth and made of materials that have no stiffness and mass discontinuities. The modal assurance criterion (MAC) value [1] in percent between $\mathbf{Z}^{d,23}$ and $\mathbf{Z}^{u,23}$ is 99.95%, which indicates that they are almost identical to each other and validates the assumption on the existence of relatively small damage. A similar technique has been proposed in Ref. [125] to approximate mode shapes of an undamaged beam using polynomials that fit corresponding mode shapes of the damaged one. Mode shapes of an undamaged plate corresponding to those of a damaged one are not measured in this work, and it is proposed that a mode shape of an undamaged plate be obtained from a polynomial of a properly determined order that fits the corresponding mode shape of the damaged plate:

$$z^p(x,y) = \sum_{k=0}^{n}\sum_{i=0}^{k} a_{i,k-i} x^i y^{k-i} \tag{4.56}$$

where n is the order of the polynomial, which controls the level of approximation of the polynomial fit to the mode shape of the damaged plate, (x, y) are xy-coordinates of a point on an undeformed plate, and $a_{i,k-i}$ are coefficients of the polynomial that can be obtained by solving a linear equation

$$\mathbf{Va} = \mathbf{z} \tag{4.57}$$

in which $\mathbf{z}$ is the N-dimensional mode shape vector of the damaged plate to be fit, $\mathbf{V}$ is the $N \times \left(\sum_{p=1}^{n+1} p\right)$-dimensional bivariate Vandermonde matrix which can be expressed by

$$\mathbf{V}=\begin{bmatrix} 1 & x_1 & y_1 & \dots & x_1^n & \dots & x_1^i y_1^{n-i} & \dots & y_1^n \\ 1 & x_2 & y_2 & \dots & x_2^n & \dots & x_2^i y_2^{n-i} & \dots & y_2^n \\ \vdots & \vdots & \vdots & \ddots & \vdots & \ddots & \vdots & \ddots & \vdots \\ 1 & x_N & y_N & \dots & x_N^n & \dots & x_N^i y_N^{n-i} & \dots & y_N^n \end{bmatrix} \tag{4.58}$$

and $\mathbf{a}$ is the $\left(\sum_{p=1}^{n+1} p\right)$-dimensional coefficient vector which can be expressed by

$$\mathbf{a}=\begin{bmatrix} a_{0,0} & a_{1,0} & a_{0,1} & \dots & a_{n,0} & \dots & a_{i,n-i} & \dots & a_{0,n} \end{bmatrix}^{\mathrm{T}} \tag{4.59}$$

Solving Eq. (4.57) for the coefficient vector is equivalent to solving an unconstrained least-squares problem $\min \frac{1}{2}\left\|\mathbf{Va}^* - \mathbf{z}\right\|^2$ for an optimum minimizer $\mathbf{a}^*$ [112], which is usually an over-determined problem, i.e., $N > \sum_{p=1}^{n+1} p$. A solution can be obtained using the singular-value decomposition of $\mathbf{V}$ [112], which gives

$$\mathbf{V}=\mathbf{U}\begin{bmatrix} \mathbf{S} \\ 0 \end{bmatrix}\mathbf{W}^{\mathrm{T}} \tag{4.60}$$

where $\mathbf{U}$ and $\mathbf{W}$ are $N \times N$ and $\left(\sum_{p=1}^{n+1} p\right) \times \left(\sum_{p=1}^{n+1} p\right)$ orthogonal matrices, respectively, and $\mathbf{S}$ is a $\left(\sum_{p=1}^{n+1} p\right) \times \left(\sum_{p=1}^{n+1} p\right)$ diagonal matrix. An optimum minimizer $\mathbf{a}^*$ based on the singular-value decomposition of $\mathbf{V}$ can be obtained by

$$\mathbf{a}^* = \mathbf{W}\mathbf{S}^{-1}\mathbf{U}_{\mathbf{1}}^{\mathrm{T}}\mathbf{z} \tag{4.61}$$

where $\mathbf{U}_1$ is a matrix formed by the first $\sum_{p=1}^{n+1} p$ columns of $\mathbf{U}$. When n in Eq. (4.56) becomes a large value, $\mathbf{S}$ can be ill-conditioned, which can result in a low level of approximation of the associated polynomial fit. To avoid ill-conditioning of $\mathbf{S}$, it is proposed that x and y in Eq. (4.56) be normalized using the "center and scale" technique [113] before formulation of the linear equation in Eq. (4.57). Normalized coordinates $\tilde{x}$ and $\tilde{y}$ can be expressed by

$$\begin{cases} \tilde{x} = \frac{2x-2\bar{x}}{l_1} \\ \tilde{y} = \frac{2y-2\bar{y}}{l_2} \end{cases} \tag{4.62}$$

where $\bar{x}$ and $\bar{y}$ are x- and y-coordinates of the center point of the plate, respectively, and l_1 and l_2 are lengths of the plate along x- and y-axes, respectively.

An increase of n in the polynomial fit in Eq. (4.56) can improve its level of approximation of the resulting mode shape to that to be fit. To quantify the level of approximation, a fitting index fit in percent, defined by

$$\mathrm{fit}\,(n) = \frac{\mathrm{RMS}\,(\mathbf{z})}{\mathrm{RMS}\,(\mathbf{z}) + \mathrm{RMS}\,(\mathbf{e})} \times 100\% \tag{4.63}$$

is used, where $\mathrm{RMS}\,(\cdot)$ denotes the root-mean-square value of a vector and $\mathbf{e}$ is the error vector between the mode shape to be fit and the corresponding one from the current polynomial fit, i.e., $\mathbf{e} = \mathbf{V}\mathbf{a}^* - \mathbf{z}$. When the fitting index is close to 100%, the mode shape from the current polynomial fit is almost identical to $\mathbf{z}$; the lower the fitting index, the lower the level of approximation of the mode shape from the current polynomial fit. Fitting indices fit associated with $\mathbf{Z}^{d,23}$ for different n are shown in Fig. 4.63(a). It can be seen in Fig. 4.63(b) that fit converges to a certain value as n increases. To determine the proper order of a polynomial fit, a convergence index con for the polynomial fit with $n \geqslant 3$ is defined based on fit, which can be expressed by

$$\operatorname{con}(n) = \operatorname{fit}(n) - \operatorname{fit}(n-2) \tag{4.64}$$

Convergence indices con associated with $\mathbf{Z}^{d,23}$ for different n are shown in Fig. 4.63(c). It can be seen that when n is larger than a certain value, con starts to decrease. When con is sufficiently small after its start of decrease, there is no significant improvement in the level of approximation of the polynomial fit. To determine a proper value of n, it is proposed that the value be the smallest one with which con is smaller than a prescribed threshold value. In this work, the prescribed threshold value for con is 0.50%. Hence, the proper value of n associated with $\mathbf{Z}^{d,23}$ is determined to be 15, with which con $=$ 0.42%, as shown in Fig. 4.63(d). Maximum-CDIs, Minimum-CDIs, Mean-CDIs and Gaussian-CDIs associated with noise-free $\mathbf{Z}^{d,23}$ and the corresponding mode shape from the polynomial fit with $n = 15$ are shown in Fig. 4.62(a) through (d), respectively. Similar to the CDIs associated with noise-free $\mathbf{Z}^{d,23}$ and $\mathbf{Z}^{u,23}$ in Fig. 4.61, the damage can be identified near regions with higher values of CDIs.

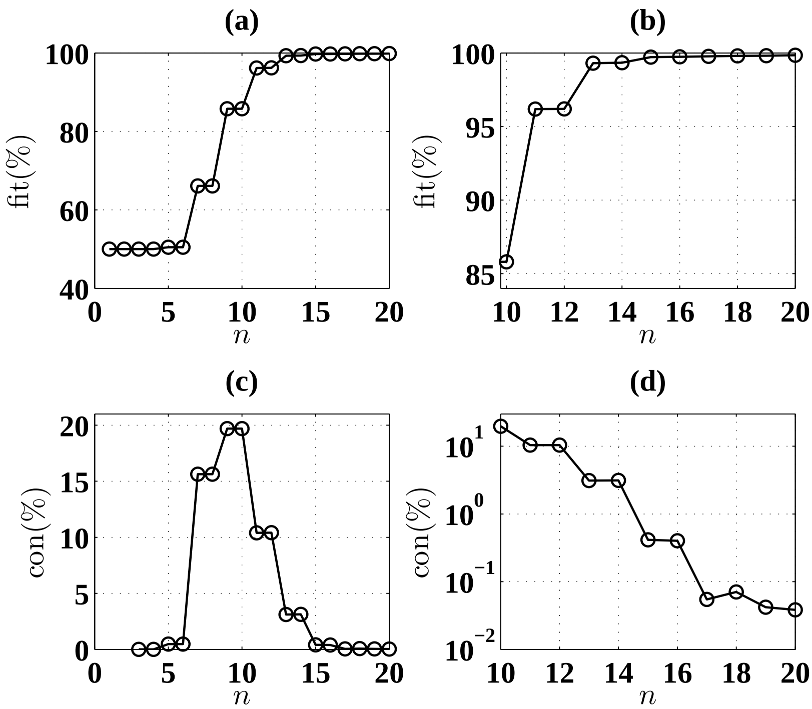

Figure 4.63: (a) Fitting indices fit associated with $\mathbf{Z}^{d,23}$ for different n, (b) an enlarged view of fit, (c) the convergence indices con associated with $\mathbf{Z}^{d,23}$ for different n and (d) an enlarged view of con.

4.3.2.5 Denoising of CDIs

Use of CDIs to identify damage depends on calculation of CMSs, which are usually subject to measurement noise that can fuzz existence of damage in the CDIs. A suitable value of s in the scheme can alleviate adverse effects of measurement noise. Since the noise level of a measured mode shape is usually unknown, one needs to progressively test different values of s from smaller to larger ones until a proper one is obtained, with which the existence of the damage becomes prominent in associated CDIs. However, the process of seeking a proper value of s can be time-consuming and inefficient. Figures 4.64(a) and (b) show Maximum-CDIs associated with $\mathbf{Z}^{d,23}$ with measurement noise and the corresponding mode shape from the polynomial fit with $s = 0.002$ m and 0.005 m in the scheme, respectively, but the damage cannot be identified due to the measurement noise. When $s = 0.015$ m, the damage can be identified near regions of higher values of Maximum-CDIs, as shown in Fig. 4.64(c). To manifest the effects of damage on the proposed CDIs with a smaller s in the scheme, a two-dimensional discrete weight function is applied to differences between CMSs before calculating the CDIs. The weight function for a mesh with square elements is expressed by

$$W_{M_w}(k_1, k_2) = \mathrm{e}^{-4\left[\left(\frac{k_1}{M_w}\right)^2 + \left(\frac{k_2}{M_w}\right)^2\right]} \tag{4.65}$$

where M_w is the scale of the weight function; k_1 and k_2 are integer coordinates associated with x- and y-axes of the weight function, respectively, and $k_1, k_2 \in [-M_w, M_w]$. For a mesh with non-square elements, one can interpolate a mode shape on a mesh with square elements so that the weight function can have equal weights along x- and y-axes. An interpolation can also be conducted to obtain a mode shape on a finer mesh with better spatial resolution in resulting CDIs. Weighted CDIs $\tilde{\delta}^{\mathrm{Max}}$, $\tilde{\delta}^{\mathrm{Min}}$, $\tilde{\delta}^{\mathrm{Mean}}$ and $\tilde{\delta}^{\mathrm{Gaussian}}$ at a point $\mathbf{p}$ on a plate, based on the CDIs in Eqs. (4.52) through (4.55), respectively, can be expressed by

$$\tilde{\delta}^{\mathrm{Max}}(\mathbf{p}) = \left\{ \sum_{k_1=-M_w}^{M_w} \sum_{k_2=-M_w}^{M_w} \left[\left(\kappa^{\mathrm{Max}}_{\mathbf{Z}^{d,j},\mathbf{p}_{k_1,k_2}} - \kappa^{\mathrm{Max}}_{\mathbf{Z}^{u,j},\mathbf{p}_{k_1,k_2}} \right) \times W_{M_w}(k_1, k_2) \right] \right\}^2 \tag{4.66}$$

$$\tilde{\delta}^{\text{Min}}(\mathbf{p}) = \left\{ \sum_{k_1=-M_w}^{M_w} \sum_{k_2=-M_w}^{M_w} \left[\left(\kappa^{\text{Min}}_{\mathbf{Z}^{d,j},\mathbf{p}_{k_1,k_2}} - \kappa^{\text{Min}}_{\mathbf{Z}^{u,j},\mathbf{p}_{k_1,k_2}} \right) \times W_{M_w}(k_1, k_2) \right] \right\}^2 \tag{4.67}$$

$$\tilde{\delta}^{\text{Mean}}(\mathbf{p}) = \left\{ \sum_{k_1=-M_w}^{M_w} \sum_{k_2=-M_w}^{M_w} \left[\left(H_{\mathbf{Z}^{d,j},\mathbf{p}_{k_1,k_2}} - H_{\mathbf{Z}^{u,j},\mathbf{p}_{k_1,k_2}} \right) \times W_{M_w}(k_1, k_2) \right] \right\}^2 \tag{4.68}$$

$$\tilde{\delta}^{\text{Gaussian}}(\mathbf{p}) = \left\{ \sum_{k_1=-M_w}^{M_w} \sum_{k_2=-M_w}^{M_w} \left[\left(G_{\mathbf{Z}^{d,j},\mathbf{p}_{k_1,k_2}} - G_{\mathbf{Z}^{u,j},\mathbf{p}_{k_1,k_2}} \right) \times W_{M_w}(k_1, k_2) \right] \right\}^2 \tag{4.69}$$

where $\mathbf{p}_{k_1,k_2}$ is a point with xy-coordinates $(x_{\mathbf{p}} + k_1\Delta d, y_{\mathbf{p}} + k_2\Delta d)$, in which $x_{\mathbf{p}}$ and $y_{\mathbf{p}}$ are x- and y-coordinates of $\mathbf{p}$, respectively, and Δd is the side length of an element of the mesh. Applying the weight function with $M_w = 7$, weighted Maximum-CDIs associated with $\mathbf{Z}^{d,23}$ and the corresponding mode shape from the polynomial fit with $s = 0.002$ m, 0.005 m and 0.015 m in the scheme are shown in Fig. 4.64(d) through (f), respectively. When $s = 0.002$ m, the damage cannot be identified in the weighted Maximum-CDIs; however, when $s = 0.005$ m, the damage can be identified near the region with higher values of Maximum-CDIs, and some disturbing regions with relatively high values of Maximum-CDIs can also be observed. When $s = 0.015$ m, the damage can be identified with smaller disturbing regions with lower values of CDIs.

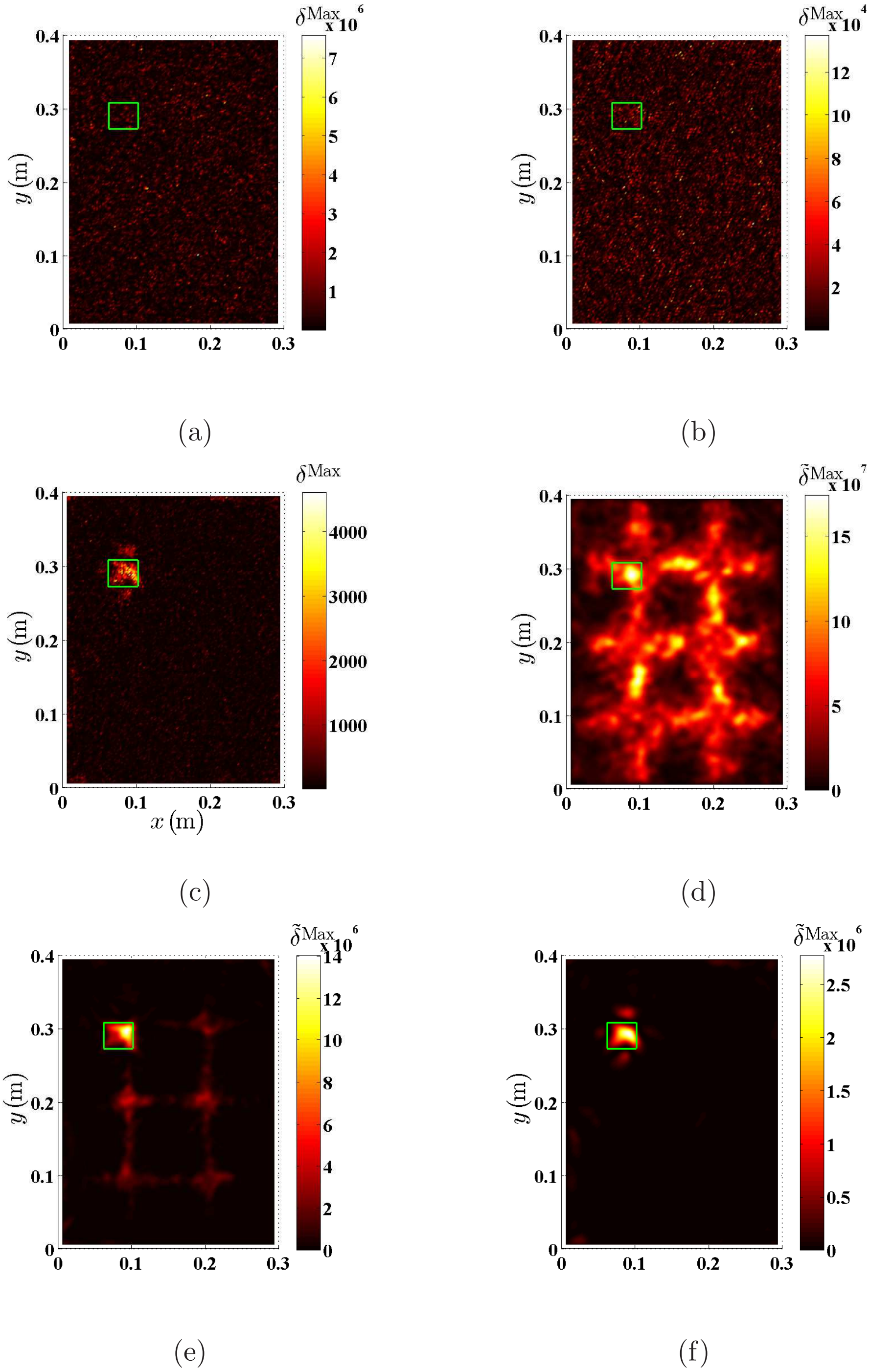

Figure 4.64: Maximum-CDIs associated with $\mathbf{Z}^{d,23}$ and the corresponding mode shape from the polynomial fit with (a) $s = 0.002$ m, (b) $s = 0.005$ m and (c) $s = 0.015$ m in the scheme; weighted Maximum-CDIs associated with $\mathbf{Z}^{d,23}$ and the corresponding mode shape from the polynomial fit with (d) $s = 0.002$ m, (e) $s = 0.005$ m and (f) $s = 0.015$ m in the scheme. The order of the polynomial fit is $n = 15$, and the scale of the weight function is $M_w = 7$.

4.3.2.6 Applicability and Robustness of the Method

The applicability and robustness of the proposed method for identifying damage using a mode shape associated with a low elastic mode are numerically investigated here; use of the mode shape on a coarse measurement grid and that of the weight function for the mode shape with high and low signal-to-noise ratios are also discussed. Undamped mode shapes of the damaged and undamaged plates associated with their second elastic modes are calculated and denoted by $\mathbf{Z}^{d,2}$ and $\mathbf{Z}^{u,2}$, respectively; $\mathbf{Z}^{d,2}$ and $\mathbf{Z}^{u,2}$ are in the same phase, and they are normalized so that their maximum absolute values are equal to one, as shown in Fig. 4.65(a) and (b), respectively. The MAC value in percent between $\mathbf{Z}^{d,2}$ and $\mathbf{Z}^{u,2}$ is 99.9998%, which indicates that they are almost identical to each other and validates the assumption on the existence of relatively small damage again. Fitting indices and convergence indices associated with $\mathbf{Z}^{d,2}$ are shown in Figs. 4.66, and the proper value of n associated with $\mathbf{Z}^{d,2}$ is determined to be 8. The mode shape from the polynomial fit with $n = 8$, denoted by $\mathbf{Z}^{p,2}$, is shown in Fig. 4.65(c); the MAC value in percent between $\mathbf{Z}^{d,2}$ and $\mathbf{Z}^{p,2}$ is almost 100%.

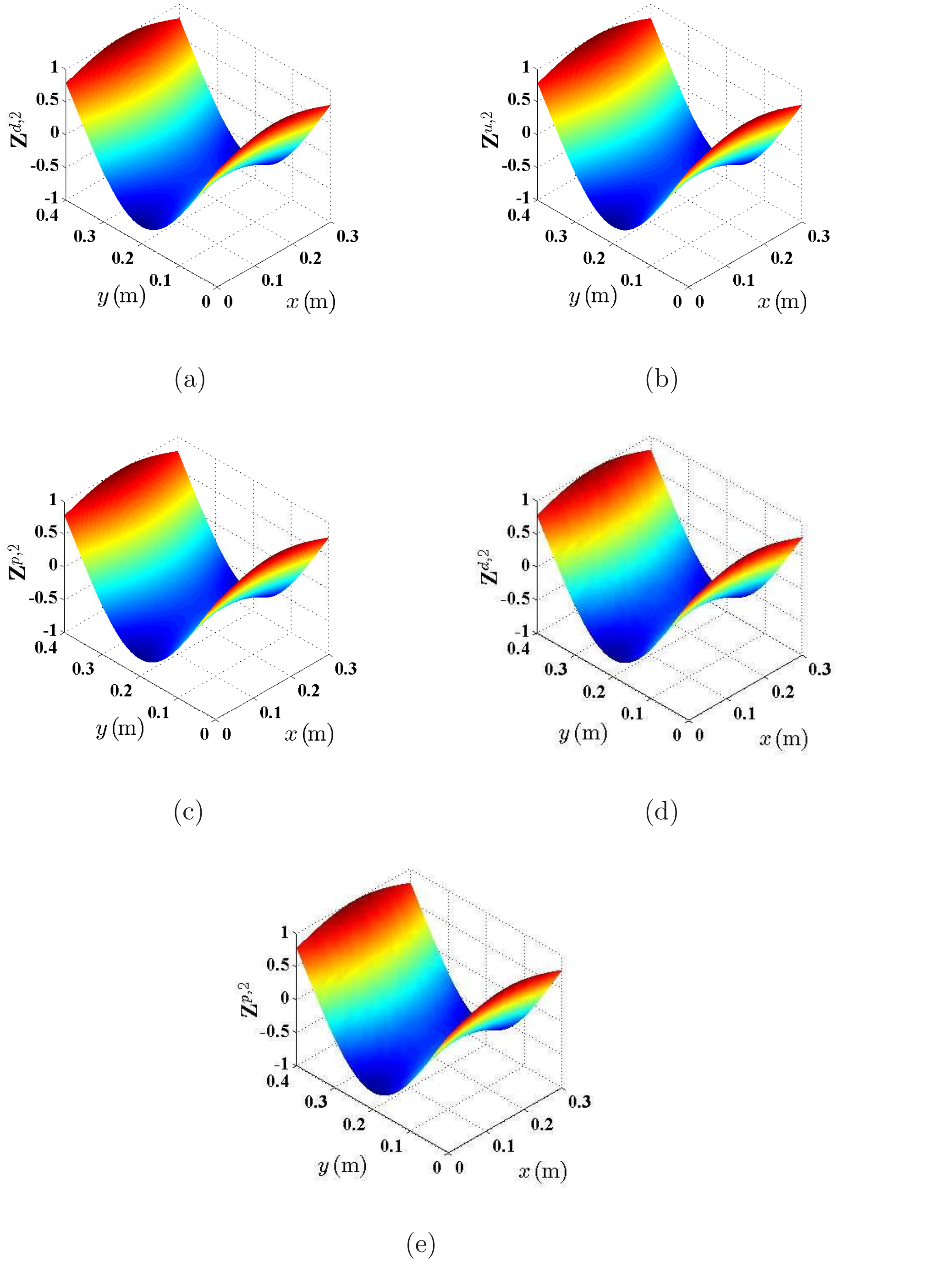

Figure 4.65: (a) Mode shape $\mathbf{Z}^{d,2}$ of the damaged plate, (b) $\mathbf{Z}^{u,2}$ of the undamaged plate, (c) $\mathbf{Z}^{p,2}$ from a polynomial that fits $\mathbf{Z}^{d,2}$ in (a) with $n = 8$, (d) $\mathbf{Z}^{u,2}$ of the damaged plate on a coarse measurement grid and (e) $\mathbf{Z}^{p,2}$ from a polynomial that fits $\mathbf{Z}^{d,2}$ in (d) with $n = 8$.

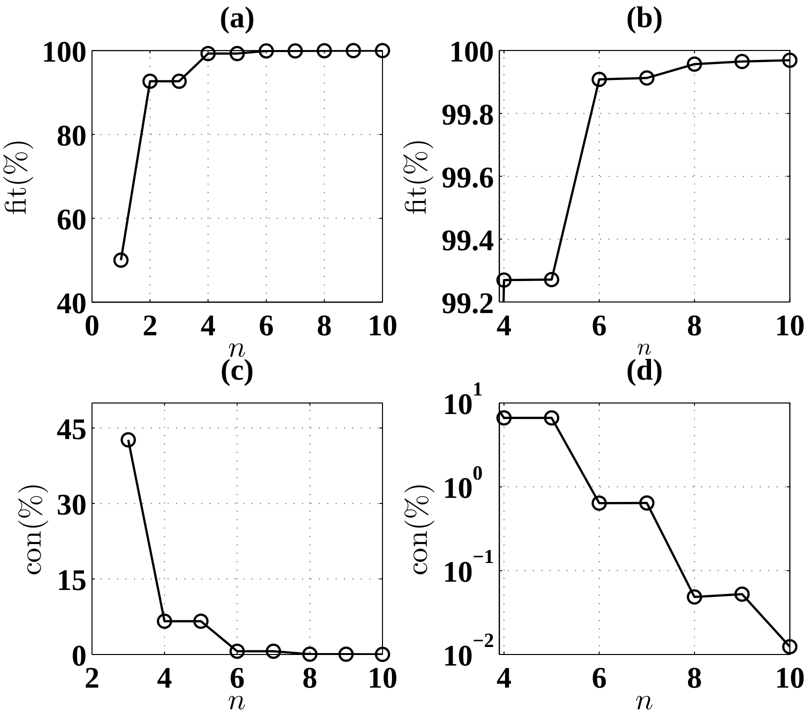

Figure 4.66: (a) Fitting indices fit associated with $\mathbf{Z}^{d,2}$ for different n, (b) an enlarged view of fit, (c) the convergence indices con associated with $\mathbf{Z}^{d,2}$ for different n and (d) an enlarged view of con.

Maximum-CDIs, Minimum-CDIs, Mean-CDIs and Gaussian-CDIs associated with noise-free $\mathbf{Z}^{d,2}$ and $\mathbf{Z}^{u,2}$ with $s = 0.002$ m in the scheme are shown in Figs. 4.67(a) through (d), respectively. The damage can be identified near regions with consistently higher values of the Maximum-CDIs, Minimum-CDIs and Mean-CDIs. Relatively high values of the Gaussian-CDIs can be observed beyond the damage, near its edges. Maximum-CDIs, Minimum-CDIs, Mean-CDIs and Gaussian-CDIs associated with noise-free $\mathbf{Z}^{d,2}$ and the corresponding mode shape from the polynomial fit are shown in Figs. 4.68(a) through (d), respectively, based on which observations similar to those associated with noise-free $\mathbf{Z}^{d,2}$ and $\mathbf{Z}^{u,2}$ in Fig. 4.67

can be made, and the damage can also be clearly identified. White noise is then added to $\mathbf{Z}^{d,2}$ with a signal-to-noise ratio of 60 db to simulate measurement noise. Maximum-CDIs, Minimum-CDIs, Mean-CDIs and Gaussian-CDIs associated with $\mathbf{Z}^{d,2}$ and the corresponding mode shape from the polynomial fit with $s = 0.015$ m in the scheme are shown in Figs. 4.69(a) through (d), respectively; the existence of the damage is fuzzed in the CDIs due to the measurement noise. Weighted Maximum-CDIs, Minimum-CDIs, Mean-CDIs and Gaussian-CDIs associated with $\mathbf{Z}^{d,2}$ and the corresponding mode shape from the polynomial fit are shown in Figs. 4.70(a) through (d), respectively, with $s = 0.015$ m in the scheme and $M_w = 7$ in the weight function. Note that $s = 0.015$ m is used here to alleviate adverse effects of the measurement noise on calculating the CDIs, while $s = 0.002$ m can be used to calculate the CDIs associated with noise-free $\mathbf{Z}^{d,2}$. While the weight function has been applied, the weighted Gaussian-CDIs cannot be used to identify the damage due to the measurement noise. Similar to the results associated with noise-free $\mathbf{Z}^{d,2}$ in Fig. 4.68, the damage can be identified in regions with consistently higher values of the weighted Maximum-CDIs, Minimum-CDIs and Mean-CDIs. While some regions formed by higher values of the CDIs due to the measurement noise can be observed beyond the damage, they do not consistently occur in the weighted CDIs and would not be identified as damage. However, the damage cannot be identified in the weighted Gaussian-CDIs possibly because they are less sensitive to the damage and less robust against measurement noise, compared with the other three weighted CDIs. A possible worse case is that more than one CDI associated with a mode shape are less sensitive to the damage and/or less robust against measurement noise, and one may not identify the damage based on the CDIs. In this case, use of CDIs associated with other mode shapes may be necessary for one to confirm existence of damage, since there does not exist a mode shape that can be used to identify all possible damage and so do not its associated CDIs.

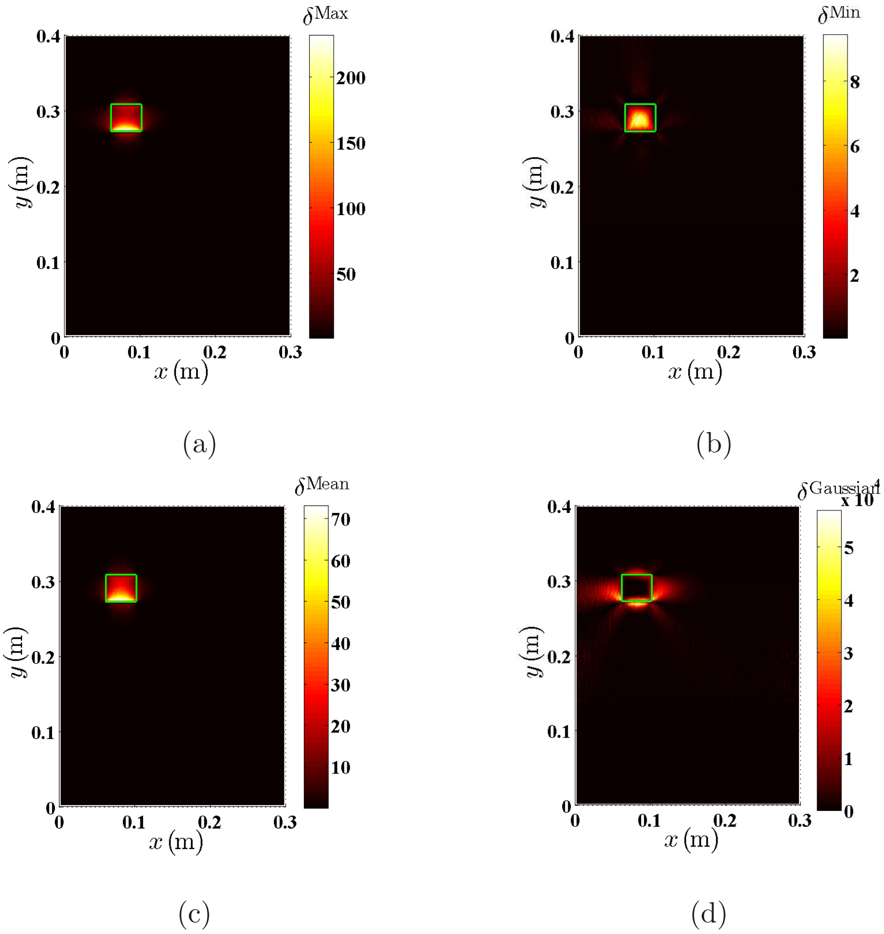

Figure 4.67: (a) Maximum-CDIs, (b) Minimum-CDIs, (c) Mean-CDIs and (d) Gaussian-CDIs associated with noise-free $\mathbf{Z}^{d,2}$ and $\mathbf{Z}^{u,2}$; $s = 0.002$ m in the scheme.

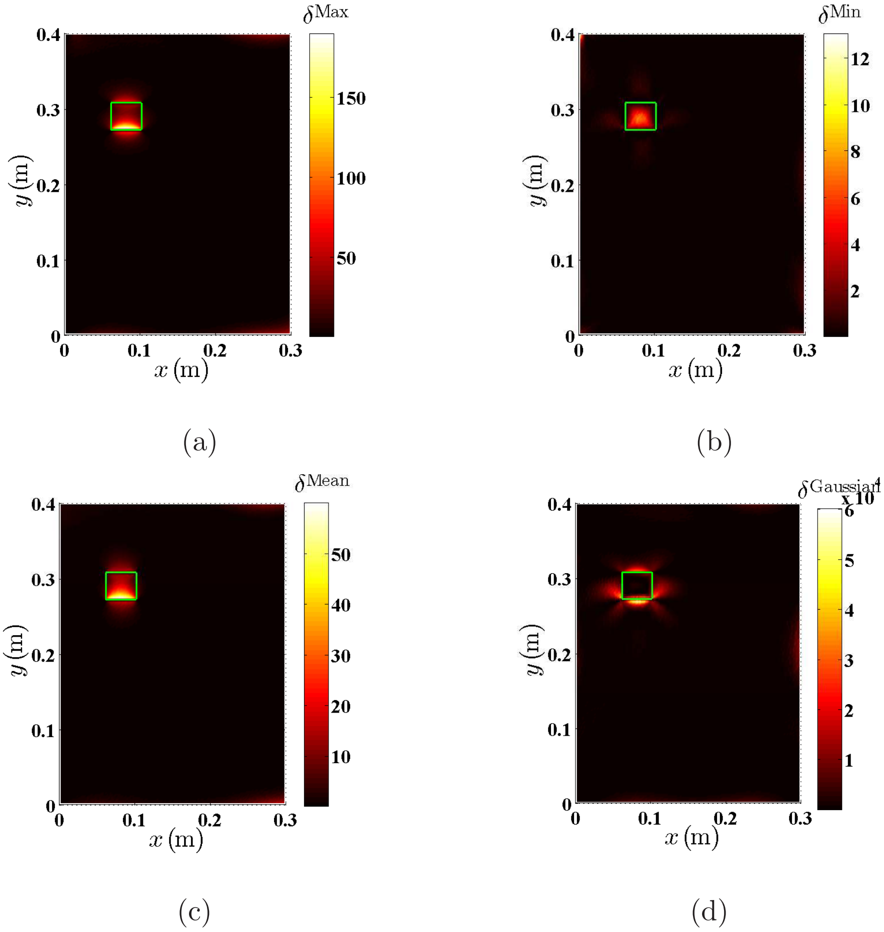

Figure 4.68: (a) Maximum-CDIs, (b) Minimum-CDIs, (c) Mean-CDIs and (d) Gaussian-CDIs associated with noise-free $\mathbf{Z}^{d,2}$ and the corresponding mode shape from the polynomial fit with $n = 8$; $s = 0.002$ m in the scheme.

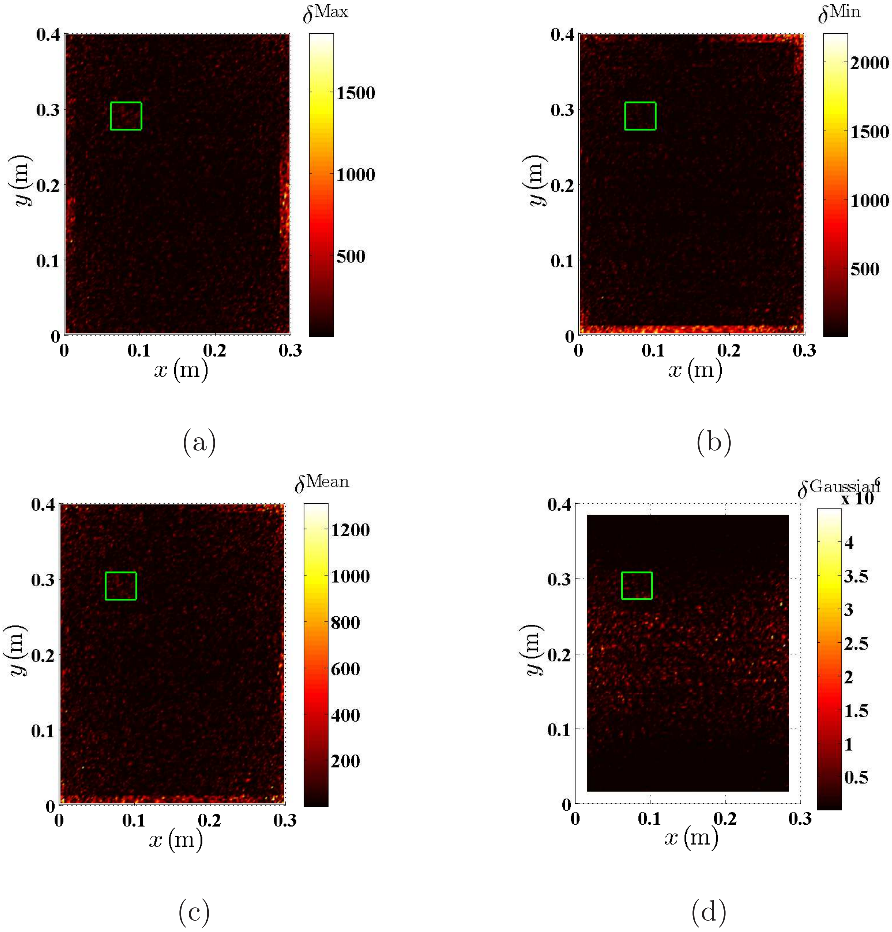

Figure 4.69: (a) Maximum-CDIs, (b) Minimum-CDIs, (c) Mean-CDIs and (d) Gaussian-CDIs associated with $\mathbf{Z}^{d,2}$ and the corresponding mode shape from the polynomial fit with $n = 8$; $s = 0.015$ m in the scheme.

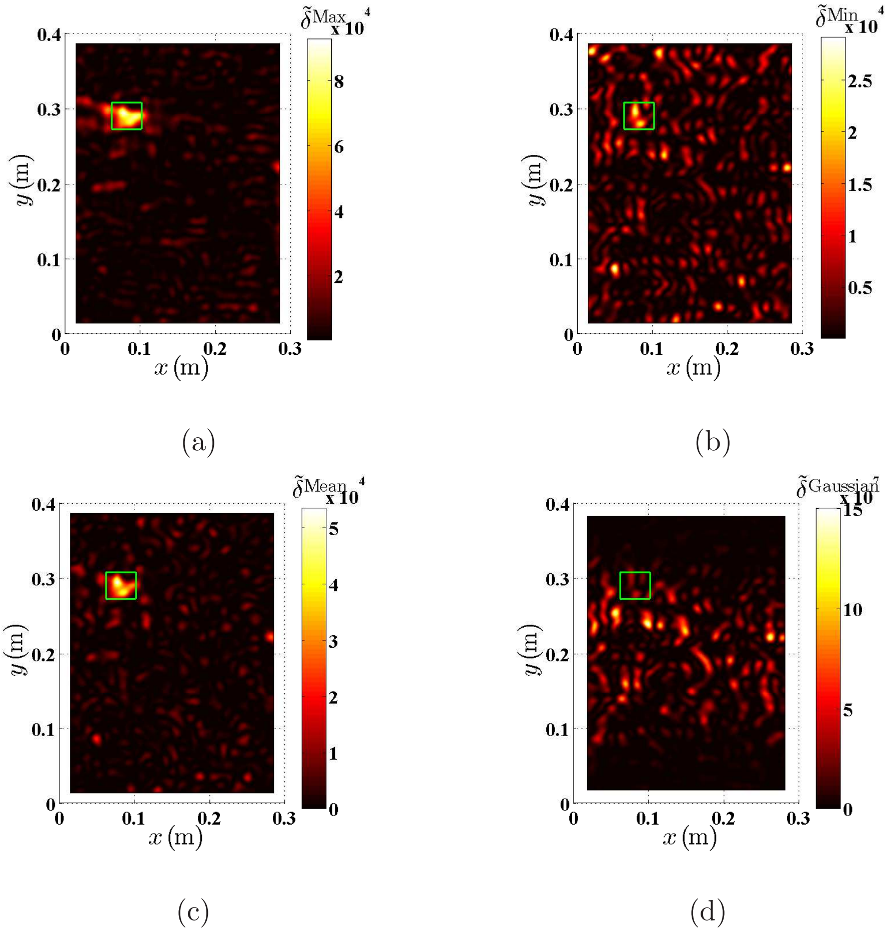

Figure 4.70: (a) Weighted Maximum-CDIs, (b) weighted Minimum-CDIs, (c) weighted Mean-CDIs and (d) weighted Gaussian-CDIs associated with $\mathbf{Z}^{d,2}$ and the corresponding mode shape from the polynomial fit with $n = 8$; $s = 0.015$ m in the scheme and $M_w = 7$ in the weight function.

Another finite element model of the damaged plate in Fig. 4.56(a) is constructed with a dense measurement grid; the model has a total of 240×320 square plate elements. A mode shape $\mathbf{Z}^{d,2}$ from the finite element model is presented on a coarse measurement grid with a total of 31×41 points, as shown in Fig. 4.65(d). The proper value of n associated with $\mathbf{Z}^{d,2}$ on the coarse grid is determined to be 8, and the mode shape from the polynomial fit with $n = 8$, denoted by $\mathbf{Z}^{p,2}$, is shown in Fig. 4.65(e). Maximum-CDIs, Minimum-CDIs, Mean-CDIs and Gaussian-CDIs associated with noise-free $\mathbf{Z}^{d,2}$ on the coarse grid and the corresponding mode shape from the polynomial fit with $s = 0.002$ m in the scheme are shown in Figs. 4.71(a) through (d), respectively. Similar to the results associated with $\mathbf{Z}^{d,2}$ on the dense grid in Fig. 4.68, the damage can also be clearly identified from the CDIs in Fig. 4.71.

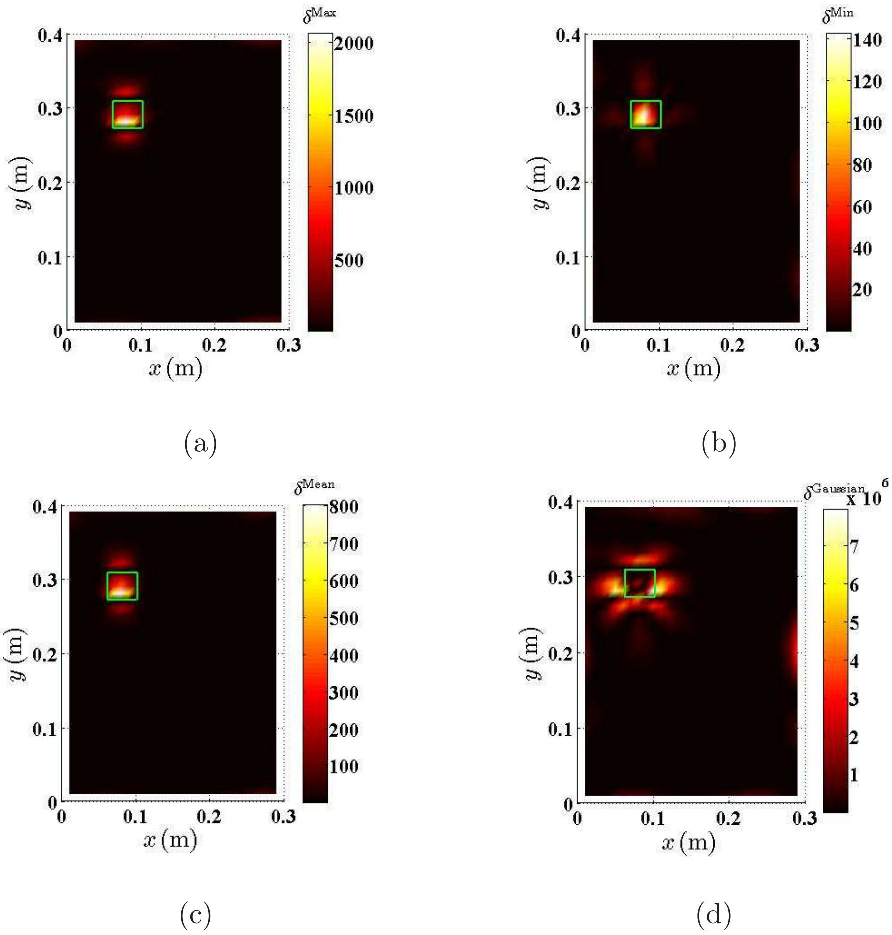

Figure 4.71: (a) Maximum-CDIs, (b) Minimum-CDIs, (c) Mean-CDIs and (d) Gaussian-CDIs associated with noise-free $\mathbf{Z}^{d,2}$ on the coarse measurement grid and the corresponding mode shape from the polynomial fit with $n = 8$; $s = 0.002$ m in the scheme.

White noise is then added to $\mathbf{Z}^{d,2}$ on the coarse grid with a signal-to-noise ratio of 60 db to simulate measurement noise. Maximum-CDIs, Minimum-CDIs, Mean-CDIs and Gaussian-CDIs associated with the mode shape and the corresponding mode shape from the polynomial fit with $s = 0.015$ m in the scheme are shown in Figs. 4.72(a) through (d), respectively. Similar to Fig. 4.69, the existence of the damage is fuzzed in the CDIs due to the measurement noise. Associated weighted Maximum-CDIs, Minimum-CDIs, Mean-CDIs and Gaussian-CDIs with $s = 0.015$ m in the scheme and $M_w = 7$ in the weight function are shown in Figs. 4.73(a) through (d), respectively, where the damage cannot be identified. When white noise is added to $\mathbf{Z}^{d,2}$ on the coarse grid with an increased signal-to-noise ratio of 75 db, the damage still cannot be identified in its Maximum-CDIs, Minimum-CDIs, Mean-CDIs and Gaussian-CDIs with $s = 0.015$ m in the scheme, as shown in Figs. 4.74(a) through (d), respectively. However, the damage can be identified in associated weighted Maximum-CDIs, Minimum-CDIs and Mean-CDIs with $s = 0.015$ m in the scheme and $M_w = 7$ in the weight function, as shown in Figs. 4.75(a) through (c), respectively, which is similar to the case of $\mathbf{Z}^{d,2}$ on the dense grid with a signal-to-noise ratio of 60 db.

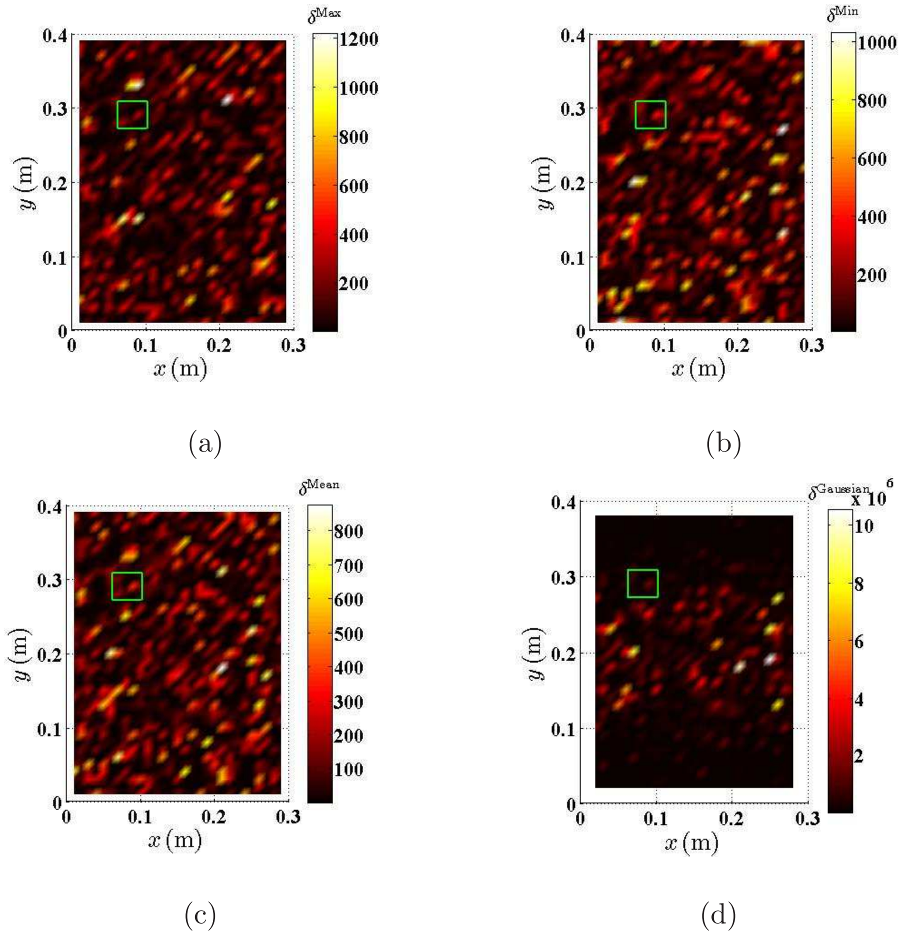

Figure 4.72: (a) Maximum-CDIs, (b) Minimum-CDIs, (c) Mean-CDIs and (d) Gaussian-CDIs associated with $\mathbf{Z}^{d,2}$ with a signal-to-noise ratio of 60 db on the coarse measurement grid and the corresponding mode shape from the polynomial fit with $n = 8$; $s = 0.015$ m in the scheme.

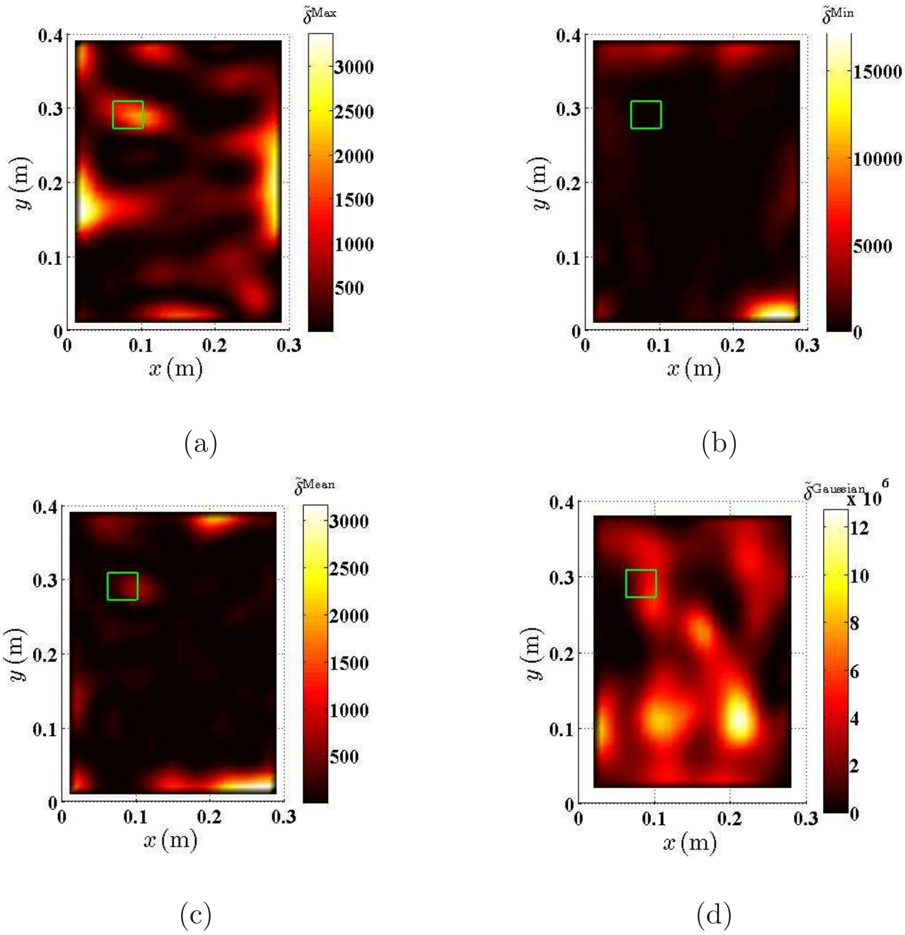

Figure 4.73: (a) Weighted Maximum-CDIs, (b) weighted Minimum-CDIs, (c) weighted Mean-CDIs and (d) weighted Gaussian-CDIs associated with $\mathbf{Z}^{d,2}$ with a signal-to-noise ratio of 60 db on the coarse measurement grid and the corresponding mode shape from the polynomial fit with $n = 8$; $s = 0.015$ m in the scheme and $M_w = 7$ in the weight function.

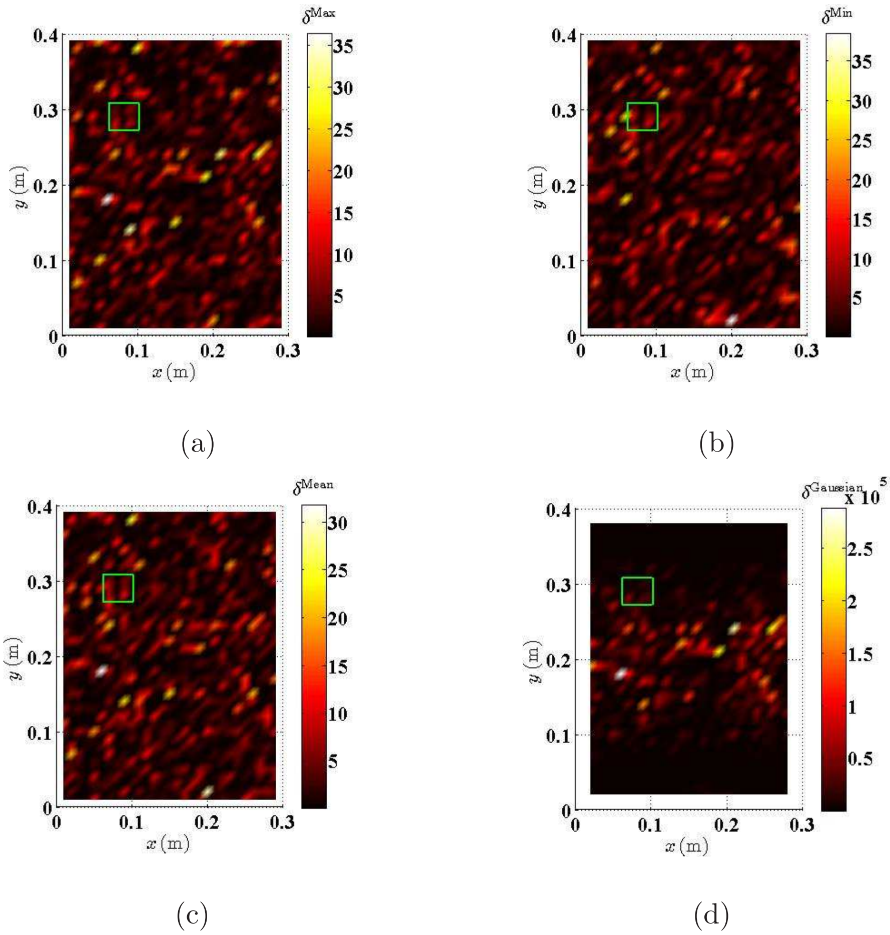

Figure 4.74: (a) Maximum-CDIs, (b) Minimum-CDIs, (c) Mean-CDIs and (d) Gaussian-CDIs associated with $\mathbf{Z}^{d,2}$ with a signal-to-noise ratio of 75 db on the coarse measurement grid and the corresponding mode shape from the polynomial fit with $n = 8$; $s = 0.015$ m in the scheme.

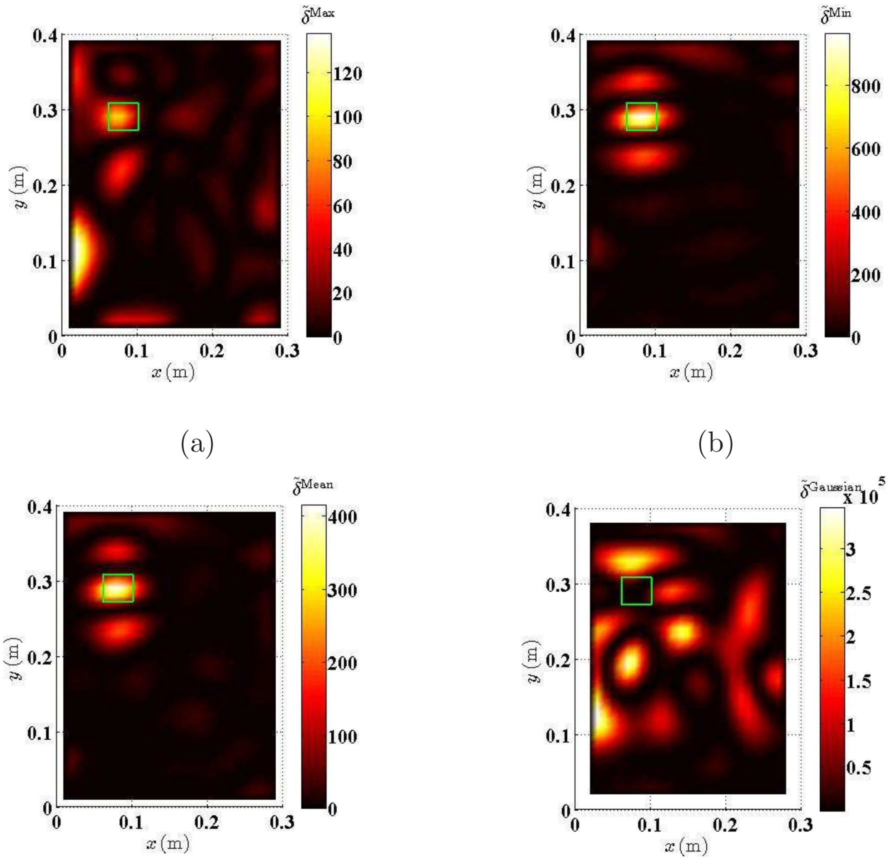

(a)

(b)

(c)

(d)

Figure 4.75: (a) Weighted Maximum-CDIs, (b) weighted Minimum-CDIs, (c) weighted Mean-CDIs and (d) weighted Gaussian-CDIs associated with $\mathbf{Z}^{d,2}$ with a signal-to-noise ratio of 75 db on the coarse measurement grid and the corresponding mode shape from the polynomial fit with $n = 8$; $s = 0.015$ m in the scheme and $M_w = 7$ in the weight function.

CDIs in Eqs. (4.52) through (4.55) consist of differences between CMSs of damaged and undamaged plates. Use of the weight function in Eqs. (4.66) through (4.69) at a point is equivalent to calculation of weighted sums of the differences within a region centered around the point. The size of the region is determined by the density of a measurement grid and M_w in the weight function. The smaller the density, the larger the region; the larger the weight M_w, the larger the region. Due to the use of the weight function, differences between the CMSs at a point and its neighboring points are attenuated in resulting weighted CDIs. Note that the differences to be attenuated consist of measurement noise and differences between CMSs associated with the corresponding noise-free mode shape of the damaged and undamaged plates. For a mode shape with a certain signal-to-noise ratio and certain M_w, the smaller the density of the measurement grid, the larger the differences to be attenuated, and damage may become unidentifiable in resulting weighted CDIs when the differences are too large; it can be verified by comparing Figs. 4.69 and 4.73, where the signal-to-noise ratios of $\mathbf{Z}^{d,2}$ are 60 db and $M_w = 7$. Since the density of the measurement grid in the former is large enough, the damage can be identified, but it cannot be in the latter due to the relatively small density of the measurement grid. For a mode shape on a measurement grid with a certain density and certain M_w, the higher the signal-to-noise ratio of the mode shape, the smaller the differences to be attenuated, and damage might become identifiable in resulting weighted CDIs when the differences are small; it can be verified by comparing Figs. 4.73 and 4.75, where densities of the measurement grids are the same and $M_w = 7$. Since the signal-to-noise ratio of $\mathbf{Z}^{d,2}$ in the latter is high enough, the damage can be identified, but it cannot be in the former due to the low signal-to-noise ratio of $\mathbf{Z}^{d,2}$.

The proposed damage identification method is applicable and robust to mode shapes associated with low and high elastic modes on dense and coarse measurement grids. One can infer that use of a coarse measurement grid can lead to a lower spatial resolution in resulting CDIs and the smallest size of identifiable damage would be larger. For a mode shape with relatively large measurement noise, i.e., a mode shape with a relatively low signal-to-noise ratio, use of a dense measurement grid is recommended so that effects of the measurement noise can be alleviated and the existence of damage can be manifested in weighted CDIs. In practice, one can increase the signal-to-noise ratio of a mode shape by increasing accuracy of measurement and/or increasing the level of excitation, and damage can still be identifiable even when a relatively coarse measurement grid is used in this case. The method can be applied to some real structures with curved surfaces, such as wind turbine blades.

4.3.3 Experimental Investigation

4.3.3.1 Experimental Setup

A damaged aluminum plate that had a length of 500.00 mm, a width of 400.00 mm and a thickness of 4.75 mm was constructed; its dimensions are shown in Fig. 4.76(a). The plate was hung using two nylon cords to simulate free boundary conditions, as shown in Fig. 4.76(b). The damage was a machined thickness reduction area, which had a length of 40.00 mm, a width of 40.00 mm and a depth of 0.5 mm; the depth was about 10% of the thickness of the undamaged portion of the plate, as shown in Fig. 4.76(c). In order to validate the simulated free boundary conditions of the plate, an experimental modal analysis was performed on it, where a PCB 086-D80 miniature impact hammer and a Polytec PSV-500 scanning laser Doppler vibrometer system were used to excite the plate and measure its response (Fig. 4.76(b)), respectively. In the experimental modal analysis, a fixed excitation point was impacted using the hammer, and the response of a measurement point was measured to yield five FRFs, which were averaged and analyzed using PolyMax of LMS Test.Lab Rev.9b to obtain natural frequencies of the plate. The lowest measured elastic natural frequency of the plate was 76.5 Hz. Since the highest measured natural frequency of rigid body modes of the plate in the setup was 2.1 Hz, which was much smaller than 10% of the lowest measured elastic natural frequency, the free boundary conditions were validated [1]. A rectangular measurement area of the opposite surface of the plate to the damaged one was used for mode shape measurement; it had a length of 395.9 mm and a width of 488.1 mm, as shown in Fig. 4.76(d). The rectangular area is slightly smaller than that of the plate in that there were two holes drilled on two top corners of the plate for hanging and clearances between edges of the plate and the rectangular area were reserved to prevent the laser of the scanning laser Doppler vibrometer system from reaching the two holes. The measurement area was sprayed with spot checker to enhance laser reflection that directly determined signal-to-noise ratios of laser measurements.

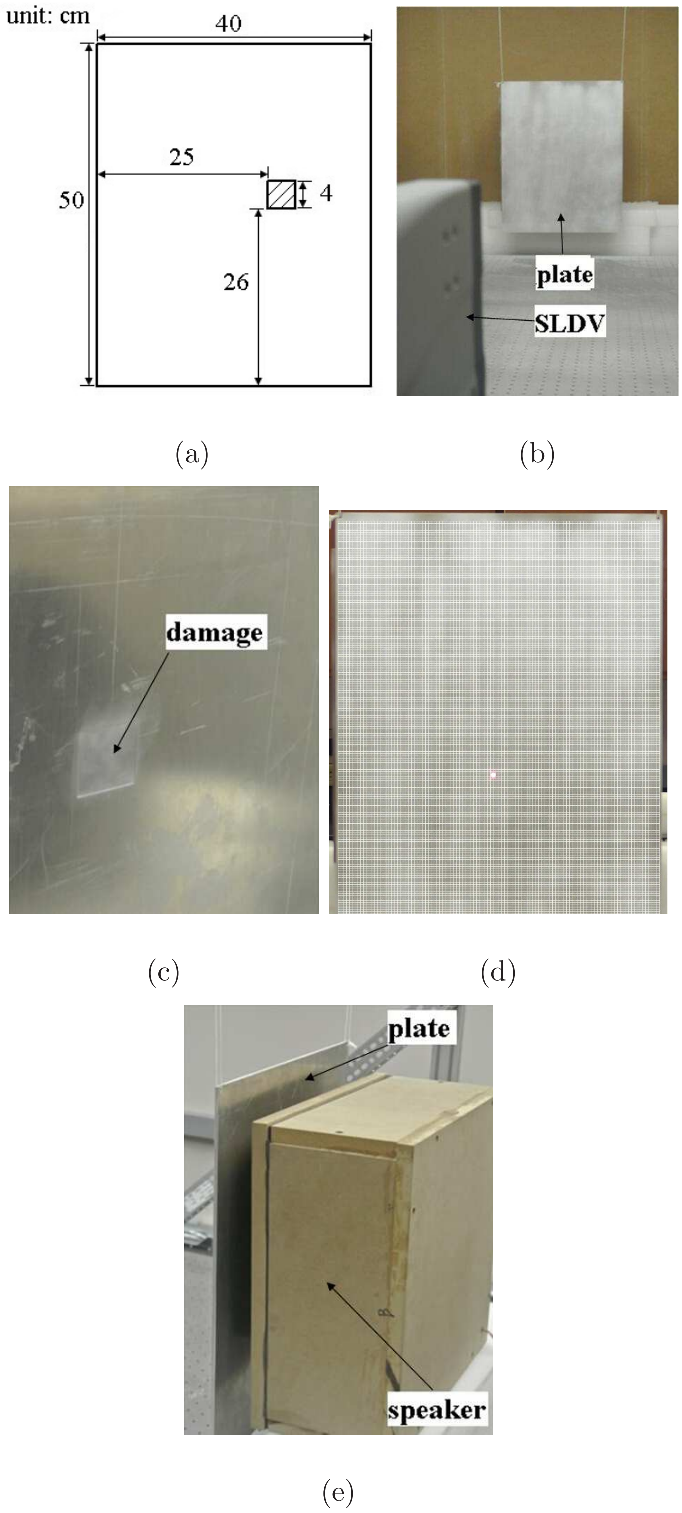

Figure 4.76: (a) Dimensions of the damaged plate, (b) the test setup for response measurements of the measurement surface, (c) the damaged surface of the plate, (d) the measurement grid on the measurement surface and (e) the electric speaker facing the damaged surface. Note that SLDV stands for scanning laser Doppler vibrometer in (b).

In order to accurately measure mode shapes of the damaged plate without incurring unwanted mass loading, non-contact excitation and measurements were performed [114], as shown in Figs. 4.76(b) and (e): an electric speaker with a wood box faced the damaged surface of the plate and generated acoustic excitation onto it, and the scanning laser Doppler vibrometer system measured velocities of measurement points in the measurement area. There were totally 115×177 measurement points in a measurement grid on the area, whose elements were rectangular and had a length of 3.44 mm and a width of 2.76 mm, as shown in Fig. 4.76(d). Acoustic excitation in the form of a sine wave with a constant magnitude and frequency was used to excite the plate, and the velocities of the measurement points were measured using the "FastScan" mode of the scanning laser Doppler vibrometer system. In the "FastScan" mode, a laser spot from the scanning laser Doppler vibrometer system stays at a measurement point on a structure to measure its response for a user-defined number of periods of the sine wave and then moves to the next measurement point. The duration for the laser spot to stay at one measurement point depends on the number of periods of the sine wave and sampling frequency of the system, and it can be as short as a ten-thousandth of a second. Due to this feature, a steady-state vibration shape of the structure under sinusoidal excitation can be measured in a point-by-point, but automatic and rapid, manner. In this measurement, the excitation signal given to the speaker was used for a reference signal, with which a vibration shape with a correct phase at each measurement point can be obtained [103]. The mode shape of the plate at the natural frequency of 1349 Hz, denoted by $\mathbf{Z}^{exp}$, was measured with an excitation frequency of 1349 Hz to experimentally investigate the effectiveness of the proposed method; the duration for the laser spot to stay at each measurement point was about 0.06 s. In order to transform the current measurement grid to one with square elements and increase spatial resolution of CDIs, $\mathbf{Z}^{exp}$ was interpolated using the Matlab function "griddata" with the option "natural" on a measurement grid with 199×245 measurement points, as shown in Fig. 4.77(a), which has square elements with a side length of 1.99 mm. For simplicity, the interpolated $\mathbf{Z}^{exp}$ is denoted by $\mathbf{Z}^{exp}$ herein.

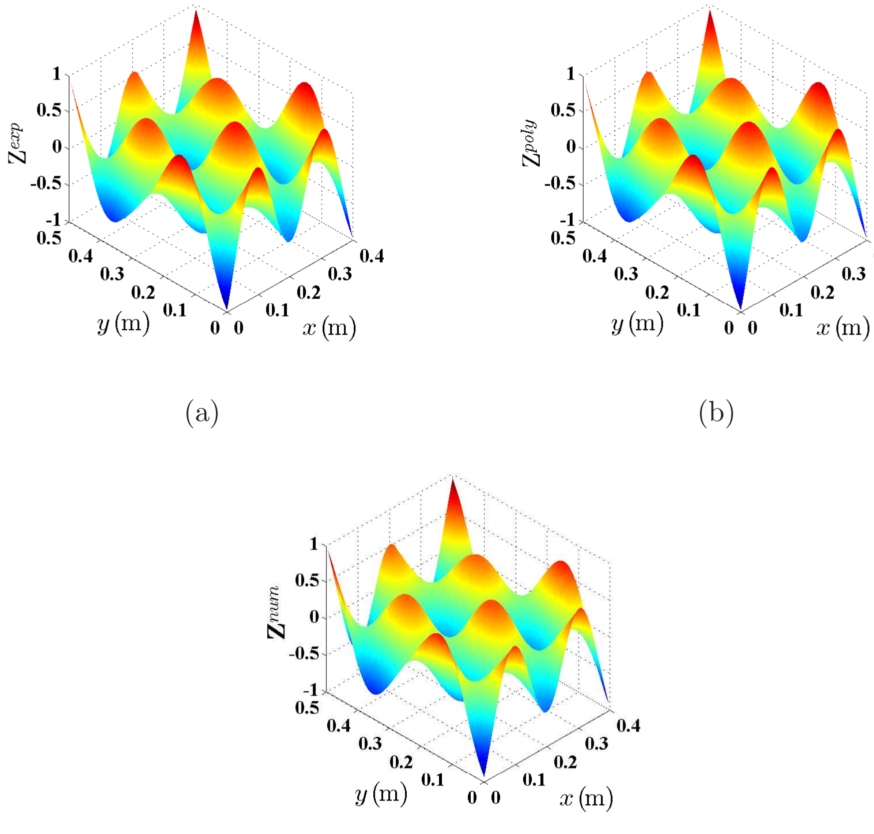

(a) (b)

(c)

Figure 4.77: (a) Interpolated measured mode shape $\mathbf{Z}^{exp}$ of the damaged plate at the natural frequency of 1349 Hz, (b) the mode shape from the polynomial that fits $\mathbf{Z}^{exp}$ with $n = 15$ and (c) the mode shape associated with the same mode as that of $\mathbf{Z}^{exp}$ from a finite element model of the damaged plate.

4.3.3.2 CMS and Damage Identification Results

Maximum, minimum, mean and Gaussian CMSs associated with $\mathbf{Z}^{exp}$ from the scheme with $s = 0.002$ m, $s = 0.005$ m and $s = 0.015$ m are shown in Figs. 4.78 through 4.80, respectively. In Fig. 4.78, global trends of the four CMSs associated with $\mathbf{Z}^{exp}$ from the scheme with $s = 0.002$ m could be observed with severe noise caused by measurement noise. When $s = 0.005$ m, the scheme yielded CMSs with much lower noise levels and their global trends became clearer than those from the scheme with $s = 0.002$ m, as shown in Fig. 4.79. When $s = 0.015$ m, associated CMSs were of the best qualities compared with those from the scheme with $s = 0.002$ m and 0.005 m. Adverse effects of measurement noise were mostly eliminated with a larger value of s.

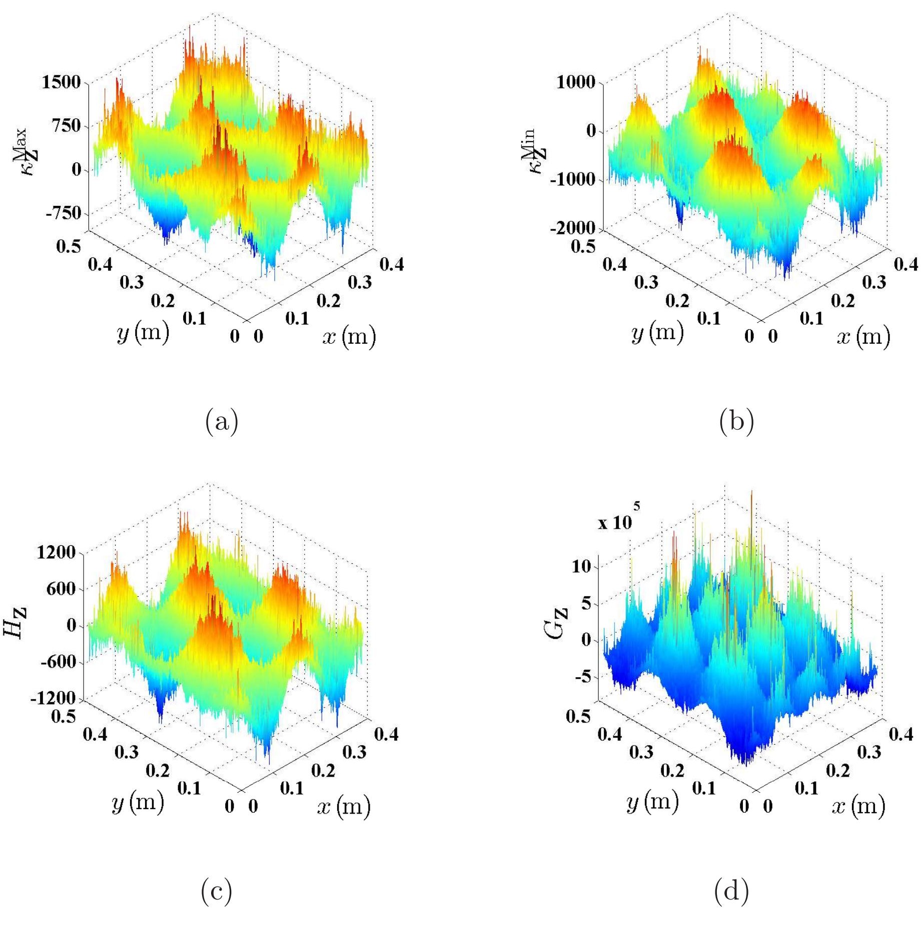

Figure 4.78: (a) Maximum, (b) minimum, (c) mean and (d) Gaussian CMSs associated with $\mathbf{Z}^{exp}$ from the scheme with $s = 0.002$ m.

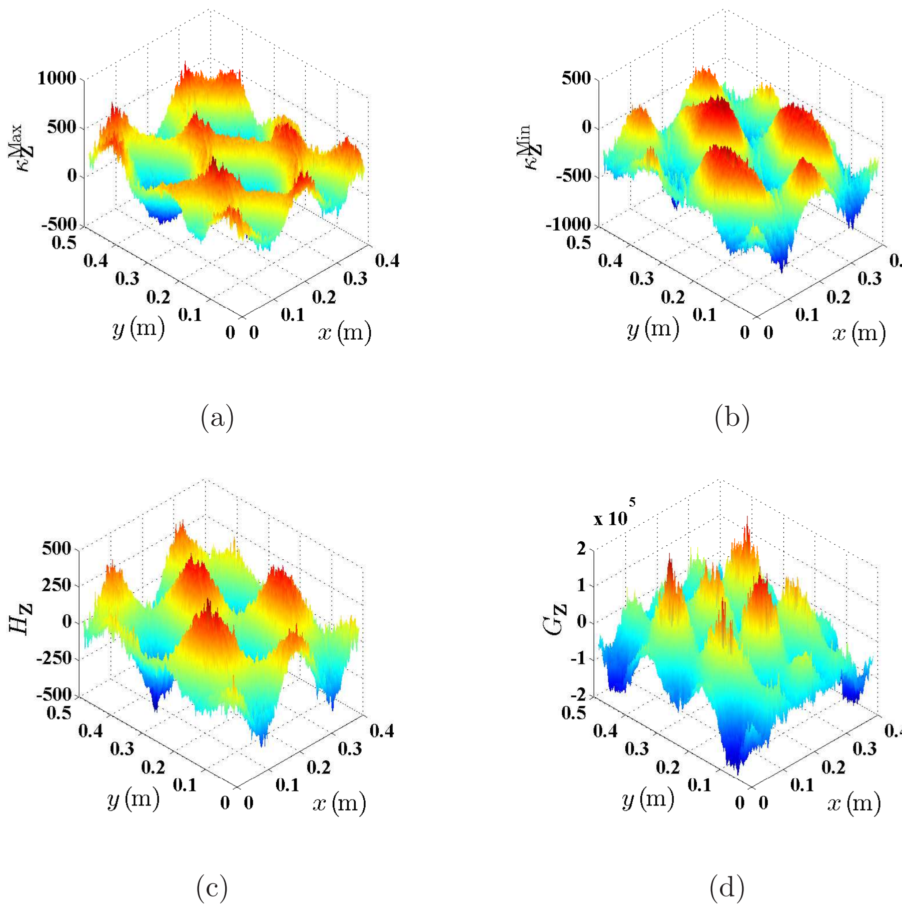

Figure 4.79: (a) Maximum, (b) minimum, (c) mean and (d) Gaussian CMSs associated with $\mathbf{Z}^{exp}$ from the scheme with $s = 0.005$ m.

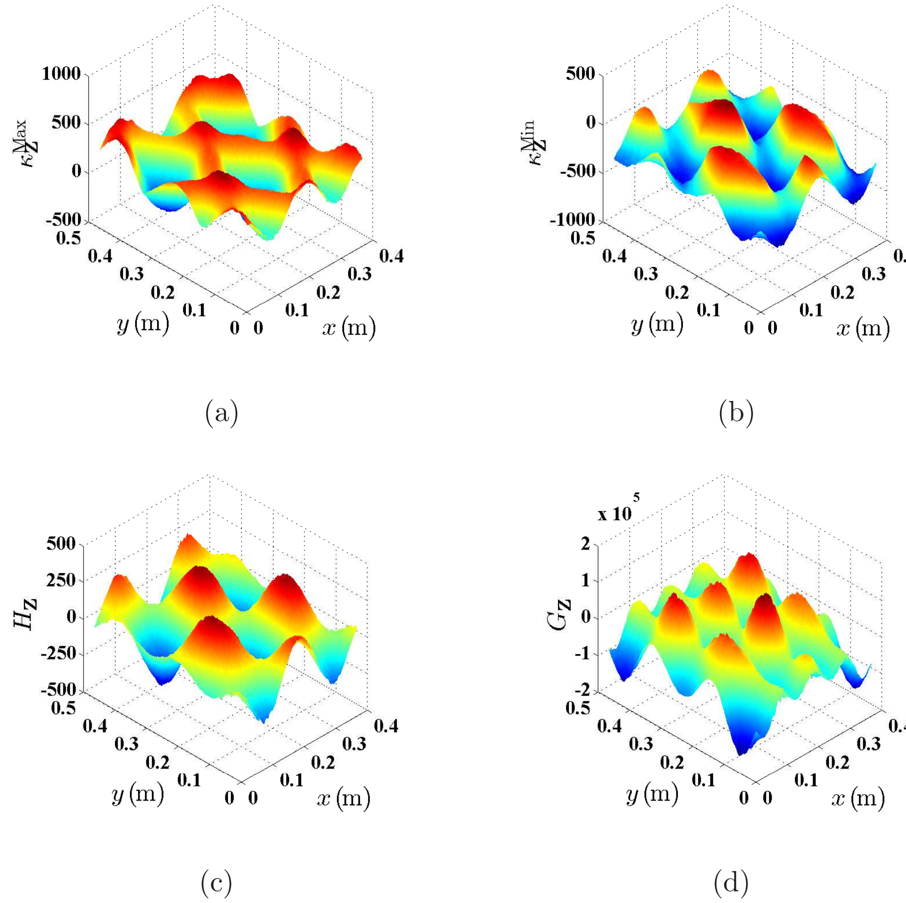

Figure 4.80: (a) Maximum, (b) minimum, (c) mean and (d) Gaussian CMSs associated with $\mathbf{Z}^{exp}$ from the scheme with $s = 0.015$ m.

To determine the proper order of a polynomial to fit $\mathbf{Z}^{exp}$, fit associated with $\mathbf{Z}^{exp}$ for different n were calculated, as shown in Fig. 4.81(a). Similar to the numerical example in Sec. 2.4, fit converged to a certain value as n increased, as shown in Fig. 4.81(b). Associated con for different n were calculated, as shown in Fig. 4.81(c). The proper order of the polynomial to fit $\mathbf{Z}^{exp}$ was determined to be 15, since con = 0.35%, which was lower than the prescribed threshold value for con, as shown in Fig. 4.81(d). The mode shape from the polynomial fit with $n = 15$ is shown in Fig. 4.77(b), and the MAC value associated with the mode shape from the polynomial fit and $\mathbf{Z}^{exp}$ was 99.99%.

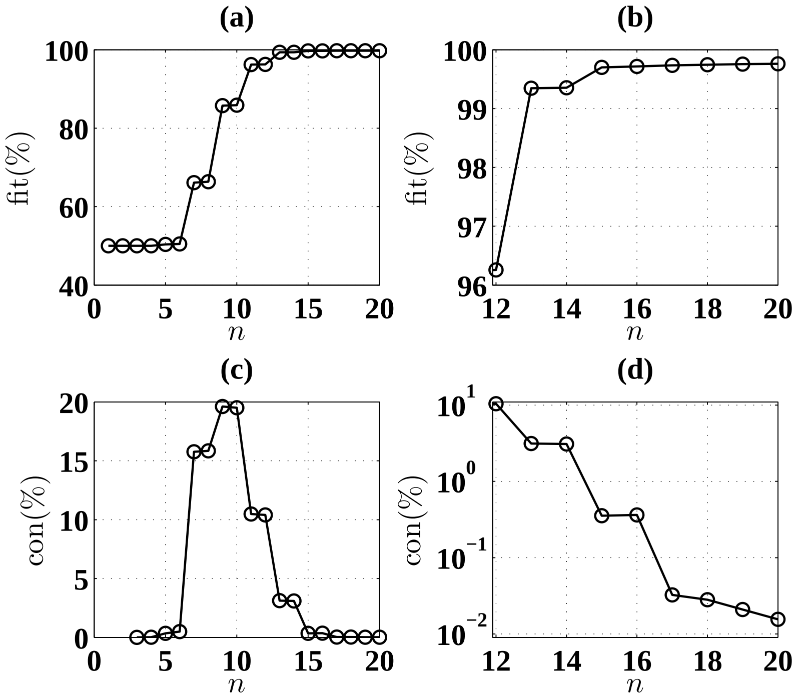

Figure 4.81: (a) Fitting indices fit associated with $\mathbf{Z}^{exp}$ for different n , (b) an enlarged view of fit, (c) the convergence indices con associated with $\mathbf{Z}^{exp}$ for different n and (d) an enlarged view of con.

Maximum-CDIs, Minimum-CDIs, Mean-CDIs and Gaussian-CDIs associated with $\mathbf{Z}^{exp}$ and the corresponding mode shape from the polynomial fit with $s = 0.002$ m, 0.005 m and 0.015 m in the scheme are shown in Figs. 4.82 through 4.84, respectively. In Fig. 4.82, the damage could not be identified from the four CDIs. The reason was that the associated CMSs were noisy since effects of measurement noise were amplified, and those of the damage on the CMSs were fussed. When s increased to 0.005 m in the scheme, ridges and regions that were formed by higher values of the CDIs in the neighborhood of and beyond the damage could be observed, as shown in Fig. 4.83. However, one could not identify the damage based on the CDIs due to the ridges and regions beyond the damage. When $s = 0.015$ m, ridges and regions similar to those in Fig. 4.83(a), (b) and (c) could still be observed in the Maximum-CDIs, Minimum-CDIs and Mean-CDIs, as shown in Fig. 4.84(a), (b) and (c), respectively. The difference is that higher values of the CDIs could be observed in the neighborhood of the damage when $s = 0.015$ m. In 4.84(d), higher values of the CDIs could be observed in the neighborhood of the damage; some higher values of the CDIs could also be observed in some regions beyond the damage. By use of the four CDIs in Fig. 4.84, one can identify the damage in regions with consistently higher values of the CDIs.

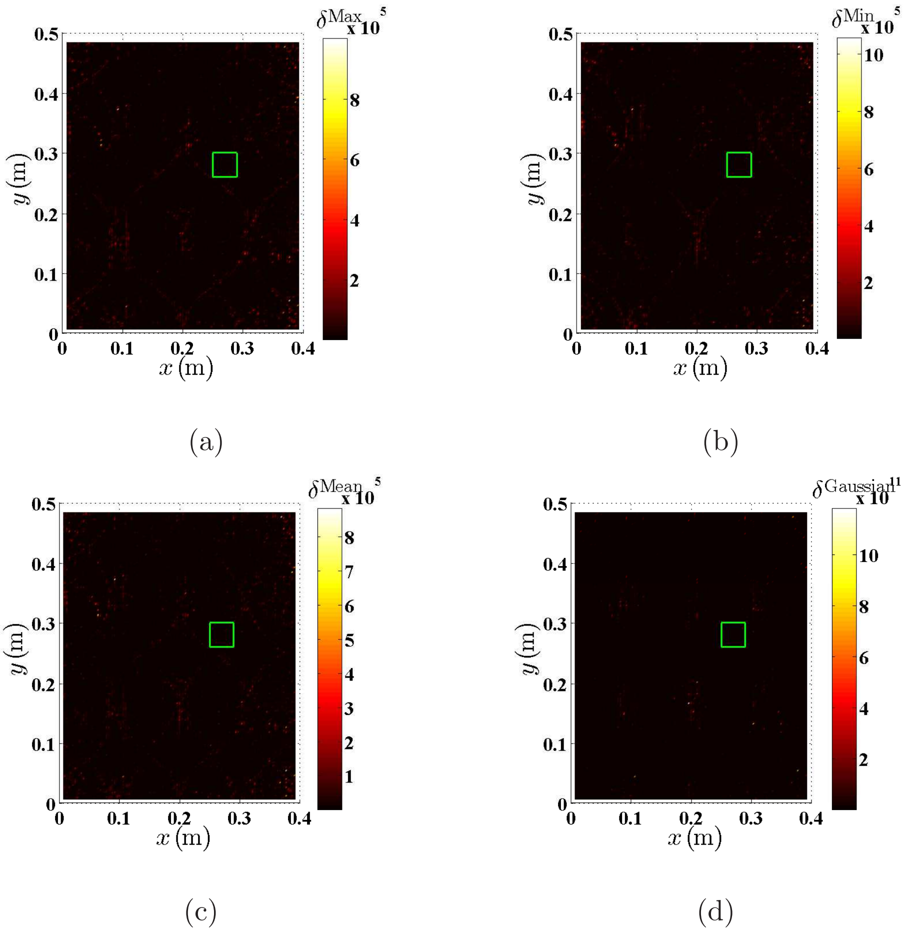

Figure 4.82: (a) Maximum-CDIs, (b) Minimum-CDIs, (c) Mean-CDIs and (d) Gaussian-CDIs associated with $\mathbf{Z}^{exp}$ and the corresponding mode shape from the polynomial fit with $n = 15$; $s = 0.002$ m in the scheme.

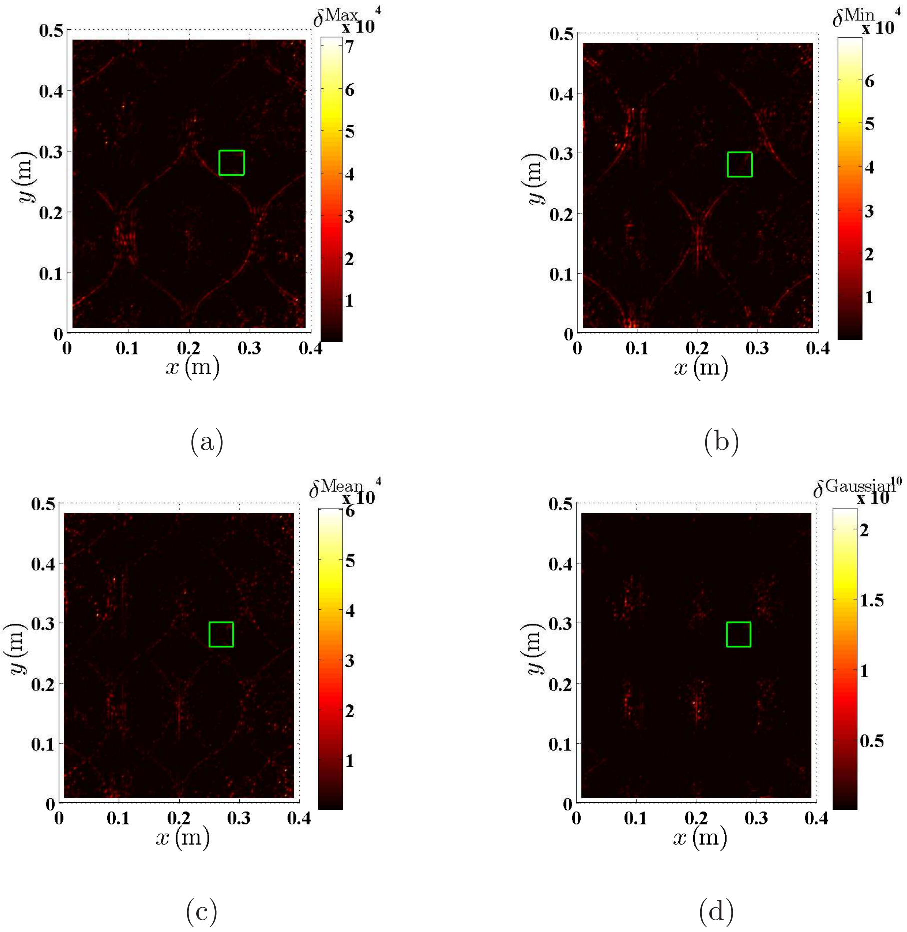

Figure 4.83: (a) Maximum-CDIs, (b) Minimum-CDIs, (c) Mean-CDIs and (d) Gaussian-CDIs associated with $\mathbf{Z}^{exp}$ and the corresponding mode shape from the polynomial fit with $n = 15$; $s = 0.005$ m in the scheme.

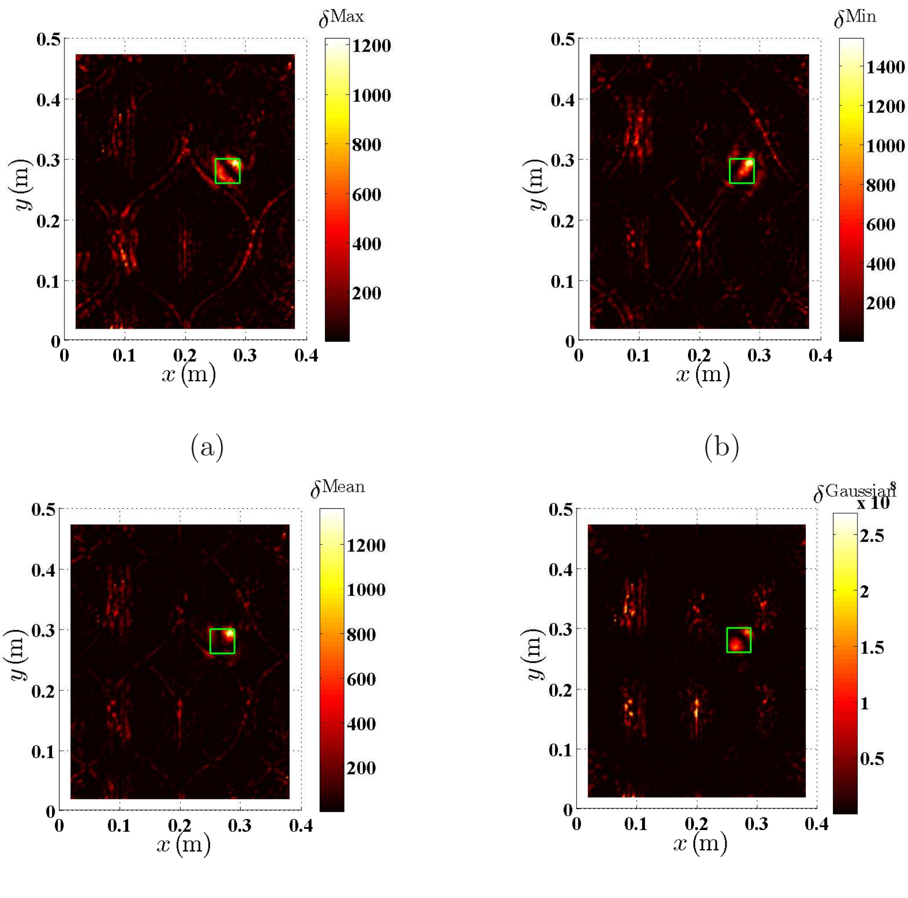

(a) (b) (c) (d)

Figure 4.84: (a) Maximum-CDIs, (b) Mininum-CDIs, (c) Mean-CDIs and (d) Gaussian-CDIs associated with $\mathbf{Z}^{exp}$ and the corresponding mode shape from the polynomial fit with $n = 15$; $s = 0.015$ m in the scheme.

To alleviate adverse effects of measurement noise on the CDIs, the weight function in Eq. (4.65) with $M_w = 7$ was applied to the CDIs in Figs. 4.82 through 4.84, based on Eqs. (4.66) through (4.69), and resulting weighted CDIs are shown in Figs. 4.85 through 4.87, respectively. When $s = 0.002$ m, relatively high values could be observed in the weighted Maximum-CDIs, Minimum-CDIs and Gaussian-CDIs in the neighborhood of and beyond the damage, and one could not identify the damage based on the three CDIs; higher values of the weighted Mean-CDIs could be identified in the neighborhood of the damage. When $s = 0.005$ m and 0.015 m, one could clearly identify the damage in neighborhoods of consistently higher values of weighted CDIs, as shown in Figs. 4.86 and 4.87, respectively. CDIs in Fig. 4.87 were less noisy than those in Fig. 4.86; consistently higher values of CDIs were mainly in the neighborhood of the damage in Fig. 4.87. Comparing CDIs with the same value of s in the scheme, one could see that use of the weight function could denoise the CDIs and manifest the damage with a smaller value of s.

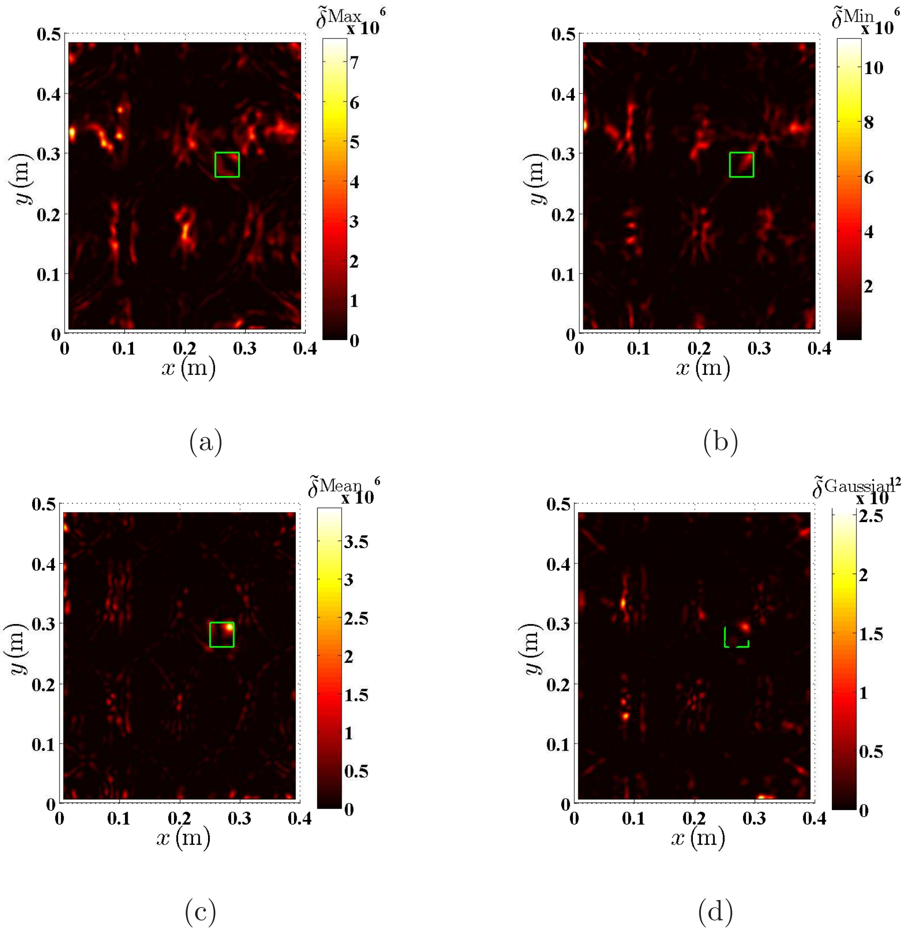

(a) (b) (c) (d)

Figure 4.85: (a) Weighted Maximum-CDIs, (b) weighted Minimum-CDIs, (c) weighted Mean-CDIs and (d) weighted Gaussian-CDIs associated with $\mathbf{Z}^{exp}$ and the corresponding mode shape from the polynomial fit with $n = 15$; $s = 0.002$ m in the scheme and $M_w = 7$ in the weight function.

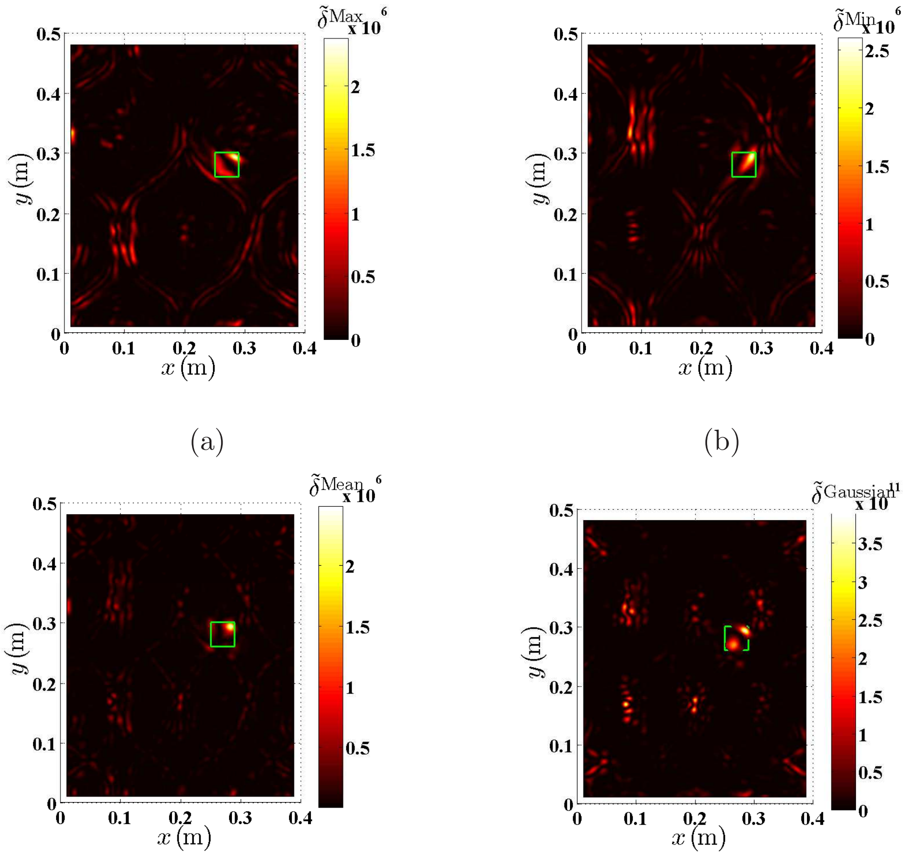

(a) (b) (c) (d)

Figure 4.86: (a) Weighted Maximum-CDIs, (b) weighted Minimum-CDIs, (c) weighted Mean-CDIs and (d) weighted Gaussian-CDIs associated with $\mathbf{Z}^{exp}$ and the corresponding mode shape from the polynomial fit with $n = 15$; $s = 0.005$ m in the scheme and $M_w = 7$ in the weight function.

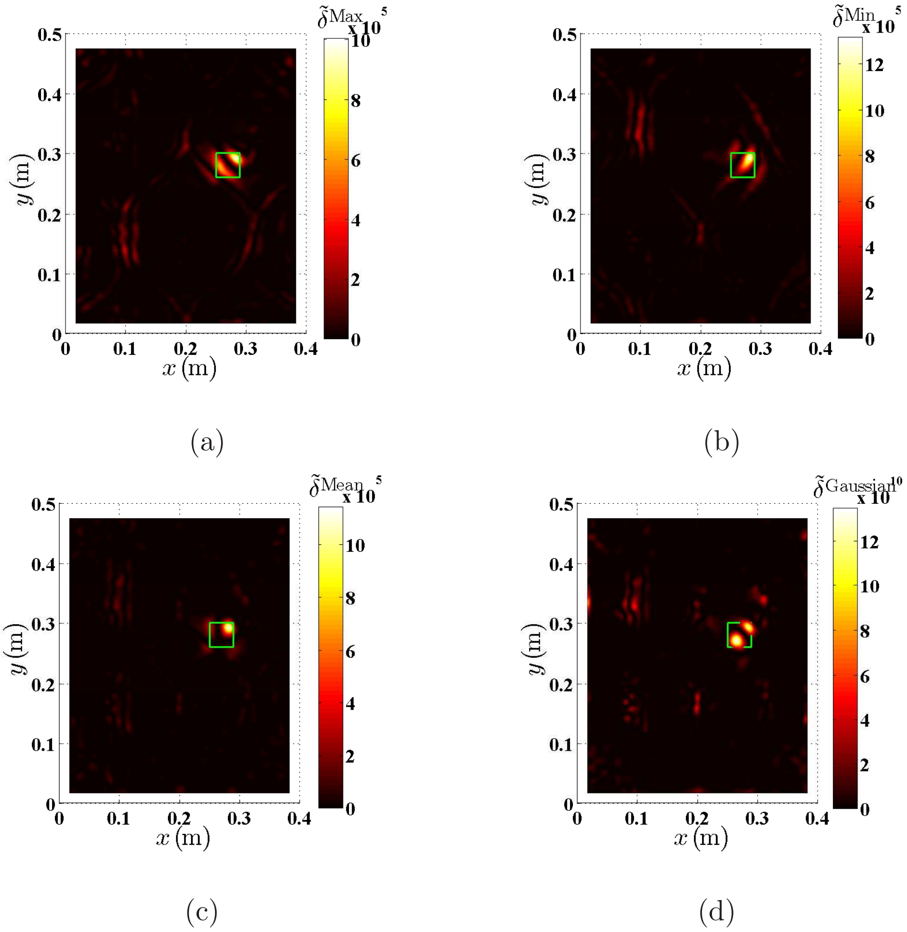

Figure 4.87: (a) Weighted Maximum-CDIs, (b) weighted Minimum-CDIs, (c) weighted Mean-CDIs and (d) weighted Gaussian-CDIs associated with $\mathbf{Z}^{exp}$ and the corresponding mode shape from the polynomial fit with $n = 15$; $s = 0.015$ m in the scheme and $M_w = 7$ in the weight function.

A finite element model of the damaged plate was constructed, and a noise-free undamped mode shape associated with the same mode as that of $\mathbf{Z}^{exp}$ was calculated and denoted by $\mathbf{Z}^{num}$, as shown in Fig. 4.77(c). Maximum-CDIs, Minimum-CDIs, Mean-CDIs and Gaussian-CDIs associated with $\mathbf{Z}^{num}$ and the corresponding mode shape from the polynomial fit with $s = 0.015$ m in the scheme are shown in Figs.

4.88(a) through (d), respectively; weighted Maximum-CDIs, Minimum-CDIs, Mean-CDIs and Gaussian-CDIs associated with $\mathbf{Z}^{num}$ and the corresponding mode shape from the polynomial fit with $s = 0.015$ m in the scheme and $M_w = 7$ in the weight function are shown in Figs. 4.89(a) through (d), respectively. Similar to the experimental damage identification results in Figs. 4.84 and 4.87, consistently higher values of the CDIs and weighted CDIs associated with $\mathbf{Z}^{num}$ occur in the neighborhood of the damage, and they resemble those associated with $\mathbf{Z}^{exp}$, which verifies the experimental damage identification results. The CDIs associated with $\mathbf{Z}^{num}$ and the corresponding mode shape from the polynomial fit resemble the associated weighted CDIs, as shown in Figs. 4.88 and 4.89, respectively, which indicates that use of the weight function does not affect damage identification results when a mode shape is noise-free. Effectiveness of using the weight function in alleviating adverse effects of measurement noise on the CDIs and manifesting existence of damage in the CDIs can be verified by comparing the CDIs associated with $\mathbf{Z}^{num}$ in Fig. 4.88 with the weighted CDIs associated with $\mathbf{Z}^{exp}$ in Fig. 4.87, since the latter, which have lower noise levels than the CDIs associated with $\mathbf{Z}^{exp}$ in Fig. 4.84, resemble the former.

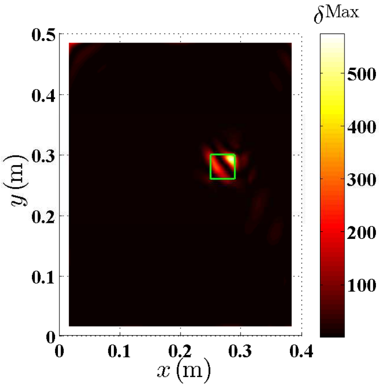

(a)

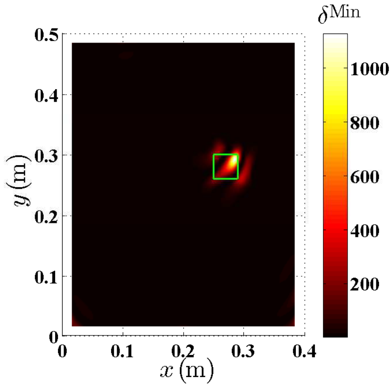

(b)

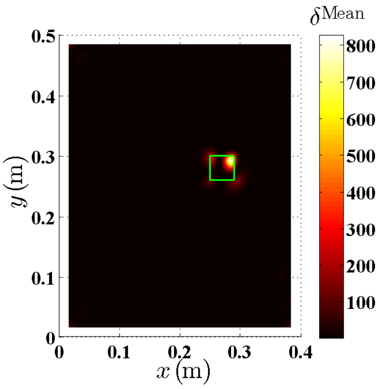

(c)

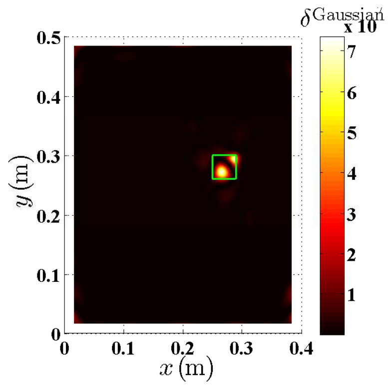

(d)

Figure 4.88: (a) Maximum-CDIs, (b) Mininum-CDIs, (c) Mean-CDIs and (d) Gaussian-CDIs associated with $\mathbf{Z}^{num}$ and the corresponding mode shape from the polynomial fit with $n = 15$; $s = 0.015$ m in the scheme.

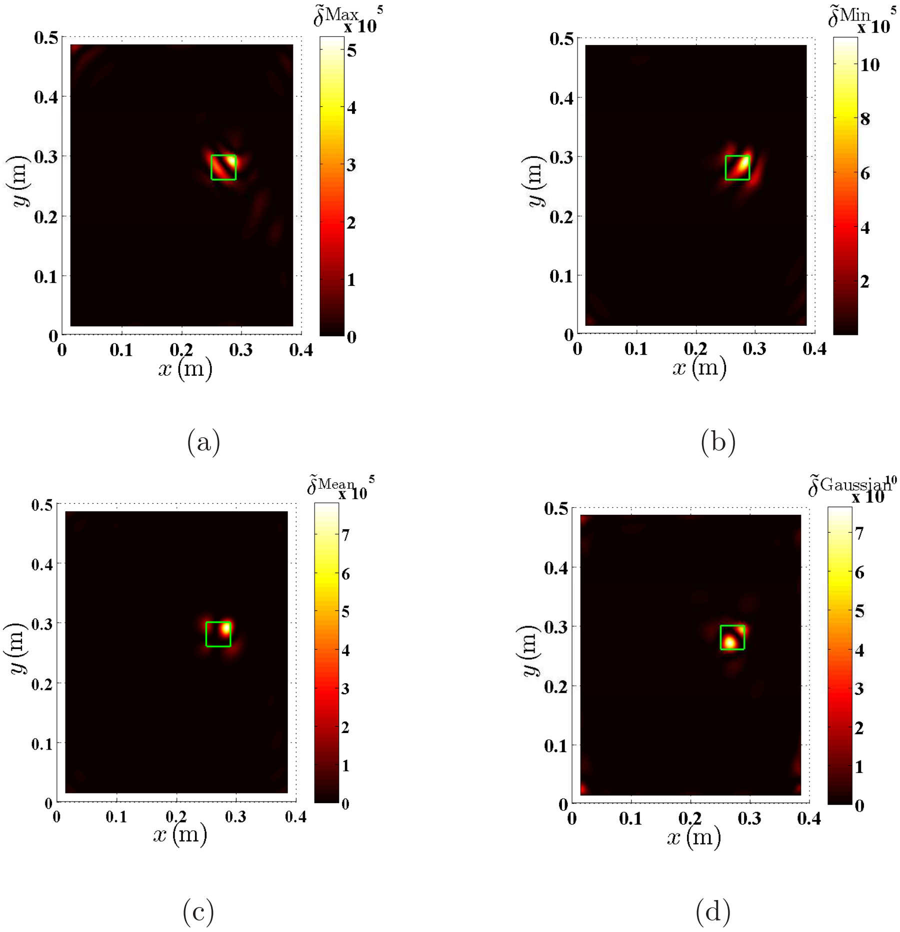

(a) (b)

(c) (d)

Figure 4.89: (a) Weighted Maximum-CDIs, (b) weighted Minimum-CDIs, (c) weighted Mean-CDIs and (d) weighted Gaussian-CDIs associated with $\mathbf{Z}^{num}$ and the corresponding mode shape from the polynomial fit with $n = 15$; $s = 0.015$ m in the scheme and $M_w = 7$ in the weight function.

4.3.4 Conclusion

A new non-model-based plate damage identification method based on principal, mean and Gaussian CMSs is proposed. It can be applied to a damaged plate without use of any a priori information of the associated undamaged one, if the undamaged plate is geometrically smooth and made of materials that have no stiffness and mass discontinuities. A multi-scale differential-geometry scheme is proposed to calculate the CMSs associated with a mode shape. The advantage of the scheme is that adverse effects of measurement noise could be alleviated with use of a larger value of the scale parameter. Differences between the aforementioned CMSs of a damaged plate and those associated with a mode shape from a polynomial that fits the corresponding mode shape of the damaged plate are processed to yield four CDIs. Based on the fitting index, a mode shape from a polynomial that fits the corresponding mode shape of a damaged plate would have a higher level of approximation as the order of the polynomial increases. A threshold value is used for the convergence index, based on which the order of the polynomial can be properly determined. CMSs associated with a mode shape from a polynomial of a properly determined order can be used to eliminate global trends of CMSs associated with the corresponding mode shape of a damaged plate. Use of a weight function can alleviate effects of measurement noise on the CDIs and shorten the process of progressively testing different values of the scale parameter. The proposed method is applicable and robust to mode shapes associated with low and high elastic modes; it is recommended that one increase the signal-to-noise ratio of a mode shape and use a dense measurement grid to alleviate effects of measurement noise. The proposed method was experimentally applied to a plate with damage in the form of a machined thickness reduction area. The damage was successfully identified by locating consistently higher values of the CDIs. A larger value of the scale parameter in the scheme can manifest existence of damage in the CDIs; use of the weight function can manifest existence of damage even with a small value of the scale parameter in the scheme. The experimental damage identification results were numerically verified by applying the proposed method to the mode shape associated with the same mode as that of the measured mode shape from a finite element model of the damaged plate.

Chapter 5

STRUCTURAL IDENTIFICATION USING FREE RESPONSE SHAPES

5.1 Introduction

Vibration-based damage detection has become a major research topic of structural dynamics in the past few decades [85]. Changes of physical properties of a structure, such as mass, stiffness and damping, are directly related to those of modal properties of the structure, i.e., natural frequencies, mode shapes MSs and modal damping ratios [1]. Damage that exist in a structure can be detected, located and characterized by use of modal characteristics. Methods that use changes of natural frequencies due to damage have been investigated by many researchers. They require a minimum amount of vibration measurement and can accurately detect damage, since natural frequencies are global characteristics of a structure and relatively easy to measure [126, 127, 82, 83, 115, 116]. However, spatial information of structural property changes due to occurrence of damage cannot be directly obtained by use of natural frequencies, and one needs to construct accurate, physics-based models in order to apply the methods [126, 127, 82, 83, 115, 116], which can be difficult to achieve in practice, especially for complex large-scale structures. Since occurrence of damage can introduce local abnormalities in MSs near damage regions

[84], unlike use of natural frequencies, the damage can be identified by inspecting smoothness of MSs without necessity of constructing models of structures. Being more sensitive to damage of small extent than MSs, CMSs are more often used to locate damage [86]. Effects of damage in a beam structure can be observed as severer local abnormalities in its CMSs than in MSs, and one can isolate the effects by comparing a CMS of the damaged beam structure with that of an undamaged one. It was shown that relatively large differences between a CMS of a damaged beam structure and that of an undamaged one mainly occur near a region of damage and the differences increase as severity of damage increases [86]. A gapped-smoothing method was proposed in Refs. [87, 88] to locate damage in beam structures by use of CMSs and curvatures of ODSs, where those of undamaged beam structures are not needed. The gapped-smoothing method and a global fitting method were then synthesized to locate damage in beam structures [89, 90], where measured MSs and ODSs of damaged beam structures were fitted by generic MSs to approximate MSs of undamaged ones, and the method was further extended for plate structures [106]. CMS-based and wavelet-transform-based methods were proposed in Ref. [9] to identify embedded horizontal cracks in beam structures, where global trends of CMSs and wavelet transforms were eliminated by use MSs from polynomials that fit MSs of cracked beam structures with properly determined orders in a global manner.

A laser Doppler vibrometer (LDV) system is capable of accurate, non-contact surface vibration measurement; its mechanism is based on Doppler shifts between the incident light from and scattered light to the system [10]. An advantage of the system is that unwanted local stiffening and mass loading effects can be avoided, while use of attached transducers inevitably incurs such effects that can deteriorate accuracy of measurement, especially for lightweight structures. When equipped with a scanner that consists of a pair of orthogonal scan mirrors, a LDV becomes a scanning LDV. The laser beam from a scanning LDV can be directed to any visible position on a structure, and LDV measurement in an automatic manner can be achieved with a properly designed control scheme. However, it can take a relatively long acquisition time for a scanning LDV system to measure a large-scale structure with a dense measurement grid. The concept of a continuously scanning LDV (CSLDV) system was first proposed in Refs. [128, 129]. A CSLDV system continuously sweeps its laser over a surface of a structure under sinusoidal excitation to obtain its ODSs, which can be approximated by Chebysev series with coefficients determined by processing velocities measured by the system. Two CSLDV measurement methods were later proposed to obtain ODSs of a structure under sinusoidal excitation: demodulation and polynomial methods [130, 131]. In the demodulation method, velocities measured by a CSLDV system is modulated by multiplying a sinusoid at an excitation frequency, and a low-pass filter is applied to the modulated signal to obtain an ODS associated with the excitation frequency. In the polynomial method, it is assumed that an ODS can be represented by a polynomial, and coefficients of the polynomial can be determined by use of discrete Fourier transforms of measured velocities by a CSLDV system. The two methods were extended for structures under impact and multi-sine excitation in Refs. [132] and [133], respectively. A "lifting" method was proposed to obtain MSs from measured free response of a structure, where measured velocities by a CSLDV system are treated as output of linear time-periodic systems [134]. The "lifting" method was extended to output-only modal analysis to identify modal characteristics of a structure with use of harmonic transfer functions [135]. Use of a CSLDV system for damage identification was first proposed in Ref. [136], where the demodulation method was used to obtain ODSs of various structures by scanning their cracked surfaces, and effects of cracks could be observed as local abnormalities in obtained ODSs. The demodulation and polynomial methods were synthesized to identify damage in beams, where damage can be identified by use of a CSLDV system that scans intact surfaces of damaged beam structures [137].

In this section, a new type of vibration shapes called a free response shape (FRS) that can be obtained by use of a CSLDV system is introduced. An analytical expression of FRSs of a damped beam structure is derived. It is shown in the analytical expression that amplitudes of FRSs exponentially decay to zero with time. Numbers of non-zero FRSs associated with a mode can be determined by use of the short-time Fourier transform (STFT) of free response of the structure measured by a CSLDV system. A finite element model of a damped beam structure is constructed, and a CSLDV system is simulated to measure its free response. FRSs associated with the structure are obtained from the response maesured by the simulated CSLDV system from the demodulation method, and they are compared with those from the analytical expression. A new damage identification methodology that uses FRSs is proposed for beam structures. A free-response damage index (FRDI) is defined, which consists of differences between curvatures of FRSs obtained by use of a CSLDV system and those from polynomials that fit the FRSs, and damage regions can be identified near neighborhoods with consistently high values of FRDIs associated with different modes; an auxiliary FRDI is proposed to assist identification of the neighborhoods. A criterion based on a convergence index is proposed to determine orders of the polynomial fits. Effectiveness of the methodology for identifying damage in beam structures is numerically and experimentally investigated, and effects of the scan frequency of a CSLDV system on qualities of obtained FRSs were experimentally investigated.

5.2 Methodology

5.2.1 Free Response of a Damped Beam Structure

A linear time-invariant Euler-Bernoulli beam structure with a uniform cross-section is considered. The structure has a length L, a bending stiffness EI and a linear mass density m. It is viscously damped, and damping effects are modeled using the Kelvin-Voigt viscoelastic model with a damping coefficient c [54, 35]. Excitation in the form of a single impulse with an intensity G_0 is applied to the structure at position $x = L_0$ at time $t = 0$. Response of the structure can be obtained by solving its governing partial differential equation

$$EI\left[\frac{\partial^4 y(x,t)}{\partial x^4} + c\frac{\partial}{\partial t}\left(\frac{\partial^4 y(x,t)}{\partial x^4}\right)\right] + m\frac{\partial^2 y(x,t)}{\partial t^2} = G_0\delta(x-L_0)\delta(t) \tag{5.1}$$

with given boundary and initial conditions, where $y(x,t)$ is the displacement of the structure at position x at time t. Based on the expansion theorem [54], a solution to Eq. (5.1) can be expressed by

$$y(x,t) = \sum_{h=1}^{\infty} Y_h(x) F_h(t) \tag{5.2}$$

where $Y_h(x)$ is the eigenfunction of the h-th mode of the corresponding undamped structure and $\eta_h(t)$ is the corresponding time function. The eigenfunction $Y_h(x)$ can be expressed by

$$Y_h(x) = C_1 \sin \beta_h x + C_2 \cos \beta_h x + C_3 \sinh \beta_h x + C_4 \cosh \beta_h x \tag{5.3}$$

where C_1, C_2, C_3, C_4 and β_h are determined by the boundary conditions and the orthonormality condition of eigenfunctions

$$\int_0^L m Y_h(x) Y_j(x) \, \mathrm{d}x = \delta_{h,j} \tag{5.4}$$

in which $\delta_{h,j}$ is the Kronecker delta. The time function $F_h(t)$ can be obtained by solving an ordinary differential equation

$$\ddot{F}_h(t) + c(2\pi f_h)^2 \dot{F}_h(t) + (2\pi f_h)^2 F_h(t) = G_0 Y_h(L_0) \delta(t) \tag{5.5}$$

with initial conditions $F_h(0)$ and $\dot{F}_h(0)$ determined by those of Eq. (5.1), where f_h is the natural frequency of the undamped structure in Hz associated with its h-th mode. A relation between β_h and f_h can be expressed by

$$\beta_h^4 = \frac{(2\pi f_h)^2 m}{EI} \tag{5.6}$$

The solution to Eq. (5.5) can be expressed by [138]

$$
\begin{aligned}
F_h(t) &= \mathrm{e}^{-2\pi\zeta_h f_h t}\left[F_h(0)\cos(2\pi f_{h,d}t) + \left(\tfrac{\dot{F}_h(0)+2\pi\zeta_h f_h F(0)}{2\pi f_{h,d}} + \tfrac{G_0 Y_h(L_0)}{2\pi f_{h,d}}\right)\sin(2\pi f_{h,d}t)\right] \\
&= A_h \mathrm{e}^{-2\pi\zeta_h f_h t}\cos(2\pi f_{h,d}t - \gamma_h)
\end{aligned}
\tag{5.7}
$$

where

$$
A_h = \sqrt{(F_h(0))^2 + \left[\frac{\dot{F}_h(0) + 2\pi\zeta_h f_h F(0)}{2\pi f_{h,d}} + \frac{G_0 Y_h(L_0)}{2\pi f_{h,d}}\right]^2} \tag{5.8}
$$

is an amplitude constant and

$$
\gamma_h = \mathrm{arctan2}\left(\frac{\dot{F}_h(0) + 2\pi\zeta_h f_h F(0)}{2\pi f_{h,d}} + \frac{G_0 Y_h(L_0)}{2\pi f_{h,d}}, F_h(0)\right) \tag{5.9}
$$

is a phase angle;

$$
\zeta_h = c\pi f_h \tag{5.10}
$$

and

$$
f_{h,d} = f_h\sqrt{1-\zeta_h^2} \tag{5.11}
$$

are the damping ratio and damped natural frequency of the structure associated with its h-th mode, respectively. Based on Eqs. (5.2) and (5.7), $y(x,t)$ can be expressed by

$$
y(x,t) = \sum_{h=1}^{\infty} A_h Y_h(x)\,\mathrm{e}^{-2\pi\zeta_h f_h t}\cos(2\pi f_{h,d}t - \gamma_h) \tag{5.12}
$$

5.2.2 FRS

A FRS associated with the h-th mode of the beam structure can be defined by

$$\phi_h(x,t) = A_h Y_h(x)\,\mathrm{e}^{-2\pi\zeta_h f_h t} \tag{5.13}$$

and Eq. (5.12) becomes

$$y(x,t) = \sum_{h=1}^{\infty} \phi_h(x,t)\cos\left(2\pi f_{h,d} t - \gamma_h\right) \tag{5.14}$$

It can be seen that Y_h, which can be considered as a MS associated with the h-th mode, exists in the definition of a FRS in Eq. (5.13). A similarity between Y_h and ϕ_h is that they both correspond to the same mode of the structure. Since a MS describes amplitude ratios of displacement, velocity or acceleration at different positions on the structure while it vibrates, the multiplication factor of the MS can be an arbitrarily chosen non-zero constant, and the MS can be considered time-invariant. However, ϕ_h differs from Y_h due to two extra terms in Eq. (5.13), i.e., A_h and $\mathrm{e}^{-2\pi f_h \xi_h t}$. The coefficient A_h is determined by the initial conditions of and impulse to the structure, and $\mathrm{e}^{-2\pi f_h \xi_h t}$ indicates that amplitudes of ϕ_h at different positions exponentially decay to zero with time. Hence, A_h cannot be arbitrarily chosen, and ϕ_h is time-varying.

A CSLDV system continuously sweeps its laser spot over a vibrating structure surface with a specific scan pattern. It can measure response of a measurement point, where its laser spot is located during a scan, and a finite number of modes of a structure are included in free response measured by a CSLDV system. Let $\tilde{x}(t)$ be the position of a laser spot on a beam structure at time t; free response of the strucure measured by the CSLDV system with a straight scan line along its length can be expressed by

$$\tilde{y}(t) = \sum_{h=1}^{n} \tilde{\phi}_h(\tilde{x}(t))\,\tilde{\eta}_h(t) \tag{5.15}$$

where n is the number of measured modes, and $\tilde{\phi}_h$ and $\tilde{\eta}_h$ are the FRS and time function associated with the h-th mode measured by the system, respectively. The FRS $\tilde{\phi}_h$ in Eq. (5.15) can be defined in a way similar to ϕ_h in Eq. (5.13):

$$\tilde{\phi}_h(t) = A_h Y_h(\tilde{x}(t))\,\mathrm{e}^{-2\pi f_h \zeta_h t} \tag{5.16}$$

A major difference between ϕ_h in Eq. (5.13) and $\tilde{\phi}_h$ is that x in the former becomes $\tilde{x}$ in the latter, which is a function of t and is unique in a scan of the system. Similar to ϕ_h, $\tilde{\phi}_h$ contains both A_h and $\mathrm{e}^{-2\pi f_h \zeta_h t}$, and it is time-varying. The time function $\tilde{\eta}_h$ can be expressed by

$$\tilde{\eta}_h(t) = \cos(2\pi f_h t - \alpha_h - \theta_h) \tag{5.17}$$

where α_h is the difference between a phase determined by the initial conditions and impulse associated with the h-th mode and that by a mirror feedback signal, and θ_h is a phase variable that controls amplitudes of in-phase and quadrature components of $\tilde{\phi}_h$, which can be expressed by

$$\tilde{\phi}_{I,h} = \tilde{\phi}_h \cos(\alpha_h + \theta_h) \tag{5.18}$$

and

$$\tilde{\phi}_{Q,h} = \tilde{\phi}_h \sin(\alpha_h + \theta_h) \tag{5.19}$$

respectively [137].

5.2.3 Demodulation Method for FRSs

The demodulation method has been proposed to obtain ODSs of a structure under sinusoidal excitation [131], where its steady-state response measured by a CSLDV system are analyzed. FRSs of a linear damped beam structure measured by a CSLDV system, as described by $\tilde{\phi}_h$ in Eq. (5.16), can also be obtained from the demodulation method by analyzing its free response of half-scan periods measured by the system, and each obtained $\tilde{\phi}_h$ corresponds to a mode in a half-scan period. A half-scan period starts when the laser spot of the system arrives at one end of a scan line, and it ends when the laser spot arrives at the other end. Hence, multiple $\tilde{\phi}_h$ can be obtained from free response of the structure measured by the system in one scan. To identify the start and end of a half-scan period, one can refer to mirror feedback signals of a CSLDV system and determine instants when its laser spot arrives at ends of a scan line.

Application of the demodulation method for obtaining $\tilde{\phi}_h$ associated with the h-th mode in a half-scan period measured by a CSLDV system is described below.

Based on Eqs. (5.15) through (5.19), a half-scan period of free response of the structure that is measured by a CSLDV system can be expressed by

$$\begin{aligned}\tilde{y}(t) &= \sum_{h=1}^{n}\tilde{\phi}_h(\tilde{x}(t))\cos(2\pi f_h t-\alpha_h-\theta_h)\\ &= \sum_{h=1}^{n}\left[\tilde{\phi}_{I,h}(\tilde{x}(t))\cos(2\pi f_h t)+\tilde{\phi}_{Q,h}(\tilde{x}(t))(x,t)\sin(2\pi f_h t)\right]\end{aligned} \tag{5.20}$$

The response $\tilde{y}(t)$ is then multiplied by $\cos(2\pi f_k t)$ and $\sin(2\pi f_k t)$, which gives

$$\begin{aligned}\tilde{y}(t)\cos(2\pi f_k t) &= \tilde{\phi}_{I,k}(\tilde{x}(t))\cos(2\pi f_k t)\cos(2\pi f_k t)+\tilde{\phi}_{Q,k}(\tilde{x}(t))\sin(2\pi f_k t)\cos(2\pi f_k t)+\\ &\quad \sum_{h=1,h\neq k}^{n}\tilde{\phi}_h(\tilde{x}(t))\tilde{\eta}_h(t)\cos(2\pi f_k t)\\ &= \tfrac{1}{2}\tilde{\phi}_{I,k}(\tilde{x}(t))+\tfrac{1}{2}\tilde{\phi}_{I,k}(\tilde{x}(t))\cos(4\pi f_k t)+\tfrac{1}{2}\tilde{\phi}_{Q,k}(\tilde{x}(t))\sin(4\pi f_k t)+\\ &\quad \sum_{h=1,h\neq k}^{n}\tilde{\phi}_h(\tilde{x}(t))\tilde{\eta}_h(t)\cos(2\pi f_k t)\end{aligned} \tag{5.21}$$

and

$$\begin{aligned}\tilde{y}(t)\sin(2\pi f_k t) &= \tilde{\phi}_{Q,k}(\tilde{x}(t))\cos(2\pi f_k t)\sin(2\pi f_k t)+\tilde{\phi}_{Q,k}(\tilde{x}(t))\sin(2\pi f_k t)\sin(2\pi f_k t)+\\ &\quad \sum_{h=1,h\neq k}^{n}\tilde{\phi}_h(\tilde{x}(t))\tilde{\eta}_h(t)\sin(2\pi f_k t)\\ &= \tfrac{1}{2}\tilde{\phi}_{Q,k}(\tilde{x}(t))-\tfrac{1}{2}\tilde{\phi}_{Q,k}(\tilde{x}(t))\cos(4\pi f_k t)+\tfrac{1}{2}\tilde{\phi}_{I,k}(\tilde{x}(t))\sin(4\pi f_k t)+\\ &\quad \sum_{h=1,h\neq k}^{n}\tilde{\phi}_h(\tilde{x}(t))\tilde{\eta}_h(t)\sin(2\pi f_k t)\end{aligned} \tag{5.22}$$

respectively. A low-pass filter is then applied to $\tilde{y}(t)\cos(2\pi f_k t)$ and $\tilde{y}(t)\sin(2\pi f_k t)$ in Eqs. (5.21) and (5.22) to obtain $\frac{1}{2}\tilde{\phi}_{I,k}$ and $\frac{1}{2}\tilde{\phi}_{Q,k}$, respectively, and the second and third terms on the third lines and terms on the fourth lines of Eqs. (5.21) and (5.22) are removed. Further, $\tilde{\phi}_{I,k}$ and $\tilde{\phi}_{Q,k}$ can be obtained by multiplying the corresponding filtered signals by two. The value of θ_h in Eq. (5.20) can be optimized so that $\tilde{\phi}_{I,h}$ and $\tilde{\phi}_{Q,h}$ attain their maximum and minimum amplitudes, respectively. In what follows, all FRSs are represented by their in-phase components with maximum amplitudes.

5.2.4 FRDI

It is shown in Sec. 2.2 that a FRS corresponds to a mode of a beam structure, and its amplitude is time-varying and exponentially decays to zero with time. In order to obtain non-zero FRSs from the demodulation method, one needs to determine natural frequencies of the structure and instants when amplitudes of the FRSs decay to zero. While the natural frequencies can be determined by use of the fast Fourier transform of $\tilde{y}(t)$, the instants can be determined by use of the STFT of $\tilde{y}(t)$ [139], denoted by $\tilde{V}_w(t,f)$, which can be expressed by

$$\tilde{V}_w(t,f) = \int_{-\infty}^{\infty} \tilde{y}(\tau)\, g_s^*(\tau - t)\, \mathrm{e}^{-2\pi \mathrm{j} f \tau} \mathrm{d}\tau \tag{5.23}$$

where g_s is a window function with a scale s, the superscript $*$ denotes complex conjugation, and $\mathrm{j} = \sqrt{-1}$. The scale s determines the width of g_s in the time domain, which should be smaller than that of a half-scan period. When $\tilde{V}_w$ at the natural frequency associated with the h-th mode becomes almost zero at an instant $t_{h,0}$, the amplitude of $\tilde{\phi}_h$ is considered to be zero. Multiple non-zero $\tilde{\phi}_h$ can be obtained using $\tilde{V}_w$ of the first N_h half-scan periods, where N_h is an integer that can be defined as

$$\arg\max_{N_h} \frac{N_h T_h}{2} \leqslant t_{h,0} - t_1 \tag{5.24}$$

in which T is the length of a scan period and t_1 is the instant when the first half-scan period starts. In this section, $\tilde{V}_w(t, f)$ is visualized by use of a spectrogram whose intensity denotes the power spectral density associated with $\tilde{V}_w(t, f)$ in Eq. (5.23), where g_s is a Hamming function that can be expressed by

$$g_s(t) = \begin{cases} 0.54 - 0.46\cos\left(\frac{2\pi t}{s}\right) & , \quad 0 \leqslant t \leqslant s \\ 0 & , \quad \text{otherwise} \end{cases} \tag{5.25}$$

A CMS Y_h'' is the second-order spatial derivative of Y_h, where a prime denotes first-order spatial differentiation with respect to x. A curvature FRS $\tilde{\phi}_h''$ can be defined as

$$\tilde{\phi}_h''(\tilde{x}(t)) = \frac{\partial^2 \tilde{\phi}_h}{\partial \tilde{x}^2} = A_h Y_h''(\tilde{x}(t))\, \mathrm{e}^{-2\pi f_h \zeta_h t} \tag{5.26}$$

Since Y_h'' is related to bending stiffness of a beam structure that can decrease due to occurrence of damage and regions of the decrease correspond to damage regions, it can be used for damage identification [86], and so can $\tilde{\phi}_h''$, since it explicitly contains Y_h'' as shown in Eq. (5.26).

Since a MS of an undamaged beam structure can be well approximated by that from a polynomial that fits a MS of a damaged beam structure [9], it can be inferred that a FRS of an undamaged structure can also be well approximated by that from a polynomial that fits a FRS of a damaged structure. A damage index similar to that in Ref. [9] can be defined by comparing $\tilde{\phi}_h''$ of a damaged beam structure and that from a polynomial that fits $\tilde{\phi}_h$ with a properly determined order, which can be expressed by

$$\delta_h\left(\tilde{x}\right) = \sum_{i=1}^{N_d} \left[\tilde{\phi}_{h,i}''\left(\tilde{x}\right) - \tilde{\phi}_{h,i}^{p\prime\prime}\left(\tilde{x}\right)\right]^2 \tag{5.27}$$

where N_d is the number of FRSs to be included in the index with $N_d \leq N_h$, $\tilde{\phi}_{h,i}$ is a FRS associated with the h-th mode in the i-th half-scan period, and $\tilde{\phi}_{h,i}^p$ is a FRS from a polynomial that fits $\tilde{\phi}_{h,i}$ with a properly determined order. The index $\delta_h\left(\tilde{x}\right)$ in Eq. (5.27) is termed as a free-response damage index (FRDI) at $\tilde{x}$. Since there can be FRSs associated with multiple modes corresponding to $\tilde{y}$ measured by a CSLDV system in one scan, FRDIs associated with multiple modes can be obtained using measurement by a CSLDV system in one scan, and damage regions can be identified near neighborhoods with consistently high values of FRDIs associated with different modes. Note that use of δ_h associated with rigid-body modes should be excluded in damage identification as curvatures of their FRSs are zero, and one should use δ_h associated with elastic modes in damage identification. An auxiliary FRDI associated with the FRDI in Eq. (5.27) can be defined to assist identification of the neighborhoods, which can be expressed by

$$\delta_{\mathrm{a}}\left(\tilde{x}\right) = \sum_{h=1}^{H} \hat{\delta}_h\left(\tilde{x}\right) \tag{5.28}$$

where H is the number of FRDIs to be included in the auxiliary index and $\hat{\delta}_h\left(\tilde{x}\right)$ is a normalized FRDI associated with the h-th mode with the maximum amplitude of one. Since border distortions occur in curvature ODSs associated with ODSs obtained from the demodulation method [137], similar distortions would also occur in curvature FRSs associated with FRSs obtained from the demodulation method. Hence, regions containing such distortions are excluded in presenting $\delta_h(\tilde{x})$ and $\delta_\mathrm{a}(\tilde{x})$ and in normalization of $\delta_h(\tilde{x})$ in $\delta_\mathrm{a}(\tilde{x})$. Neighborhoods with consistently high values of the FRDIs associated with the H modes can be identified in those with high values of the auxiliary FRDI.

A polynomial that fits $\tilde{\phi}_{h,i}$ with an order r can be expressed by

$$\tilde{\phi}^{p}_{h,i}(\tilde{x}) = \sum_{q=0}^{r} a_q \tilde{x}^q \tag{5.29}$$

where a_q are coefficients of the polynomial that can be obtained by solving a linear equation

$$\mathbf{U}\mathbf{a} = \tilde{\Phi} \tag{5.30}$$

in which $\mathbf{U}$ is an $M \times (r+1)$ Vandermonde matrix with M being the number of measurement points of $\tilde{\phi}_{h,i}$:

$$\mathbf{U} = \begin{bmatrix} 1 & \tilde{x}_1 & \tilde{x}_1^2 & \cdots & \tilde{x}_1^r \\ 1 & \tilde{x}_2 & \tilde{x}_2^2 & \cdots & \tilde{x}_2^r \\ \vdots & \vdots & \vdots & \ddots & \vdots \\ 1 & \tilde{x}_M & \tilde{x}_M^2 & \cdots & \tilde{x}_M^r \end{bmatrix} \tag{5.31}$$

$\mathbf{a} = \begin{bmatrix} a_0 & a_1 & \dots & a_r \end{bmatrix}^\mathrm{T}$ is an $(r+1)$-dimensional coefficient vector, and $\tilde{\boldsymbol{\Phi}}$ is the

FRS vector of the structure to be fit. To avoid ill-conditioning of $\mathbf{U}$, it is proposed that $\tilde{x}$ in Eq. (5.29) be normalized using the "center and scale" technique [113] before formulation of the linear equation in Eq. (5.29). Normalized coordinates $\hat{x}$ can be expressed by

$$\hat{x} = \frac{2\tilde{x} - 2\bar{x}}{l} \tag{5.32}$$

where $\bar{x}$ is the x-coordinate of the center point of a scan line and l is its length.

As pointed out in Ref. [9], an increase of r in the polynomial in Eq. (5.29) can improve the level of approximation of $\tilde{\phi}^p_{h,i}$ to $\tilde{\phi}_{h,i}$. To determine the proper order of the polynomial fit, a convergence index can be defined:

$$con\left(r\right) = \frac{\mathrm{RMS}\left(\tilde{\mathbf{\Phi}}\right)}{\mathrm{RMS}\left(\tilde{\mathbf{\Phi}}\right) + \mathrm{RMS}\left(\mathbf{e}\right)} \times 100\% \tag{5.33}$$

where $\mathrm{RMS}\left(\cdot\right)$ denotes the root-mean-square value of a vector and $\mathbf{e} = \mathbf{Ua} - \tilde{\mathbf{\Phi}}$ is an error vector. When the convergence index is close to 100%, $\phi^p_{h,i}$ converges to $\phi_{h,i}$; the lower the index, the lower the level of convergence of $\phi^p_{h,i}$ to $\phi_{h,i}$. It is proposed in this section that the proper value of r be two plus the least value of r with which $con\left(r\right)$ is above 95%. Two is added here in order to preserve smoothness of a curvature FRS from the polynomial fit, since calculation of a curvature incurs second-order differentiation that reduces the order of a polynomial by two.

5.3 Numerical Investigation

5.3.1 FRSs from Analytical and FE Models

Based on Eq. (5.1), the analytical model of an undamaged aluminum cantilever beam structure with $L = 0.8$ m, $E = 68.9$ GPa, $m = 0.2700$ kg/m and $c = 8\times10^{-7}$ s is formulated; the structure has a uniform square cross-section with a side length of 0.01 m. The structure has fixed and free ends at $x = 0$ and $x = L$, respectively, and it has zero initial conditions. A single impulse with an intensity of 0.01 $\mathrm{N}\cdot\mathrm{s}$ is applied to the free end of the structure. A corresponding FE model of the structure under the same initial conditions and excitation is constructed using ABAQUS with 16384 two-node linear beam (B21) elements for comparison purposes, where the damping in the analytical model can be equivalently modeled using the Rayleigh damping [54]. The formulation of the FE model can be expressed by

$$\mathbf{M}\ddot{\mathbf{z}}(t) + \mathbf{C}\dot{\mathbf{z}}(t) + \mathbf{K}\mathbf{z}(t) = \mathbf{f}(t) \tag{5.34}$$

with initial conditions $\mathbf{z}(0) = \mathbf{0}$ and $\dot{\mathbf{z}}(0) = \mathbf{0}$, where $\mathbf{M}$, $\mathbf{C}$ and $\mathbf{K}$ are mass, damping and stiffness matrices, respectively, in which $\mathbf{C} = \alpha\mathbf{M} + \beta\mathbf{K}$ with Rayleigh damping coefficients $\alpha = 0$ and $\beta = c$, i.e., $\mathbf{C} = c\mathbf{K}$, and $\mathbf{z}$ and $\mathbf{f}$ are displacement and force vectors, respectively. Table 5.1 compares damped natural frequencies of the first five modes of the structure from its analytical and FE models, and the largest difference between the damped natural frequencies from the two models is 0.61 %. Note that differences between the natural frequencies of the two models arise due to use of the B21 elements and they can be greatly reduced if two-node cubic beam (B22) elements were used. Mass-normalized MSs of the first five modes from the analytical and FE models compare well, as shown in Fig. 5.1.

Table 5.1: Comparison between damped natural frequencies of the cantilever beam structure from its analytical and FE models.

Mode	Analytical Frequency (Hz)	FE Frequency (Hz)	Difference (%)
1	12.75	12.75	0.01
2	79.91	79.84	0.09
3	223.74	223.28	0.21
4	438.44	436.77	0.38
5	724.77	720.38	0.61

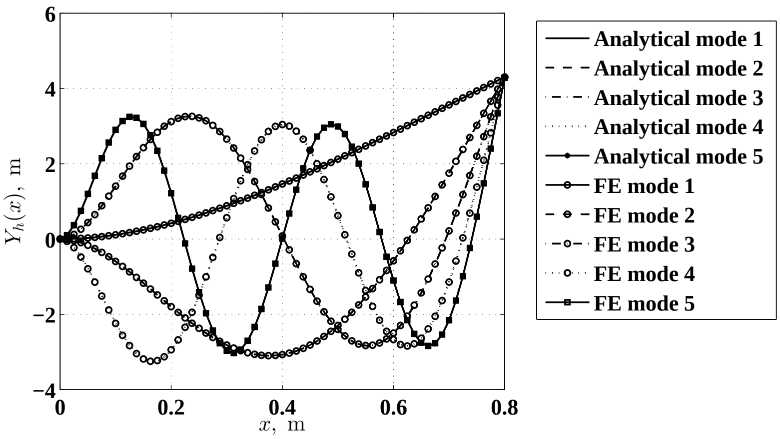

Figure 5.1: Mass-normalized MSs of the cantilever beam structure associated with its first five modes from its analytical and FE models.

Response of the beam structure is then measured by a simulated CSLDV system with a scan period of $T = 2$ s and a sampling frequency of 16384 Hz; the simulated CSLDV system is capable of measuring response in the form of displacement. The position of its laser spot is shown in Fig. 5.2(a); the first half-scan period starts at $t = 0.0625$ s, and measured response of the structure from the analytical and FE models in the first half-scan period, second half-scan period and first eight seconds are shown in Figs. 5.2(b) through (d), respectively. Spectrograms of the response from the analytical and FE models in the first eight seconds are shown in Figs. 5.3(a) and (b), respectively, and they compare well with each other. It can be seen from Figs. 5.3(a) and (b) that STFTs at the first and second natural frequencies of the structure do not decay much in the first eight seconds, while those at the third through fifth natural frequencies decay more. More importantly, the STFTs associated with the fifth natural frequency of the structure drastically decay within the first second of the CSLDV measurement. As a result, FRSs associated with the fifth elastic mode cannot be obtained in this scan. Hence, only FRSs associated with the first four elastic modes can be obtained from the response.

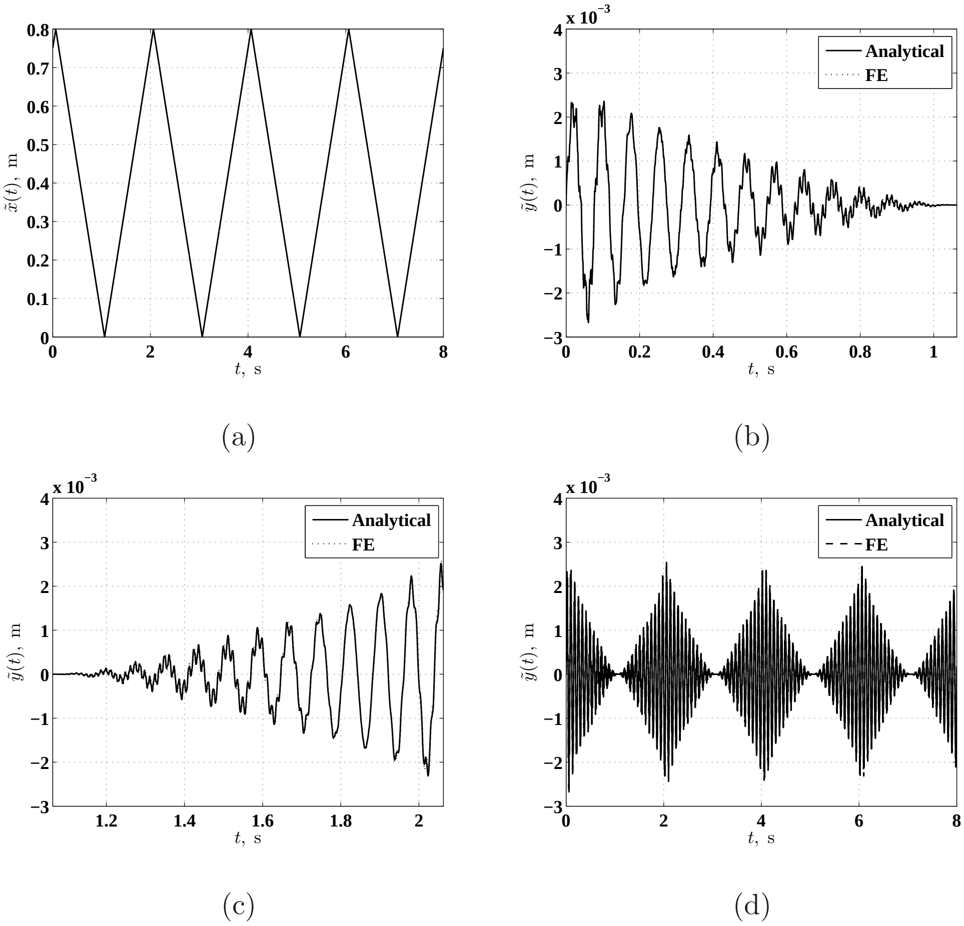

Figure 5.2: (a) Position of the laser spot of a simulated CSLDV system on the beam structure, (b) response from its analytical and FE models measured by the simulated CSLDV system in the first half-scan period, (c) response from its analytical and FE models measured by the simulated CSLDV system in the second half-scan period and (d) response from its analytical and FE models measured by the simulated CSLDV system in the first eight second.

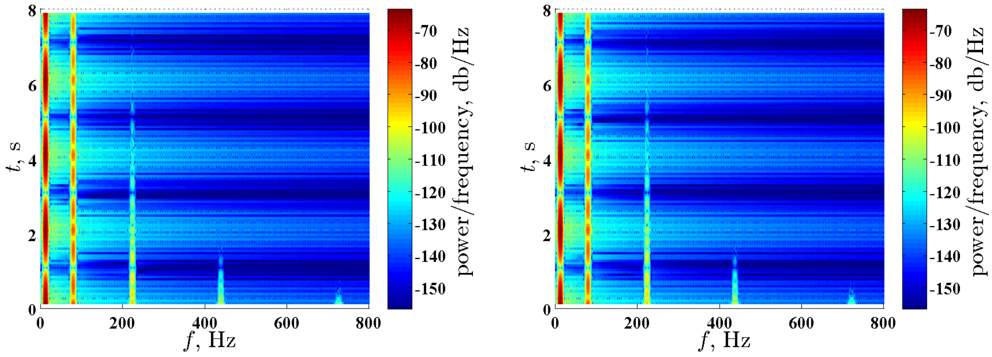

(a)

(b)

Figure 5.3: Spectrograms of the response of the beam structure from its (a) analytical and (b) FE models measured by the simulated CSLDV system shown in Fig. 5.2(d).

Based on Eq. (5.16), FRSs from the analytical model associated with the first four modes of the beam structure in the first three half-scan periods of the simulated CSLDV system are shown in Figs. 5.4(a) through (d), respectively. FRSs from the FE model obtained by use of the simulated CSLDV system, which are obtained from the demodulation method, are shown in Fig. 5.5. It can be seen from Figs. 5.4 and 5.5 that the FRSs from the analytical and FE models are in good agreement. Amplitudes of the FRSs associated with the fourth mode of the structure in the second and third half-scan periods drastically decrease to almost zero due to the damping; the FRS in the first half-scan period is included in $\delta_h(\tilde{x})$ associated with the fourth mode for damage identification that follows.

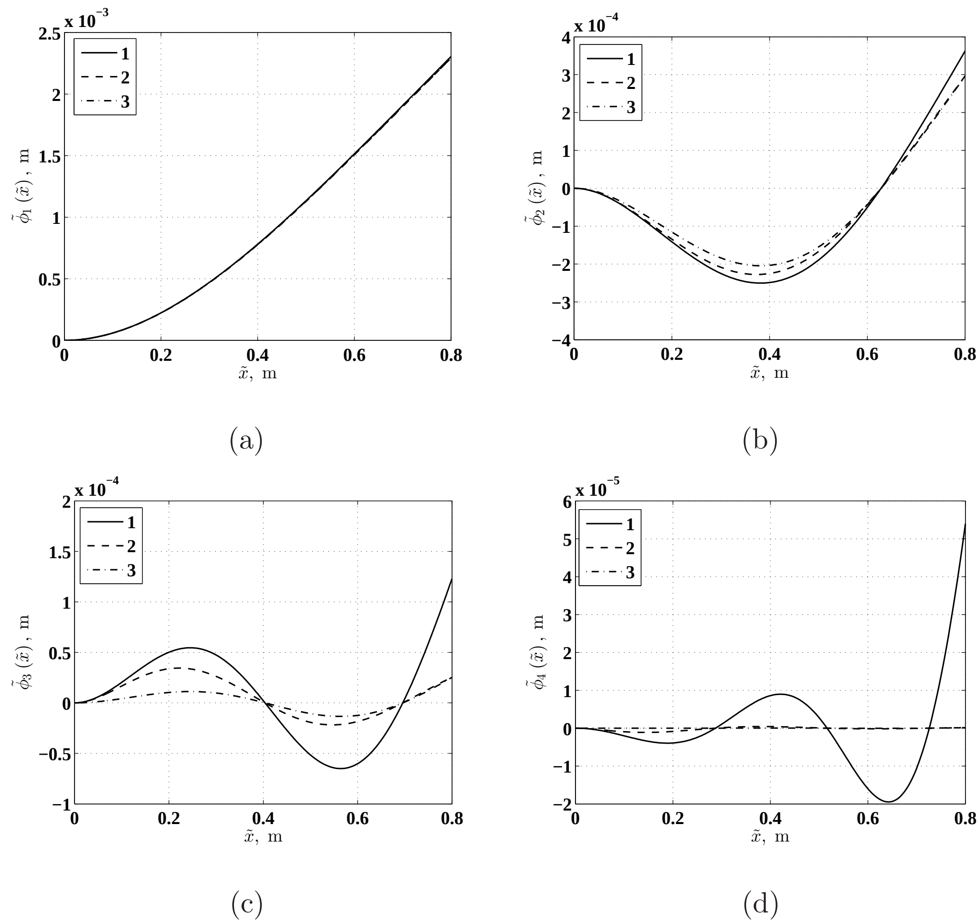

Figure 5.4: FRSs of the beam structure from its analytical model associated with its (a) first, (b) second, (c) third and (d) fourth modes in the first three half-scan periods of the simulated CSLDV system.

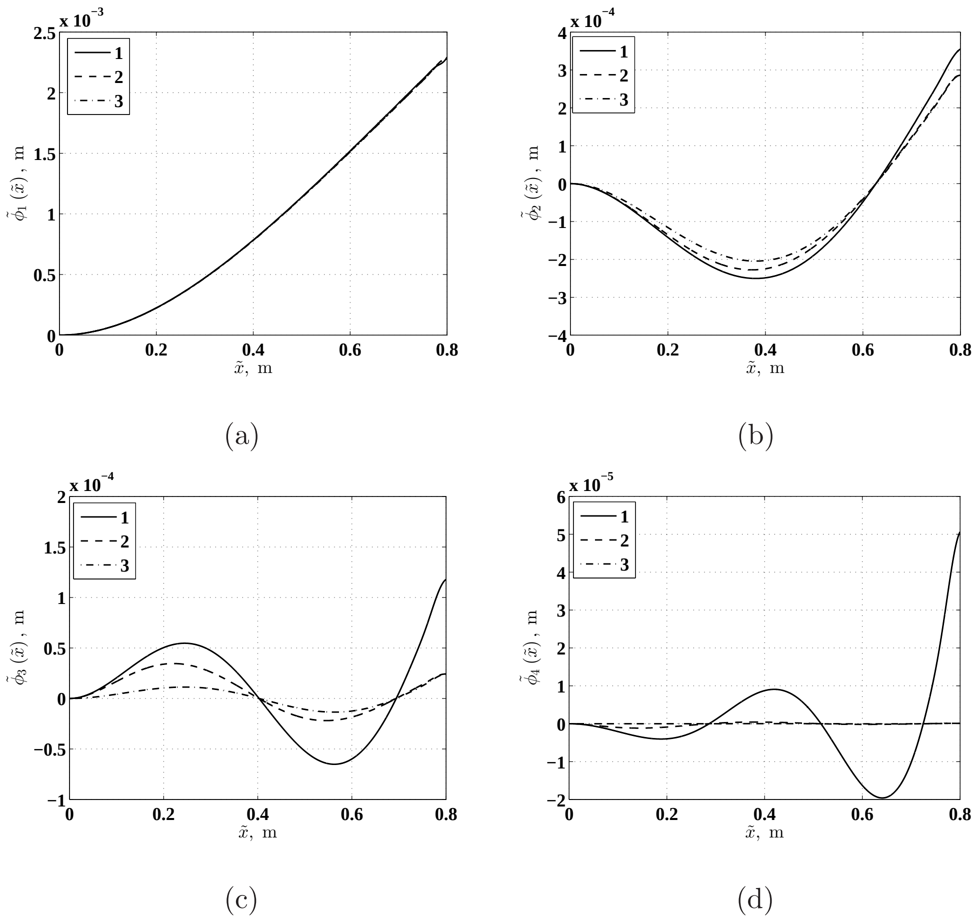

Figure 5.5: FRSs of the beam structure from its FE model associated with its (a) first, (b) second, (c) third and (d) fourth modes obtained by use of the simulated CSLDV system in the first three half-scan periods.

5.3.2 Damage Identification Using FRDIs

Since fidelity of the FE model of the undamaged cantilever beam structure has been validated in Sec. 3.1, the FE model can be adapted to model such a beam structure with damage in the form of thickness reduction to numerically investigate the proposed damage identification methodology. The thickness of the section of the structure between $x = \frac{6}{16}L$ and $x = \frac{7}{16}L$ is reduced by 10 %, while its E and volume mass density remain unchanged. Table 5.2 compares natural frequencies of the first five modes of the damaged and undamaged structures from the FE models, and the largest difference is 1.27 %. Response of the damaged structure from its FE model is measured by the simulated CSLDV system with the same settings as those in Sec. 3.1, and it is used to obtain FRSs of the damaged structure associated with the first four modes in the first three half-scan periods, as shown in Fig. 5.6.

Table 5.2: Comparison between damped natural frequencies of the damaged and undamaged cantilever beam structures from their FE models.

Mode	Damaged Frequency (Hz)	Undamaged Frequency (Hz)	Difference (%)
1	12.64	12.75	-0.88
2	79.04	79.84	-1.00
3	222.03	223.28	-0.56
4	434.80	436.77	-0.45
5	711.23	720.38	-1.27

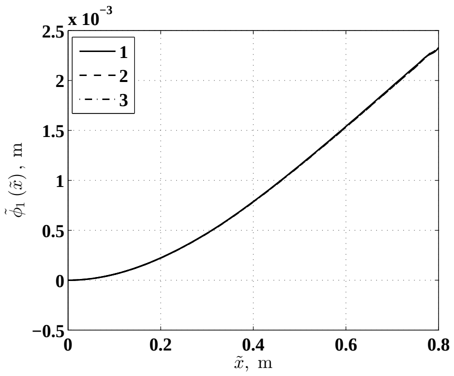

(a)

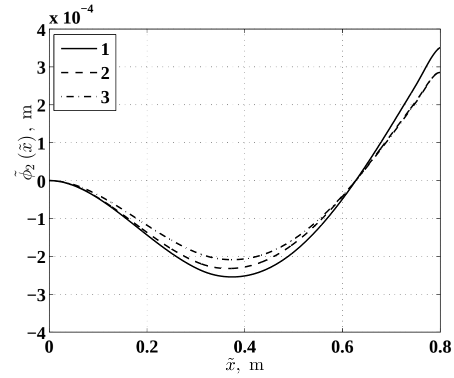

(b)

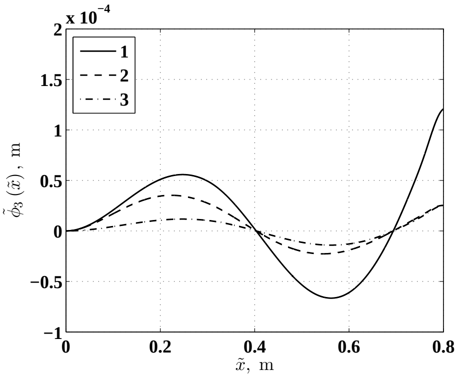

(c)

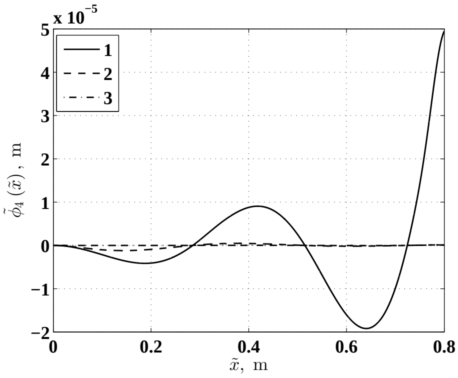

(d)

Figure 5.6: FRSs from the FE model of the damaged beam structure obtained by use of the simulated CSLDV system associated with the (a) first, (b) second, (c) third and (d) fourth modes in the first three half-scan periods.

Convergence indices *con* corresponding to the FRSs associated with the first through fourth modes of the damaged beam structure are shown in Figs. 5.7 through 5.10, respectively. Proper orders of polynomials that fit the FRSs associated with the first mode in the first through third half-scan periods are determined to be 4, 4 and 4, respectively; those associated with the second mode are determined to be 6, 6 and 6, respectively; those associated with the third mode are determined to be 7, 7 and 7, respectively; and that associated with the fourth mode is determined to be 9.

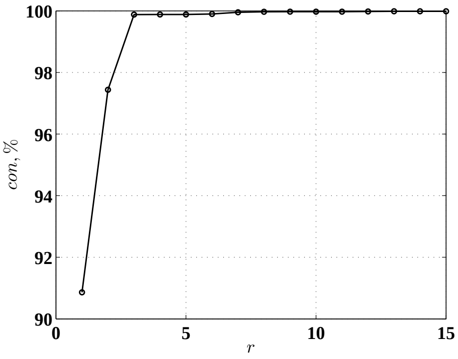

(a)

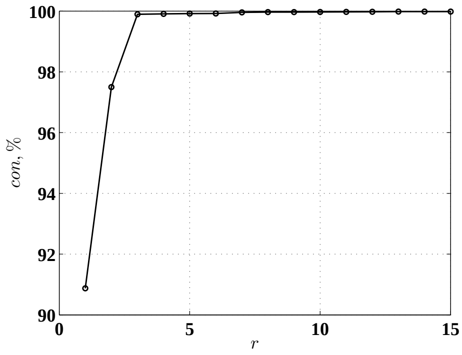

(b)

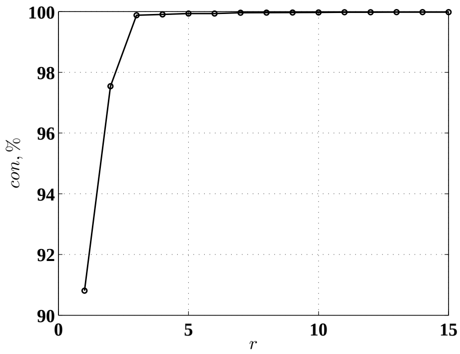

(c)

Figure 5.7: Convergence indices *con* corresponding to the FRSs associated with the first mode in the (a) first, (b) second and (c) third half-scan periods.

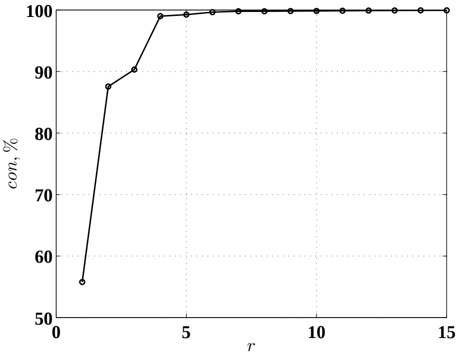

(a)

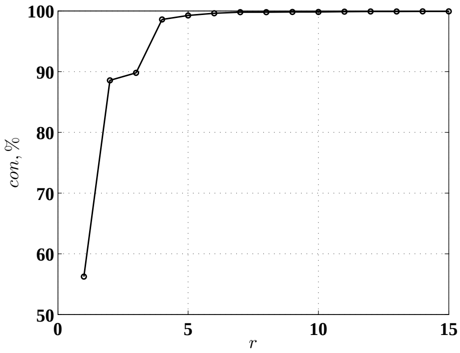

(b)

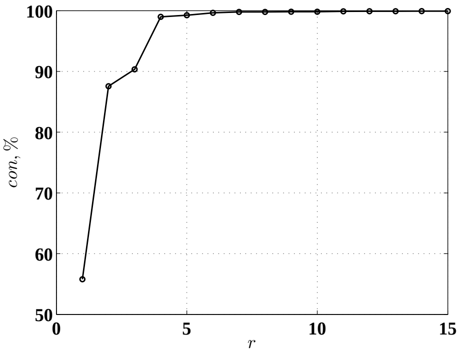

(c)

Figure 5.8: Convergence indices *con* corresponding to the FRSs associated with the second mode in the (a) first, (b) second and (c) third half-scan periods.

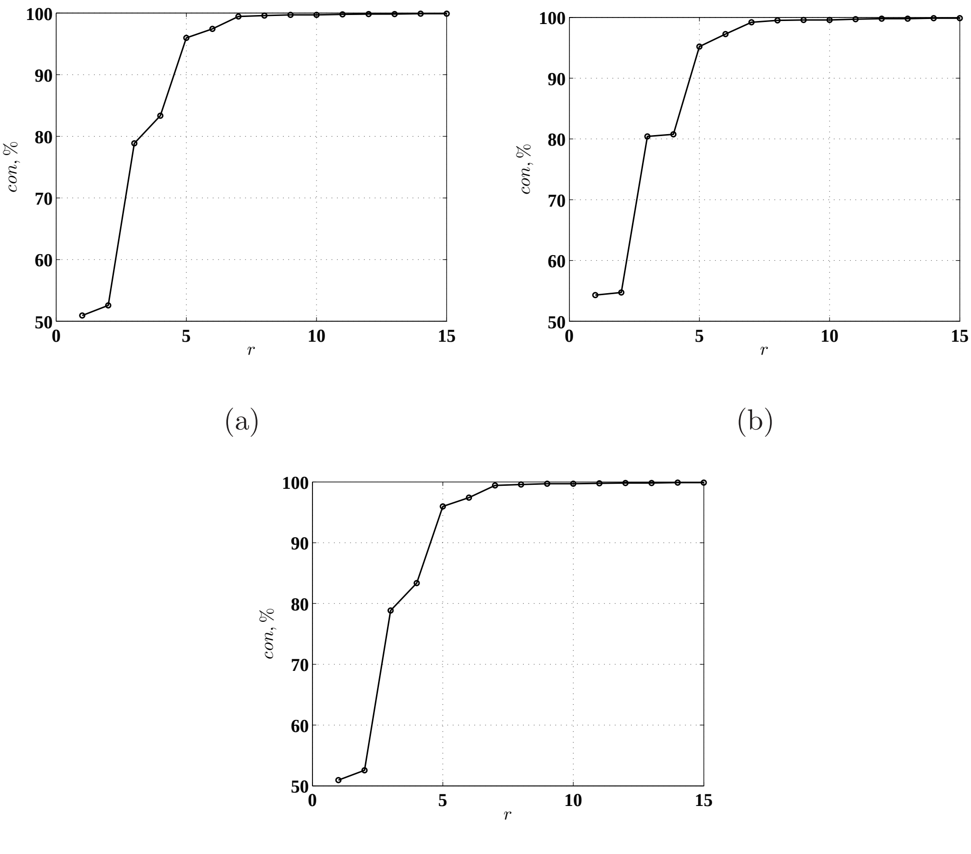

(a) (b)

(c)

Figure 5.9: Convergence indices *con* corresponding to the FRSs associated with the third mode in the (a) first, (b) second and (c) third half-scan periods.

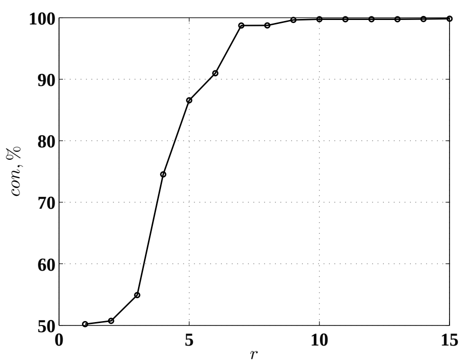

Figure 5.10: Convergence index *con* corresponding to the FRS associated with the fourth mode in the first half-scan period.

FRDIs in Eq. (5.27) associated with the first through fourth modes are shown in Figs. 5.11(a) through (d), respectively, and the auxiliary FRDI in Eq. (5.28) is shown in Fig. 5.11(e). Note that numbers of FRSs included in the FRDIs associated with the first through fourth modes are 3, 3, 3 and 1, respectively. The damage can be clearly identified near neighborhoods with consistently high values of the FRDIs and that with high values of the auxiliary FRDI.

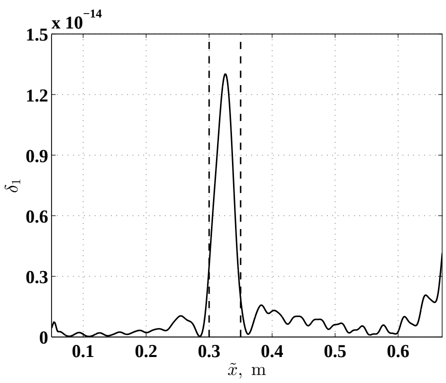

(a)

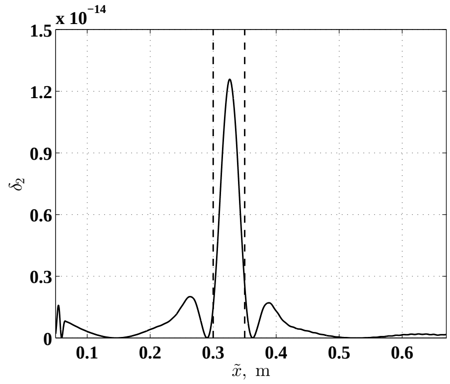

(b)

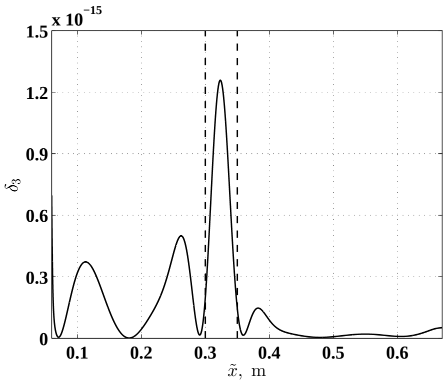

(c)

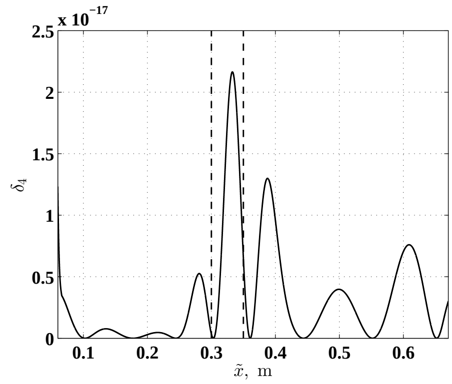

(d)

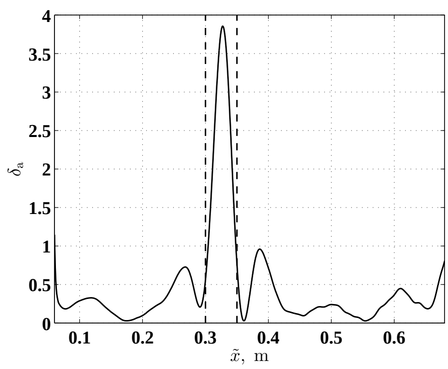

(e)

Figure 5.11: FRDIs associated with the (a) first, (b) second, (c) third and (d) fourth modes of the damaged beam structure, and (e) the auxiliary FRDI associated with the four modes. Locations of damage ends are indicated by two vertical dashed lines.

5.4 Experimental Investigation

5.4.1 CSLDV System

A CSLDV system shown in Fig. 5.12 is developed in this section. It consists of a Cambridge 6240H scanner, a Polytec OFV-353 single-point laser vibrometer and a dSPACE MicroLabBox controller board that controls a pair of orthogonal scan mirrors of the scanner termed as X and Y mirrors; the control software ControlDesk Next Generation is used to design and implement a control scheme for the system. The mirrors are connected to two independent stepper motors in the scanner. Input signals to each stepper motor directly control rotation angles of the mirrors, and different scan patterns of the laser spot can be created. In the control scheme, triangular and constant input signals are given to the X and Y mirrors here, respectively, and the laser spot is continuously swept along the length of a beam structure. It can be assumed that the resultant velocity of the laser spot on the structure is constant along a scan line, when the system is sufficiently far away from the structure and the rotation angle amplitude is sufficiently small. A triggering sub-scheme is embedded in the control scheme using a toolbox of the control software called Signal Editor. Starts of continuous scanning and measurement of the CSLDV system are triggered, when it registers a voltage with an absolute value higher than a prescribed threshold via the laser vibrometer.

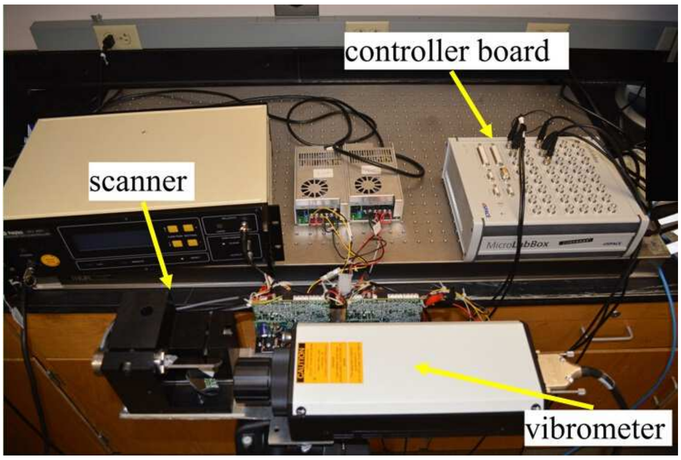

Figure 5.12: A CSLDV system developed in this work.

An experiment was set up to obtain FRSs of a damaged aluminum cantilever beam structure using the CSLDV system for damage identification. A schematic diagram that shows the experimental setup and dimensions of the structure is shown in Fig. 5.13(a). The undamaged portion of the structure had a thickness of 6.35 mm, and there was a region of machined thickness reduction of 1.27 mm on one side of the structure along its length, as shown in Figs. 5.13(a) and (b). The damage was selected in this form in order to show that its region can be accurately identified by the proposed methodology. The thickness reduction is about 20% of the thickness of the undamaged portion; its location and length are shown in Fig. 5.13(a). A bench vice was used to clamp the left end of the structure to simulate a fixed boundary. A straight scan line was assigned on the intact side of the structure along its length as shown in Fig. 5.13(a) and (c). A strip of retroreflective tape was attached on the intact side to enhance laser reflection that directly determined signal-to-noise ratios of measurement by the CSLDV system. The scan line was non-dimensionalized to range from 0% to 100%, where 0% and 100% represented left and right ends of the scan line, respectively. The damage was located between 45.71% and 51.43% on the scan line. The experimental setup is shown in Figs. 5.13(a), (c) and (d), where the CSLDV system was used to measure free response of the structure along the scan line. In this section, the sampling frequency of the system was $250,000$ Hz, and the threshold for triggering was 0.1 V. The laser spot of the system stayed at 80% on the scan line before its starts of continuous scanning and measurement were triggered, and continuous scanning started by sweeping the laser spot towards 100% on the scan line.

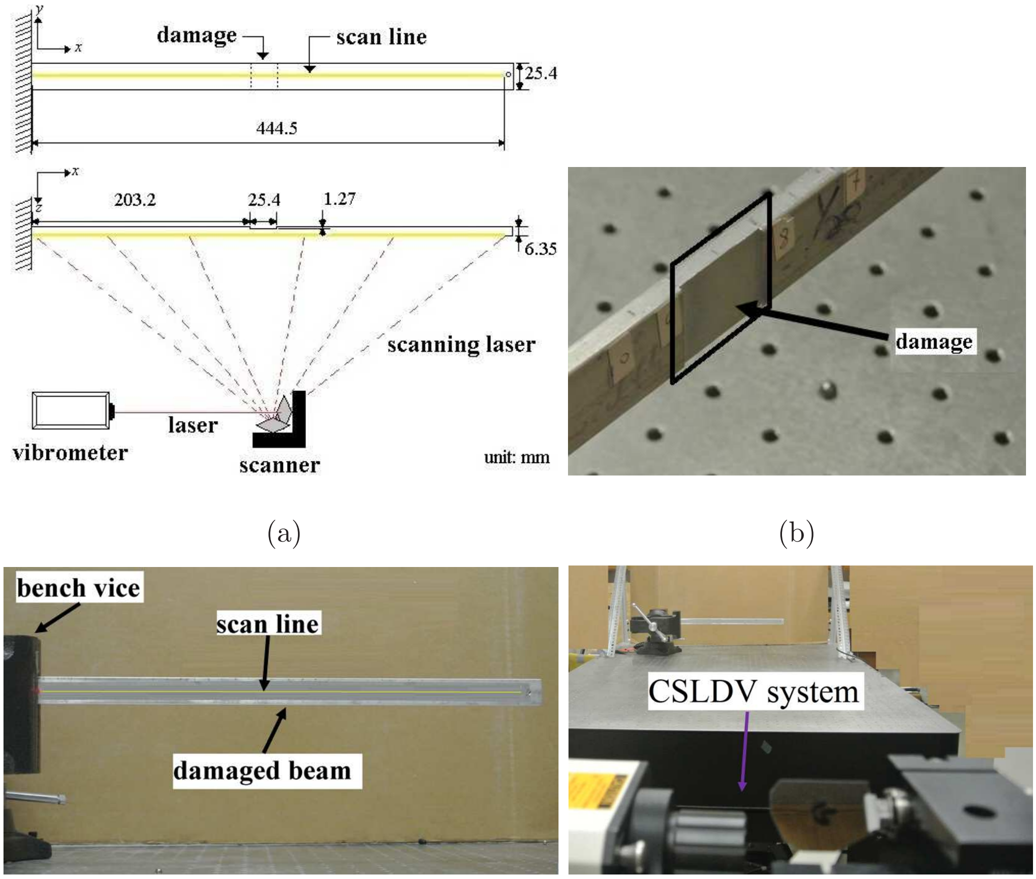

(a) (b)

(c) (d)

Figure 5.13: (a) Schematic diagram of the test setup and dimensions of a damaged aluminum cantilever beam structure with a region of machined thickness reduction, (b) the region of machined thickness reduction, (c) the structure with its left end clamped by a bench vice and (d) the experimental setup for FRS measurement of the structure.

An impact test was first conducted on the beam structure in Fig. 5.13 to measure its first five natural frequencies; a PCB 086E80 pen-sized impact hammer and the single-point laser Doppler vibrometer in Fig. 5.12 were used to excite the structure at an impact point and measure its response at a measurement point, respectively. Both the impact and measurement points on the structure were arbitrarily selected as long as they did not coincide with nodal points of its first five modes. The first five natural frequencies of the structure were measured to be 22.07 Hz, 135.74 Hz, 393.36 Hz, 746.48 Hz and 1261.07 Hz.

Velocity response of the beam structure in Fig. 5.13 under two forms of excitation were measured by the CSLDV system with different scan frequencies. One is initial non-zero bending deformation of the structure along its length under a transverse concentrated force at its free end, with zero initial velocity, for damage identification using FRDIs associated with low modes of the structure; the other is an impact on the structure with zero initial conditions for damage identification using FRDIs associated with its high modes. The impact point was on the damaged side of the structure, and the distance between the impact point and fixed end of the structure was 80 mm. FRSs of the structure associated with its first five modes were obtained from the demodulation method using velocity response measured by the CSLDV system with different scan frequencies of 0.1 Hz, 1.0 Hz and 10.0 Hz. Effects of the scan frequency of the CSLDV system on obtained FRSs and damage identification results were investigated. As measurement noise exists in obtained FRSs and its adverse effects can be amplified in calculating associated curvature FRSs, a numerical smoothing technique was applied to alleviate the adverse effects before calculating the curvature FRSs, which is local regression using weighted linear least squares and a second-order polynomial model [140]. In the smoothing technique, weighted quadratic least squares are calculated at each measurement point within an interval that consists of a certain number of its neighboring points, which was 15% of the total number of measurement points in this investigation. It is the width of the interval that determines how good the technique is in smoothing an obtained FRS. One should be cautious about choosing the width, as the technique can smooth out effects of damage in a curvature FRS and compromise effectiveness of the proposed damage identification methodology if a chosen width is too large, though the method can still alleviate adverse effects of measurement noise on the curvature FRS. Unfortunately, a general guideline for choosing an optimal width of the interval for damage identification does not exist, as existence of damage and quality of an obtained FRS are usually unknown in practice. Hence, one should test different widths of the interval from small to large ones and compare resulting FRDIs associated with different modes. If signal-to-noise ratios of FRS measurements are adequately high, it would be adverse effects of measurement noise on curvature FRSs that are first smoothed out by the technique, and effects of damage would be preserved in the curvature FRSs and observed in resulting FRDIs. In this case, damage can be clearly identified in neighborhoods with consistently high values of the FRDIs in Eq. (5.27) and in those with high values of the auxiliary FRDI in Eq. (5.28).

5.4.2 FRS Measurement and Damage Identification Results

Velocity response of the beam structure under the initial non-zero bending deformation was measured by the CSLDV system with a scan frequency of 0.1 Hz. The measured response and X-mirror feedback signal are shown in Figs. 5.14(a) and (b), respectively, and a spectrogram of the response is shown in Fig. 5.14(c). It can be seen from Fig. 5.14(c) that STFTs at the second through fifth modes of the structure drastically decayed in less than one second after the scan started. Since the length of a half-scan period in this scan is five seconds, FRSs associated with the second through fifth modes could not be obtained by the system with the scan frequency, while those associated with the first mode could be. FRSs associated with the first mode in the first three half-scan periods are shown in Fig. 5.15. Similar to those in the numerical investigation, amplitudes of the FRSs decreased from one half-scan period to the next.

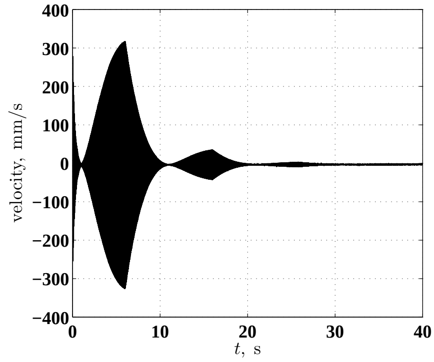

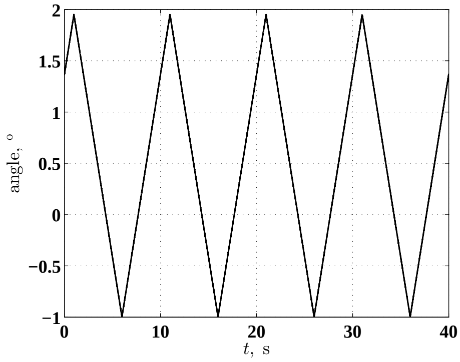

(a) (b)

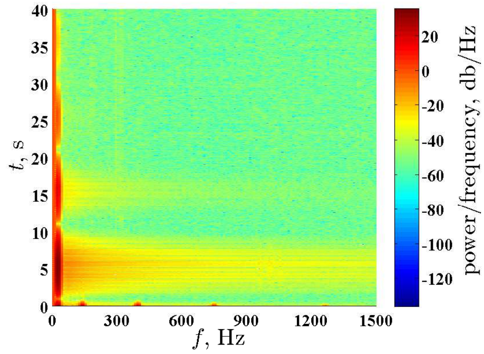

(c)

Figure 5.14: (a) Velocity response of the beam structure under the initial non-zero bending deformation measured by the CSLDV system with a scan frequency of 0.1 Hz, (b) the X-mirror feedback signal with a triangular input signal and (c) a spectrogram of the response in (a).

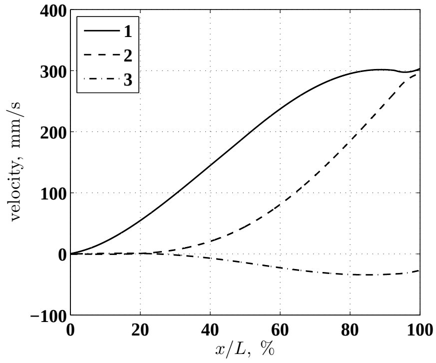

Figure 5.15: Obtained FRSs associated with the first mode in the first three half-scan periods of the CSLDV system with a scan frequency of 0.1 Hz.

Velocity response of the beam structure under the impact was measured by the CSLDV system with a scan frequency of 1.0 Hz. The measured response and X-mirror feedback signal are shown in Figs. 5.16(a) and (b), respectively, and a spectrogram of the response is shown in Fig. 5.16(c). It can be seen from Fig. 5.16(c) that STFTs at the second through fifth natural frequencies of the beam drastically decayed in the first three, two, one and half seconds of the scan, respectively. FRSs associated with the fifth natural frequency of the structure could not be obtained, since the length of a half-scan period in this case is 0.5 s and the first half scan ended at $t = 0.6$ s. FRSs associated with the first through fourth modes in the first three half-scan periods are shown in Fig. 5.15(a) through (d), respectively.

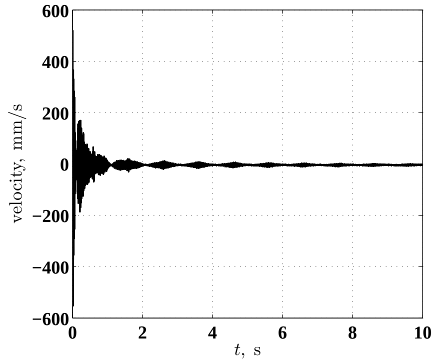

(a)

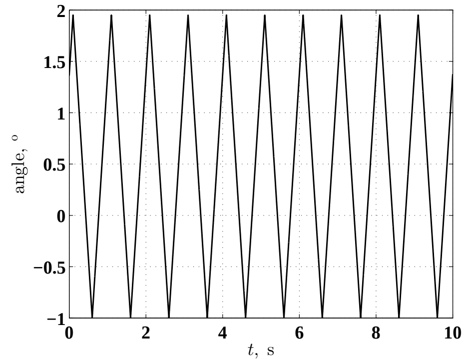

(b)

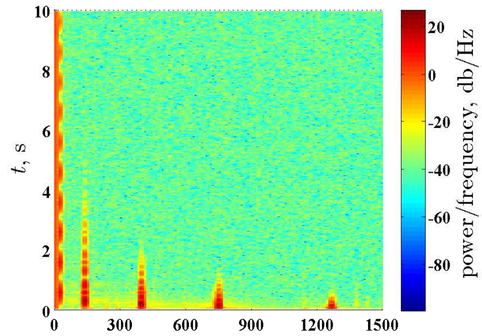

(c)

Figure 5.16: (a) Velocity response of the beam structure under the impact measured by the CSLDV system with a scan frequency of 1.0 Hz, (b) the X-mirror feedback signal with a triangular input signal and (c) a spectrogram of the response in (a).

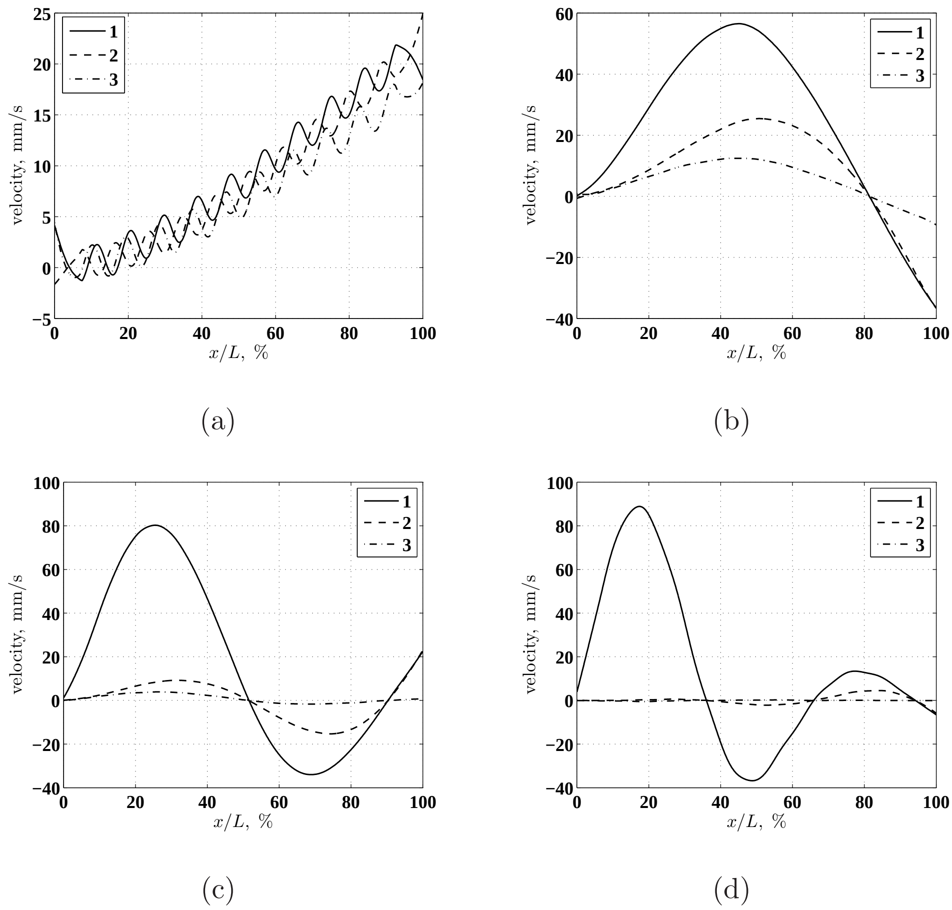

Figure 5.17: Obtained FRSs associated with the (a) first, (b) second, (c) third and (d) fourth modes in the first three half-scan periods of the CSLDV system with a scan frequency of 1.0 Hz.

Velocity response of the beam structure under the impact was then measured by the CSLDV system with a scan frequency of 10.0 Hz. The measured response and X-mirror feedback signal are shown in Figs. 5.18(a) and (b), respectively, and a spectrogram of the response are shown in Fig. 5.18(c). It can be seen from Fig. 5.18(c) that STFTs at the second through fifth natural frequencies of the structure drastically decayed in the first three, two, one and half seconds of the scan, respectively. FRSs associated with the first through fourth modes in the first three half-scan periods are shown in Figs. 5.19(a) through (e), respectively. A critical observation can be made by comparing Figs. 5.16(a) and 5.18(a) that the measured response by the CSLDV system with a scan frequency of 1.0 Hz had a higher signal-to-noise ratio than that by the system with a scan frequency of 10.0 Hz, as the former seemed to be dominated by measurement noise after $t = 9$ s and the latter after $t = 1.5$ s. Since the structure was under the same impact in the measurement, the theory that speckle noise in measurement by a CSLDV system, which directly results in a lower signal-to-noise ratio in its measurement and lower-quality MSs, increases with its scan frequency [141, 142] was validated.

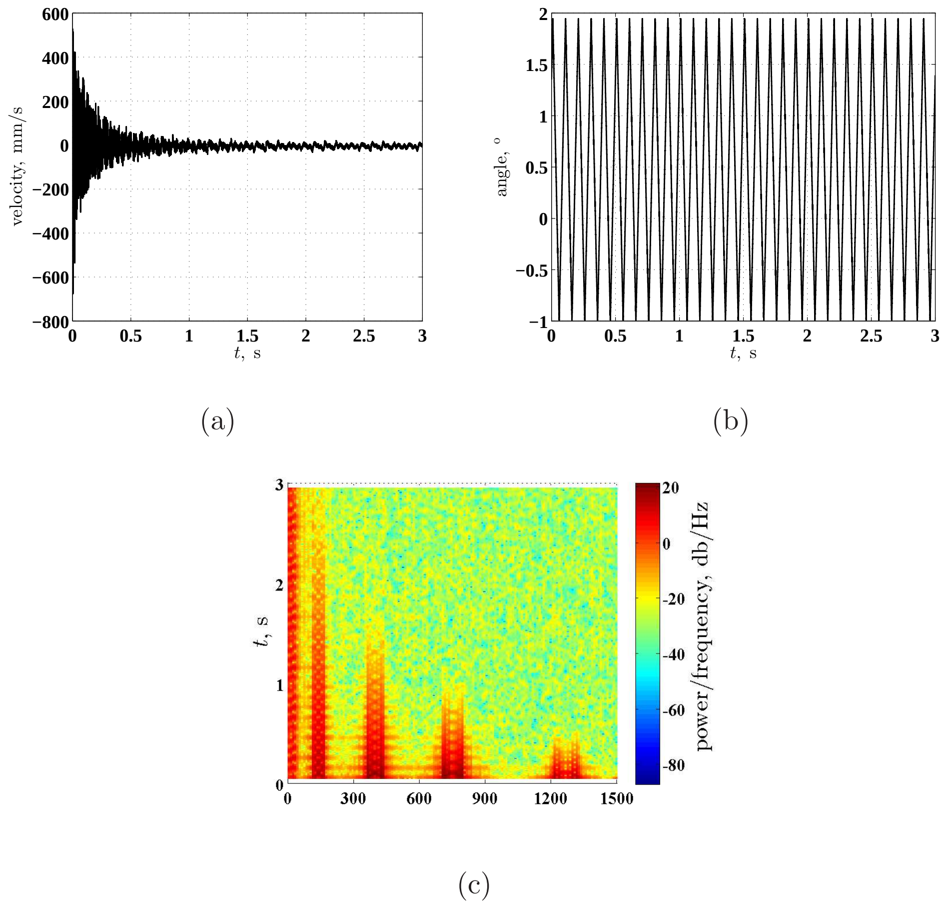

Figure 5.18: (a) Velocity response of the beam structure under the impact measured by the CSLDV system with a scan frequency of 10.0 Hz, (b) the X-mirror feedback signal with a triangular input signal and (c) a sprectrogram of the response in (a).

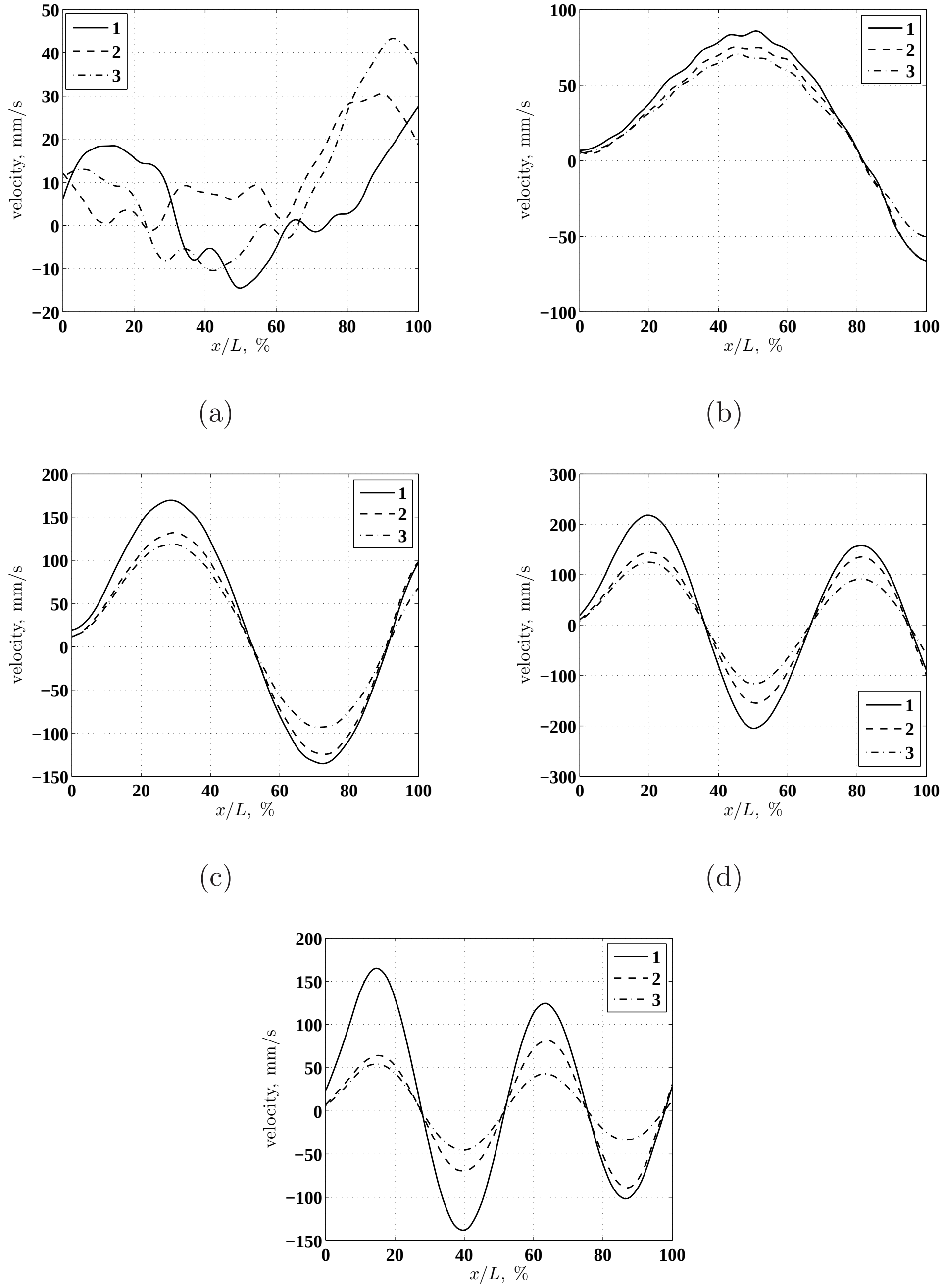

(a) (b)

(c) (d)

(e)

Figure 5.19: Obtained FRSs associated with the (a) first, (b) second, (c) third, (d) fourth and (e) fifth modes in the first three half-scan periods of the CSLDV system with a scan frequency of 10.0 Hz.

Effects of the scan frequency on qualities of FRSs of the beam structure can be seen by comparing FRSs of the structure associated with its first through fourth modes obtained by use of the CSLDV system with different scan frequencies, as shown in Figs. 5.15, 5.17 and 5.19. For the FRSs associated with the first mode, their qualities were the best when a low scan frequency of 0.1 Hz was used, and their qualities became worse when the CSLDV system had a higher scan frequency. Similar observations can be made for the FRSs associated with the second and third modes, since their qualities when the scan frequency was 1.0 Hz were better than those when the scan frequency was 10.0 Hz. One can conclude that effects of the scan frequency on qualities of FRSs are similar to those on qualities of MSs: increasing the scan frequency of a CSLDV system can lower qualities of obtained FRSs. Hence, it is recommended that a low scan frequency be used to measure response of a structure for obtaining its FRSs at a low natural frequency, as long as the scan period corresponding to the scan frequency of a CSLDV system is large enough for it to measure the response of at least one half-scan period at the natural frequency. FRDIs in Eq. (5.27) associated with the first five modes of the structure were calculated and shown in Fig. 5.20(a) through (e) using the FRSs obtained by use of the CSLDV system with different scan frequencies in different numbers of half-scan periods, and the associated auxiliary FRDI in Eq. (5.28) was calculated and shown in Fig. 5.20(f). The damage can be clearly identified near neighborhoods with consistently high values of the FRDIs and that with high values of the auxiliary FRDI. Scan frequencies and numbers of half-scan periods associated with different modes of the structure for calculating the FRDIs are listed in Table 5.3.

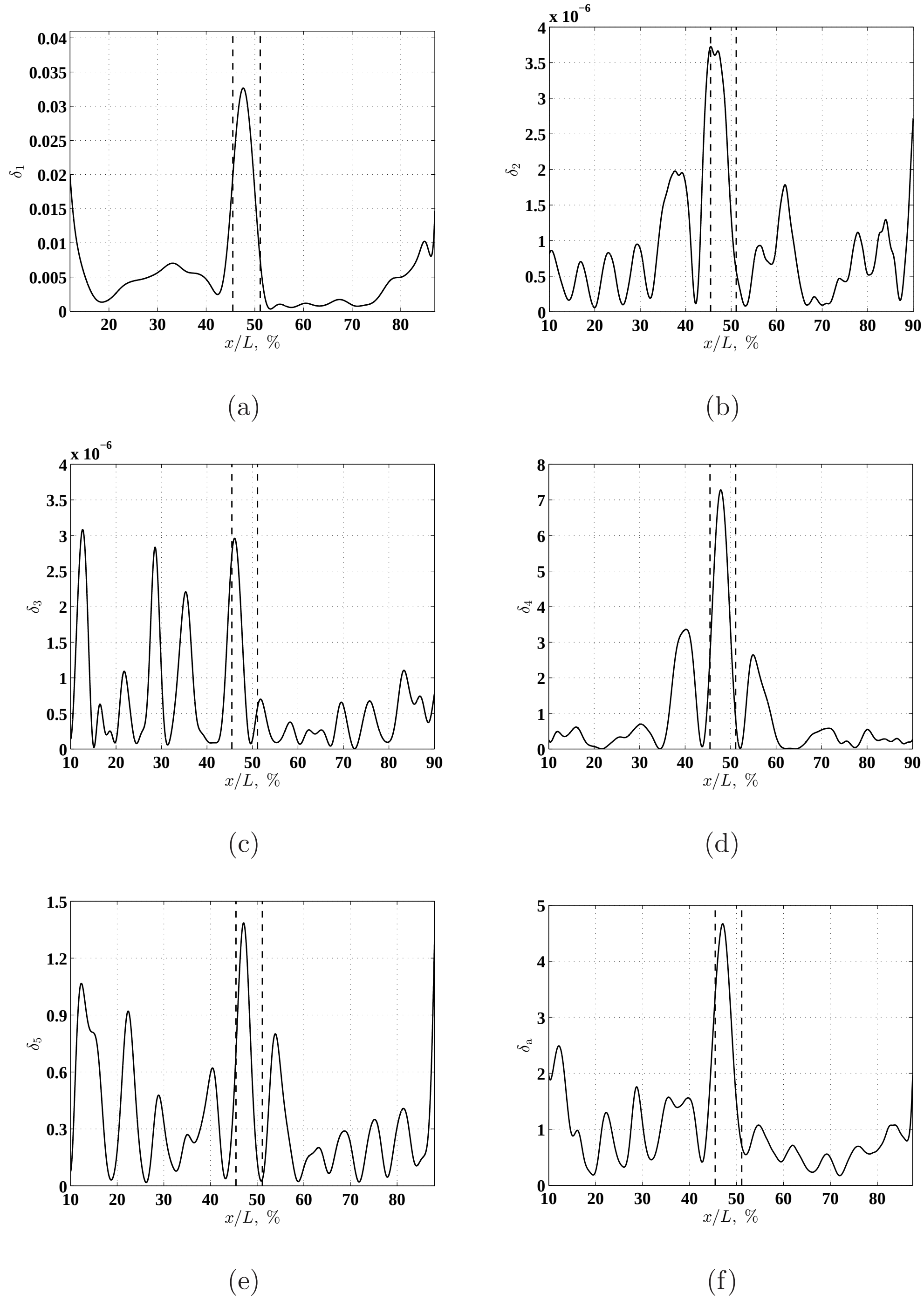

Figure 5.20: FRDIs associated with the FRSs associated with the (a) first, (b) second, (c) third, (d) fourth and (e) fifth modes, and (f) the auxiliary FRDI associated with the five modes. Locations of damage ends are indicated by two vertical dashed lines.

Table 5.3: Scan frequencies and numbers of half-scan periods for calculating FRDIs associated with the first five modes of the beam structure.

Mode	1	2	3	4	5
Scan frequency (Hz)	0.1	1.0	1.0	10.0	10.0
Number of half-scan periods	5	4	3	4	3

5.5 Conclusions

A new type of vibration shapes called a FRS is introduced in this section. A FRS can be obtained by use of a CSLDV system, and it can be obtained from the demodulation method using free response of a structure. An analytical expression of a FRS is derived for a beam structure with damping that can be modeled by the Kelvin-Voigt viscoelastic model. FRSs from the analytical expression compare well with those from a FE model. A FRDI that uses differences between curvatures of FRSs associated with a mode and those from polynomial fits is proposed, and damage regions can be accurately identified near neighboorhoods with consistently high values of FRDIs associated with different modes; an auxiliary FRDI can assist identification of the neighborhoods. A polynomial fits a FRS of a damaged beam structure whose order can be properly determined using a convergence index, and a FRS from the polynomial fit can be considered to be that of an undamaged beam structure, if the undamaged structure is geometrically smooth and made of materials that have no stiffness and mass discontinuities. It was numerically and experimentally shown that amplitudes of FRSs decrease from one half-scan period to the next, and spectrograms of response measured by a CSLDV system can be used to determine instants before which non-zero FRSs can be obtained. Effects of the scan frequency of a CSLDV system were experimentally investigated, and it was observed that a lower scan frequency could yield higher-quality FRSs and a higher scan frequency could yield lower-quality FRSs; it is recommended that a low scan frequency be used for FRSs at a low natural frequency. The proposed methodology was numerically and experimentally applied to damaged beam structures with machined thickness reductions along their lengths. Damage regions were successfully identified near neighborhoods with consistently high values of FRDIs associated with different modes and that with high values of the auxiliary FRDI.

Chapter 6

SUMMARY

This dissertation presents new methods in modal analysis and structural damage identification. Detailed theories behind the new methods have been presented. The methods developed in this dissertation have been validated in numerical and/or experimental investigations.

Chapter 2 presents two new modal analysis methods. A non-contact OMA test method is presented to measure the out-of-plane and in-plane modes of a rectangular plate using white noise acoustic excitation. It is shown that OMA can be performed when types of measurement at the measurement points and the reference point are different. In-plane modes of a plate can be identified by comparing out-of-plane and mixed CPSDs. A VMT method is developed, where an impact hammer roves over the test structure and sound pressure transducers at fixed locations are used to measure its dynamic responses. The formulation of a structurally damped structural-acoustic system in an open environment and the associated eigenvalue problem are provided. The biorthonormality relations between the left and right eigenvectors and the relations between the structural and acoustic components of the left and right eigenvectors are proved. The FRFs used in the VMT method are derived.

Chapter 3 presents new methods to accurately and efficiently calculate correlation functions, power spectra, FRFs, and IRFs. A methodology for calculating cross-correlation functions of non-negative time delays and associated half spectra is developed. Qualities of measured cross-correlation functions and associated cross-power spectra can be evaluated using a coherence function, a convergence function in the frequency domain, and a convergence index. Calculation time for one cross-correlation function from the new methodology can be greatly reduced, compared with that by directly applying its definition. A cross-correlation function from the new methodology is in perfect accordance with that by directly applying its definition, and so is the associated cross-power spectrum. A methodology for calculating discrete FRFs and IRFs is proposed. Excitation and response measurements in the proposed methodology are similar to those in EMA using burst random excitation. The methodology is computationally efficient, since matrix inversion can be avoided and calculation time can be greatly shortened due to use of the FFT and IFFT. In the methodology, fewer spectral lines are needed in calculation of associated DFTs, and accuracies of resulting FRFs and IRFs from the proposed methodology can be maintained, compared with those by directly applying the DFT to excitation and response series, which need more spectral lines. The relationship between an IRF from the proposed methodology and that from the LS method is shown.

Chapter 4 presents new methods to identify damage in beam and plate structures. Two new non-model-based methods are developed to identify embedded horizontal cracks in beams without use of any a priori information of associated undamaged beams, if the beams are geometrically smooth and made of materials that have no stiffness discontinuities. Differences between measured MSs of a damaged beam with an embedder horizontal crack and those from polynomials that fit the MSs of the damaged beam are converted to CDIs and CWTDIs, which are used to locate the crack tips. MSs from polynomials that fit the MSs of a damaged beam can well approximate those of the associated undamaged beam. The methods are then extended to plate structures. A new non-model-based plate damage identification method using measured MSs is proposed. The method can be applied to a damaged plate without use of MSs of the associated undamaged plate. Use of differences between MSs of a damaged plate and those of an associated pseudo-undamaged plate from polynomials that fit the MSs of the damaged plate is shown to be better than that between MSs of a damaged plate and those of an associated undamaged plate with respect to effectiveness of damage identification. A proper order of a polynomial fit can be determined as proposed; a polynomial fit with an order lower than the proper order for MSDIs cannot be used to identify damage and that with an order reasonably higher than the proper order can be. A new non-model-based plate damage identification method based on principal, mean and Gaussian CMSs is proposed. A multi-scale differential-geometry scheme is proposed to calculate the CMSs associated with a mode shape. The advantage of the scheme is that adverse effects of measurement noise could be alleviated with use of a larger value of the scale parameter. A larger value of the scale parameter in the scheme can manifest existence of damage in the CDIs; use of the weight function can manifest existence of damage even with a small value of the scale parameter in the scheme.

Chapter 5 presents a new type of vibration shapes called a FRS that can be obtained by use of a CSLDV system is introduced. An analytical expression of

FRSs of a damped beam structure is derived. It is shown in the analytical expression that amplitudes of FRSs exponentially decay to zero with time. Numbers of non-zero FRSs associated with a mode can be determined by use of the STFT of free response of the structure measured by a CSLDV system. A new damage identification methodology that uses FRSs is proposed for beam structures. A FRDI is defined, which consists of differences between curvatures of FRSs obtained by use of a CSLDV system and those from polynomials that fit the FRSs, and damage regions can be identified near neighborhoods with consistently high values of FRDIs associated with different modes; an auxiliary FRDI is proposed to assist identification of the neighborhoods.

Bibliography

[1] D. J. Ewins, Modal Testing: Theory, Practice and Application, 2nd Edition, Research Studies Press, Hertfordshire, UK, 2000.

[2] W. Heylen, S. Lammens, P. Sas, Modal Analysis Theory and Testing, Departement Werktuigkunde, Katholieke Universiteit, Leuven, Belgium, 1995.

[3] G. H. James, T. G. Carne, J. P. Lauffer, A. R. Nard, Modal testing using natural excitation, in: Proceedings of the 10th IMAC, San Diego, CA, USA, 1992.

[4] B. Cauberghe, P. Guillaume, P. Verboven, E. Parloo, Identification of modal parameters including unmeasured forces and transient effects, Journal of Sound and Vibration 265 (3) (2003) 609–625.

[5] P. Guillaume, P. Verboven, S. Vanlanduit, Frequency-domain maximum likelihood identification of modal parameters with confidence intervals, in: Proceedings of the international seminar on modal analysis, Vol. 1, Katholieke Universiteit Leuven, 1998, pp. 359–366.

[6] L. Zhang, R. Brincker, An overview of operational modal analysis: major development and issues.

[7] S. W. Doebling, C. R. Farrar, M. B. Prime, et al., A summary review of vibration-based damage identification methods, Shock and vibration digest 30 (2) (1998) 91–105.

[8] K. He, Vibration-based structural damage detection with applications to structures with bolted joints, Ph.D. thesis (2011).

[9] Y. F. Xu, W. D. Zhu, J. Liu, Y. M. Shao, Identification of embedded horizontal cracks in beams using measured mode shapes, Journal of Sound and Vibration 333 (23) (2014) 6273–6294.

[10] S. Rothberg, J. Baker, N. A. Halliwell, Laser vibrometry: pseudo-vibrations, Journal of Sound and Vibration 135 (3) (1989) 516–522.

[11] P. Sriram, S. Hanagud, J. Craig, N. Komerath, Scanning laser doppler technique for velocity profile sensing on a moving surface, Applied Optics 29 (16) (1990) 2409–2417.

[12] P. Sriram, S. Hanagud, J. Craig, Mode shape measurement using a scanning laser doppler vibrometer, International Journal of Analytical and Experimental Modal Analysis 5 (3) (1992) 169–178.

[13] A. Stanbridge, D. Ewins, Using a continuously-scanning laser doppler vibrometer for modal testing, in: International Modal Analysis Conference(IMAC), 14 th, Dearborn, MI, 1996, pp. 816–822.

[14] A. Stanbridge, D. Ewins, Modal testing using a scanning laser doppler vibrometer, Mechanical Systems and Signal Processing 13 (2) (1999) 255–270.

[15] A. Stanbridge, D. Ewins, A. Khan, Modal testing using impact excitation and a scanning ldv, Shock and Vibration 7 (2) (2000) 91–100.

[16] D. Di Maio, D. Ewins, Continuous scan, a method for performing modal testing using meaningful measurement parameters; part i, Mechanical Systems and Signal Processing 25 (8) (2011) 3027–3042.

[17] M. S. Allen, M. W. Sracic, A new method for processing impact excited continuous-scan laser doppler vibrometer measurements, Mechanical Systems and Signal Processing 24 (3) (2010) 721–735.

[18] S. Yang, M. S. Allen, Lifting approach to simplify output-only continuous-scan laser vibrometry, Mechanical Systems and Signal Processing 45 (2) (2014) 267–282.

[19] S. Yang, M. S. Allen, Harmonic transfer function to measure translational and rotational velocities with continuous-scan laser doppler vibrometry, Journal of Vibration and Acoustics 136 (2) (2014) 021025.

[20] A. Khan, A. B. Stanbridge, D. J. Ewins, Detecting damage in vibrating structures with a scanning ldv, Optics and Lasers in Engineering 32 (6) (1999) 583–592.

[21] M. Verhees, Experimental modal analysis of a turbine blade, Traineship Report, Technische Universiteit Eindhoven, Eindhoven, The Netherlands.

[22] S.-E. Rosenow, P. Andersen, Operational modal analysis of a wind turbine mainframe using crystal clear ssi, in: Structural Dynamics and Renewable Energy, Volume 1, Springer, 2011, pp. 153–162.

[23] C. Rebelo, E. Julio, H. Varum, A. Costa, Cable tensioning control and modal identification of a circular cable-stayed footbridge, Experimental Techniques 34 (4) (2010) 62–68.

[24] W.-X. Ren, Z.-H. Zong, Output-only modal parameter identification of civil engineering structures, Structural Engineering and Mechanics 17 (3-4) (2004) 429–444.

[25] A. Bayraktar, B. Sevim, A. Altunişik, T. Türker, Analytical and operational modal analyses of turkish style reinforced concrete minarets for structural identification, Experimental Techniques 33 (2) (2009) 65–75.

[26] R. Brincker, Arma models in modal space, in: The International Modal Analysis Conference, 1999, pp. 330–334.

[27] A. Benveniste, J.-J. Fuchs, Single sample modal identification of a nonstationary stochastic process, IEEE Transactions on Automatic Control 30 (1) (1985) 66–74.

[28] B. Peeters, G. De Roeck, Stochastic system identification for operational modal analysis: a review, Journal of Dynamic Systems, Measurement, and Control 123 (4) (2001) 659–667.

[29] R. Brincker, L. Zhang, P. Andersen, Modal identification from ambient responses using frequency domain decomposition, in: Proc. of the 18*International Modal Analysis Conference (IMAC), San Antonio, Texas, 2000.

[30] P. Guillaume, P. Verboven, S. Vanlanduit, H. Van Der Auweraer, B. Peeters, A poly-reference implementation of the least-squares complex frequency-domain estimator, in: Proceedings of IMAC, Vol. 21, 2003, pp. 183–192.

[31] B. H. Kim, N. Stubbs, T. Park, A new method to extract modal parameters using output-only responses, Journal of sound and vibration 282 (1) (2005) 215–230.

[32] D. Larsson, In-plane modal testing of a free isotropic rectangular plate, Experimental mechanics 37 (3) (1997) 339–343.

[33] R. Brincker, Modal parameters from a wind turbine wing by operational modal analysis.

[34] E. Pierro, E. Mucchi, L. Soria, A. Vecchio, On the vibro-acoustical operational modal analysis of a helicopter cabin, Mechanical Systems and Signal Processing 23 (4) (2009) 1205–1217.

[35] T. K. Caughey, M. E. J. Okelly, Classical normal modes in damped linear dynamic systems, Journal of Applied Mechanics 32 (3) (1965) 583–588.

[36] P. Mohanty, D. J. Rixen, Operational modal analysis in the presence of harmonic excitation, Journal of sound and vibration 270 (1) (2004) 93–109.

[37] B. Peeters, H. Van der Auweraer, et al., Polymax: a revolution in operational modal analysis, in: 1st International Operational Modal Analysis Conference, Copenhagen, Denmark, Apr, 2005, pp. 26–27.

[38] F. J. Fahy, P. Gardonio, Sound and structural vibration: radiation, transmission and response, Academic press, 2007.

[39] L. Cremer, M. Heckl, E. E. Ungar, Structure-borne sound.

[40] C. E. Webb, J. D. Jones, Handbook of Laser Technology and Applications: Laser design and laser systems, Vol. 2, CRC Press, 2004.

[41] R. J. Allemang, The modal assurance criterion–twenty years of use and abuse, Sound and vibration 37 (8) (2003) 14–23.

[42] H. Van der Auweraer, Structural dynamics modeling using modal analysis: applications, trends and challenges, in: Instrumentation and Measurement Technology Conference, 2001. IMTC 2001. Proceedings of the 18th IEEE, Vol. 3, IEEE, 2001, pp. 1502–1509.

[43] Q. Yang, G. Lim, R. Lin, F. Yap, H. Pang, Z. Wang, Experimental modal analysis of pbga printed circuit board assemblies, in: Electronic Packaging Technology Conference, 1997. Proceedings of the 1997 1st, IEEE, 1997, pp. 290–296.

[44] M. R. Ashory, Assessment of the mass-loading effects of accelerometers in modal testing, in: Proceedings of the 20th International Modal Analysis Conference, 2002, pp. 1027–1031.

[45] S. Vanlanduit, F. Daerden, P. Guillaume, Experimental modal testing using pressurized air excitation, Journal of sound and vibration 299 (1) (2007) 83–98.

[46] R. J. Allemang, W. R. Shapton, Using modal techniques to guide acoustic signature analysis, Tech. rep., SAE Technical Paper (1978).

[47] W. Elwali, H. Satakopan, V. Shauche, R. Allemang, A. Phillips, Modal parameter estimation using acoustic modal analysis, in: Structural Dynamics, Volume 3, Springer, 2011, pp. 23–33.

[48] A. Craggs, The transient response of coupled acousto-mechanical systems, Vol. 1421, National Aeronautics and Space Administration, 1969.

[49] H. C. Gea, Modal sensitivity analysis of coupled acoustic-structural systems, Journal of Vibration and Acoustics 119 (1997) 545.

[50] Z.-D. Ma, I. Hagiwara, Sensitivity analysis methods for coupled acoustic-structural systems part i: modal sensitivities, AIAA journal 29 (11) (1991) 1787–1795.

[51] K. Wyckaert, F. Augusztinovicz, P. Sas, Vibro-acoustical modal analysis: Reciprocity, model symmetry, and model validity, The Journal of the Acoustical Society of America 100 (5) (1996) 3172–3181.

[52] J.-T. Xing, W. Price, A mixed finite element method for the dynamic analysis of coupled fluid-solid interaction problems, in: Proceedings of the Royal Society of London A: Mathematical, Physical and Engineering Sciences, Vol. 433, The Royal Society, 1991, pp. 235–255.

[53] S. H. Sung, D. J. Nefske, D. A. Feldmaier, A structural-acoustic finite element method for predicting automobile vehicle interior road noise, in: ASME 2009 International Mechanical Engineering Congress and Exposition, American Society of Mechanical Engineers, 2009, pp. 527–534.

[54] L. Meirovitch, Principles and techniques of vibrations, Prentice Hall New Jersey, 1997.

[55] F. Fahy, Some applications of the reciprocity principle in experimental vibroacoustics, Acoustical Physics 49 (2) (2003) 217–229.

[56] W. D. Zhu, N. A. Zheng, C. N. Wong, A stochastic model for the random impact series method in modal testing, Journal of Vibration and Acoustics 129 (3) (2006) 265–275.

[57] Y. F. Xu, W. D. Zhu, Operational modal analysis of a rectangular plate using non-contact excitation and measurement, Journal of Sound and Vibration 332 (20) (2013) 4927–4939.

[58] C. Rebelo, E. Julio, H. Varum, A. Costa, Cable tensioning control and modal identification of a circular cablestayed footbridge, Experimental Techniques 34 (4) (2010) 62–68.

[59] C. R. Farrar, S. W. Doebling, P. J. Cornwell, E. G. Straser, Variability of modal parameters measured on the Alamosa Canyon Bridge, in: Proceedings of the SPIE International Society For Optical Engineering, Vol. 4, 1997, pp. 257–263.

[60] S. Rosenow, P. Andersen, Operational modal analysis of a wind turbine mainframe using crystal clear SSI, in: Proceedings of the 28th IMAC, Jacksonville, FL, USA, 2010.

[61] W. X. Ren, Z. H. Zong, Output-only modal parameter identification of civil engineering structures, Structural Engineering and Mechanics 17 (3–4) (2004) 429–444.

[62] A. Bayraktar, B. Sevim, A. C. Altuniik, T. Trker, Analytical and operational modal analyses of Turkish style reinforced concrete minarets for structural identification, Experimental Techniques 33 (2) (2009) 65–75.

[63] B. Cauberghe, Applied frequency-domain system identification in the field of experimental and operational modal analysis, Ph.D. thesis, Vrije Universiteit Brussel (May 2004).

[64] S. R. Ibraham, Efficient random decrement computation for identification of ambient responses, in: Proceedings of the 19th IMAC, Kissimmee, FL, USA, 2001.

[65] B. Peeters, G. De Roeck, Stochastic system identification for operational modal analysis: a review, Journal of Dynamic Systems, Measurement, and Control 123 (4) (2001) 659–667.

[66] R. Brincker, L. Zhang, P. Andersen, Modal identication from ambient responses using frequency domain decomposition, in: Proceedings of the 18th IMAC, San Antonio, TX, USA, 2000.

[67] Y. Yang, S. Nagarajaiah, Output-only modal identification with limited sensors using sparse component analysis, Journal of Sound and Vibration 332 (19) (2013) 4741–4765.

[68] Y. Yang, S. Nagarajaiah, Time-frequency blind source separation using independent component analysis for output-only modal identification of highly damped structures, Journal of Structural Engineering 139 (10) (2012) 1780–1793.

[69] W. L. Briggs, V. E. Henson, The DFT: An Owners' Manual for the Discrete Fourier Transform, Society for Industrial and Applied Mathematics, Philadelphia, PA, 1987.

[70] W. H. Press, B. P. Flannery, S. A. Teukolsky, W. T. Vetterling, Numerical Recipes in C: The Art of Scientific Computing, 2nd Edition, Cambridge University Press, Cambridge, UK, 1992.

[71] L. Meirovitch, Principles and Techniques of Vibrations, Prentice-Hall Publishing Company, Upper Saddle River, NJ, 1996.

[72] W. M. Telford, L. P. Geldart, R. E. Sheriff, Applied Geophysics, 2nd Edition, Cambridge University Press, Cambridge, UK, 1990.

[73] J. M. Liu, W. D. Zhu, Q. H. Lu, G. X. Ren, An efficient iterative algorithm for accurately calculating impulse response functions in modal testing, Journal of Vibration and Acoustics 133 (6) (2011) 064505.

[74] M. J. Hinich, A statistical theory of signal coherence, Oceanic Engineering, IEEE Journal of 25 (2) (2000) 256–261.

[75] The Mathworks. Inc., Natick, MA, MATLAB User's Guide (2010).

[76] W. Fladung, R. Rost, Application and correction of the exponential window for frequency response functions, Mechanical Signal and Signal Processing 11 (1) (1997) 23–36.

[77] LMS International, Leuven, Belgium, Manual on LMS Test.Lab 9b (2008).

[78] Y. F. Xu, J. M. Liu, W. D. Zhu, Accurate and efficient calculation of discrete correlation functions and power spectra, Journal of Sound and Vibration 347 (2015) 246–265.

[79] S. S. Rao, Mechanical Vibrations, 5th Edition, Prentice Hall, Upper Saddle River, NJ, 2010.

[80] A. Jerri, Integral and Discrete Transforms with Applications and Error Analysis, CRC Press, Boca Raton, FL, 1992.

[81] M. I. Friswell, Damage identification using inverse methods, Philosophical Transactions of the Royal Society of London A: Mathematical, Physical and Engineering Sciences 365 (1851) (2007) 393–410.

[82] K. He, W. D. Zhu, Detection of damage and loosening of bolted connections in structures using changes in natural frequencies, ASNT Materials Evaluation 68 (6) (2010) 721–732.

[83] K. He, W. D. Zhu, Vibration-based structural damage detection method and its applications to engineering structures, International Journal of Smart and Nano Materials 2 (3) (2011) 194–218.

[84] C. Surace, R. Archibald, R. Saxena, On the use of the polynomial annihilation edge detection for locating cracks in beam-like structures, Computers & Structures 114 (2013) 72–83.

[85] W. Fan, P. Qiao, Vibration-based damage identification methods: a review and comparative study, Structural Health Monitoring 10 (1) (2011) 83–111.

[86] A. K. Pandey, M. Biswas, M. M. Samman, Damage detection from changes in curvature mode shapes, Journal of Sound and Vibration 145 (2) (1991) 321–332.

[87] C. P. Ratcliffe, W. J. Bagaria, Vibration technique for locating delamination in a composite beam, AIAA journal 36 (6) (1998) 1074–1077.

[88] C. P. Ratcliffe, A frequency and curvature based experimental method for locating damage in structures, Journal of Vibration and Acoustics 122 (3) (2000) 324–329.

[89] M.-K. Yoon, D. Heider, J. W. Gillespie Jr, C. P. Ratcliffe, R. M. Crane, Local damage detection with the global fitting method using mode shape data in notched beams, Journal of Nondestructive Evaluation 28 (2) (2009) 63–74.

[90] M.-K. Yoon, D. Heider, J. W. Gillespie Jr, C. P. Ratcliffe, R. M. Crane, Local damage detection with the global fitting method using operating deflection shape data, Journal of Nondestructive Evaluation 29 (1) (2010) 25–37.

[91] E. Sazonov, P. Klinkhachorn, Optimal spatial sampling interval for damage detection by curvature or strain energy mode shapes, Journal of sound and vibration 285 (4) (2005) 783–801.

[92] M. Cao, P. Qiao, Novel laplacian scheme and multiresolution modal curvatures for structural damage identification, Mechanical Systems and Signal Processing 23 (4) (2009) 1223–1242.

[93] E. Douka, S. Loutridis, A. Trochidis, Crack identification in beams using wavelet analysis, International Journal of Solids and Structures 40 (13) (2003) 3557–3569.

[94] M. Rucka, K. Wilde, Application of continuous wavelet transform in vibration based damage detection method for beams and plates, Journal of Sound and Vibration 297 (3) (2006) 536–550.

[95] M. Solís, M. Algaba, P. Galvín, Continuous wavelet analysis of mode shapes differences for damage detection, Mechanical Systems and Signal Processing 40 (2) (2013) 645–666.

[96] A. Żak, M. Krawczuk, W. Ostachowicz, Numerical and experimental investigation of free vibration of multilayer delaminated composite beams and plates, Computational Mechanics 26 (3) (2000) 309–315.

[97] J. Lee, Free vibration analysis of delaminated composite beams, Computers & Structures 74 (2) (2000) 121–129.

[98] M.-H. Shen, J. Grady, Free vibrations of delaminated beams, AIAA journal 30 (5) (1992) 1361–1370.

[99] A. C. Okafor, K. Chandrashekhara, Y. Jiang, Delamination prediction in composite beams with built-in piezoelectric devices using modal analysis and neural network, Smart materials and structures 5 (3) (1996) 338.

[100] Q. Wang, N. Wu, Detecting the delamination location of a beam with a wavelet transform: an experimentalstudy, Smart Materials and Structures 20 (1) (2010) 012002.

[101] S. Mallat, A wavelet tour of signal processing, Academic press, 1999.

[102] M. Cao, L. Cheng, Z. Su, H. Xu, A multi-scale pseudo-force model in wavelet domain for identification of damage in structural components, Mechanical Systems and Signal Processing 28 (2012) 638–659.

[103] B. Schwarz, S. Richardson, M. Richardson, Using mode shapes for real time ods animation, in: Topics in Modal Analysis, Volume 10, Springer, 2015, pp. 103–113.

[104] J. Nocedal, S. J. Wright, Numerical optimization 2nd (2006).

[105] Y. Xu, W. Zhu, Operational modal analysis of a rectangular plate using non-contact excitation and measurement, Journal of Sound and Vibration 332 (20) (2013) 4927–4939.

[106] M.-K. Yoon, D. Heider, J. W. Gillespie Jr, C. P. Ratcliffe, R. M. Crane, Local damage detection using the two-dimensional gapped smoothing method, Journal of Sound and Vibration 279 (1) (2005) 119–139.

[107] Y. Zhang, L. Wang, S. T. Lie, Z. Xiang, Damage detection in plates structures based on frequency shift surface curvature, Journal of Sound and Vibration 332 (25) (2013) 6665–6684.

[108] W. Xu, M. Cao, W. Ostachowicz, M. Radzieński, N. Xia, Two-dimensional curvature mode shape method based on wavelets and teager energy for damage detection in plates, Journal of Sound and Vibration 347 (2015) 266–278.

[109] D. Wu, S. S. Law, Damage localization in plate structures from uniform load surface curvature, Journal of Sound and Vibration 276 (1) (2004) 227–244.

[110] P. Qiao, K. Lu, W. Lestari, J. Wang, Curvature mode shape-based damage detection in composite laminated plates, Composite Structures 80 (3) (2007) 409–428.

[111] C. Surace, R. Saxena, M. Gherlone, H. Darwich, Damage localisation in plate like-structures using the two-dimensional polynomial annihilation edge detection method, Journal of Sound and Vibration 333 (21) (2014) 5412–5426.

[112] J. Nocedal, S. Wright, Numerical optimization, Springer Science & Business Media, 2006.

[113] I. Cox, M. Gaudard, Discovering Partial Least Squares with JMP, SAS Institute, 2013.

[114] Y. F. Xu, W. D. Zhu, Operational modal analysis of a rectangular plate using non-contact excitation and measurement, Journal of Sound and Vibration 332 (20) (2013) 4927–4939.

[115] W. D. Zhu, K. He, Detection of damage in space frame structures with l-shaped beams and bolted joints using changes in natural frequencies, Journal of Vibration and Acoustics 135 (5) (2013) 051001.

[116] K. He, W. D. Zhu, Detecting loosening of bolted connections in a pipeline using changes in natural frequencies, Journal of Vibration and Acoustics 136 (3) (2014) 034503.

[117] G. Teza, A. Galgaro, F. Moro, Contactless recognition of concrete surface damage from laser scanning and curvature computation, NDT & E International 42 (4) (2009) 240–249.

[118] C.-C. Chang, L.-W. Chen, Damage detection of a rectangular plate by spatial wavelet based approach, Applied Acoustics 65 (8) (2004) 819–832.

[119] M. Rucka, K. Wilde, Application of continuous wavelet transform in vibration based damage detection method for beams and plates, Journal of Sound and Vibration 297 (3) (2006) 536–550.

[120] E. Douka, S. Loutridis, A. Trochidis, Crack identification in plates using wavelet analysis, Journal of sound and vibration 270 (1) (2004) 279–295.

[121] P. Cornwell, S. W. Doebling, C. R. Farrar, Application of the strain energy damage detection method to plate-like structures, Journal of Sound and Vibration 224 (2) (1999) 359–374.

[122] B. O'neill, Elementary differential geometry, 2nd Edition, Academic press, 2006.

[123] S. Timoshenko, S. Woinowsky-Krieger, Theory of Plates and Shells, 2nd Edition, McGraw-hill New York, 1959.

[124] M. Meyer, M. Desbrun, P. Schröder, A. H. Barr, Discrete differential-geometry operators for triangulated 2-manifolds, in: Visualization and mathematics III, Springer, 2003, pp. 35–57.

[125] Y. F. Xu, W. D. Zhu, J. Liu, Y. M. Shao, Identification of embedded horizontal cracks in beams using measured mode shapes, Journal of Sound and Vibration 333 (23) (2014) 6273–6294.

[126] C. N. Wong, W. D. Zhu, G. Y. Xu, On an iterative general-order perturbation method for multiple structural damage detection, Journal of Sound and Vibration 273 (1) (2004) 363–386.

[127] G. Y. Xu, W. D. Zhu, B. H. Emory, Experimental and numerical investigation of structural damage detection using changes in natural frequencies, Journal of Vibration and Acoustics 129 (6) (2007) 686–700.

[128] P. Sriram, S. Hanagud, J. Craig, N. Komerath, Scanning laser doppler technique for velocity profile sensing on a moving surface, Applied Optics 29 (16) (1990) 2409–2417.

[129] P. Sriram, S. Hanagud, J. Craig, Mode shape measurement using a scanning laser doppler vibrometer 7 (3) (1992) 169–178.

[130] A. Stanbridge, D. Ewins, Using a continuously-scanning laser doppler vibrometer for modal testing, in: Proceedings of the International Modal Analysis Conference, 1996, pp. 816–822.

[131] A. Stanbridge, D. Ewins, Modal testing using a scanning laser doppler vibrometer, Mechanical Systems and Signal Processing 13 (2) (1999) 255–270.

[132] A. Stanbridge, D. Ewins, A. Khan, Modal testing using impact excitation and a scanning ldv, Shock and Vibration 7 (2) (2000) 91–100.

[133] D. Di Maio, D. Ewins, Continuous scan, a method for performing modal testing using meaningful measurement parameters: Part i, Mechanical Systems and Signal Processing 25 (8) (2011) 3027–3042.

[134] M. S. Allen, M. W. Sracic, A new method for processing impact excited continuous-scan laser doppler vibrometer measurements, Mechanical Systems and Signal Processing 24 (3) (2010) 721–735.

[135] S. Yang, M. S. Allen, Lifting approach to simplify output-only continuous-scan laser vibrometry, Mechanical Systems and Signal Processing 45 (2) (2014) 267–282.

[136] A. Khan, A. B. Stanbridge, D. J. Ewins, Detecting damage in vibrating structures with a scanning ldv, Optics and Lasers in Engineering 32 (6) (1999) 583–592.

[137] D.-M. Chen, Y. F. Xu, W. D. Zhu, Damage identification of beams using a continuous scanning laser doppler vibrometer system, Journal of Vibration and Acoustics.

[138] S. S. Rao, Mechanical Vibrations, 4th Edition, Pearson Prentice Hall, 2004.

[139] F. Hlawatsch, F. Auger, Time-frequency Analysis, John Wiley & Sons, 2013.

[140] M. U. Guide, The mathworks, Inc., Natick, MA 5 (1998) 333.

[141] M. W. Sracic, M. S. Allen, Experimental investigation of the effect of speckle noise on continuous scan laser doppler vibrometer measurements, in: Proceedings of the International Modal Analysis Conference, 2009, pp. 9–12.

[142] S. Yang, Modal identification of linear time periodic systems with applications to continuous-scan laser doppler vibrometry, Ph.D. thesis, Univeristy of Wisconsin-Madison (2013).